**BRANCH POINT MITIGATION OF THERMAL BLOOMING
PHASE COMPENSATION INSTABILITY**

THESIS

Mark F. Spencer, Civilian

AFIT/OSE/ENP/11-M02

**DEPARTMENT OF THE AIR FORCE
AIR UNIVERSITY**

AIR FORCE INSTITUTE OF TECHNOLOGY

Wright-Patterson Air Force Base, Ohio

APPROVED FOR PUPLIC RELEASE; DISTRIBUTION UNLIMITED

AFIT/OSE/ENP/11-M02

**BRANCH POINT MITIGATION OF THERMAL BLOOMING
PHASE COMPENSATION INSTABILITY**

THESIS

Presented to the Faculty

Department of Engineering Physics

Graduate School of Engineering and Management

Air Force Institute of Technology

Air University

Air Education and Training Command

In Partial Fulfillment of the Requirements for the

Degree of Master of Science in Optical Sciences and Engineering

Mark F. Spencer, BS

Civilian

March, 2011

BRANCH POINT MITIGATION OF THERMAL BLOOMING
PHASE COMPENSATION INSTABILITY

Mark F. Spencer, BS

Civilian

Approved:

_____   _____
Salvatore J. Cusumano, PhD (Chairman)   Date

_____   _____
Steven T. Fiorino, PhD (Member)   Date

_____   _____
Maj Jason D. Schmidt (Member)   Date

AFIT/OSE/ENP/11-M02

Abstract

Thermal blooming can have a major impact on high-energy laser (HEL) beam propagation in the atmosphere. In theory, an adaptive-optics (AO) system can mitigate the nonlinear optical effects induced by thermal blooming; however, when a single deformable mirror is used for phase-only compensation, analysis predicts the possibility of instability. This instability is appropriately termed phase compensation instability (PCI) and arises with the time-dependent development of spatial perturbations found within the HEL beam. These spatial perturbations act as local hot spots that produce negative-lens-like optical effects in the atmosphere. An AO system corrects for the hot spots by applying positive-lens-like phase compensations. In turn, this increases the strength of the thermal blooming and leads to a runaway condition, i.e. positive feedback in the AO control loop. This study uses a series of computational wave-optics experiments to explore the conditions for insipient PCI. Horizontal propagation is modeled with the effects of extinction, thermal blooming, and turbulence for a focused Gaussian beam. In addition, a nominal AO system is used for phase compensation from a point source beacon. Results show that the development of branch points under strong thermal blooming reduces the possibility of PCI. Parameters within the AO system, such as the number of actuators on the deformable mirror and the resolution of the wavefront sensor, are varied to determine the impact of branch points in the development of PCI.

To Mom and Dad

Acknowledgments

First and foremost, I would like to thank my thesis advisor, Dr. Cusumano. I think we have come a long way as advisor and advisee. We continually learn from one another, and I greatly appreciate the countless hours we spent together reviewing this thesis. Without his expertise in the field of directed energy, our research together would lack creativity and continuity. For these reasons, I look forward to completing my dissertation work under his advisement. Secondly, I would like to thank my committee members, Dr. Fiorino and Maj Schmidt. Dr. Fiorino taught me more about the atmosphere and its constituents than I ever thought I would need to know. Nonetheless, I am grateful for his advice, as it has come in handy, especially in completing this thesis. Maj Schmidt and I have had a unique student professor relationship, as I have had him for five different optics classes here at the Air Force Institute of Technology (AFIT). For this, I am extremely grateful. His expertise in the optical sciences and his ability to teach has greatly impacted my education and my ability to effectively perform research.

I would also like to thank the OPTECS research group here at AFIT. They continually set the bar high and have given me the necessary feedback to communicate my research effectively. In particular, I would like to thank Capt Hyde for his mathematical advise, Maj Wheeler and Maj Tellez for their senior student leadership, and Capt Pellizzari for his friendship and his award winning thesis work. All of these components greatly impacted my own abilities in completing this thesis. Furthermore, I would like to thank Lt Col Hawks and Dr. Marciniak, as I have had them as professors

for a combined total of eight different optics courses here at AFIT. Without their teaching efforts, my research abilities would not have grown into what they are today.

Lastly, I would like to thank my industry support. The help I received from the Optical Sciences Company (tOSC) essentially made this thesis possible. Their support of academia, especially at AFIT, is unmatched. Dr. Brennan of tOSC was patient enough to satisfy all of my requests for technical reports written by members of the tOSC team. The attention to detail contained in these technical reports greatly impacted my own abilities as a student and researcher. I would also like to thank Dr. Mann of tOSC for his countless emails back and forth. His effort in consolidating all of tOSC's research in thermal blooming over the past 30 years made his expertise of particular value and is a point which cannot be overlooked in this thesis. Moreover, I would like to thank Mr. Albertine for his interest and support in my research efforts. His constructive comments at conferences and by email helped me to progress my research, particularly when I was stuck in my own development. Last but not least, I would like to thank Mr. Barchers of Nutronics, Inc. We had the privilege of essentially working on the same problem at the same time. His approach was quite different than my own and I learned a lot from his creativity and willingness to share ideas. Additionally, his constructive comments and ability to find inconsistencies in my research greatly impacted this thesis. Without his intuition into the problem, this thesis would have lacked some of the finishing touches that I am proud to call my own. For all the help I received from everybody, I am extremely grateful.

<div align="center">Mark F. Spencer</div>

Table of Contents

List of Figures

xii

xiii

List of Tables

BRANCH POINT MITIGATION OF THERMAL BLOOMING

PHASE COMPENSATION INSTABILITY

1. Introduction

According to Major General David Scott, USAF, directed energy (DE) weapons
will be the most significant technological change most of us will see in our military
careers [1]. The innovation DE weapons provide is truly inspiring, as they could
revolutionize the way conflicts are handled and resolved. Specifically, DE weapons
present game-changing capabilities by offering weapons with varying lethality, speed-of-
light delivery, and unparalleled precision. It is exciting to be part of the young field of
DE, and it is important that the technology DE offers makes its way onto the battlefield in
the near future.

Half a century has passed since the invention of the laser by Theodore Maiman in
1960. Since then, the laser has undergone many advances, particularly in the field of DE.
Maiman's ruby laser originally boasted only a few milliwatts of power; however, by the
1970's, laser powers reached the megawatt level [2]. Thus, the term high-energy laser
(HEL) was coined.

The potential HEL weapons have to defend against multiple threats at the same
time has been a powerful lure for military research [3]. Associated with this claim is a
short list of legacy projects, some more successful than others. The flagship for HEL
weapon systems in the United States is of course the Airborne Laser Testbed (ALTB).

Completed in late 2009, the ALTB hosts a megawatt class chemical laser on a Boeing 747 freighter.

On 11 February 2010, the ALTB was successful in shooting down a theater-ballistic missile while still in boost phase. This demonstration test was the first of its kind. From a technological standpoint, no other weapon system in the world presents the tactical strength of the ALTB [3].

There are still multiple logistics burdens to overcome in the near future, in terms of fielding HEL weapons on the battlefield. This is especially the case when it comes to HEL weapon systems needed for ground- and or sea-based tactical-engagement scenarios. The Tactical High-Energy Laser (THEL) is the current state of the art when it comes to ground-based HEL weapon systems.

Built by a joint effort between the US Army and Israel, THEL hosts a chemical class laser in a fixed location. In 2000, 2001, and 2002, THEL shot down multiple Katyusha rockets in a test environment and clearly demonstrated its ability to safeguard against multiple short-range threats. Nonetheless, future designs for tactical ground-based HEL weapons will require mobility, high-powered solid-state lasers, and adaptive optics (AO) systems.

Such design considerations are currently being implemented on the High Energy Laser Technology Demonstrator project (HEL TD)—a three-phase ground-based program being headed by the US Army [3]. The goal here is to extend the HEL weapon's range past the current abilities of THEL, while increasing power on target.

With the desire to increase system performance come engineering constraints. These engineering constraints must be overcome in the near future to see that the

technology HEL weapons offer makes its way onto the battlefield. The research presented in this thesis brings us one step closer to this ultimate goal.

1.1 Problem Statement

The atmosphere can significantly degrade a HEL weapon's ability to deposit energy on target. One particular atmospheric effect is termed thermal blooming and is particularly detrimental in ground- and or sea-based tactical engagement scenarios for laser weapons. Thermal blooming results from the heating of molecules and dust particles as the HEL beam travels or ―propagates" through the atmosphere. An AO system can be used to mitigate the detrimental effects of thermal blooming; however, there is the potential for instability. This instability is termed phase compensation instability or PCI and results from a positive feedback mechanism in the AO system.

Thermal blooming causes a negative-lens-like optical effect in the atmosphere that blooms energy out of the beam. An obvious result from this blooming mechanism is that the HEL weapon is unable to deposit the total energy on target. An AO system corrects for the effects of thermal blooming by applying a positive-lens-like compensation to the HEL beam. In theory, by focusing the HEL beam, this should override the blooming.

Unfortunately, focusing the HEL beam only concentrates the energy contained within the beam and heats the surrounding atmosphere even more. As such, more thermal blooming is created in the atmosphere. The AO system attempts to correct for the increased blooming with even more positive-lens-like compensation and the process reinforces itself, ultimately driving the HEL weapon system to failure through PCI.

Past research efforts have studied PCI in depth; however, there is still a lot to be discovered in terms of characterizing its detrimental effects. The research conducted here, attempted to determine bounds for the onset of PCI. In so doing, an additional limitation was discovered involving branch points. The limitation of branch points was not well characterized in the literature for thermal blooming prior to this research effort. Branch points severely degrade an AO system in its ability to ―correct‖ for thermal blooming. As a result, PCI is mitigated. The discovery of branch point mitigation of PCI serves as a significant contribution to the DE community.

1.2 Thesis Overview

In this thesis, the results from a series of computational wave-optics experiments are presented. In order to explain the significance of these results, a thorough literature review and accompanying theory is presented. This is done in chapter two. In chapter three, the setup and exploration of the parameter space is presented. The goal here is to thoroughly bound the problem. Chapter four provides analysis of the obtained results. Here, the impact of spatial resolution and branch points on insipient PCI is discussed. The conclusion for the thesis is presented in chapter five. Future research ideas are also given. The analysis presented in this thesis will hopefully provide future research efforts in thermal blooming and PCI with a thorough overview of the problem.

2. Theory and Literature Review

This chapter provides an overview of the theory needed to complete a series of wave-optics experiments which search for the conditions of insipient PCI. For this purpose, each aspect of the problem is thoroughly discussed. Many references are also given, so that future research efforts can benefit from the overview provided here.

2.1 High Energy Laser Beam Propagation in the Atmosphere

The split-step beam propagation method or the beam propagation method (BPM) is a numerical algorithm used to simulate the propagation of optical disturbances through various non-vacuum optical media. This section investigates how the BPM is used to simulate HEL beam propagation in the atmosphere. Analysis of the BPM is found throughout the literature [4,5,6,7,8,9]; however, the derivation included here will combine the ideas from previous work, so that each component of simulating HEL beam propagation in the atmosphere is understood from quasi first principles. Specifically, the BPM breaks the simulation of HEL beam propagation in the atmosphere into user defined partial propagations with multiple atmospheric effects including extinction, thermal blooming, and optical turbulence. Using the BPM provides both speed and accuracy and is the preferred method for numerous computational wave-optics codes.

2.1.1 Inhomogeneous Wave Equation

The investigation of using the BPM to simulate HEL beam propagation in the atmosphere starts by examining the principles of electricity and magnetism governed by Maxwell's equations. For this purpose, the conditions describing the optical medium determine the form in which Maxwell's equations are written. The atmosphere is

typically described by a linear, dispersive, inhomogeneous, isotropic, attenuating, and non-magnetic optical medium; therefore, Maxwell's Equations, in rationalized MKS units, take the form:

$$\nabla \times \mathcal{H}(\mathbf{r},t) = \frac{\partial \mathcal{D}(\mathbf{r},t)}{\partial t} \tag{1}$$

$$\nabla \times \mathcal{E}(\mathbf{r},t) = -\frac{\partial \mathcal{B}(\mathbf{r},t)}{\partial t} \tag{2}$$

$$\nabla \cdot \mathcal{D}(\mathbf{r},t) = 0 \tag{3}$$

$$\nabla \cdot \mathcal{B}(\mathbf{r},t) = 0. \tag{4}$$

Here, $\mathcal{E}(\mathbf{r},t)$ and $\mathcal{H}(\mathbf{r},t)$ are, respectively, the electric- and magnetic-field vectors of free space, dependent on position $\mathbf{r} = (x, y, z)$, and time t. The two additional position- and time-dependent vectors, $\mathcal{D}(\mathbf{r},t)$ and $\mathcal{B}(\mathbf{r},t)$, are, respectively, the electric- and magnetic-flux densities of the atmosphere. There are also the constitutive relations:

$$\mathcal{D}(\mathbf{r},t) = \varepsilon(\mathbf{r},t)\mathcal{E}(\mathbf{r},t) \tag{5}$$

$$\mathcal{B}(\mathbf{r},t) = \mu_0 \mathcal{H}(\mathbf{r},t) \tag{6}$$

where $\varepsilon(\mathbf{r},t)$ is a parameter known as the position- and time-dependent electric permittivity of the atmosphere, and μ_0 is a constant known as the permeability of free space. Equations (1)-(6) fully describe how the principles of electricity and magnetism relate to the atmosphere.

The goal now is to discover the inhomogeneous wave equation by manipulating Eqs. (1)-(6). In general, the inhomogeneous wave equation describes how an electric-

field vector $\mathcal{E}(\mathbf{r},t)$ propagates in the atmosphere. Taking the curl of Eq. (2) and using

Eq. (1), Eq. (6), and the vector identity,

$$\nabla \times (\nabla \times \mathbf{W}) = \nabla(\nabla \cdot \mathbf{W}) - \nabla^2 \mathbf{W},$$

the following equation is obtained:

$$\nabla \left[\nabla \cdot \mathcal{E}(\mathbf{r},t) \right] - \nabla^2 \mathcal{E}(\mathbf{r},t) = -\mu_0 \frac{\partial^2 \left[\varepsilon(\mathbf{r},t)\mathcal{E}(\mathbf{r},t) \right]}{\partial t^2}. \tag{7}$$

Note that a similar equation exists in terms of the magnetic-field vector $\mathcal{H}(\mathbf{r},t)$;

however, its analysis is neglected in the present discussion, since the atmosphere behaves

like a non-magnetic optical medium. In addition, the electric-field vector $\mathcal{E}(\mathbf{r},t)$ and the

electric permittivity $\varepsilon(\mathbf{r},t)$ are related via Eq. (3) and Eq. (5), where

$$\nabla \cdot \mathcal{E}(\mathbf{r},t) = -\mathcal{E}(\mathbf{r},t) \cdot \frac{\nabla \varepsilon(\mathbf{r},t)}{\varepsilon(\mathbf{r},t)} = -\mathcal{E}(\mathbf{r},t) \cdot \nabla \ln \left[\varepsilon(\mathbf{r},t) \right]. \tag{8}$$

Substituting Eq. (8) into the first term of Eq. (7), provides what is known as the

inhomogeneous wave equation:

$$\nabla^2 \mathcal{E}(\mathbf{r},t) + \nabla \left\{ \mathcal{E}(\mathbf{r},t) \cdot \nabla \ln \left[\varepsilon(\mathbf{r},t) \right] \right\} - \mu_0 \frac{\partial^2 \left[\varepsilon(\mathbf{r},t)\mathcal{E}(\mathbf{r},t) \right]}{\partial t^2} = 0. \tag{9}$$

Equation (9) can be rewritten in terms of the position- and time-dependent index of

refraction $n(\mathbf{r},t)$ of the atmosphere using the following relationship:

$$\varepsilon(\mathbf{r},t) = \varepsilon_0 n^2(\mathbf{r},t), \tag{10}$$

where ε_0 is a constant known as the permittivity of free space. Now, the inhomogeneous

wave equation takes the form:

$$\nabla^2\mathcal{E}(\mathbf{r},t)+2\nabla\left\{\mathcal{E}(\mathbf{r},t)\boldsymbol{\cdot}\nabla\ln\left[n(\mathbf{r},t)\right]\right\}-\frac{1}{c_0^2}\frac{\partial^2\left[n^2(\mathbf{r},t)\mathcal{E}(\mathbf{r},t)\right]}{\partial t^2}=0,\qquad(11)$$

where $c_0=1/\sqrt{\varepsilon_0\mu_0}$ is the speed of light in free space. Equation (11) fully describes how

an electric-field vector $\mathcal{E}(\mathbf{r},t)$ propagates in the atmosphere with an index of refraction

$n(\mathbf{r},t)$.

Further simplifications are often made to Eq. (11), which differs from the form of

the homogenous wave equation with the inclusion of the second term. For this purpose,

the second term is omitted in the analysis. The spatial variations in the index of

refraction $n(\mathbf{r},t)$ are often considered negligible in comparison with those of the electric-

field vector $\mathcal{E}(\mathbf{r},t)$ [6,10,11]. Therefore, the first term in Eq. (11) is dominant over the

second term, and the inhomogeneous wave equation takes a form similar to the

homogeneous wave equation, where

$$\nabla^2\mathcal{E}(\mathbf{r},t)-\frac{1}{c_0^2}\frac{\partial^2\left[n^2(\mathbf{r},t)\mathcal{E}(\mathbf{r},t)\right]}{\partial t^2}=0.\qquad(12)$$

Equation (12) still involves the position- and time-dependent index of refraction $n(\mathbf{r},t)$

of the atmosphere and differs from the homogenous wave equation in that respect.

2.1.2 Index of Refraction of the Atmosphere

Up to this point in the analysis, there has been no discussion given as to the

composition of the index of refraction $n(\mathbf{r},t)$ of the atmosphere included in Eq. (12).

For this purpose, the index of refraction $n(\mathbf{r},t)$ of the atmosphere can be written

mathematically as a complex number using the following relationship [12]:

8

$$n(\mathbf{r},t) = n_R(\mathbf{r},t) + in_I(\mathbf{r},t), \tag{13}$$

where $n_R(\mathbf{r},t)$ and $n_I(\mathbf{r},t)$ are the real and imaginary components, respectively. This is done to account for refraction and extinction effects in the atmosphere as will become apparent with the analysis presented throughout the remainder of this chapter.

The real component $n_R(\mathbf{r},t)$ of Eq. (13) accounts for refraction effects. In practice, the real component $n_R(\mathbf{r},t)$ of Eq. (13) is further expanded, so that

$$n_R(\mathbf{r},t) = n_0 + \Delta n(\mathbf{r},t), \tag{14}$$

where $\Delta n(\mathbf{r},t)$ is a position- and time-dependent parameter known as the change in the index of refraction. The expansion of the real component $n_R(\mathbf{r},t)$, as given in Eq. (14), provides a mechanism needed to study refraction effects in the atmosphere caused because of deviations from the ambient index of refraction n_0 [6,7,13] These deviations are accounted for with the addition of the change in the index of refraction $\Delta n(\mathbf{r},t)$.

To fully account for extinction effects, the imaginary component $n_I(\mathbf{r},t)$ of Eq. (13) is written in terms of a position and time-dependent parameter known as the extinction coefficient $\alpha(\mathbf{r},t)$ of the atmosphere. Accordingly, the imaginary component $n_I(\mathbf{r},t)$ of Eq. (13) is given as [12]

$$n_I(\mathbf{r},t) = \frac{\alpha(\mathbf{r},t)}{2k_0}, \tag{15}$$

where the constant $k_0 = 2\pi f/c_0 = 2\pi/\lambda_0$ is coined the free-space angular wavenumber with λ_0 defined as the free-space wavelength in units of micrometers $\left(\mu m = 10^{-6} m\right)$.

Wavelengths in the optical regime typically range from 10^{-2} μm in the extreme

ultraviolet to 300 μm in the far-infrared [11]. Equation (15) accounts for extinction

effects because the propagating electric-field vector $\mathcal{E}(\mathbf{r},t)$ interacts with the atmosphere

at the atomic level [11,12]. As a result, the index of refraction $n(\mathbf{r},t)$ has an imaginary

component. This idea seems a little vague at this point in the analysis; however, the next

section will better characterize extinction effects and the extinction coefficient $\alpha(\mathbf{r},t)$ of

the atmosphere. It is now informative to study how an HEL beam, represented by a

paraxial wave, responds to the relationships provided by Eqs. (12)-(15).

2.1.3 Time-Independent Paraxial Wave Equation

If the time variations in the index of refraction of the atmosphere are sufficiently

slow, a quasi-steady-state approach is used, so that the index of refraction of the

atmosphere is considered to be time-independent, $n(\mathbf{r},t) = n(\mathbf{r})$. Thus, the

inhomogeneous wave equation, as given in Eq. (12), can be rewritten as

$$\nabla^2 \mathcal{E}(\mathbf{r},t) - \frac{n^2(\mathbf{r})}{c_0^2} \frac{\partial^2 \mathcal{E}(\mathbf{r},t)}{\partial t^2} = 0 . \tag{16}$$

Neglecting the time dependence of the refractive index, as given in Eq. (16), is a

necessary first step in the analysis of the BPM. With propagation through optical

turbulence, the time dependence of the refractive index can be handled separately. This

point will be re-addressed throughout the remainder of this chapter. However, it is

important to note that the BPM is versatile enough to model HEL beam propagation in

the atmosphere with or without this time dependence in the refractive index.

Solutions satisfying Eq. (16) take on many forms. In general, monochromatic electric-field vectors propagating in the atmosphere, in accordance with Eq. (16), take on the general form:

$$\mathcal{E}(\mathbf{r},t) = \mathbf{E}(\mathbf{r})\exp(-i2\pi ft), \tag{17}$$

where $\mathbf{E}(\mathbf{r})$ is the position-dependent complex amplitude vector, and f is the single-valued frequency in units of inverse seconds or hertz $\left(\mathrm{Hz} = \mathrm{s}^{-1}\right)$. All of the Cartesian polarization components of the electric-field vector $\mathcal{E}(\mathbf{r},t)$ represented in Eq. (17) vary as harmonic functions of time t with periods $T = 1/f$. Frequencies in the optical regime typically range from 10^{12} Hz in the far-infrared to $3x10^{16}$ Hz in the extreme ultraviolet [11]. Additionally, if Eq. (17) is substituted into Eq. (16), the inhomogeneous Helmholtz equation is obtained, where

$$\nabla^2 U(\mathbf{r}) + n^2(\mathbf{r})k_0^2 U(\mathbf{r}) = 0. \tag{18}$$

In Eq. (18), $U(\mathbf{r})$ is a position-dependent complex scalar function known as the complex amplitude and represents any of the three Cartesian polarization components of the complex amplitude vector $\mathbf{E}(\mathbf{r})$. The time dependence of the electric-field vector $\mathcal{E}(\mathbf{r},t)$ can be treated separately from the spatial relationship found between the amplitude vector $\mathbf{E}(\mathbf{r})$ and the complex amplitude $U(\mathbf{r})$ using Eq. (17).

The complex amplitude $U(\mathbf{r})$ is chosen to have units of square-root watts per meter $\left(\sqrt{\mathrm{W}}/\mathrm{m}\right)$. Namely, this is done so that the space-dependent irradiance $I(\mathbf{r})$ has

the common units of watts per square meter $\left(W/m^2\right)$ and is given by the modulus square

of the complex amplitude $U(\mathbf{r})$, where

$$I(\mathbf{r}) = \left|U(\mathbf{r})\right|^2. \qquad (19)$$

The irradiance $I(\mathbf{r})$, as given in Eq. (19), represents the flux per unit area incident on a

target and is a measureable quantity using modern-day optical detectors. Furthermore,

the magnitude of the complex amplitude vector $\mathbf{E}(\mathbf{r})$, as represented in Eq. (17), is

readily obtainable from the complex amplitude $U(\mathbf{r})$ with a simple conversion factor

given as

$$\left|\mathbf{E}(\mathbf{r})\right| = \sqrt{2\eta(\mathbf{r})}U(\mathbf{r}), \qquad (20)$$

where $\eta(\mathbf{r}) = \sqrt{\mu_0/\varepsilon(\mathbf{r})}$ is known as the impedance of the atmosphere in units of ohms

(Ω) [11]. The complex amplitude $U(\mathbf{r})$ serves as an adequate description for time-

independent optical disturbances propagating in the atmosphere. From this point forth in

the analysis, it is assumed that the complex amplitude $U(\mathbf{r})$, of any time-independent

monochromatic optical disturbance propagating in the atmosphere, satisfies Eqs. (18)-

(20).

The specific case of a time-independent monochromatic HEL beam propagating

in the atmosphere is now considered. In its simplest form, an HEL beam with a finite

spatial configuration in the $x-y$ plane is represented as a paraxial wave traveling in the

positive z direction. The complex amplitude $U(\mathbf{r})$ associated with a paraxial wave

traveling in the positive z direction is given by the following relationship:

$$U(\mathbf{r}) = A(\mathbf{r})\exp(i\beta z), \tag{21}$$

where $A(\mathbf{r})$ is a parameter known as the position-dependent complex envelope and,

$\beta = n_0 k_0$, is a phase constant dependent on the ambient index of refraction n_0 of the

atmosphere. Equation (21) is similar in form to a plane wave traveling in the positive z

direction; however, differs slightly because of modulations from the slowly varying

position-dependent complex envelope $A(\mathbf{r})$. These modulations are often induced by the

effects of diffraction, refraction, and extinction as will become apparent with the analysis

to follow.

A paraxial wave responds in a unique way to Eq. (18). For example, substituting

Eq. (21) into Eq. (18) provides the time-independent paraxial wave equation:

$$\nabla_\perp^2 A(\mathbf{r}) + i2\beta\frac{\partial A(\mathbf{r})}{\partial z} + \left[k_0^2 n^2(\mathbf{r}) - \beta^2\right]A(\mathbf{r}) = 0, \tag{22}$$

where $\nabla_\perp^2 = \partial^2/(\partial x^2) + \partial^2/(\partial y^2)$ is the transverse Laplacian operator. Note that an

approximation is made in obtaining Eq. (22) where the term involving $\partial^2 A(\mathbf{r})/(\partial z^2)$ is

omitted. This approximation is made under what is often coined the paraxial, parabolic,

Fresnel, slowly varying envelope, or small-angle approximation. Regardless of the title,

if the change in propagation distance along the z direction is on the order of the

wavelength being propagated in the atmosphere, $\Delta z \approx \lambda_0/n_0$, the assumption is made that

the change in the complex envelope is much smaller than the complex envelope,

13

$\Delta A(\mathbf{r}) \ll A(\mathbf{r})$. It follows that $\Delta A(\mathbf{r}) = (\partial A(\mathbf{r})/\partial z)\Delta z = (\partial A(\mathbf{r})/\partial z)\lambda_0/n_0$ and

$\partial A(\mathbf{r})/\partial z \ll A(\mathbf{r})n_0/\lambda_0 = A(\mathbf{r})\beta/(2\pi)$; therefore,

$$\frac{\partial^2 A(\mathbf{r})}{\partial z^2} \ll \beta^2 A(\mathbf{r}) \tag{23}$$

validating the approximation made in obtaining Eq. (22) [11]. Furthermore, using Eqs. (13)-(15), the time-independent paraxial wave equation, represented by Eq. (22), can be rewritten as

$$\nabla_\perp^2 A(\mathbf{r}) + i2\beta \frac{\partial A(\mathbf{r})}{\partial z} + 2\beta k_0 \Delta n(\mathbf{r}) A(\mathbf{r}) + i\beta\alpha(\mathbf{r}) A(\mathbf{r}) = 0, \tag{24}$$

where,

$$n^2(\mathbf{r}) \approx n_0^2 + 2n_0\Delta n(\mathbf{r}) + in_0\frac{\alpha(\mathbf{r})}{k_0}. \tag{25}$$

The approximation provided by Eq. (25) is typically valid since both the change in the index of refraction $\Delta n(\mathbf{r})$ and the extinction coefficient $\alpha(\mathbf{r})$ are considered to be on the order of parts per million. The time-independent methods used above to acquire Eq. (24) will prove informative in the following time-dependent analysis.

2.1.4 Time-Dependent Paraxial Wave Equation

The time-dependent behavior of the index of refraction $n(\mathbf{r},t)$ of the atmosphere is now accounted for, and solutions satisfying the inhomogeneous wave equation, must satisfy the form given in Eq. (12), which is rewritten here for convenience:

$$\nabla^2 \mathcal{E}(\mathbf{r},t) - \frac{1}{c_0^2}\frac{\partial^2\left[n^2(\mathbf{r},t)\mathcal{E}(\mathbf{r},t)\right]}{\partial t^2} = 0 \tag{26}$$
.

14

Including the time dependence of the refractive index, as given in Eq. (26), is a necessary second step in the analysis of the BPM. It will be shown that the time dependence of the refractive index cannot be neglected when accounting for the refraction effects of thermal blooming. This point will become clearer with the analysis of thermal blooming provided later on in this chapter. In general, solutions satisfying the inhomogeneous wave equation, as given in Eq. (26), take the general form, where

$$\mathcal{E}(\mathbf{r},t) = \mathbf{E}(\mathbf{r},t)\exp(-i2\pi ft). \tag{27}$$

All of the Cartesian polarization components of the electric-field vector $\mathcal{E}(\mathbf{r},t)$, as given in Eq. (27), vary as harmonic functions of time t and represent monochromatic electric-field vectors propagating in the atmosphere. The main difference found between the form of the time-independent solutions given by Eq. (17) and the form of the time-dependent solutions found in Eq. (27) is the position- and time-dependent amplitude vector $\mathbf{E}(\mathbf{r},t)$.

The amplitude vector $\mathbf{E}(\mathbf{r},t)$ represents the Cartesian polarization components of the electric-field vector $\mathcal{E}(\mathbf{r},t)$ propagating in the atmosphere. As such, an HEL beam traveling in the positive z direction with a finite spatial configuration in the $x-y$ plane is represented using a complex scalar function called the complex wave function $U(\mathbf{r},t)$, so that

$$U(\mathbf{r},t) = A(\mathbf{r},t)\exp(i\beta z - i2\pi f), \tag{28}$$

where $A(\mathbf{r},t)$ is a parameter known as the position- and time-dependent complex envelope. It is informative to note that the same harmonic behavior of the electric-field

vector $\mathcal{E}(\mathbf{r},t)$, represented in Eq. (27), is found in the complex wave function $U(\mathbf{r},t)$

using the relationship found in Eq. (28). The complex wave function $U(\mathbf{r},t)$, as given in

Eq. (28), essentially represents any of the three Cartesian polarization components of the

electric-field vector $\mathcal{E}(\mathbf{r},t)$. Again, Eq. (28) is similar in form to a plane wave traveling

in the positive z direction; however, differs slightly because of the modulations from the

slowly varying complex envelope $A(\mathbf{r},t)$. The effects of diffraction, refraction, and

extinction cause these position- and time-dependent modulations as will be studied in the

analysis to come.

Similar to the complex amplitude $U(\mathbf{r})$, the complex wave function $U(\mathbf{r},t)$ is

chosen to have units of square-root watts per meter $\left(\sqrt{W}/m\right)$. This is done so that the

space- and time-dependent irradiance $I(\mathbf{r},t)$ has the common units of watts per square

meter $\left(W/m^2\right)$ and is given by the modulus square of the complex wave function

$U(\mathbf{r},t)$, where

$$I(\mathbf{r},t)=\left|U(\mathbf{r},t)\right|^2. \tag{29}$$

Moreover, the magnitude of the electric-field vector $\mathcal{E}(\mathbf{r},t)$, as represented in Eq. (27),

are readily obtained from a similar unit conversion factor as that given in Eq. (20), so that

$$\left|\mathcal{E}(\mathbf{r},t)\right|=\sqrt{2\eta(\mathbf{r})}U(\mathbf{r},t). \tag{30}$$

It is now assumed that the complex wave function $U(\mathbf{r},t)$ of any position- and time-dependent monochromatic optical disturbance propagating in the atmosphere satisfies both Eq. (29) and Eq.(30).

With the properties defined above, the form of the complex wave function $U(\mathbf{r},t)$ found in Eq. (28) can be directly substituted into Eq. (26) for the electric-field vector $\mathcal{E}(\mathbf{r},t)$. In response, the following relationship for the complex wave function $U(\mathbf{r},t)$ is obtained:

$$\nabla_{\perp}^2 U(\mathbf{r},t) + \frac{\partial^2 U(\mathbf{r},t)}{\partial z^2} + \frac{\partial^2 n^2(\mathbf{r},t)}{\partial t^2} U(\mathbf{r},t) + 2\frac{\partial n^2(\mathbf{r},t)}{\partial t}\frac{\partial U(\mathbf{r},t)}{\partial t} + n^2(\mathbf{r},t)\frac{\partial^2 U(\mathbf{r},t)}{\partial t^2} = 0 \tag{31}$$

A couple of approximations can be made to simplify Eq. (31) before substituting in the form of the complex wave function $U(\mathbf{r},t)$ given in Eq. (28). Using the relationships found in Eqs. (13)-(15) for the index of refraction $n(\mathbf{r},t)$ of the atmosphere, the following approximation is made:

$$n^2(\mathbf{r},t) \approx n_0^2 + 2n_0\Delta n(\mathbf{r},t) + in_0\frac{\alpha(\mathbf{r},t)}{k_0}, \tag{32}$$

since both the change in the index of refraction $\Delta n(\mathbf{r},t)$ and the extinction coefficient $\alpha(\mathbf{r},t)$ are considered to be on the order of parts per million. With this in mind, the third and fourth terms of Eq. (31) can be neglected. Now, the form of the complex wave function $U(\mathbf{r},t)$, as given in Eq. (28), can be directly substituted into Eq. (31) to obtain the time-dependent paraxial wave equation, where

$$\nabla_\perp^2 A(\mathbf{r},t) + i2\beta \frac{\partial A(\mathbf{r},t)}{\partial z} + 2\beta k_0 \Delta n(\mathbf{r},t) A(\mathbf{r},t) + i\beta\alpha(\mathbf{r},t) A(\mathbf{r},t) = 0. \qquad (33)$$

Inherent in Eq. (33) is the same paraxial approximation found in the time-independent analysis and given in Eq. (23); however, the complex envelope $A(\mathbf{r},t)$ in this case contains time dependence.

In writing Eq. (33), the time-dependent form of the paraxial wave equation takes on a similar form to that of the time-independent paraxial wave equation given in Eq. (24). Differences found between Eq. (24) and Eq. (33) arise because of the addition of time dependence to the appropriate terms. Likewise, solutions satisfying Eq. (24) will also satisfy Eq. (33), with the addition of time dependence to the appropriate terms. This is an important point which cannot be overlooked in the analysis. It is now informative to look for solutions to the time-independent paraxial wave equation, which will also provide solutions to the time-dependent paraxial wave equation with the addition of time dependence to the appropriate terms.

2.1.5 Split-Step Beam Propagation Method

The time-independent paraxial wave equation, as given in Eq. (24), is first analyzed assuming only homogeneous and non-attenuating conditions. This analysis will provide insight as to how the BPM is used to approximate solutions to the time-independent and time-dependent paraxial wave equations. Now, the refractive index of the atmosphere is equal to the ambient refractive index of the atmosphere, $n(\mathbf{r},t) = n_0$, and Eq. (24) is rewritten in the following way:

$$\frac{\partial A(\mathbf{r})}{\partial z} = \frac{i}{2\beta} \nabla_\perp^2 A(\mathbf{r}). \qquad (34)$$

18

Solutions to Eq. (34) are readily obtainable as long as the complex envelope $A(\mathbf{r})$ of an HEL beam is transformable. For example, using the definition of the two-dimensional Fourier transform,

$$
\begin{aligned}
\mathcal{W}\left(f_x, f_y, z\right) &= \int_{-\infty}^{\infty} \int_{-\infty}^{\infty} W(x, y, z) \exp\left[-i 2\pi\left(f_x x + f_y y\right)\right] dx\, dy \\
&= \hat{\mathcal{F}}\left[W(x, y, z)\right]
\end{aligned}
\tag{35}
$$

and its properties, Eq. (34) transforms into the following ordinary differential equation:

$$
\frac{\partial \mathcal{A}\left(f_x, f_y, z\right)}{\partial z} = -\frac{i\pi\lambda_0}{n_0}\left(f_x^2 + f_y^2\right) \mathcal{A}\left(f_x, f_y, z\right).
\tag{36}
$$

Equation (36) is solved analytically or computationally for an HEL beam propagating from the source plane at z_j to the observation plane at z_{j+1} with

$$
\mathcal{A}\left(f_x, f_y, z_{j+1}\right) = \mathcal{A}\left(f_x, f_y, z_j\right) \exp\left(i\beta\Delta z\right) \exp\left[-i\pi \frac{\lambda_0}{n_0}\left(f_x^2 + f_y^2\right)\Delta z\right],
\tag{37}
$$

where $\Delta z = z_{j+1} - z_j$. The exponential terms to the right of the equals sign in Eq. (37) are often referred to as the transfer function of the Fresnel diffraction integral [14].

In acquiring Eq. (37), the linear systems analysis used is analogous to the way the convolution form of the Fresnel diffraction integral is solved to account for diffraction effects in propagating optical disturbances. For instance, the mathematics are equivalent to decomposing the complex envelope, $A(x, y, z_j)$, of an HEL beam in the source plane at z_i into its spatial frequency components, $\mathcal{A}(f_x, f_y, z_j)$, using the Fourier transform and propagating those spatial frequency components a distance, Δz, using the transfer

19

function of the Fresnel diffraction integral. It is also important to note that with the use of the two-dimensional inverse Fourier transform,

$$W(x,y,z) = \int_{-\infty}^{\infty} \int_{-\infty}^{\infty} \mathcal{W}(f_x, f_y, z) \exp\left[i2\pi(f_x x + f_y y)\right] df_x df_y$$
$$= \hat{\mathcal{F}}^{-1}\left[\mathcal{W}(f_x, f_y, z)\right]$$

(38)

the frequency components $\mathcal{A}(f_x, f_y, z_{j+1})$ in the observation plane at z_{j+1}, can be

transformed back into the spatial domain to acquire the complex envelope $A(x, y, z_{j+1})$ of

an HEL beam. The above homogeneous analysis will prove useful in accounting for

diffraction effects with inhomogeneous conditions.

Inhomogeneous and attenuating conditions are now accounted for and Eq. (24) is

analyzed in its entirety. To perform the necessary breakdown, the time-independent

paraxial wave equation, as given in Eq. (24), is rewritten in the following way:

$$\frac{\partial A(\mathbf{r})}{\partial z} = \frac{i}{2\beta} \nabla_{\perp}^2 A(\mathbf{r}) + ik_0 \Delta n(\mathbf{r}) A(\mathbf{r}) - \frac{\alpha(\mathbf{r})}{2} A(\mathbf{r}).$$

(39)

Equation (39) differs from Eq. (34) by the second and third term to the right hand side of

the equals sign. Moreover, in contrast to Eq. (34), Eq. (39) is a partial differential

equation that does not provide easily obtainable analytic solutions. Computational

solutions are often sought after as a result. The BPM is a numerical algorithm that is

used to approximate solutions to Eq. (24) with speed and accuracy.

In order to define the BPM formally, an understanding is needed as to how the

different components of Eq. (39) affect an HEL beam propagating in the atmosphere.

Firstly, based on the linear systems analysis of Eq. (34), the first term to the right of the

equals sign in Eq. (39) accounts for diffraction effects due to propagation in the

atmosphere. As an HEL beam propagates in an atmosphere with inhomogeneous conditions, it experiences similar diffraction effects as that of an atmosphere with homogeneous conditions. Secondly, investigation of the second term in Eq. (39) reveals a coupling between the complex envelope $A(\mathbf{r})$ of an HEL beam and the change in the index of refraction $\Delta n(\mathbf{r})$ of the atmosphere. This coupling accounts for how refraction, due to the change in the index of refraction $\Delta n(\mathbf{r})$, affects an HEL beam propagating in the atmosphere. Lastly, examination of the third term reveals a coupling between the complex envelope $A(\mathbf{r})$ of an HEL beam and the extinction coefficient $\alpha(\mathbf{r})$ of the atmosphere. Extinction effects are accounted for through this coupling. It is now noted that Eq. (39) essentially contains three atmospheric effects: diffraction, refraction, and extinction.

With the breakdown of Eq. (39) completed, it is informative to think of the different atmospheric effects in terms of operators. Now, Eq. (39) is rewritten in operator form as

$$\frac{\partial A(\mathbf{r})}{\partial z} = \left[\hat{D} + \hat{R}(\mathbf{r}) + \hat{A}(\mathbf{r}) \right] A(\mathbf{r}), \tag{40}$$

where $\hat{D} = i\nabla_\perp^2 / (2n_0 k_0)$, is a linear operator that accounts for diffraction effects, $\hat{R}(\mathbf{r}) = ik_0 \Delta n(\mathbf{r})$, is a position-dependent operator that accounts for refraction effects, and, $\hat{A}(\mathbf{r}) = -\alpha(\mathbf{r})/2$, is a position-dependent operator that accounts for attenuation effects due to extinction. Furthermore, if the refraction operator $\hat{R}(\mathbf{r})$ and the attenuation operator $\hat{A}(\mathbf{r})$ are considered to be depth independent, so that

$\Delta n(\mathbf{r}) = \Delta n(x, y, \Delta z)$ and $\alpha(\mathbf{r}) = \alpha(x, y, \Delta z)$, the operator-form solution to Eq. (40) can be written as

$$A(x, y, z_{j+1}) = A(x, y, z_j) \exp\left\{\left[\hat{D} + \hat{R}(x, y, \Delta z) + \hat{A}(x, y, \Delta z)\right]\Delta z\right\}. \qquad (41)$$

Equation (41) corresponds to an HEL beam propagating from the source plane at z_i, to

the observation plane at z_{j+1}, where again $\Delta z = z_{j+1} - z_j$. With the help of the Baker-

Campbell-Hausdorff formula, it can be shown that the diffraction operator $\hat{D}$, refraction

operator $\hat{R}(\mathbf{r})$, and attenuation operator $\hat{A}(\mathbf{r})$ are independent of one another to a first-

order approximation [4,7,8]. Thus, Eq. (41) can be rewritten in the form of the BPM:

$$A(x, y, z_{j+1}) =$$
$$A(x, y, z_j) \exp\left(\hat{D}\frac{\Delta z}{2}\right) \qquad\qquad (42)$$
$$\exp\left[\int_{z_j}^{z_{j+1}} \hat{R}(x, y, z)dz\right] \exp\left[\int_{z_j}^{z_{j+1}} \hat{A}(x, y, z)dz\right] \exp\left(\hat{D}\frac{\Delta z}{2}\right)$$

In Eq. (42), the refraction operator $\hat{R}(\mathbf{r})$ and attenuation operator $\hat{A}(\mathbf{r})$ are allowed to

maintain their depth dependence with path integrals over the propagation distance Δz.

The same analysis leading up to Eq. (42) for the time-independent paraxial wave

equation is valid for the time-dependent paraxial wave equation. For example, starting

with Eq. (33), the analysis performed above is completely suitable with the addition of

time dependence to the appropriate terms. Equation (42) can be written with time

dependence using the following relationship:

$$A(x, y, z_{j+1}, t) =$$

$$A(x, y, z_j, t) \exp\left(\hat{D} \frac{\Delta z}{2} \right)$$

$$\exp\left[\int_{z_j}^{z_{j+1}} \hat{R}(x, y, z, t) \, dz \right] \exp\left[\int_{z_j}^{z_{j+1}} \hat{A}(x, y, z, t) \, dz \right] \exp\left(\hat{D} \frac{\Delta z}{2} \right)$$

, (43)

where again, $\hat{D} = i\nabla_\perp^2 / (2n_0 k_0)$, is a linear operator that accounts for diffraction effects; however, $\hat{R}(\mathbf{r}, t) = ik_0 \Delta n(\mathbf{r}, t)$, is a position- and time-dependent operator that accounts for refraction effects, and $\hat{A}(\mathbf{r}, t) = -\alpha(\mathbf{r}, t)/2$, is a position- and time-dependent operator that accounts for attenuation effects due to extinction. Equation (42) and Eq. (43) essentially have the same form, but the ability to add time-dependence provides versatility to the analysis.

Both Eq. (42) and Eq. (43) account for the atmospheric effects of diffraction, refraction, and extinction separately. That is what makes the BPM so powerful in simulating HEL beam propagation in the atmosphere. For instance, the problem of diffraction due to an HEL beam propagating in the atmosphere can now be solved using only the term involving the diffraction operator $\hat{D}$ in Eq. (42) or Eq. (43). Note that the diffraction operator $\hat{D}$ is applied twice for an arbitrary user-defined partial propagation distance Δz, as described in Figure 1. This is accomplished using the same linear systems approach used in analyzing Eq. (34), and the process is repeated until the HEL beam propagates a distance Z to the target plane.

The refraction an HEL beam experiences from propagating in the atmosphere is accounted for using the time-independent refraction operator $\hat{R}(\mathbf{r})$ in Eq. (42) or the

time-dependent refraction operator $\hat{R}(\mathbf{r},t)$ in Eq. (43). For example, the cumulative

effects of refraction, due to the time-independent change in the index of refraction $\Delta n(\mathbf{r})$

or time-dependent change in the index of refraction $\Delta n(\mathbf{r},t)$, are summed up over the

propagation distance Δz with a path integral. These cumulative refraction effects over

the propagation path can be solved for computationally with the idea of a position-

dependent and possibly time-dependent phase screen $\Phi(x,y,z_{j+1};t)$ placed in the middle

of the partial propagation path, as discussed in Figure 1. The phase screen $\Phi(x,y,z_{j+1};t)$

is defined by the following relationship:

$$\Phi(x,y,z_{j+1};t) = k_0 \int_{z_j}^{z_{j+1}} \Delta n(x,y,z;t)dz . \tag{44}$$

The integral provided in Eq. (44) is the definition of optical path difference (OPD) and

corresponds to a change in the index of refraction $\Delta n(\mathbf{r},t)$ summed up over the partial

propagation distance Δz. In using Eq. (44), the physical process causing the change in

the index of refraction $\Delta n(\mathbf{r},t)$ must be accounted for, i.e. thermal blooming and or

optical turbulence.

The amplitude attenuation an HEL beam experiences from propagating in the

atmosphere with the effects of extinction is also described in Figure 1. For this purpose,

the time-independent attenuation operator $\hat{A}(\mathbf{r})$ in Eq. (42) or the time-dependent

attenuation operator $\hat{A}(\mathbf{r},t)$ in Eq. (43) is used. The cumulative effects of amplitude

attenuation, due to the time-independent extinction coefficient $\alpha(\mathbf{r})$ or the time-

dependent extinction coefficient $\alpha(\mathbf{r},t)$ are summed up over the partial propagation

distance Δz with a path integral. Different physical constituents, i.e. molecules and

aerosols, cause extinction effects in the atmosphere and must be accounted for

accordingly. This topic will be discussed in detail in the next section.
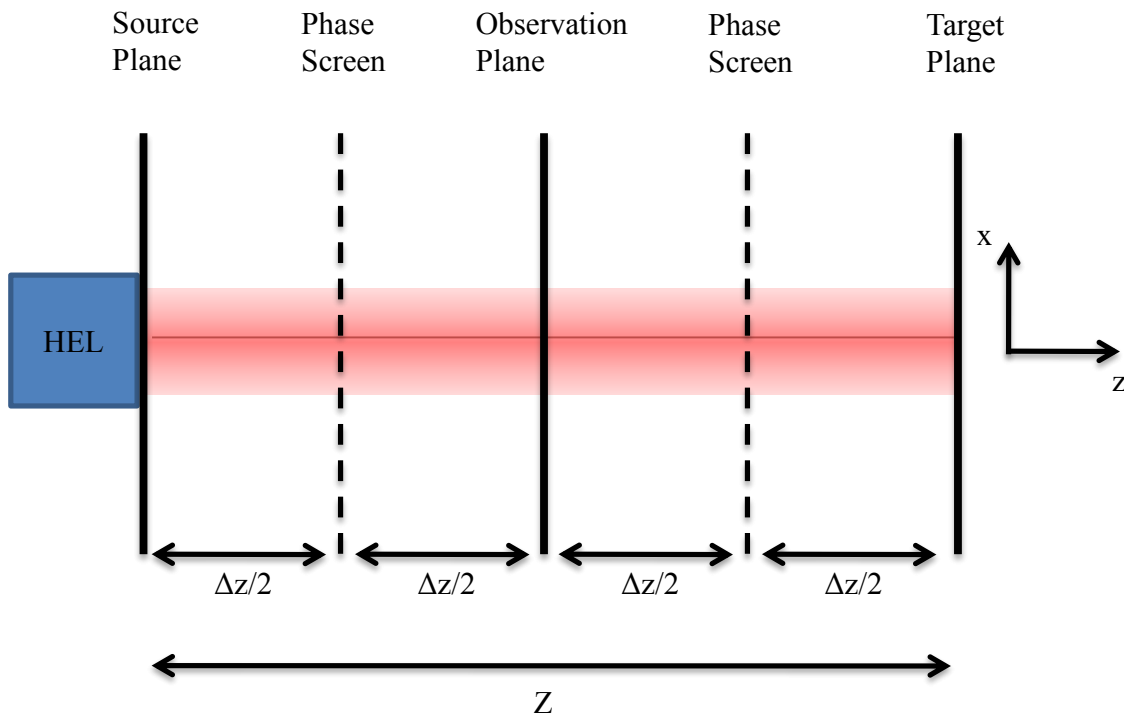
Figure 1. Sketch describing the BPM for two partial propagations of distance Δz. The HEL beam profile in the source plane is diffracted half the partial propagation distance Δz/2, refracted due to a phase screen, attenuated in amplitude, and diffracted again half the partial propagation distance Δz/2 to the observation plane. The process is repeated once more and the HEL beam propagates to the target plane a total distance Z away from the source plane.

Altogether, the BPM gives the ability to independently solve for different

atmospheric effects found within the time-independent or time-dependent paraxial wave

equations and accurately simulate HEL beam propagation in the atmosphere. An

algorithm describing the BPM for the time-independent paraxial wave equation is found

in Figure 2. It is important to note that the addition of time-dependence to the appropriate terms, i.e. the complex envelope $A(\mathbf{r},t)$, the change in the index of refraction $\Delta n(\mathbf{r},t)$, and the extinction coefficient $\alpha(\mathbf{r},t)$ provides the appropriate algorithm describing the BPM for the time-dependent paraxial wave equation. In the analysis to follow, the time dependence of both extinction and refraction effects will be included and assumed unless otherwise stated.

Most modern day computational wave-optics codes utilize the BPM for its computational speed. Nevertheless, there are details which cannot be overlooked when implementing the algorithm given in Figure 2. These details include the use *NxN* grids and the discrete Fourier transform (DFT). Thus, proper grid sampling is a crucial component in combating aliasing, which can significantly corrupt wave-optics results. A recent publication by Schmidt addresses these details for the purpose of computational wave-optics experiments [9]. The goal now is to study how extinction and refraction effects arise due to HEL propagation in the atmosphere.

$$A(x, y, z_j)$$ — HEL beam profile in the source plane

Atmospheric effects

Initial diffraction

$$A\left(x, y, z_{j+\frac{1}{2}}\right) = \hat{\mathcal{F}}^{-1}\left\{\mathcal{A}\left(f_x, f_y, z_j\right)\exp\left(i\beta\frac{\Delta z}{2}\right)\exp\left[-i\pi\frac{\lambda_0}{n_0}\left(f_x^2 + f_y^2\right)\frac{\Delta z}{2}\right]\right\}$$

Refraction due to a phase screen

$$A\left(x, y, z_{j+\frac{1}{2}}\right) = A\left(x, y, z_{j+\frac{1}{2}}\right)\exp\left[ik_0\int_{z_j}^{z_{j+1}}\Delta n(x, y, z)dz\right]$$

Amplitude attenuation due to extinction

$$A\left(x, y, z_{j+\frac{1}{2}}\right) = A\left(x, y, z_{j+\frac{1}{2}}\right)\exp\left[-\int_{z_j}^{z_{j+1}}\frac{\alpha(z)}{2}dz\right]$$

Final diffraction

$$A\left(x, y, z_{j+1}\right) = \hat{\mathcal{F}}^{-1}\left\{\mathcal{A}\left(f_x, f_y, z_{j+\frac{1}{2}}\right)\exp\left(i\beta\frac{\Delta z}{2}\right)\exp\left[-i\pi\frac{\lambda_0}{n_0}\left(f_x^2 + f_y^2\right)\frac{\Delta z}{2}\right]\right\}$$

$$A(x, y, z_{j+1})$$ — HEL beam profile in the observation plane
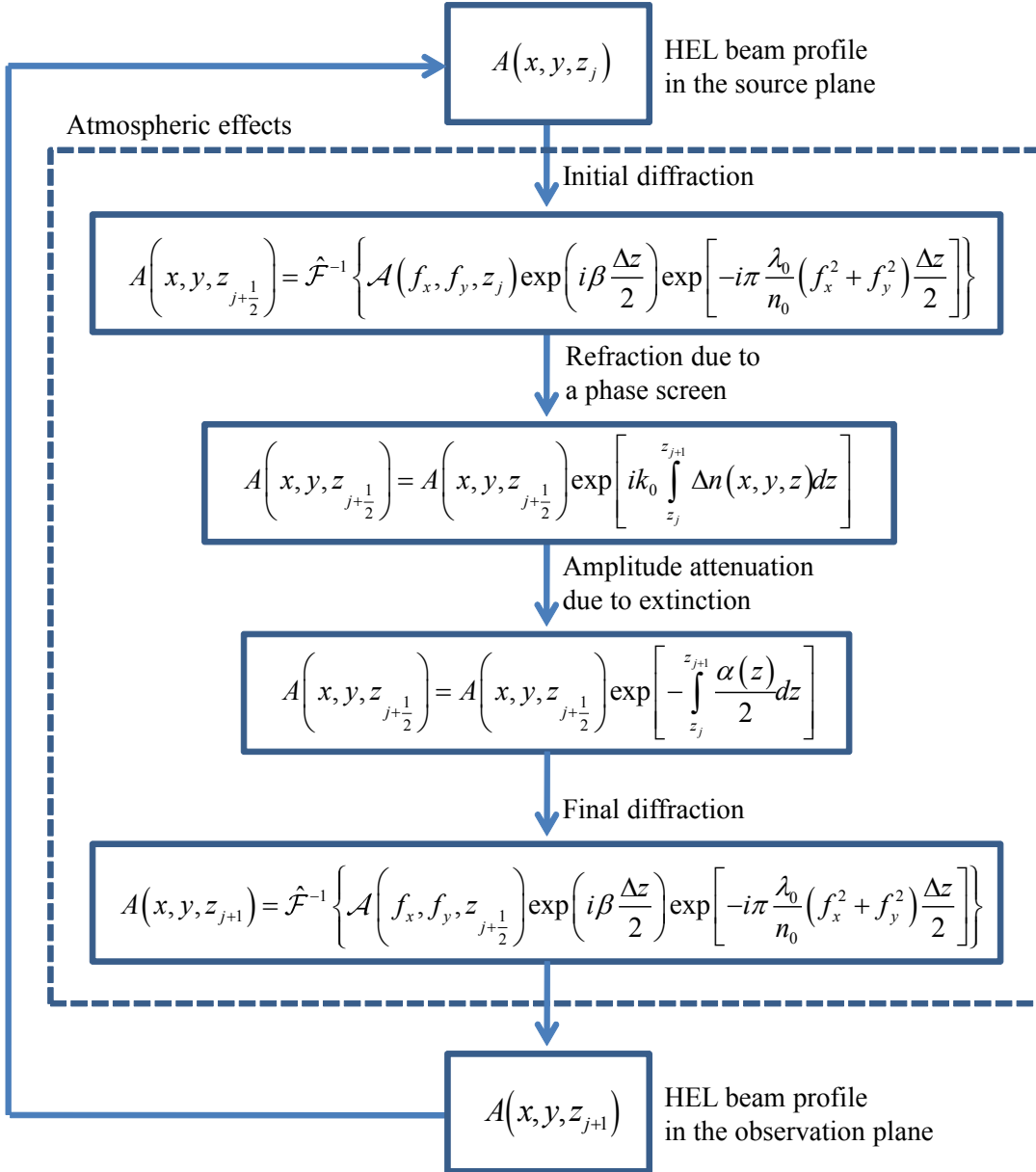
Figure 2. Flow chart describing the BPM. The HEL beam profile in the source plane is diffracted half the partial propagation distance Δz/2, refracted due to a phase screen, attenuated in amplitude, and diffracted again half the partial propagation distance Δz/2 to the observation plane. The HEL beam profile in the observation plane becomes the HEL beam profile in the source plane and the process is repeated until the HEL beam propagates to the user-defined target plane a distance Z away from the source plane.

27

2.2 Extinction in the Atmosphere

Light interacts with matter in discrete units. This concept is known from the study of quantum optics; however, is not all that intuitive based on the wave-optics analysis performed in the previous section. For example, light propagates as a wave, and as a result, experiences effects such as diffraction, refraction, and amplitude attenuation. When considering the interaction between matter within the atmosphere and an HEL beam, the particle nature of light must be accounted for. In this case, a HEL beam can be thought of as a stream of particles, known as photons, which interact discretely with matter contained within the atmosphere. Provided this knowledge, it is relatively simple to relate the concepts provided by quantum optics to explain extinction effects in the atmosphere. The purpose of this section is to provide an understanding as to how different constituents, i.e. molecules and aerosols in the atmosphere, give rise to extinction effects such as absorption and scattering.

2.5.1 Absorption and Scattering

The atmosphere is comprised of both gases and tiny particles. For instance, atmospheric gases include molecules such as N_2, O_2, CO_2, etc., and atmospheric aerosols include water droplets and dust [15]. As an HEL beam propagates in the atmosphere, it interacts with molecules and aerosols discretely through the absorption and the scattering of photons.

Absorption and scattering occurs at the atomic level when the energy, $E = hf$, associated with the photons of the HEL beam is large enough to excite electrons contained within the atmospheric constituents into higher discrete energy levels. This process is explained further using the field of quantum optics [16]; however, is beyond

the scope of the present discussion. At the macroscopic level, photons from the HEL beam interact with molecules and aerosols in the atmosphere probabilistically. Nielsen's treatment of the topic is particularly informative and is outlined here [15]. As an HEL beam propagates through a small distance Δz of the atmosphere with cross-sectional area A, individual photons are absorbed and scattered, as described in Figure 3. The number of photons within the HEL beam essentially becomes attenuated. For example, contained within the volume $A\Delta z$ of atmosphere are N molecules and or aerosols, each with their own cross-sectional areas a. The probability of the photons from the HEL beam being absorbed or scattered is expressed in terms of the depth-dependent cross section $s(z)$ with the relationship:

$$\frac{a}{A} = Ns(z)\Delta z .\tag{45}$$

This means that if n photons enter the region shown in Figure 3, $nNs(z)\Delta z$, photons will be lost from the HEL laser beam through absorption and or scattering due to a fraction, a/A, of the HEL beam being blocked.
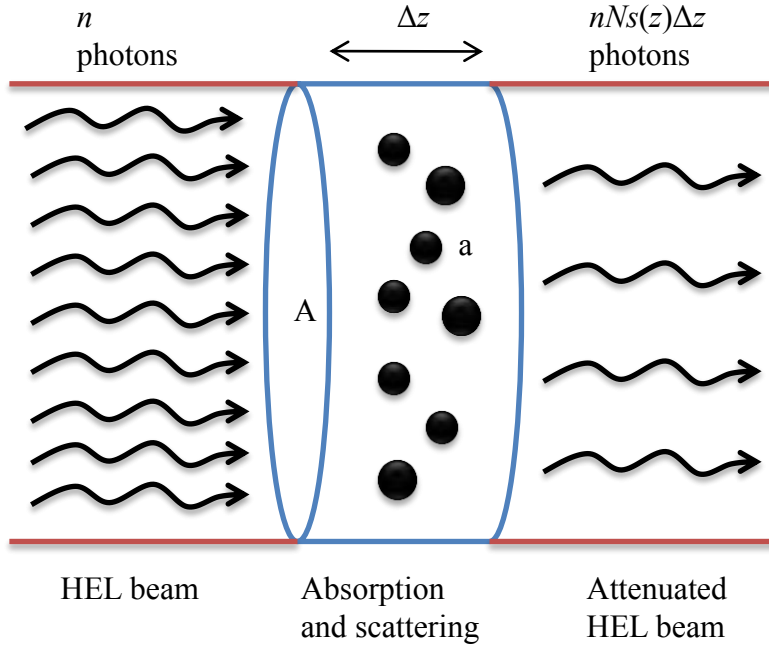
Figure 3. Absorption and scattering cross sections in the atmosphere. Photons from a HEL beam interact with molecules and aerosols in the atmosphere through propagation and become attenuated. The fraction of area blocked provides the probability that a photon is either absorbed and or scattered.

The quantity Ns, found within Eq. (45), is typically referred to as the depth-dependent absorption coefficient $\alpha_a(z)$ and or the depth-dependent scattering coefficient $\alpha_s(z)$. With units of inverse meters (m^{-1}), both the absorption coefficient $\alpha_a(z)$ and the scattering coefficient $\alpha_s(z)$ are measurable quantities. Together, the coefficients constitute extinction. The role extinction effects play in HEL beam propagation in the atmosphere will become more apparent with the development provided in the next subsection.

2.5.2 Extinction Coefficient of the Atmosphere

If extinction effects are taken into account, the interaction between the propagating HEL beam and molecules and aerosols in the atmosphere essentially causes

the index of refraction $n(\mathbf{r},t)$ of the atmosphere to contain an imaginary component

$n_I(\mathbf{r},t)$. This point was described above using Eq. (13) and Eq. (15) and is rewritten

here for convenience [11,12]:

$$n_I(\mathbf{r},t) = \frac{\alpha(\mathbf{r},t)}{2k_0}. \tag{46}$$

In Eq. (46), the imaginary component $n_I(\mathbf{r},t)$ is dependent on the extinction coefficient

$\alpha(\mathbf{r},t)$. With units of inverse meters (m^{-1}), the depth-dependent extinction coefficient

$\alpha(z)$ is determined from the sum of the absorption coefficient $\alpha_a(z)$ and scattering

coefficient $\alpha_s(z)$, where

$$\alpha(z) = \alpha_a(z) + \alpha_s(z). \tag{47}$$

In the wave-optics theory developed in the previous section, the extinction coefficient

$\alpha(\mathbf{r},t)$ was written as a function of position $\mathbf{r}$ and time t, as rewritten in Eq. (46).

However, as found in Eq. (47), the extinction coefficient $\alpha(z)$ is only dependent on the

depth of propagation z. The reason for this discrepancy is explained with the simplistic

model used above in Figure 3 to describe extinction effects due to absorption and

scattering. For all intents and purposes, simplifying the position dependence and

dropping the time dependence is sufficient when simulating HEL beam propagation in

the atmosphere with extinction effects caused by absorption and scattering. This is the

method employed here; however, future analysis in the subject may include a more robust

statistical treatment of how aerosols and molecules are distributed throughout the

atmosphere [17,18]. Such an analysis could rely on the position- and time-dependent nature of the extinction coefficient developed in the wave-optics theory above.

Provided the relationship given in Eq. (47) for the depth-dependent extinction coefficient $\alpha(z)$, the amount of amplitude attenuation associated with HEL beam propagation in the atmosphere can be determined. This is accomplished using Eq. (42) or Eq. (43) for the time-independent or time-dependent cases, respectively. It is now important to relate the extinction coefficient $\alpha(z)$ to a measurable quantity using modern-day optical detectors.

2.5.3 Transmittance

The extinction coefficient $\alpha(z)$, as given in Eq. (47), can be related to irradiance $I(\mathbf{r},t)$, which is a measurable quantity using modern-day optical detectors. For instance, using Eq. (19) or Eq. (29), the position-dependent and possibly time-dependent irradiance $I(\mathbf{r};t)$ is found from the complex wave function $U(\mathbf{r},t)$, as given in Eq. (28), or the complex amplitude $U(\mathbf{r})$, as given in Eq. (21), using the following relationship:

$$I(x,y,z;t) = I_0(x,y;t)\exp\left[-\alpha(z)z\right].\tag{48}$$

Here, Eq. (48) gives the general form for the irradiance $I(\mathbf{r};t)$ of aHEL beam propagating in the atmosphere. Note that the initial irradiance, $I_0(x,y;t) = I(x,y,0;t) = |A(x,y,0;t)|^2$, of an HEL beam essentially attenuates with propagation in the atmosphere due to exponential decay associated with the extinction coefficient $\alpha(z)$. This irradiance attenuation is often referred to as transmission losses.

Associated with the idea of transmission losses is a parameter known as the depth-dependent transmittance $\tau(z)$, which can be determined from Eq. (48). Specifically, the transmittance $\tau(z)$ associated with a user-defined partial propagation from the source plane at z_j to the observation plane at z_{j+1} can be determined using the following relationship:

$$\tau(z_{j+1}) = \frac{I(x,y,z_{j+1};t)}{I(x,y,z_j;t)} = \exp\left\{-\int_{z_j}^{z_{j+1}} \alpha(z)\,dz\right\}. \tag{49}$$

Here, the depth dependence of the extinction coefficient $\alpha(z)$ is accounted for with a path integral over the user-defined partial propagation distance $\Delta z = z_{i+1} - z_i$. Known as Beers' law, Eq. (49) provides a normalized measure for the amount of power or energy lost due to attenuation associated with propagating a HEL beam in the atmosphere ("the thicker the brew the less that gets through"). As seen in Figure 4, the transmittance for a particular engagement scenario with a propagation range Z is a wavelength dependent parameter, $\tau(Z) = \tau(\lambda_0)$. This is so because the extinction coefficient is also a wavelength dependent parameter, $\alpha(Z) = \alpha(\lambda_0)$. When considering HEL engagement scenarios with quasi-monochromatic light, this wavelength dependence is dropped for convenience in the notation. With this in mind, the refraction effect of thermal blooming is now studied.
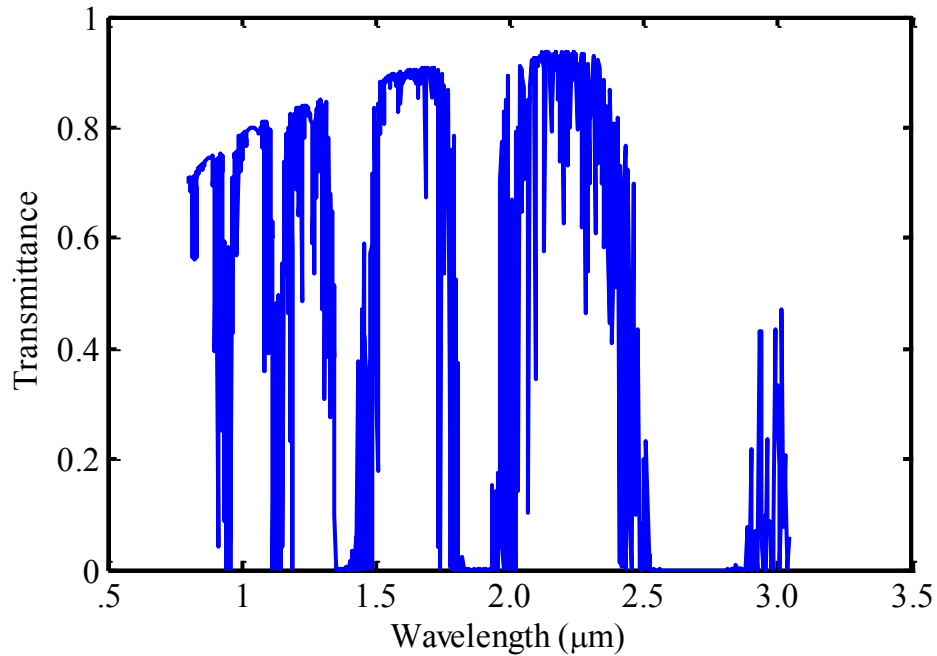
Figure 4. Example of calculated transmittance versus wavelength for a particular engagement scenario. The 1000 data points were calculated using LEEDR3 for a propagation range, *Z*=5000 m, and commonly used HEL beam wavelengths.

2.3 Thermal Blooming in the Atmosphere

The nonlinear optical effect of thermal blooming results from heat-induced distortion of the HEL beam propagating in the atmosphere. As depicted in Figure 5, absorption of the HEL beam irradiance essentially increases the atmospheric temperature through heating, which decreases the local refractive index. This causes the HEL beam irradiance to spread out or ―bloom‖ due to a negative-lens-like optical effect. Additionally, atmospheric advection cools the HEL beam irradiance and creates a tilt-like optical effect which causes the HEL beam to wander into the transverse wind direction. Starting with a Gaussian-shaped beam profile in the source plane, the nonlinear optical

effect of thermal blooming causes the HEL beam to have a crescent-shaped beam profile in the target plane.
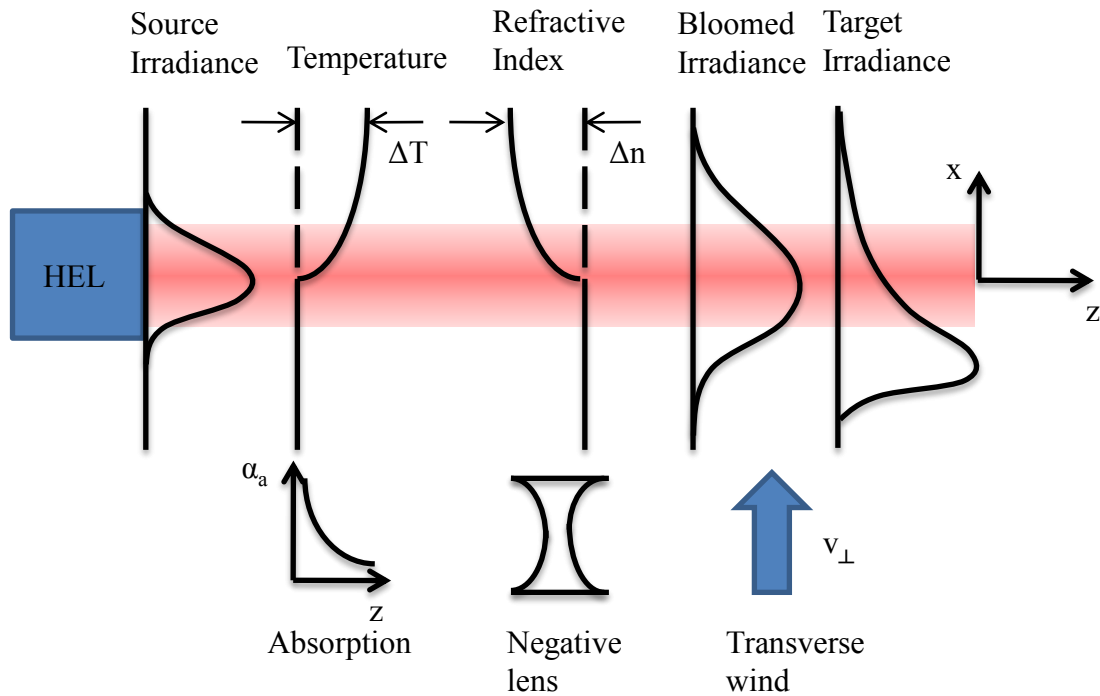
Figure 5. HEL propagation with the effects of thermal blooming. Absorption of the HEL beam irradiance causes an increase in temperature resulting in a decrease in the refractive index. This induces a negative-lens-like optical effect that blooms the beam. Cooling through atmospheric advection induces a tilt-like optical effect that causes the beam to wander into the transverse wind direction.

Thermal blooming has been studied in earnest since the late 1960's. In particular, the foundational work performed by Gebhardt [19,20,21,22,23,24] and Smith [25,26,27] helped shape everyone's understanding of the problem [28,29,30,31,32]. Their theoretical, computational, and experimental research in thermal blooming spanned over a 25-year period, and is well cited throughout the literature. In addition, the writings by Hogge [33], Walsh and Ulrich [6], and Weichel [34] give excellent introductory overviews on thermal blooming. Despite such an invaluable list of sources, there is still a

lot to be discovered in terms of characterizing the refraction effects of thermal blooming. As such, a few reoccurring research themes exist throughout the literature, which are unfortunately beyond the scope of the analysis presented here. They include investigations of stagnation zones [35,36], focusing studies [37,38], developing scaling laws [39,40,41], and pulsed propagation studies [4,5,42,43,44,36]. The purpose of this section; however, is to introduce the physics involved in simulating the change in the index of refraction $\Delta n(\mathbf{r},t)$ caused by thermal blooming for continuous wave (CW) HEL beam propagation in the atmosphere.

2.3.1 Energy Balance Equation

The refraction caused by thermal blooming is explained using the principles thermodynamics. For this purpose, thermodynamics deals with the movement of energy within a system. The system of interest here is the atmosphere. As with any thermodynamic system, energy within the atmosphere cannot be measured directly. Instead, the notion of energy within the atmosphere is quantified in terms of a change in some measurable quantity such as temperature, pressure, density, or phase transitions. The main thing to remember is that measureable quantities found within the atmosphere and how they relate to energy depend highly on the conditions describing the thermodynamic process of interest. With this in mind, it is informative to quickly review the three laws of thermodynamics, so that they can be understood in terms of measurable quantities found within the atmosphere and thermal blooming.

The three laws of thermodynamics tell us how energy can be related to measurable quantities found within the atmosphere. For example, the zeroth law of thermodynamics tells us that if the atmosphere is in equilibrium with two other systems,

than the two other systems must be in equilibrium as well. This statement is probably the most intuitive of the three laws of thermodynamics; however, it is worth mentioning here for insight into the thermodynamic process being described. Thermal blooming arises in the atmosphere as a result of HEL propagation. This means that the atmosphere, the HEL system, and the AO system must reach thermodynamic equilibrium, according to the zeroth law, before steady-state operation is attained. Moreover, energy is neither created nor destroyed in the atmosphere. This statement is basically a rehash of the first law of thermodynamics—any change in the internal energy ΔE found within the atmosphere must be a result of heat Q or work W, so that

$$\Delta E = Q - W . \tag{50}$$

The internal energy found within the atmosphere essentially represents the kinetic and potential energy of molecules distributed throughout the atmosphere. Physically, any change in the internal energy ΔE found within the atmosphere manifests itself in the motion of molecules. This motion of molecules distributed throughout the atmosphere can be measured using the temperature T found within the atmosphere.

Temperature T represents the most probable speed for molecules distributed throughout the atmosphere. For instance, a change in temperature ΔT represents the change in the speed of the molecules distributed in the atmosphere. Heat Q deposited in the atmosphere is required to make the molecules move faster or for the change in temperature ΔT to increase. However, it is impossible for the atmosphere to have as its sole result the transfer of heat Q from a cooler body to a warmer body. This is a direct consequence of the second law of thermodynamics. When pressure P (force per unit

37

area) is applied to a volume of air in the atmosphere, the work being done on the atmosphere manifests from a change in volume, $W = P\Delta V$. An increase in volume results in positive work and a decrease in volume results in negative work. Accordingly, the second law of thermodynamics states that it is impossible for the atmosphere to convert all heat Q into work W, which is quite unfortunate but reality.

With all three laws of thermodynamics in mind, it is informative to revisit the first law of thermodynamics. Now, Eq. (50) is rewritten in differential form:

$$dE = dQ - PdV . \tag{51}$$

This is done so that it is easier to relate the first law of thermodynamics to the measureable quantity of temperature T found within the atmosphere. To continue the analysis, two constants are of particular interest. Both represent the amount of differential heat in Joules needed to raise the temperature of a unit of molecular mass in kilograms found within the atmosphere one degree Kelvin $\left(\text{Jkg}^{-1}\text{K}^{-1}\right)$. The first one is defined as the specific heat at constant volume C_V, where

$$C_V = \left(\frac{dQ}{dT}\right)_{dV=0} , \tag{52}$$

and for dry air in the atmosphere, $C_V = 718 \text{ Jkg}^{-1}\text{K}^{-1}$. Similarly, the second constant is known as the specific heat at constant pressure C_P, and

$$C_P = \left(\frac{dQ}{dT}\right)_{dP=0} . \tag{53}$$

For dry air in the atmosphere, $C_P = 1005\ \mathrm{Jkg^{-1}K^{-1}}$. Together, these constants provide the mechanism needed to relate the differential change in energy dE or differential change in heat dQ to a differential change in temperature dT in the atmosphere.

Under conditions of an isochoric thermodynamic process (constant volume), a differential change in volume is zero, $dV = 0$. For all intents and purposes, the atmosphere behaves in an isochoric manner. The inability of the molecules distributed in the atmosphere to deform under the addition or removal of heat establishes the isolation needed for a closed thermodynamic system with approximately constant-volume conditions. Provided this, Eq. (51) and Eq. (52) can now be used to relate the differential change in internal energy per unit molecular mass, dE/m, and consequently, the differential change in heat per unit molecular mass, dQ/m, to the specific heat at constant volume, C_V, where

$$\frac{dE}{m} = \frac{dQ}{m} = C_V dT \ .$$ (54)

Additionally, if the differential change in pressure is accounted for, the relationship provided in Eq. (54) is equivalently rewritten as

$$\frac{dQ}{m} = C_V dT + d\left(\frac{P}{\rho}\right) - \frac{1}{\rho} dP \ ,$$ (55)

where $\rho = V/m$ is the density of air in the atmosphere. Note that the additional terms added to Eq. (54) in Eq. (55) essentially equate to zero. Since the atmosphere behaves in isochoric manner, the differential change in the density of air is zero, $d\rho = 0$. Thus, Eq. (55) is further manipulated with a modified form of the ideal gas law:

$$\frac{P}{\rho} = R_S T, \tag{56}$$

where here, $R_S = C_P - C_V = 287 \text{ Jkg}^{-1}K^{-1}$ is a constant often referred to as the specific

gas constant. Using Eq. (56), Eq. (55) is now rewritten as

$$\frac{dQ}{m} = C_V dT + R_S dT - \frac{1}{\rho} dP = (C_V + R_S) dT - \frac{1}{\rho} dP = C_P dT - \frac{1}{\rho} dP. \tag{57}$$

It is informative to note that Eq. (57) is often referred to as the general form of the first

law of thermodynamics for the atmosphere. To make use of Eq. (57), the mechanism

adding or removing heat in the atmosphere must be accounted for.

A diabatic process is a thermodynamic process which involves heat transfer in

accordance with the second law of thermodynamics. In atmospheric physics, the concept

of the diabatic heating rate J, in units of Joules per kilogram per second $\left(\text{Jkg}^{-1}\text{s}^{-1}\right)$, is

often used to study the time rate of change of heating in the atmosphere. As such, Eq.

(57) can be rewritten in terms of the diabatic heating rate J, so that

$$Jdt = C_P dT - \frac{1}{\rho} dP. \tag{58}$$

Here, dt represents the differential change in time during some diabatic heating process.

If terms are rearranged, Eq. (58) provides a relationship for the time rate of change of

temperature T in the atmosphere due to diabatic heating, where

$$\frac{dT}{dt} = \frac{1}{C_P \rho} \frac{dP}{dt} + \frac{J}{C_P}. \tag{59}$$

Provided Eq. (59), further analysis must be done to determine the mechanism driving the formation of the diabatic heating rate J. Continuous wave HEL beam propagation in the atmosphere is of thermodynamic interest here.

Under conditions of an isobaric thermodynamic process (constant pressure), the differential change in pressure is zero, $dP = 0$. For all intents and purposes, this is a great approximation to use when accounting for CW HEL propagation in the atmosphere. Changes in the irradiance of a CW HEL beam typically occur much slower than the speed of sound [4]; therefore, a constant-pressure approximation is valid. Provided this knowledge, the position- and time-dependent temperature $T(\mathbf{r},t)$ of the atmosphere can be determined from the amount of heat being deposited by absorption of the HEL beam irradiance $I(\mathbf{r},t)$. This heating relation drives the thermal blooming process and is governed by the time rate of change of temperature $T(\mathbf{r},t)$. As such, Eq. (59) can be rewritten as the following differential equation:

$$\frac{dT(\mathbf{r},t)}{dt} = \mu_T(z) I(\mathbf{r},t),\tag{60}$$

where the diabatic heating rate per specific heat at constant pressure is equivalently recognized as the absorbed irradiance of the CW HEL beam, $J/C_P = \mu_T(z) I(\mathbf{r},t)$. Note that in writing Eq. (60), $\mu_T(z)$ is a depth-dependent absorption parameter that contains all the thermodynamic information about the surrounding atmosphere, so that

$$\mu_T(z) = \frac{\alpha_a(z)}{C_p \rho(z)},\tag{61}$$

where $\rho(z)$ is defined as the depth-dependent density of air, respectively. The

absorption parameter $\mu_T(z)$, as given in Eq. (61), has the units of degrees Kelvin meters

squared per Joule $\left(Km^2J^{-1}\right)$. Thus, Eq. (60) relates a measureable thermodynamic

quantity, temperature $T(\mathbf{r},t)$, to a measureable optical quantity, irradiance $I(\mathbf{r},t)$, for

HEL beam propagation in the atmosphere.

To continue the analysis, Eq. (60) can be rewritten in terms of the change in the

index of refraction $\Delta n(\mathbf{r},t)$. For this purpose, it has been determined that the index of

refraction $n(\mathbf{r},t)$ is related to the depth-dependent pressure $P(z)$ and temperature

$T(\mathbf{r},t)$ through the following empirical relationship [45]:

$$n(\mathbf{r},t)=1+77.6x10^{-6}\left(1+7.52x10^{-3}\lambda^{-2}\right)\frac{P(z)}{T(\mathbf{r},t)}. \tag{62}$$

Provided Eq. (62), it is easy to relate the index of refraction $n(\mathbf{r},t)$ of the atmosphere to

the density of air $\rho(z)$ using the modified form of the ideal gas law given in Eq. (56),

and written here as

$$P(z)=R_S\rho(z)T_0(z), \tag{63}$$

where $T_0(z)$ is the depth-dependent ambient temperature of the atmosphere. Now, Eq.

(62) can be rewritten, so that

$$n(\mathbf{r},t)=1+77.6x10^{-6}\left(1+7.52x10^{-3}\lambda^{-2}\right)R_S\frac{\rho(z)T_0(z)}{T(\mathbf{r},t)}. \tag{64}$$

42

The relationship provided by Eq. (64) shows that the index of refraction $n(\mathbf{r},t)$ and temperature $T(\mathbf{r},t)$ are inversely proportional to one another. This is an important point to remember in the analysis of thermal blooming.

Provided Eq. (64), Eq. (60) still needs to be rewritten in terms of the change in the index of refraction $\Delta n(\mathbf{r},t)$. For this purpose, the chain rule relation

$$\frac{dn}{dt} = \frac{dn}{dT}\frac{dT}{dt} \tag{65}$$

can be used to relate the time rate of change of the index of refraction to the time rate of change of the temperature. The temperature rate of change of the index of refraction with respect to the ambient temperature must first be determined and is done so using the following relationship [46]:

$$\left(\frac{dn}{dT}\right)_{T=T_0}. \tag{66}$$

It is also important to remember that the index of refraction $n(\mathbf{r},t)$ can be expanded into a complex number using Eqs. (13)-(15), such that

$$n(\mathbf{r},t) = n_0 + \Delta n(\mathbf{r},t) + i\frac{\alpha(z)}{2k_0}, \tag{67}$$

where again, the position- and time-dependence of the extinction coefficient have been reduced to only a depth-dependence, $\alpha(\mathbf{r},t) = \alpha(z)$. This was done based on the analysis from the previous section. Consequently, using Eqs. (64)-(67), the following relationship is obtained:

43

$$\left[\frac{dn(\mathbf{r},t)}{dT(\mathbf{r},t)}\right]_{T(\mathbf{r},t)=T_0(z)} = \left[\frac{d\Delta n(\mathbf{r},t)}{dT(\mathbf{r},t)}\right]_{T(\mathbf{r},t)=T_0(z)}$$

$$= \left[-\frac{n_0-1}{T^2(\mathbf{r},t)}T_0(z)\right]_{T(\mathbf{r},t)=T_0(z)} \qquad (68)$$

$$= -\frac{n_0-1}{T_0(z)}$$

Equation (68) provides the temperature $T(\mathbf{r},t)$ rate of change of the index of refraction $n(\mathbf{r},t)$, and equivalently the temperature $T(\mathbf{r},t)$ rate of change of the change in the index of refraction $\Delta n(\mathbf{r},t)$, with respect to the ambient temperature $T_0(z)$. The relationships given by Eqs. (64)-(68) provide a way to relate the change in the index of refraction $\Delta n(\mathbf{r},t)$ to the temperature $T(\mathbf{r},t)$ of the atmosphere.

Equation (60) is now re-written in terms of the change in the index of refraction $\Delta n(\mathbf{r},t)$ due to thermal blooming. Using Eqs. (64)-(68), the following relationship is obtained:

$$\frac{d\Delta n(\mathbf{r},t)}{dt} = -\mu(z)I(\mathbf{r},t), \qquad (69)$$

where again, $\mu(z)$ is a depth-dependent absorption parameter, in units of squared meters per Joule $\left(m^2 J^{-1}\right)$, that contains all the thermodynamic information about the surrounding atmosphere, provided

$$\mu(z) = \frac{(n_0-1)\alpha_a(z)}{C_p \rho_0 T_0(z)}. \qquad (70)$$

Note that in writing Eq. (70), the depth-dependence of the density of air has been

dropped, $\rho(z) = \rho_0$. This is an appropriate approximation, as will be seen with the

following analysis.

If there is no addition or removal of heat to the atmosphere, both the index of

refraction and the temperature of the atmosphere become their ambient values, so that

$n(\mathbf{r},t) = n_0$ and $T(\mathbf{r},t) = T_0(z)$. Equation (64) is now determined as

$$n_0 = 1 + 77.6x10^{-6}\left(1 + 7.52x10^{-3}\lambda^{-2}\right)R_S\rho_0, \tag{71}$$

where again, the depth-dependence of the density of air has been dropped, $\rho(z) = \rho_0$.

This is done since the ambient index of refraction n_0 is constant. In reality, the ambient

index of refraction is a depth-dependent parameter, $n_0 = n_0(z)$, which varies, according

to Eq. (71), with the depth-dependent density of air $\rho(z)$. This depth dependence is

neglected here because the difference between the depth-dependent ambient index of

refraction and the vacuum index of refraction is approximately zero, $\Delta n_0(z) - 1 \approx 0$, as

determined from Eq. (71) for optical wavelengths. Thus, the empirical relationship found

in Eq. (71) basically requires that the ratio $(n_0 - 1)/\rho_0$ in Eq. (70) be constant. From this

point on in the analysis, the density of air will assume its ambient value at zero degrees

Kelvin, so that $\rho(z) = \rho_0 = 1.293 \text{ kg/m}^3$.

The integrated solution to Eq. (69) grows without bound as time progresses. This

is physically unrealizable. Inherent in Eq. (69) is the idea that the energy acquired in

heating the atmosphere due to an absorbed irradiance $\mu(z)I(\mathbf{r},t)$ is balanced by removal

of energy or heat. If the right hand side of Eq. (69) is expanded using the definition of the total derivative, this removal of heat or cooling is realized as atmospheric advection caused by a depth-dependent transverse wind velocity vector $\mathbf{v}_\perp(z)=\left[v_x(z),v_y(z),0\right]$ of the atmosphere, where

$$\frac{\partial \Delta n(\mathbf{r},t)}{\partial t}+\mathbf{v}_\perp(z)\bullet\nabla_\perp\Delta n(\mathbf{r},t)=-\mu(z)I(\mathbf{r},t). \tag{72}$$

Equation (72) says that the energy acquired in heating the atmosphere due to an absorbed irradiance $\mu(z)I(\mathbf{r},t)$ is balanced by loss of energy due to cooling from atmospheric advection caused by a transverse wind velocity vector $\mathbf{v}_\perp(z)$ of the atmosphere blowing across the beam. As a result, Eq. (72) is often referred to as the energy balance equation.

2.3.2 Time-Dependent Thermal Blooming

Solutions to the energy balance equation, as given in Eq. (72), for the change in the index of refraction $\Delta n(\mathbf{r},t)$ caused by thermal blooming are now sought after. To start the analysis, Eq. (72) is re-written in operator form as

$$\hat{L}(z)\Delta n(x,y,z,t)=-f(x,y,z,t), \tag{73}$$

where $\hat{L}(z)=\left[\partial/\partial t+\mathbf{v}_\perp(z)\bullet\nabla_\perp\right]$, is a depth-dependent linear operator that represents cooling of the atmosphere through atmospheric advection and, $f(x,y,z,t)=\mu(z)I(\mathbf{r},t)$, is a forcing function that represents heating of the atmosphere due to an absorbed irradiance. In re-writing Eq. (72) in the operator form of Eq. (73), it is easy to see that a Green's function $G(x,y,z,t;\xi,\eta,\zeta,\tau)$ analysis can now be utilized, so that

$$\hat{L}(z)G(x,y,z,t;\xi,\eta,\zeta,\tau)=-\delta(x-\xi,y-\eta,z-\zeta,t-\tau), \tag{74}$$

46

where here, the change in the index of refraction $\Delta n(\mathbf{r},t)$ and the forcing function

$f(x,y,z,t)$, found in Eq. (73), are replaced with a Green's function

$G(x,y,z,t;\xi,\eta,\zeta,\tau)$ and a shifted Dirac-delta function $\delta(x-\xi,y-\eta,z-\zeta,t-\tau)$,

respectively [47]. The Green's function $G(x,y,z,t;\xi,\eta,\zeta,\tau)$ defined in Eq. (74) is

equivalent to the impulse response function that is often sought after for linear shift-

invariant systems. With this in mind, the Green's function $G(x,y,z,t;\xi,\eta,\zeta,\tau)$

determines solutions to Eq. (72) for the change in the index of refraction $\Delta n(\mathbf{r},t)$ using

the following relationship:

$$\Delta n(x,y,z,t) = \int_{-\infty}^{\infty}\int_{-\infty}^{\infty}\int_{-\infty}^{-\infty}\int_{-\infty}^{\infty} G(x,y,z,t;\xi,\eta,\zeta,\tau)f(\xi,\eta,\zeta,\tau)d\xi d\eta d\zeta d\tau. \qquad (75)$$

Once the Green's function $G(x,y,z,t;\xi,\eta,\zeta,\tau)$ is determined from Eq. (74), it can be

substituted into Eq. (75) to determine the change in the index of refraction $\Delta n(\mathbf{r},t)$

caused by thermal blooming.

Linear systems theory is used again to determine the Green's function

$G(x,y,z,t;\xi,\eta,\zeta,\tau)$ from Eq. (74). For example, using the definition of the two-

dimensional Fourier transform, as given in Eq. (35), and the unilateral Laplace transform

$$\begin{aligned}\mathcal{W}(s) &= \int_{0}^{\infty} W(t)\exp[-st]dt \\ &= \hat{\mathcal{L}}[W(t)]\end{aligned} \qquad (76)$$

where $s = \sigma + i2\pi f$, is a complex number and, $\sigma \geq 0$, is a constant, Eq. (74) is

transformed into the following algebraic expression:

$$\left\{s+2\pi i\left[v_x(z)f_x+v_y(z)f_y\right]\right\}\mathscr{G}\left(f_x,f_y,z,s;\xi,\eta,\zeta,\tau\right)$$
$$=-\exp\left(-i2\pi f_x\xi\right)\exp\left(-i2\pi f_y\eta\right)\delta\left(z-\zeta\right)\exp\left(-s\tau\right)\,. \tag{77}$$

Here, $G(x,y,z,0;\xi,\eta,\zeta,\tau)=0$, since it is assumed that there is no initial heating of the

atmosphere, $\Delta n(\mathbf{r},0)=0$. The utility employed in transforming Eq. (74) is that Eq. (77)

can be rearranged algebraically to solve for the transformed Green's function

$\mathscr{G}\left(f_x,f_y,z,s;\xi,\eta,\zeta,\tau\right)$, so that

$$\mathscr{G}\left(f_x,f_y,z,s;\xi,\eta,\zeta,\tau\right)=$$
$$-\frac{\exp\left(-i2\pi f_x\xi\right)\exp\left(-i2\pi f_y\eta\right)\delta\left(z-\zeta\right)\exp\left(-s\tau\right)}{s+2\pi i\left[v_x(z)f_x+v_x(z)f_y\right]}\,. \tag{78}$$

Now, the two-dimensional inverse Fourier transform, as given in Eq. (38), and the

inverse Laplace transform

$$W(t)=\frac{1}{2\pi i}\int_{\sigma-i\infty}^{\sigma+i\infty}\mathcal{W}(s)\exp[st]ds \tag{79}$$
$$=\hat{\mathcal{L}}^{-1}\left[\mathcal{W}(s)\right]$$

can be used to transform Eq. (78) back into the spatial and temporal domain, so that

$$G\left(x,y,z,t;\xi,\eta,\zeta,\tau\right)=$$
$$-\delta\left\{x-\xi+v_x(z)(t-\tau),y-\eta-v_y(z)(t-\tau),z-\zeta\right\}\text{step}(t-\tau)\,. \tag{80}$$

Here, $\text{step}(t-\tau)$ is a shifted unit-step or Heaviside function [47]. Equation (80)

provides the Green's function $G(x,y,z,t;\xi,\eta,\zeta,\tau)$ needed in Eq. (75).

By substituting Eq. (80) into Eq. (75), the refraction effect of thermal blooming can be accounted for in HEL propagation in the atmosphere. With a little manipulation, the change in the index of refraction $\Delta n(\mathbf{r},t)$ is determined as

$$\Delta n(x,y,z,t) = -\mu(z)\int_0^t I\big[x - v_x(z)(t-\tau), y - v_y(z)(t-\tau), z, \tau\big]d\tau . \qquad (81)$$

Equation (81) serves as an analytically determined time-dependent solution to the energy balance equation, as given in Eq. (72), for the change in the index of refraction $\Delta n(\mathbf{r},t)$ caused by thermal blooming. The introductory description of thermal blooming given above in Figure 5 makes complete sense now based on the relationship provided by Eq. (81). With inspection of Eq. (81), it is readily seen that as time t progresses from some previous time τ, the change in the index of refraction $\Delta n(\mathbf{r},t)$ decreases. This causes a negative-lens-like optical effect in the atmosphere. Additionally, atmospheric advection causes the HEL beam irradiance $I(\mathbf{r},t)$ to wander or shift into the direction of the transverse wind velocity vector $\mathbf{v}_\perp(z)$. This causes a tilt-like optical effect in the atmosphere. With this in mind, everything needed to describe thermal blooming, at least for CW HEL beams propagating in the atmosphere, is contained in Eq. (81).

Equation (81) can be modeled computationally. For this purpose, the following expression is readily used [48,46,49]:

$$\begin{aligned}\Delta n(x,y,z,t_{j+1}) = \\ -\mu(z)I(x,y,z,t_{j+1})\Delta t + \Delta n(x - v_x(z)\Delta t, y - v_y(z)\Delta t, z, t_j)\end{aligned}, \qquad (82)$$

where here, the change in the index of refraction $\Delta n(\mathbf{r},t)$ is updated from the previous time t_j to the present time t_{j+1} with the time step $\Delta t = t_{j+1} - t_j$. Equation (82) discretely samples the time-dependent analytical solution given in Eq. (81). As a result, everything needed to simulate time-dependent thermal blooming for CW HEL beams propagating in the atmosphere, is contained in Eq. (82). For instance, heating of the atmosphere at the present time t_{j+1} corresponds to the amount of absorbed irradiance $\mu(z)I(x,y,z,t_{j+1})\Delta t$. This heating is being added from the previous time t_j during the time step Δt.

Furthermore, previous heating of the atmosphere at time t_j is cooled by the wind through atmospheric advection. This cooling through atmospheric advection corresponds to a spatial shift in the change of the index of refraction $\Delta n(x - v_x(z)\Delta t, y - v_y(z)\Delta t, z, t_j)$. The amount of atmospheric advection or spatial shift is governed by the transverse wind speeds, $v_x(z)$ and $v_y(z)$, and the time step Δt.

When using $N \times N$ grids to implement Eq. (82) into wave-optics simulations, it is important to note that the amount of spatial shift is often less than or greater than the grid spacing. As a result, it is common practice to break the time-development of Eq. (82) into sub-time steps [46,49]. Linear interpolation is then used for each sub-spatial shift. The DFT and a translation filter function $\mathcal{T}(f_x, f_y, z, t)$ can also be used to overcome this problem [4,5,50,51,49]. The translation filter function $\mathcal{T}(f_x, f_y, z, t)$ is given as

$$\mathcal{T}(f_x, f_y, z, t) = \exp\left\{-i2\pi\left[v_x(z)f_x + v_y(z)f_y\right]t\right\}. \tag{83}$$

Thus, Eq. (82) is equivalently written in terms of the translation filter function

$\mathcal{T}\left(f_x, f_y, z, t\right)$, as given in Eq. (83), using the following relationship:

$$\Delta n\left(x, y, z, t_{j+1}\right) = \\ -\mu(z) I\left(x, y, z, t_{j+1}\right) \Delta t + \hat{\mathcal{F}}^{-1}\left\{\hat{\mathcal{F}}\left[\Delta n\left(x, y, z, t_j\right)\right] \mathcal{T}\left(f_x, f_y, z, t\right)\right\}. \tag{84}$$

Equation (84) serves as an alternative way to simulate time-dependent thermal blooming.

In practice, additional spatial filtering or zero padding is often needed when using *NxN*

grids and the DFT to simulate time-dependent thermal blooming with Eq. (84). This is

done to prevent aliasing.

As stated before, proper grid sampling is a crucial component in combating

aliasing when using the BPM to simulate HEL beam propagation in the atmosphere.

Related to this issue, Fried analytically determined, using a plane-wave analysis, that for

weak heating conditions, spatial frequencies above $1/\sqrt{2\lambda_0 \Delta z / n_0}$ should be removed

from the HEL beam irradiance $I(\mathbf{r}, t)$ [52,49]. The Fresnel integral transfer function

used in the BPM tends to amplify high spatial frequencies in the HEL beam irradiance

$I(\mathbf{r}, t)$ with multiple partial propagations of distance Δz [9]. Accordingly, to remove

these unnecessary high spatial frequencies, the HEL beam irradiance $I(\mathbf{r}, t)$, in Eq. (82)

or Eq. (84), is filtered with a super-Gaussian filter function $\mathcal{S}\left(f_x, f_y\right)$, so that

$$I'\left(x, y, z, t_{j+1}\right) = \hat{\mathcal{F}}^{-1}\left\{\hat{\mathcal{F}}\left[I\left(x, y, z, t_{j+1}\right)\right] \mathcal{S}\left(f_x, f_y\right)\right\}, \tag{85}$$

where $I'(\mathbf{r}, t)$ is the spatially filtered HEL beam irradiance. The super-Gaussian filter

function $\mathcal{S}\left(f_x, f_y\right)$ is given as

$$\mathcal{S}\left(f_x, f_y\right) = \exp\left\{ -\left[\sqrt{\frac{2\lambda_0 \Delta z}{n_0}} \left(f_x + f_y\right) \right]^{20} \right\},$$

(86)

where the factor of 20 has been empirically determined to work well [49]. Replacing the

HEL beam irradiance $I(\mathbf{r},t)$, in Eq. (82) or Eq. (84), with the spatially filtered HEL

beam irradiance $I'(\mathbf{r},t)$, as determined in Eq. (85), ultimately helps to alleviate

numerical noise. This numerical noise artificially increases the severity of time-

dependent thermal blooming [52,49].

The relationships found in Eqs. (82)-(86) serve as the tricks of the trade for

simulating time-dependent thermal blooming. Provided these relationships, the important

thing to remember in the study of time-dependent thermal blooming is that the heating

and cooling of the atmosphere causes the HEL beam to develop crescent-shaped target

irradiance. As time progresses, the development of the crescent-shaped target irradiance

increasingly degrades system performance.

2.3.3 Steady-State Thermal Blooming

The heating and cooling of the atmosphere as described by time-dependent

thermal blooming can reach steady state if there are no variations in the output source

irradiance of the HEL beam. For instance, steady-state thermal blooming results in static

behavior of the change in the index of refraction $\Delta n(\mathbf{r},t)$. This static behavior causes the

time rate of change of the change in index of refraction to be zero, $\partial \Delta n(\mathbf{r})/\partial t = 0$.

Consequently, the time-dependence in the change in the index of refraction is dropped,

$\Delta n(\mathbf{r}, t) = \Delta n(\mathbf{r})$, and steady-state thermal blooming is found from Eq. (72) and equivalently Eq. (81), as

$$\Delta n(x, y, z) = -\frac{\mu(z)}{v_\perp(z)} \int_{-\infty}^{x} I(\xi, y, z) d\xi, \tag{87}$$

where $v_\perp(z)$ is the transverse wind speed. In Eq. (87), the coordinates of the HEL beam propagating in the atmosphere have been rotated, so that the transverse wind velocity vector is assumed to be solely in the x direction, $\mathbf{v}_\perp(z) = [v_\perp(z), 0, 0]$. Equation (87) serves as an analytically determined steady-state solution to Eq. (72) for the change in the index of refraction $\Delta n(\mathbf{r})$ caused by thermal blooming. Provided Eq. (87), the refraction effect of steady-state thermal blooming can be accounted for in HEL propagation in the atmosphere. To model the refraction caused by steady-state thermal blooming computationally, the integral in Eq. (87) must be sampled discretely.

Steady-state thermal blooming, as described by Eq. (87), only holds for engagement scenarios in which the HEL beam has been propagating in the atmosphere for a significant amount of time, i.e. some multiple of the wind clearing time t_c. For this purpose, the wind clearing time t_c is defined as the time needed for the transverse wind speed in the source plane $v_\perp(0)$ to travel across the initial beam diameter D_0, where

$$t_c = \frac{D_0}{v_\perp(0)}. \tag{88}$$

Varying engagement scenario parameters will require different multiples of the wind clearing time t_c, as provided in Eq. (88), to reach steady-state thermal blooming.

However, once steady-state thermal blooming is achieved, the development of the crescent-shaped target irradiance is static in behavior or fully formed. This fully-formed crescent pattern in the target plane is sometimes referred to as whole-beam thermal blooming. Here, the fully-formed crescent pattern is referred to as steady-state thermal blooming—a refraction effect which severely degrades system performance.

2.3.4 Distortion Number

It is useful to describe the refraction caused by steady-state thermal blooming in terms of a position-dependent phase distortion $\phi(\mathbf{r})$ measured in radians (rad). For this purpose, the phase distortion $\phi(\mathbf{r})$ accumulated along the propagation path is provided from the change in the index of refraction $\Delta n(\mathbf{r})$ using the following relationship:

$$\phi(x,y,Z) = k_0 \int_0^Z \Delta n(x,y,z)\,dz , \qquad (89)$$

where Z is the entire propagation range. Equation (89) is similar to the time-independent phase screen $\Phi(x,y,z_{j+1})$ derived in Eq. (44). The integral over the change in the index of refraction $\Delta n(\mathbf{r})$, as given in Eq. (89), is again known as the definition of OPD. Moreover, substituting Eq. (87) into Eq. (89) provides the phase distortion $\phi(\mathbf{r})$ accumulated along the propagation path induced by steady-state thermal blooming, where

$$\phi(x,y,Z) = -k_0 \int_0^Z \frac{\mu(z)}{v_x(z)} \int_{-\infty}^x I(\xi,y,z)\,d\xi\,dz . \qquad (90)$$

Equation (90) serves as an analytically determined steady-state solution to Eq. (72) for the phase distortion $\phi(\mathbf{r})$ caused by thermal blooming. Provided Eq. (90), different HEL

beam parameters can be accounted for to characterize the radians of distortion induced by steady-state thermal blooming.

For uniform circularly collimated HEL beams propagating in the atmosphere, Eq. (90) can be rewritten in terms of a parameter known as the Bradley and Herrmann distortion number N_D [53]. In so doing, Eq. (90) is rewritten in the following form [54,22]:

$$\phi(x,y,Z) = -N_D \frac{D_0}{4\sqrt{2}P_0} \int_{-\infty}^{x} I_0(\xi,y)d\xi, \tag{91}$$

so that the distortion number N_D is given as

$$N_D = \frac{4\sqrt{2}k_0 P_0}{D_0} \int_0^Z \frac{\mu(z)\tau(z)}{v_\perp(z)}dz, \tag{92}$$

where P_0 is the initial beam power. The transmittance $\tau(z)$, as defined in Eq. (49), is included in the definition of the distortion number N_D because extinction effects known as transmission losses limit the effects of thermal blooming. According to Eq. (91), the distortion number N_D, as given in Eq. (92), provides an amplitude gauge for the integrated radians of distortion accumulated along the entire propagation range Z for a uniform circularly collimated HEL beam. Thus, the distortion number N_D is widely used as a measure for the strength of thermal blooming.

It is clear, at this point in the analysis, that thermal blooming causes heating of the atmosphere and an associated temperature rise. This temperature rise is proportional to the irradiance $I(\mathbf{r})$ of the HEL beam propagating in the atmosphere. For uniform circularly collimated HEL beams propagating in the atmosphere, the irradiance is

proportional to the ratio of the initial beam power over the beam area,

$I(\mathbf{r}) \propto P_0 \big/ \big[\pi (D_0/2)^2 \big]$. As written in Eq. (92), the distortion number N_D is

proportional to the ratio of the initial beam power over the initial beam diameter,

$4\sqrt{2} P_0 / D_0$. Consequently, there is a $1/D_0$ discrepancy between the irradiance

proportionality and the proportionality used in defining the distortion number N_D in Eq.

(92). This may seem surprising; however, the important thing to realize is that the

temperature rise associated with thermal blooming is also proportional to the wind

clearing time t_c, as defined in Eq. (88). How long the surrounding atmosphere is

exposed to the HEL beam plays a big role in determining the strength of thermal

blooming.

Equation (92) is often modified when considering uniform circularly focused

HEL beams propagating in the atmosphere. For instance, the depth-dependent beam

diameter $D(z)$ for a uniform circularly focused HEL beam can be determined from

geometrical optics as

$$D(z) = D_0 \frac{Z - z}{Z}. \tag{93}$$

From the source plane, $z = 0$, to the target plane, $z = Z$, the optical leverage $(Z-z)/Z$

causes the initial beam diameter D_0 to converge. Thus, uniform circularly focused HEL

beams are conical in shape and the distortion number N_D, given in Eq. (92), is rewritten,

so that [55]

$$N_D = 4\sqrt{2} k_0 P_0 \int_0^Z \frac{Z - z}{Z} \frac{\mu(z)\tau(z)}{D(z)v_\perp(z)} dz. \tag{94}$$

Similar to Eq. (92), Eq. (94) provides an amplitude gauge for the integrated radians of

distortion accumulated along the entire propagation range Z for a uniform circularly

focused HEL beam. If Eq. (93) is substituted in to Eq. (94), the optical leverage

$(Z-z)/Z$ cancels. As a result, the distortion number N_D found using Eq. (94) is

equivalent to the distortion number N_D found using Eq. (92). Throughout the literature;

however, there are different definitions of the beam diameter $D(z)$ used in Eq. (94) for

uniform circularly focused HEL beams propagating in the atmosphere.

Diffraction effects prevent the beam diameter $D(z)$, as defined in Eq. (93), from

reaching zero. For example, a uniform circularly focused HEL beam will have a

diffraction-limited bucket diameter D_B determined by the following quantity:

$$D_B = 2.44 \frac{\lambda_0 Z}{n_0 D_0}.$$
(95)

The bucket diameter D_B is defined as the region in the target plane, $z = Z$, that contains

the central bright spot of the HEL beam irradiance $I(\mathbf{r})$ after diffraction limited

propagation to the far field. In Eq. (95), the bucket diameter D_B is derived from the

irradiance $I(\mathbf{r})$ given by the following relationship:

$$I(x,y,Z) = |A|^2 \left(\frac{\pi n_0 D_0^2}{4\lambda_0 Z} \right)^2 \mathrm{somb}^2 \left(\frac{n_0 D_0 \sqrt{x^2 + y^2}}{\lambda_0 Z} \right).$$
(96)

Equation (96) corresponds to the irradiance $I(\mathbf{r})$ (neglecting transmission losses) of the

Fraunhofer diffraction pattern obtained for a circular aperture of diameter D_0 illuminated

with an HEL beam amplitude A. The first nulls of the squared sombrero function, $\text{somb}^2\left[n_0 D_0 D_B/(2\lambda_0 Z)\right] = 0$, in Eq. (96), determines the bucket diameter D_B [56].

It is common practice to add diffraction effects to the beam diameter $D(z)$ used in Eq. (94). For this purpose, the root sum square of the quantities found in Eq. (93) and Eq. (95) can be used to approximate the beam diameter $D(z)$ with diffraction effects, so that

$$D(z) = \sqrt{\left(D_0 \frac{Z-z}{Z}\right)^2 + \left(2.44 \frac{\lambda_0 z}{n_0 D_0}\right)^2}.$$

(97)

With the use of the Binomial approximation, Eq. (97) is further approximated to whole numbers as

$$D(z) = D_0 \frac{Z-z}{Z} + \frac{\lambda_0 z}{n_0 D_0}.$$

(98)

The added term to Eq. (98), as compared with Eq. (93), accounts for diffraction effects along the entire propagation range Z. In the source plane, $z = 0$, the HEL beam is no larger than the initial beam diameter D_0, and in the target plane, $z = Z$, the HEL beam diameter $D(z)$ is approximately half of the bucket diameter D_B.

If optical turbulence effects are taken into account, Eq. (98) is rewritten in terms of the coherence diameter r_0. The coherence diameter r_0 is widely used as a descriptor of the level of turbulence in the atmosphere [57]. Thus, Eq. (98) is rewritten, so that

$$D(z) = D_0 \frac{Z-z}{Z} + \frac{\lambda_0 z}{n_0 r_0}.$$

(99)

Equation (99) is only valid if the coherence diameter is less than the initial beam diameter, $r_0 < D_0$. Under turbulent propagation conditions, the far field HEL central spot size is limited by the coherence diameter r_0 rather than the initial beam diameter D_0. For this reason, increasing the initial beam diameter D_0 does not result in a smaller bucket diameter D_B. The resolution obtainable can be no smaller than the turbulence limited bucket diameter D_T, which is similar to the diffraction limited bucket diameter D_B, as given in Eq. (95). Here, the turbulence limited bucket diameter D_T is dependent on the coherence diameter r_0 using the following relationship:

$$D_T = 2.44 \frac{\lambda_0 Z}{n_0 r_0}. \qquad (100)$$

The idea presented in Eq. (100) will become more apparent with the analysis performed in the next section. With this in mind, characterizing turbulence in the atmosphere and its effects on thermal blooming is of interest now.

2.4 Turbulence in the Atmosphere

Fluctuations in the wind velocity or temperature in the atmosphere lead to unstable air masses called eddies which form in a continuum of sizes. Within a specific range of sizes, the change in the index of refraction $\Delta n(\mathbf{r}, t)$ caused by turbulence assumes a statistically homogeneous and isotropic value. As depicted in Figure 6, propagation in the atmosphere from one eddy to another causes the HEL beam irradiance to distort unevenly. Starting with a Gaussian-shaped beam profile in the source plane, turbulence causes a random-lens-like optical effect in the atmosphere, and the HEL beam

59

irradiance in the target plane becomes scintillated. In addition, atmospheric advection causes turbulent flow, where individual eddies travel across the HEL beam. This distorts the HEL beam target irradiance even more. The purpose of this section is to introduce the physics involved in characterizing the change in the index of refraction $\Delta n(\mathbf{r},t)$ caused by turbulence.
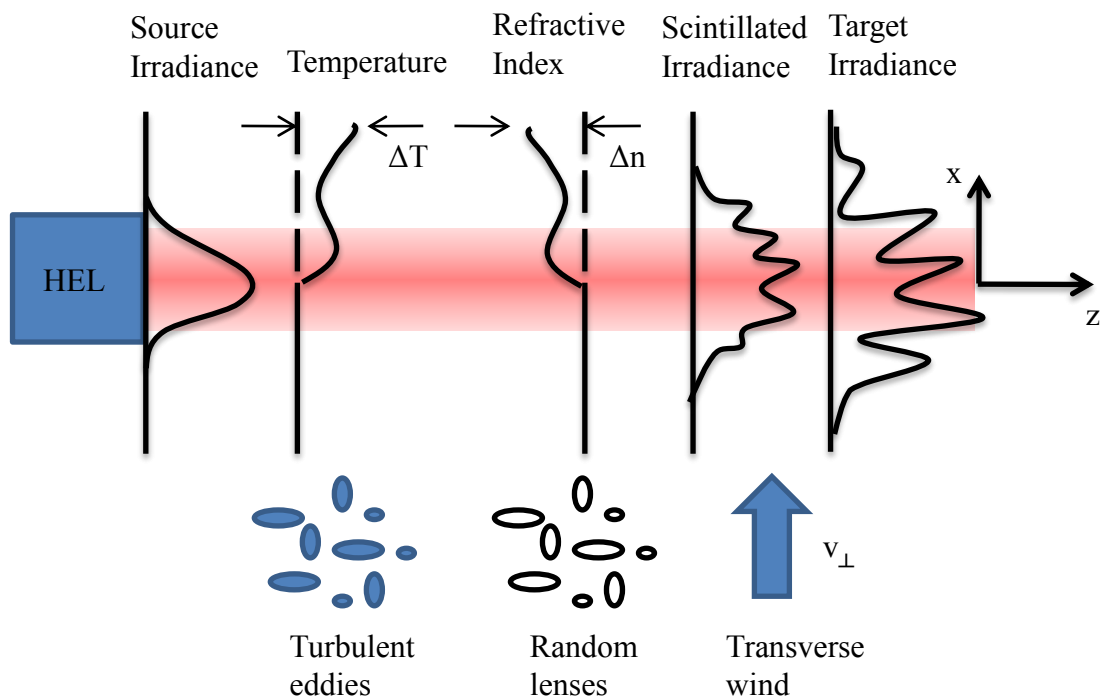
Figure 6. HEL propagation with the effects of turbulence. Random fluctuations in the temperature of the atmosphere causes turbulent eddies to form and consequently random variations in the refractive index. This induces an optical effect that scintillates the HEL beam irradiance. Atmospheric advection causes turbulent eddies to travel across the HEL beam distorting the target irradiance even more.

2.4.1 Classical Turbulence

Kolmogorov laid the foundation for a statistical analysis that is used in modeling turbulence in the atmosphere [58]. In practice, turbulence is a nonlinear process

governed by the Navier-Stokes equations. For fully formed turbulent flow in the atmosphere; however, obtaining closed-form solutions to the Navier-Stokes equations is unfeasible. There are too many random variables to account for. As a result, a statistical analysis can be used to model turbulence in the atmosphere. Kolmogorov based his statistical analysis primarily on insight after examining the behavior of fluctuations in the wind velocity. He hypothesized that within a range of eddy sizes called the inertial subrange, kinetic energy is transferrable. This idea is often referred to as energy cascade theory and asserts that the kinetic energy injected into larger eddies, by mechanisms such as atmospheric advection or wind shear, is transferrable to smaller eddies. Energy cascade theory is valid within the boundaries of the inertial subrange defined between the outer scale L_0 and the inner scale l_0. Kolmogorov assumed that eddies in the inertial subrange are locally statistically homogeneous and isotropic. From this assumption, he was able to develop a statistical analysis for turbulence in the atmosphere claiming that the wind velocity fluctuations are stationary in increments.

For a random process that is stationary in increments, the covariance is not readily applicable. Instead, the less common structure function is used to compute statistical quantities. For an arbitrary position-dependent random process $W(\mathbf{r})$, the position-dependent structure function $D_W(\mathbf{r})$ is defined as

$$D_W(\mathbf{r}_1, \mathbf{r}_2) \equiv D_W(\mathbf{r}) = \left\langle \left[W(\mathbf{r}_1) - W(\mathbf{r}_1 + \mathbf{r}) \right]^2 \right\rangle, \tag{101}$$

where the angled bracket notation represents the ensemble average and $\mathbf{r} = \mathbf{r}_2 - \mathbf{r}_1$ [13].

Provided Eq. (101), Kolmogorov was able to use dimensional analysis to determine the statistically homogeneous and isotropic wind velocity structure function $D_v(r)$ as

$$D_v(r) = \left\langle (v_1 - v_2)^2 \right\rangle = C_v^2(z) r^{2/3}, \tag{102}$$

where v_1 and v_2 represent wind velocity vector components at two points in the atmosphere separated by a distance $r = |\mathbf{r}|$. Equation (102) is only valid within the inertial subrange, $l_0 \ll r \ll L_0$. The depth-dependent parameter $C_v^2(z)$ is known as the wind velocity structure parameter and provides an amplitude measure for the strength of wind velocity fluctuations in the atmosphere. From the wind velocity structure function $D_v(r)$, as given in Eq. (102), Kolmogorov and many others were able to statistically characterize turbulence in the atmosphere.

2.4.2 Transverse Wind Velocity Vector of the Atmosphere

Up to this point in the analysis, there has been little discussion given as to the composition of the transverse wind velocity vector of the atmosphere. For example, in the derivation of the energy balance equation, given in Eq. (72), the depth-dependent transverse wind velocity vector $\mathbf{v}_\perp(z)$ of the atmosphere assumed the following form:

$$\mathbf{v}_\perp(z) = \left[v_x(z), v_y(z), 0 \right]. \tag{103}$$

Provided Eq. (103), it was discovered in the analysis of time-dependent thermal blooming that the transverse wind velocity vector $\mathbf{v}_\perp(z)$ of the atmosphere causes atmospheric advection or a spatial shift in the HEL beam irradiance. This is all well and good;

however, fluctuations in the wind velocity are not accounted for with the mathematical form of the transverse wind velocity vector $\mathbf{v}_\perp(z)$ included in Eq. (103). Wind velocity fluctuations and turbulent mixing in the atmosphere causes the transverse wind velocity vector $\mathbf{v}_\perp(z,t)$ to have both a depth and time dependence.

Fluctuations in the depth- and time-dependent transverse wind velocity vector $\mathbf{v}_\perp(z,t)$ occur statistically around a mean value. This point can be accounted for mathematically by expanding the transverse wind velocity vector $\mathbf{v}_\perp(z,t)$, as was done in Eq. (14) for the index of refraction $n(\mathbf{r},t)$ of the atmosphere, where

$$\mathbf{v}_\perp(z,t) = \mathbf{v}_0(z) + \Delta\mathbf{v}(z,t). \tag{104}$$

In Eq. (104), the depth-dependent parameter $\mathbf{v}_0(z)$ is the mean transverse wind velocity vector of the atmosphere. As such, it can now be seen that the mean transverse wind velocity vector is equivalent to the form of the transverse wind velocity vector, given in Eq. (103), such that $\mathbf{v}_0(z) = \mathbf{v}_\perp(z)$. The expansion given in Eq. (104) provides the mechanism needed to study fluctuations in the wind caused because of deviations from the mean transverse wind velocity vector $\mathbf{v}_0(z)$. These deviations are accounted for with the addition of the depth- and time-dependent change in the transverse wind velocity vector $\Delta\mathbf{v}(z,t)$.

In writing the form of the transverse wind velocity vector $\mathbf{v}_\perp(z,t)$, as given in Eq. (103), it is assumed that all of the fluctuations are temporal in nature. However, the form of the wind velocity structure function $D_v(r)$, as given in Eq. (102), alludes to idea

that classical turbulence is caused by spatial fluctuations in the wind velocity. To

account for this discrepancy, an equivalent statistically homogeneous and isotropic wind

velocity structure function $D_v(z,t)$ is proposed, so that [59]

$$D_v(z,t) = \left\langle \left[\Delta \mathbf{v}(z,t_1) - \Delta \mathbf{v}(z,t_1 + \Delta t) \right] \right\rangle = C_v^2(z) v_0^{4/3} t^{-2/3}, \qquad (105)$$

and again, is only valid within the inertial subrange, $l_0 \ll r \ll L_0$. In Eq. (105), t_1 and t_2

represent wind velocity vector at two different time stamps in the atmosphere, where

$\Delta t = t_2 - t_1$. Thus, the spatial fluctuations in the wind velocity are essentially folded into

the temporal fluctuations. These temporal fluctuations create a spatial spread in the wind

velocity.

The depth-dependent wind velocity standard deviation $\sigma_v(z)$ is used to account

for the spatial spread in the wind velocity. For this purpose, the change in the transverse

wind velocity vector $\Delta \mathbf{v}(z,t)$, as given in Eq. (104), is designated as a zero-mean

random component, so that its ensemble average is zero, $\left\langle \Delta \mathbf{v}(z,t) \right\rangle = 0$. This

mathematical trick is commonly used in the analysis of classical and optical turbulence.

Another analysis tool used here is to treat the change in the transverse wind velocity

vector $\Delta \mathbf{v}(z,t)$ like a zero-mean Gaussian random variable[1]. Consequently, the

associated position- and time-dependent probability density function (PDF) $P(\mathbf{r},t)$ is

then given in terms of wind velocity standard deviation $\sigma_v(z)$ as

---

[1] This step in the analysis is supported with empirical data and is readdressed in the next chapter.

$$P(x,y,z,t) = \frac{1}{2\pi\sigma_v^2(z)t^2} \exp\left\{-\frac{\left(x^2+y^2\right)}{2\sigma_v^2(z)t^2}\right\}. \tag{106}$$

From Eq. (106), it is more readily seen as to how the temporal fluctuations are related to the idea of a spatial spread in the wind velocity. Equation (106) says that the temporal fluctuations lead to a Gaussian distributed spatial spread in the wind velocity that grows with time. In addition, the associated position- and time- dependent characteristic function $\mathcal{P}\left(f_x, f_y, z, t\right)$ is determined by taking the Fourier transform of Eq. (106), so that

$$\mathcal{P}\left(f_x, f_y, z, t\right) = \exp\left\{-\frac{1}{2}\left[2\pi\sigma_v(z)t\right]^2\left(f_x^2+f_y^2\right)\right\}. \tag{107}$$

Equation (107) also provides a Gaussian distributed spatial spread in the wind velocity in the frequency domain. Here, as time progresses, the Gaussian distributed spatial spread decreases, as shown in Figure 7. The effects of the Gaussian distributed spatial spread in the wind velocity are of interest now in the study of time-dependent thermal blooming.
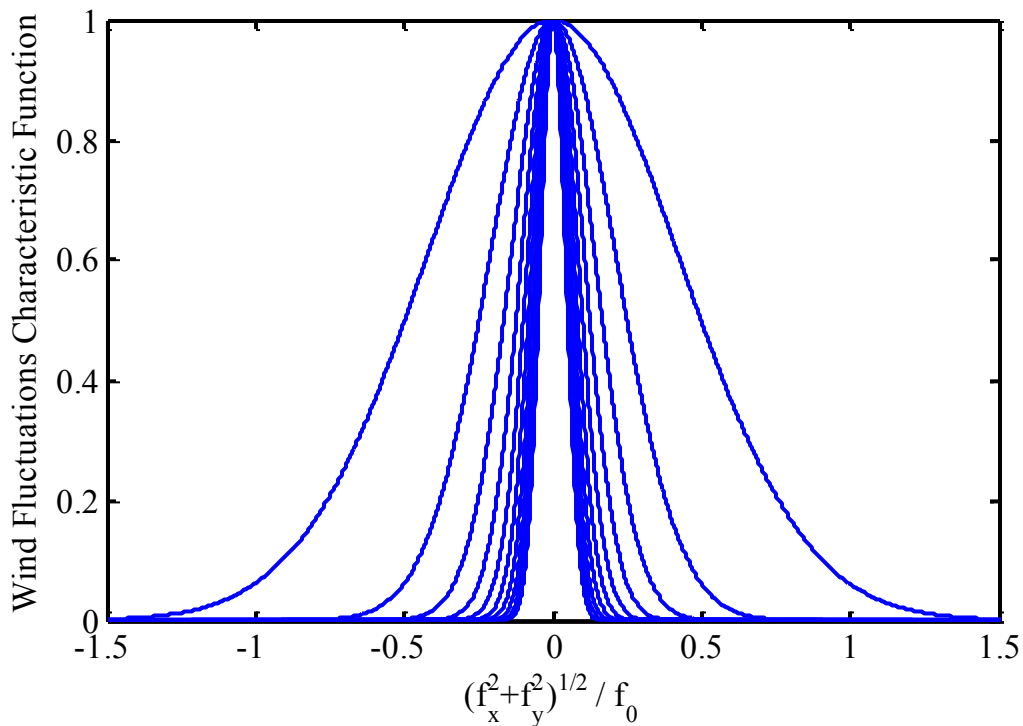
Figure 7. Ten independent realizations of the wind fluctuations characteristic function with time steps of, Δt=1 ms. In the frequency domain, as time progresses, the Gaussian distributed spatial spread in the wind velocity decreases.

2.4.3 Time-Dependent Turbulent Thermal Blooming

In the analysis of time-dependent thermal blooming performed above, the effects

of the Gaussian distributed spatial spread in the wind velocity were not accounted for.

For this purpose, Fried performed an analysis on blurring effects in time-dependent

thermal blooming [60]. In this ground breaking work, Fried recognized the Gaussian

distributed spatial spread in the wind velocity as a spatial filtering process. This spatial

filtering essentially acts like a blurring mechanism for the heating of the atmosphere

caused by time-dependent thermal blooming. Mathematically, the spatial filtering is

realized as the two-dimensional convolution between the change in the index of

refraction $\Delta n(\mathbf{r},t)$ of the atmosphere caused by time-dependent thermal blooming, and

the wind fluctuations PDF $P(\mathbf{r},t)$, as given in Eq. (106), so that

$$
\begin{aligned}
\Delta n'(x,y,z,t) &= \int_{-\infty}^{\infty} \int_{-\infty}^{\infty} \Delta n(x,y,z,t) P(x-\xi, y-\eta, z,t) d\xi d\eta \\
&= \Delta n(x,y,z,t) ** P(x,y,z,t)
\end{aligned}
\tag{108}
$$

where here, $\Delta n'(\mathbf{r},t)$ is the filtered change in the index of refraction of the atmosphere

caused by turbulent thermal blooming. With the use of the convolution theorem, Eq.

(108) is further simplified in terms of the wind fluctuations characteristic function

$\mathcal{P}(f_x, f_y, z, t)$, as given in Eq. (107), where

$$
\Delta n'(x,y,z,t) = \hat{\mathcal{F}}^{-1}\left\{ \hat{\mathcal{F}}\left[\Delta n(x,y,z,t) \right] \mathcal{P}(f_x, f_y, z, t) \right\}.
\tag{109}
$$

From Eq. (109), it is more readily seen as to how the Gaussian distributed spatial spread

in the wind velocity is related to a spatial filtering process. Equation (109) says that the

change in the index of refraction $\Delta n(\mathbf{r},t)$ caused by time-dependent thermal blooming is

filtered by the wind fluctuations characteristic function $\mathcal{P}(f_x, f_y, z, t)$, which represents

the Gaussian distributed spatial spread in the wind velocity in the frequency domain. As

time progress, this filtering becomes stronger, since in the frequency domain, the

Gaussian distributed spatial spread in the wind velocity decreases, as shown above in

Figure 7.

By substituting Eq. (81) into Eq. (109), the refraction effect of turbulent thermal

blooming can be accounted for in HEL propagation in the atmosphere. With a little

manipulation, the change in the index of refraction $\Delta n'(\mathbf{r},t)$ is determined as

$$\Delta n'(x,y,z,t)$$

$$= -\mu(z)\int_0^t \hat{\mathcal{F}}^{-1}\left\{\hat{\mathcal{F}}\left[I(x,y,z,t)\right]T\left(f_x,f_y,z,t-\tau\right)P\left(f_x,f_y,z,t\right)\right\}d\tau \quad (110)$$

where here, the translation filter function $T\left(f_x,f_y,z,t\right)$, as given in Eq. (83), was

utilized to simplify the mathematics. Equation (110) serves as an analytically determined

time-dependent solution to the energy balance equation, as given in Eq. (72), for the

change in the index of refraction $\Delta n'(\mathbf{r},t)$ caused by turbulent thermal blooming.

Equation (110) is modeled computationally by modifying Eq. (84) in terms of the

characteristic function $P\left(f_x,f_y,z,t\right)$, as given in Eq. (107). For this purpose, the

following expression is readily used [60,49]:

$$\Delta n'(x,y,z,t_{j+1}) =$$
$$\mu(z)I'(x,y,z,t_{j+1})\Delta t + \quad (111)$$
$$\sum_{m=-\infty}^{j} \hat{\mathcal{F}}^{-1}\left\{\hat{\mathcal{F}}\left[\Delta n(x,y,z,t_m)\right]T\left(f_x,f_y,z,t_m-t_{m-1}\right)P\left(f_x,f_y,z,t_m-t_{m-1}\right)\right\}$$
.

Equation (111) provides a way to simulate time-dependent turbulent thermal blooming.

The spatial filtering is realized for all previous time steps. In practice, the spatial filtering

is truncated. This is done to prevent aliasing and to increase computational performance

[49]. Simulating time-dependent thermal blooming and or time-dependent turbulent

thermal blooming using the BPM typically requires a large number of partial

propagations and phase screens $\Phi(x,y,z_{j+1},t)$. As a result, a trade-off analysis is

necessary to determine the truncation point for the spatial filtering performed by Eq.

(111).

The important thing to remember in the study of time-dependent turbulent thermal blooming is that the heating and cooling of the atmosphere causes the HEL beam to develop a crescent-shaped target irradiance that is spatially filtered. As time progresses, the spatial filtering increasing blurs the development of the crescent-shaped target irradiance. This tends to increase system performance. Consequently, the refraction caused by time-dependent turbulent thermal blooming is less severe when compared to time-dependent thermal blooming. It is important to note; however, that turbulence also causes a random-lens-like optical effect in the atmosphere. The HEL beam irradiance becomes scintillated as a result. This often overrides any gain in system performance associated with time-dependent turbulent thermal blooming. Characterizing optical turbulence is of importance now.

2.4.4 Optical Turbulence

Based on Kolmogorov's work, Obukhov and Corrsin, who worked independently of each other, were able to associate wind velocity fluctuations to potential temperature fluctuations [61,62]. Potential temperature is linearly related to temperature. Thus, Obukhov and Corrsin were able to determine the statistically homogeneous and isotropic temperature structure function $D_T(r)$ from the wind velocity structure function $D_v(r)$, determined in Eq. (102), as

$$D_T(r) = \left\langle (T_1 - T_2)^2 \right\rangle = C_T^2(z) r^{2/3}. \tag{112}$$

Here, T_1 and T_2 represent the temperature at two points in the atmosphere separated by a distance r within the inertial subrange, $l_0 \ll r \ll L_0$. The depth-dependent temperature structure parameter $C_T^2(z)$ can be related to the wind velocity structure parameter

$C_v^2(z)$; however, this relationship is often overlooked in the analysis. It is more common to relate temperature fluctuations to refractive-index fluctuations.

Provided the relationship found in Eq. (112) with respect to temperature fluctuations, a similar relationship can be determined for the index of refraction $n(\mathbf{r},t)$ of the atmosphere. For this purpose, it is important to revisit the mathematical form of the index of refraction $n(\mathbf{r},t)$ of the atmosphere. Temperature fluctuations and turbulent mixing statistically cause the index of refraction $n(\mathbf{r},t)$ of the atmosphere to fluctuate around a mean value. This point can be accounted for mathematically by expanding the real component $n_R(\mathbf{r},t)$ of the index of refraction $n(\mathbf{r},t)$ of the atmosphere, as was done in Eq. (14), where

$$n_R(\mathbf{r},t) = n_0 + \Delta n(\mathbf{r},t). \tag{113}$$

Refraction caused by optical turbulence in the atmosphere results in a change in the index of refraction $\Delta n(\mathbf{r},t)$ that represents deviations from a mean value. Here, the ambient index of refraction n_0 is this mean value and the ensemble average of the change in the index of refraction is zero, $\langle \Delta n(\mathbf{r},t) \rangle = 0$. Based on this insight, Eq. (113) provides a mechanism to study statistical quantities associated with the spatial and temporal variations in the index of refraction $n(\mathbf{r},t)$ of the atmosphere caused by optical turbulence.

Temporal variations in the index of refraction $n(\mathbf{r},t)$ of the atmosphere are often neglected in the study of optical turbulence. Consequently, Eq. (113) is rewritten without time dependence, so that

$$n_R(\mathbf{r}) = n_0 + \Delta n(\mathbf{r}). \tag{114}$$

The relationship found in Eq. (114) makes use of Taylors frozen turbulence hypothesis. This hypothesis claims that temporal variations of atmospheric quantities at a point in space are produced by atmospheric advection of these quantities due to the mean transverse wind velocity vector $\mathbf{v}_0(z)$ and not by changes in these quantities themselves [13]. Under Taylors frozen turbulence hypothesis, eddies are treated as if they were frozen in space and travel in the direction of the mean transverse wind velocity vector $\mathbf{v}_0(z)$, i.e. the change in the transverse wind velocity vector $\Delta \mathbf{v}(z,t)$ is neglected.

Temporal variations caused by turbulence in the atmosphere are accounted for with a spatial shift due to atmospheric advection. For example, the change in the index of refraction $\Delta n(\mathbf{r},t)$ caused by optical turbulence in the atmosphere and the associated time dependence is modeled computationally as

$$\Delta n(x,y,z,t_{i+1}) = \Delta n\left(x - v_x(z)\Delta t, y - v_y(z)\Delta t, z, t_i\right), \tag{115}$$

where here, the change in the index of refraction $\Delta n(\mathbf{r},t)$ is updated from the previous time t_j to the present time t_{j+1} with the time step, $\Delta t = t_{j+1} - t_j$. The validity of Taylors frozen hypothesis and Eq. (115) is supported with experimental evidence; however, different engagement scenario parameters may require additional constraints. Such is the case when in the presence of aero-optical turbulent flow [63].

Optical turbulence causes spatial variations in the time-independent index of refraction $n(\mathbf{r})$ of the atmosphere. These spatial variations in the index of refraction $n(\mathbf{r})$ are empirically related to spatial variations in the position-dependent temperature $T(\mathbf{r})$ and pressure $P(\mathbf{r})$ using Eq. (62). For this purpose, Eq. (62) is rewritten here neglecting the isobaric approximation, so that

$$n(\mathbf{r}) = 1 + 77.6x10^{-6}\left(1 + 7.52x10^{-3}\lambda^{-2}\right)\frac{P(\mathbf{r})}{T(\mathbf{r})}. \qquad (116)$$

The relationship provided by Eq. (116) says that the index of refraction $n(\mathbf{r})$ of the atmosphere is inversely proportional to the temperature $T(\mathbf{r})$ of the atmosphere. As a result, there is a direct relationship found between the statistically homogeneous and isotropic index of refraction structure function $D_n(r)$ and the temperature structure function $D_T(r)$, as given in Eq. (112), so that

$$D_n(r) = \left\langle \left[n(\mathbf{r}_1) - n(\mathbf{r}_2)\right]^2 \right\rangle = C_n^2(z)r^{2/3}. \qquad (117)$$

Equation (117) is again only valid within the inertial subrange, $l_0 \ll r \ll L_0$, where r represents the distance found between the vectors $\mathbf{r}_1$ and $\mathbf{r}_2$. The depth-dependent index of refraction structure parameter $C_n^2(z)$ is a measure for the strength of refractive-index fluctuations. In units of meters to the negative two thirds power $\left(\mathrm{m}^{-2/3}\right)$, the index of refraction structure parameter $C_n^2(z)$ is deduced from the temperature structure parameter $C_T^2(z)$ and Eq. (116) as [9]

$$C_n^2(z) = \left[77.6x10^{-6} \left(1 + 7.52x10^{-3} \lambda^{-2}\right) \frac{P(z)}{T_0(z)} \right] C_T^2(z). \tag{118}$$

Typical values for the index of refraction structure parameter $C_n^2(z)$ range from 10^{-17} m$^{-2/3}$ or less for "weak" optical turbulence to 10^{-17} m$^{-2/3}$ or more for "strong" optical turbulence [13]. With this in mind, the goal now is to develop the theory needed to review other useful parameters which characterize optical turbulence.

For a wide range of analytical calculations involving random processes, the power spectral density (PSD) is needed. As such, the statistically homogeneous and isotropic index of refraction PSD $\Phi_n(\kappa)$ is obtained from the index of refraction structure function $D_n(r)$ using the following relationship [13]:

$$\Phi_n(\kappa) = \frac{1}{4\pi^2\kappa^2} \int_0^\infty \frac{\sin(kr)}{kr} \frac{d}{dr} \left[r^2 \frac{d}{dr} D_n(r) \right] dr, \tag{119}$$

where $\kappa = 2\pi\sqrt{f_x^2 + f_y^2}$ is the angular spatial frequency magnitude in units of radians per meter (rad/m). The index of refraction PSD $\Phi_n(\kappa)$, as given in Eq. (119), determines how power found within refractive-index fluctuations is distributed with respect to spatial frequency. Within the inertial subrange, $1/l_0 \ll \kappa \ll 1/L_0$, Eq. (119) is determined as

$$\Phi_n(\kappa) = 0.033 C_n^2(z) \kappa^{-11/3} \tag{120}$$

and is often referred to as the Kolmogorov refractive-index power spectrum. Other index of refraction PSD $\Phi_n(\kappa)$ models do exist to account for refractive-index fluctuations

outside the inertial subrange. They include the Tatarsky[2], von Karmon, modified von Karmon, and Hill refractive-index power spectrums [13].

The change in the index of refraction $\Delta n(\mathbf{r})$ caused by optical turbulence in the atmosphere can be modeled computationally with the use of the index of refraction PSD $\Phi_n(\kappa)$, as given in Eq. (120). Since the change in the index of refraction caused by optical turbulence is considered to be a zero mean random process, $\langle \Delta n(\mathbf{r},t) \rangle = 0$, so is the phase screen $\Phi(x,y,z_{j+1};t)$, given in Eq. (44). Thus, refractive-index fluctuations are often modeled computationally with the concept of a Monte-Carlo phase screen $\Phi(x,y,z_{j+1};t)$. There are many fruitful methods found throughout the literature concerned with this topic—the method presented by Schmidt is particularly informative [9].

Refractive-index fluctuations are statistically related to optical-disturbance fluctuations, through use of the inhomogeneous Helmholtz equation, as found in Eq. (18). For instance, if the index of refraction $n(\mathbf{r})$ of the atmosphere is specified by a real stochastic expansion, as given in Eq. (114), Eq. (18) is rewritten in the following form:

$$\nabla^2 U(\mathbf{r}) + \left[1 + 2\Delta n(\mathbf{r})\right] k_0^2 U(\mathbf{r}) = 0, \tag{121}$$

where here,

$$n^2(\mathbf{r}) \approx 1 + 2\Delta n(\mathbf{r}). \tag{122}$$

---

[2] Sometimes spelled Tatarskii in the American literature.

The approximation provided by Eq. (122) is typically used since the ambient index of refraction is approximately equal to the vacuum index of refraction, $n_0 \approx 1$, and the change in the index of refraction $\Delta n(\mathbf{r})$ caused by optical turbulence is considered to be on the order of parts per million. As a result, Eq. (121) is often referred to as the statistical Helmholtz equation.

To compute statistical moments for optical disturbances propagating in a turbulent atmosphere, an approximate solution to the statistical Helmholtz equation is needed for the complex scalar function $U(\mathbf{r})$. For this purpose, there are numerous approaches used throughout the literature to approximate solutions to Eq. (121). The two most widely used approaches include the Born approximation and Rytov approximation [13]. Of these two approaches, the Rytov approximation is more accurate in computing statistical quantities for optical turbulence. In using the Rytov approximation, the scalar function $U(\mathbf{r})$ for optical disturbances assumes the form:

$$U(\mathbf{r}) = U_0(\mathbf{r}) \exp\left[\psi(\mathbf{r})\right], \tag{123}$$

where $U_0(\mathbf{r})$ is the vacuum solution to the statistical Helmholtz equation given in Eq. (121), so that $n(\mathbf{r}) = 1$. The complex phase perturbation $\psi(\mathbf{r})$ is used to perform successive perturbations, where

$$\psi(\mathbf{r}) = \psi_1(\mathbf{r}) + \psi_2(\mathbf{r}) + \dots. \tag{124}$$

These successive perturbations are used to compute various statistical moments of the complex phase perturbation $\psi(\mathbf{r})$, which in turn yields statistical moments for optical disturbances propagating in a turbulent atmosphere [9]. In addition, the complex phase

perturbation $\psi(\mathbf{r})$ is often written as a complex function in terms of the log-amplitude

perturbation $\chi(\mathbf{r})$ and the phase perturbation $\varphi(\mathbf{r})$, so that

$$\psi(\mathbf{r}) = \chi(\mathbf{r}) + i\varphi(\mathbf{r}). \tag{125}$$

Equation (125) provides further utility in computing statistical moments for optical

disturbances propagating in a turbulent atmosphere. The goal now is to list some of these

statistical moments and resultant parameters that are used to further characterize optical

turbulence. Their derivations are found throughout the literature [64,65,66,13].

2.4.5 Optical Turbulence Parameters

The index of refraction structure parameter $C_n^2(z)$ is a useful parameter to have

in characterizing the strength of refractive-index fluctuations caused by optical

turbulence. Nevertheless, computing statistical moments for optical disturbances provide

other useful parameters that are handy in characterizing specific effects caused by optical

turbulence [9]. The first statistical moment of interest here is the position-dependent log-

amplitude variance $\sigma_\chi^2(\mathbf{r})$ and is defined by the following relationship:

$$\sigma_\chi^2(\mathbf{r}) = \langle \chi^2(\mathbf{r}) \rangle - \langle \chi(\mathbf{r}) \rangle^2 \tag{126}$$

Equation (126) makes use of the log-amplitude perturbation $\chi(\mathbf{r})$, as given in Eq. (125).

For a particular engagement scenario, the log-amplitude variance σ_χ^2 is a measure for the

strength of the scintillation caused by optical turbulence in the atmosphere. Weak

refractive-index fluctuations are associated with $\sigma_\chi^2 < 0.25$, and strong fluctuations are

associated with $\sigma_\chi^2 \gg 0.25$. Under weak refractive-index fluctuations, the log-amplitude

variance $\sigma_{\chi,pw}^2$ for a plane-wave source is given as [9]

$$\sigma_{\chi,pw}^2 = 0.563\beta^{7/6} Z^{5/6} \int_0^Z C_n^2(z)\left(1-\frac{z}{Z}\right)^{5/6} dz, \qquad (127)$$

and for a spherical wave emitted from a point source, the log-amplitude variance

$\sigma_{\chi,sw}^2(z)$ is determined, so that

$$\sigma_{\chi,sw}^2 = 0.563\beta^{7/6} \int_0^Z C_n^2(z) z^{5/6}\left(1-\frac{z}{Z}\right)^{5/6} dz, \qquad (128)$$

where again, $\beta = n_0 k_0$. The Rytov approximation typically breaks down under strong

refractive-index fluctuations; hence, Eq. (127) and Eq. (128) are only valid for weak

refractive-index fluctuations.

The second statistical moment of interest in this analysis is the mutual coherence

function (MCF) $\Gamma(\mathbf{r}_1,\mathbf{r}_2,Z)$. Specifically, the MCF $\Gamma(\mathbf{r}_1,\mathbf{r}_2,Z)$ is a measure for spatial

coherence between two points, $\mathbf{r}_1$ and $\mathbf{r}_2$, in the target plane, $z = Z$, and is defined by the

following relationship:

$$\begin{aligned}\Gamma(\mathbf{r}_1,\mathbf{r}_2,Z) &= \left\langle U(\mathbf{r}_1,Z)U^*(\mathbf{r}_2,Z)\right\rangle \\ &= U_0(\mathbf{r}_1,Z)U_0^*(\mathbf{r}_2,Z)\left\langle \exp\left[\psi(\mathbf{r}_1,Z)+\psi^*(\mathbf{r}_2,Z)\right]\right\rangle\end{aligned}. \qquad (129)$$

Goodman's description of the MCF is particularly insightful and is outlined here [67].

- When two points in the target plane perfectly overlap, they are perfectly
  correlated and the optical source is called mutually coherent.

- As the two points move apart, the degree of correlation decreases and the optical
  source is called partially coherent.

- When the degree of correlation is zero, the optical source is called mutually incoherent.

Different engagement scenario parameters and optical turbulence parameters determine the degree of correlation described above. Furthermore, the degree of coherence (DOC) $\gamma(\mathbf{r}_1, \mathbf{r}_2, Z)$ is deduced from the MCF $\Gamma(\mathbf{r}_1, \mathbf{r}_2, Z)$ using the following relationship:

$$
\begin{aligned}
\gamma(\mathbf{r}_1, \mathbf{r}_2, Z) &= \frac{\left| \Gamma(\mathbf{r}_1, \mathbf{r}_2, Z) \right|}{\sqrt{\Gamma(\mathbf{r}_1, \mathbf{r}_1, Z) \Gamma(\mathbf{r}_2, \mathbf{r}_2, Z)}}, \\
&= \exp\left[-\frac{1}{2} D(\mathbf{r}_1, \mathbf{r}_2, Z) \right]
\end{aligned}
\tag{130}
$$

where $D(\mathbf{r}_1, \mathbf{r}_2, Z)$ is known as the wave structure function (WSF). Within the inertial subrange, $l_0 \ll r \ll L_0$, the wave structure function is determined from the index of refraction structure parameter $C_n^2(z)$ as [68]

$$
D(r, Z) = 2.91 k_0^2 r^{5/3} \int_0^Z C_n^2(z) \, dz,
\tag{131}
$$

where again, $r = |\mathbf{r}|$ and $\mathbf{r} = \mathbf{r}_2 - \mathbf{r}_1$. The $1/e$ point of the DOC $\gamma(\mathbf{r}_1, \mathbf{r}_2, Z)$ defines a parameter known as the spatial coherence radius ρ_0. This is also where the WSF is equal to two, $D[\rho_0, Z] = 2$.

The usefulness of both the MCF $\Gamma(\mathbf{r}_1, \mathbf{r}_2, Z)$ and DOC $\gamma(\mathbf{r}_1, \mathbf{r}_2, Z)$ is readily seen from the definition of the spatial coherence radius ρ_0. For example, the coherence diameter r_0 is determined from the spatial coherence radius ρ_0 using the following relationship [68]:

$$
r_0 = 2.1 \rho_0.
\tag{132}
$$

Remember that the idea of the coherence diameter r_0 was already introduced in the

definition of the distortion number N_D. For a plane-wave source, the coherence diameter

$r_{0,pw}$ is analytically determined as [66,9]

$$r_{0,pw} = \left[0.423 k_0^2 \int_0^Z C_n^2(z) dz \right]^{-3/5}. \tag{133}$$

Similarly, for a spherical wave emitted from a point source, the coherence diameter $r_{0,sw}$

is analytically determined to be [66,9]

$$r_{0,sw} = \left[0.423 k_0^2 \int_0^Z C_n^2(z) \left(\frac{z}{Z} \right)^{5/3} dz \right]^{-3/5}. \tag{134}$$

As was mentioned before, the coherence diameter r_0 is widely used as a descriptor of the

level of turbulence in the atmosphere. Apertures with a diameter larger than the

coherence diameter r_0 experience a breakdown in the degree of correlation or coherence

description [69]. For instance, if the coherence diameter r_0 is smaller than the initial

beam diameter D_0, increasing the initial beam diameter D_0 results in minimal resolution

gain for a focused HEL beam propagating in the atmosphere. This says that the

resolution obtainable after propagation in the atmosphere can be no smaller than the

coherence diameter r_0. For poor resolution conditions, the coherence diameter r_0 ranges

from under 5 cm to 20 cm with good resolution conditions [70].

2.4.6 Imaging Through Optical Turbulence

The coherence diameter r_0 is often referred to as the Fried parameter because it

was originally introduced by Fried [71]; however, in a very different way than the

relationship found in Eq. (132). In this ground breaking work, Fried analyzed the resolution of an imaging telescope. He defined what is known as the atmospheric modulation transfer function (MTF). By analyzing the area under the atmospheric MTF, he was able to define the coherence diameter r_0 as ―the knee in the curve,‖ where increasing the telescope diameter did not increase imaging resolution. In practice, characterizing an imaging system becomes particularly complicated when the imaging system does not perfectly focus the image because of aberrations present in the optical system. Imaging through optical turbulence [71,67,72] and or thermal blooming [19,73,74] also significantly degrades imaging system performance with aberrations.

The effects of aberrations can be characterized in an imaging system with the use of position-dependent wavefronts $w(x,y)$ measured in waves (λ). Wavefronts $w(x,y)$ are defined as the surfaces of optical disturbances with equal phase $\phi(x,y)$, so that $\phi(x,y) = 2\pi w(x,y)$. Accordingly, any wavefront can be represented as a series expansion. For azimuthally symmetric optical systems, it is common practice to use Zernike circle polynomials $Z_j(r,\theta)$, so that the wavefronts $w(r,\theta)$ can be written as a Zernike series with coefficients a_j, where

$$w(r,\theta) = \sum_{j=1}^{\infty} a_j Z_j(r,\theta). \tag{135}$$

Here, $x = r\cos\theta$ and $y = r\sin\theta$. Note that the index j provides the different modes of the Zernike series.

Several conventions for Zernike circle polynomials $Z_j(r,\theta)$ are defined throughout the literature [75,76,72,77,9]. The convention defined by Noll and used by Roggemann and Schmidt is particularly tractable and is outlined here [76,72,9]. For this purpose, Zernike circle polynomials $Z_j(r,\theta)$ are defined as

$$Z_j(r,\theta) = \begin{cases} \sqrt{2(n+1)}R_n^m(r)G^m(\theta) & m \neq 0 \\ R_n^0(r) & m = 0 \end{cases}, \qquad (136)$$

where m and n are non-negative integers and $m \geq n$. The mapping of $(m,n) \to i$ is complicated, but the notation is greatly simplified. In Eq. (136), the radial $R_m^n(r)$ and azimuthal $G^n(\theta)$ components are given by the following relationships:

$$R_m^n(r) = \sum_{s=0}^{(n-m)/2} \frac{(-1)^s (n-s)!}{s!\left(\dfrac{n+m}{2}-s\right)!\left(\dfrac{n-m}{2}-s\right)!} r^{n-2s} \qquad (137)$$

$$G^m(\theta) = \begin{cases} \sin(m\theta) & j \text{ odd} \\ \cos(m\theta) & j \text{ even} \end{cases}. \qquad (138)$$

The utility found in using Zernike circle polynomials $Z_j(r,\theta)$ is that they are complete and orthogonal over the unit circle. Therefore, the coefficients a_j in Eq. (135) are found as

$$a_j = \frac{\displaystyle\int_0^{2\pi}\!\!\int_0^1 w(r,\theta)Z_j(r,\theta)r\,dr\,d\theta}{\displaystyle\int_0^{2\pi}\!\!\int_0^1 Z_j^2(r,\theta)r\,dr\,d\theta}. \qquad (139)$$

81

Provided the relationship in Eq. (139), the amplitude strength of the Zernike circle polynomials $Z_j(r,\theta)$ are determined for the different modes j. With an infinite number of modes j, the wavefronts $w(r,\theta)$ obtained with Eq. (135) perfectly represent the aberrations present in the imagining system. However, a finite number of modes j are practically used to construct the wavefronts $w(r,\theta)$ given by Eq. (135). These mode-limited wavefronts $w_m(r,\theta)$ consist of the finite number modes j_m needed to characterize the aberrations present in the imaging system to a user-defined accuracy or limitation.

The wavefront variance σ^2 is one way to determine the accuracy or limitation associated with mode-limited wavefronts $w_m(r,\theta)$. As such, the wavefront variance σ^2 is determined from the coefficients a_j, provided by Eq. (139), using the following relationship [9]:

$$\sigma^2 = \sum_{j=2}^{\infty} a_j^2 \,. \tag{140}$$

Equation (140) results from using a complete orthogonal basis set to characterize aberrations via wavefronts $w(r,\theta)$. The mode-limited wavefront variance σ_m^2 is also found from Eq. (140) when the infinite sum is truncated to the finite number modes j_m. In practice, computational methods are needed to determine the mode-limited coefficients a_{j_m} given by Eq. (139). The computational methods presented by Schmidt are particularly informative with respect to imaging systems and aberrations [9].

82

Once the aberrations present within an imaging system are characterized with wavefronts $w(x,y)$, the performance of that imaging system can be evaluated with the use of a two-dimensional convolution. For example, provided the use of a spatially incoherent source, optical systems respond linearly in irradiance; thus, the image plane irradiance $I_i(u,v)$ of an incoherent imaging system is determined from the two-dimensional convolution between the object plane irradiance $I_o(\xi,\eta)$ and the point spread function (PSF) $h(u,v)$, where [9]

$$I_i(u,v) = h(u,v) ** I_o(u,v).$$

(141)

Note that in writing Eq. (141), unit magnification, $M = 1$, is assumed since in the absence of aberrations, the object plane coordinates at (ξ,η) are related to the image plane coordinates at (u,v) by the ideal image point $(u = M\xi, v = M\eta)$, as described in Figure 8. In addition, the PSF $h(u,v)$ is formally defined as the squared modulus of the space invariant amplitude impulse response $g(u,v)$ of the imaging system, where [14]

$$h(u,v) = |g(u,v)|^2.$$

(142)

The PSF $h(u,v)$, as defined in Eq. (142), is nothing more than the image plane irradiance $I_i(u,v)$ of an imaged point source. If a point source is imaged, instead of seeing a point, the optical detector will see the PSF $h(u,v)$.
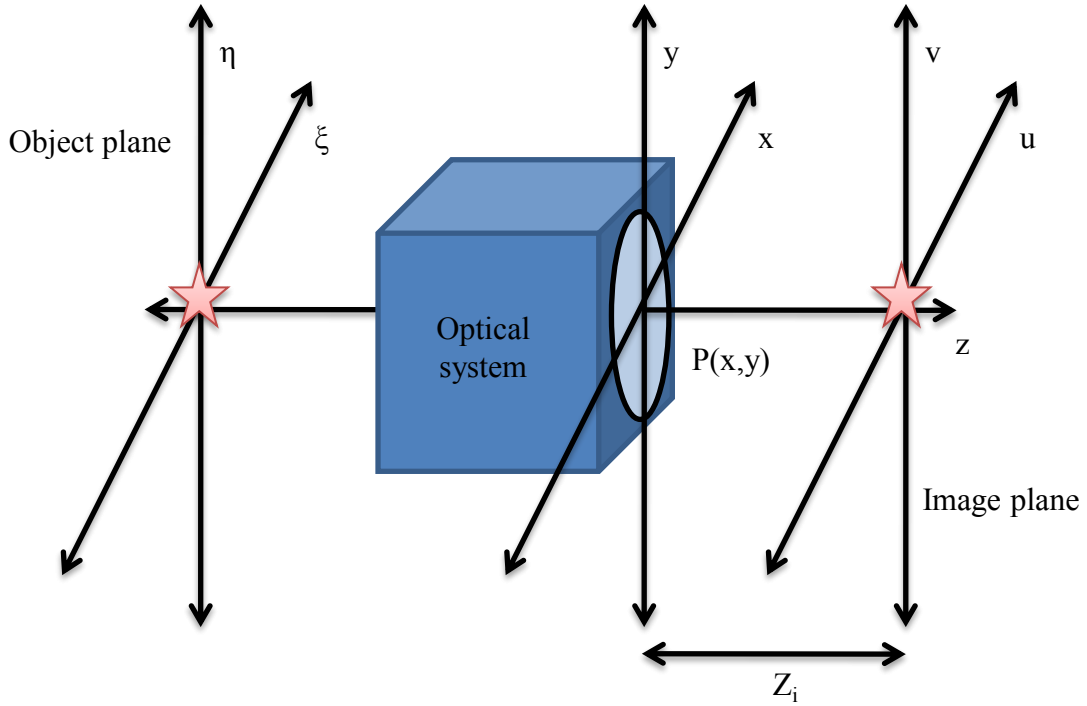
Figure 8. Description of a basic imaging system with unit magnification and no aberrations.

In the presence of aberrations, the amplitude impulse response $g(u,v)$ is simply

the Fraunhofer diffraction pattern or scaled two-dimensional Fourier transform of the

generalized pupil function $\mathcal{P}(x,y)$. For this purpose, the generalized pupil function

$\mathcal{P}(x,y)$ is determined from the wavefronts $w(x,y)$, as given in Eq. (135), as

$$\mathcal{P}(x,y) = P(x,y)\exp\left[i2\pi w(x,y)\right] \tag{143}$$

and represents the aberrations present within the imaging system. The parameter

$P(x,y)$, as given in Eq. (143), is the pupil function of the imaging system which

mathematically describes the shape of the exit pupil of the optical system. Provided Eq.

(143), the amplitude impulse response $g(u,v)$ is determined as

$$g(u,v) = \frac{n_0}{\lambda_0 Z_i} \hat{\mathcal{F}}\left[\mathcal{P}(x,y)\right]_{f_x = \frac{n_0 u}{\lambda_0 Z_i}, f_y = \frac{n_0 v}{\lambda_0 Z_i}}, \tag{144}$$

where Z_i is the image distance. In the absence of aberrations, a circular generalized

pupil function is equal to the pupil function, $\mathcal{P}(x,y) = P(x,y)$, and is defined

mathematically as

$$P(x,y) = \text{cyl}\left(\frac{\sqrt{x^2 + y^2}}{D}\right), \tag{145}$$

where $\text{cyl}\left(\sqrt{x^2 + y^2}/D\right)$ is the commonly used cylinder function associated with an exit

pupil of diameter D [56]. From Eq. (144) and Eq. (145), the PSF $h(u,v)$ is equivalent

to the irradiance $I(\mathbf{r})$ found in Eq. (96) for the Fraunhofer diffraction pattern of a

circular aperture, where $x = u$, $y = v$, and $z = Z_i$.

Using linear systems analysis, Eq. (141) is further simplified with the use of the

convolution theorem. Now, the image plane irradiance $I_i(u,v)$ is determined as

$$I_i(u,v) = \hat{\mathcal{F}}^{-1}\left\{\hat{\mathcal{F}}\left[h(u,v)\right]\hat{\mathcal{F}}\left[I_o(u,v)\right]\right\}. \tag{146}$$

Normalizing the filter function given by the Fourier transform of the PSF, $\hat{\mathcal{F}}\left[h(u,v)\right]$,

provides what is known as the optical transfer function (OTF) $H(f_x, f_y)$, where [9]

$$H(f_u, f_v) = \frac{\hat{\mathcal{F}}\left[h(u,v)\right]}{\int\limits_{-\infty}^{\infty}\int\limits_{-\infty}^{\infty} h(u,v)\,du\,dv}. \tag{147}$$

Since the MTF is given by the magnitude of the OTF, $\left|H\left(f_x,f_y\right)\right|$, Eq. (147) is widely used throughout the optics community to characterize incoherent imaging systems. The MTF $\left|H\left(f_x,f_y\right)\right|$, and consequently the OTF $H\left(f_x,f_y\right)$, is just a ratio of image contrast to object contrast at a given spatial frequency [69]. Multiple image degrading effects can be accounted for with the OTF $H\left(f_u,f_v\right)$, as defined in Eq. (147). For this purpose, the equivalent OTF $H_{EQ}\left(f_u,f_v\right)$ for an incoherent imaging system is found through the multiplication of multiple OTF's. Herein lays the fruitfulness associated with using the OTF $H\left(f_u,f_v\right)$ to characterize the performance of an incoherent imaging system.

In defining the equivalent OTF $H_{EQ}\left(f_u,f_v\right)$, each image degrading effect found within an incoherent imaging system must be accounted for separately. For example, the OTF $H_{DL}\left(f_u,f_v\right)$ associated with diffraction-limited incoherent imaging and the circular pupil function $P(x,y)$, as given in Eq. (145), is determined as

$$H_{DL}\left(f_u,f_v\right)=\mathrm{chat}\left(f_u,f_v\right),\tag{148}$$

where here, $\mathrm{chat}\left(f_u,f_v\right)$ is formally defined as the conical-hat function, so that

$$\mathrm{chat}\left(f_u,f_v\right)=$$
$$\begin{cases}\dfrac{2}{\pi}\left[\cos^{-1}\left(\dfrac{\sqrt{f_u^2+f_v^2}}{2f_0}\right)-\dfrac{\sqrt{f_u^2+f_v^2}}{2f_0}\sqrt{1-\left(\dfrac{\sqrt{f_u^2+f_v^2}}{2f_0}\right)^2}\right] & \sqrt{f_u^2+f_v^2}\le f_0 \\ 0 & \text{otherwise}\end{cases}\tag{149}$$

The quantity f_0, as given in Eq. (149) and used in Figure 7, is known as the cutoff frequency for coherent imaging conditions and is defined by the following relationship [14]:

$$f_0 = \frac{n_0 D}{\lambda_0 Z_i}.$$ (150)

As required by Eq. (150), spatial frequencies up to f_0 are allowed to pass through an incoherent imaging system. Additionally, the OTF $H_{LE}(f_u, f_v)$ associated with long-exposure incoherent imaging through optical turbulence is given by the following relationship [67]:

$$H_{LE}(f_u, f_v) = \exp\left[-3.44\left(\frac{\lambda Z_i \sqrt{f_u^2 + f_v^2}}{r_0}\right)^{5/3}\right].$$ (151)

The relationship found in Eq. (151) is often referred to as the long-exposure MTF, since $|H_{LE}(f_u, f_v)| = H_{LE}(f_u, f_v)$. Long-exposure images are collected with time periods long enough, so that the image center wanders randomly, in the image plane, $z = Z_i$, many times [9]. When compared with an imaging system with an exit pupil diameter equal to the coherence length, $D = r_0$, the result found in Eq. (151) says that an imaging system with an exit pupil diameter larger than the coherence diameter, $D > r_0$, does not provide any better image resolution. An AO system is often used to alleviate this constraint.

Time periods that are long compared with the refractive-index fluctuations in the atmosphere are needed in defining the long-exposure OTF $H_{LE}(f_u, f_v)$, as given in Eq. (151). Associated with this purpose, Greenwood investigated the effects of infinite

87

bandwidth AO system controllers on imaging system performance [78]. From this

ground breaking work, Greenwood was able to come up with the definition for a

characteristic temporal frequency. Known as the Greenwood frequency f_G, this

characteristic temporal frequency is associated with the time period in which optical

turbulence remains unchanged. Provided the index of refraction structure parameter

$C_n^2(z)$ and the depth-dependent transverse wind speed, $v_\perp(z) = |\mathbf{v}_\perp(z)|$, the Greenwood

frequency f_G is determined as

$$f_G = \left[2.91 \beta^2 \int_0^Z C_n^2(z) v_\perp^{5/3}(z) dz \right]^{3/5},$$

(152)

where again, $\beta = n_0 k_0$. The dependability of Taylors frozen hypothesis is directly related

to the time period associated the Greenwood frequency f_G. The Greenwood frequency

f_G can be used to determine how quickly an AO system must respond in order to

compensate for optical turbulence in the atmosphere [79]. With this in mind, further

analysis of AO systems is of interest now.

2.5 High Energy Laser Beam Phase Compensation using Adaptive Optics

An AO system can be used to break the constraints imposed by the coherence

diameter r_0 and improve both HEL beam resolution and imaging resolution. Associated

with this claim is the idea of phase conjugation. Optical disturbances are composed of

both an amplitude A and a phase ϕ. An arbitrary optical disturbance U manifests itself

mathematically as a phasor, such that

$$U = A \exp(-i\phi).$$

(153)

The phase conjugate of an arbitrary optical disturbance U, as given in Eq. (153), is found using the following relationship:

$$U = A\exp(-i\phi)\exp(i\phi). \tag{154}$$

This mathematically flattens the phase of an arbitrary optical disturbance U; therefore, extinguishing any unwanted aberrations present in the phase. To do this physically, an AO system is used and the process is referred to as phase compensation. The hardest part here is being able to first sense the unwanted aberrations in the phase and then to apply the phase compensation correction. Depending on the resolution of the AO system, the phase compensation process can be highly effective in improving both HEL beam resolution and imaging resolution.

Aberrations present within an optical disturbance often change at a demanding rate and the AO system has to keep up in order to accomplish effective phase compensation. Such is the case with aberrations induced by the atmosphere and HEL propagation in the atmosphere. In order to sense the aberrations present in the atmosphere, a beacon laser is used, as described in Figure 9. For HEL engagement scenarios, the beacon laser illuminates a distant target, so that incoherent light back scatters off of the target. For all intents and purposes, the beacon laser illumination can be modeled as a point source in the target plane. The point-source wavefronts back propagate through the atmosphere and are coupled into the AO system for sensing and phase compensation. It is important to note that the incoming point-source wavefronts essentially experience the same atmospheric effects as the outgoing HEL wavefronts. This is especially true when the target is stationary.
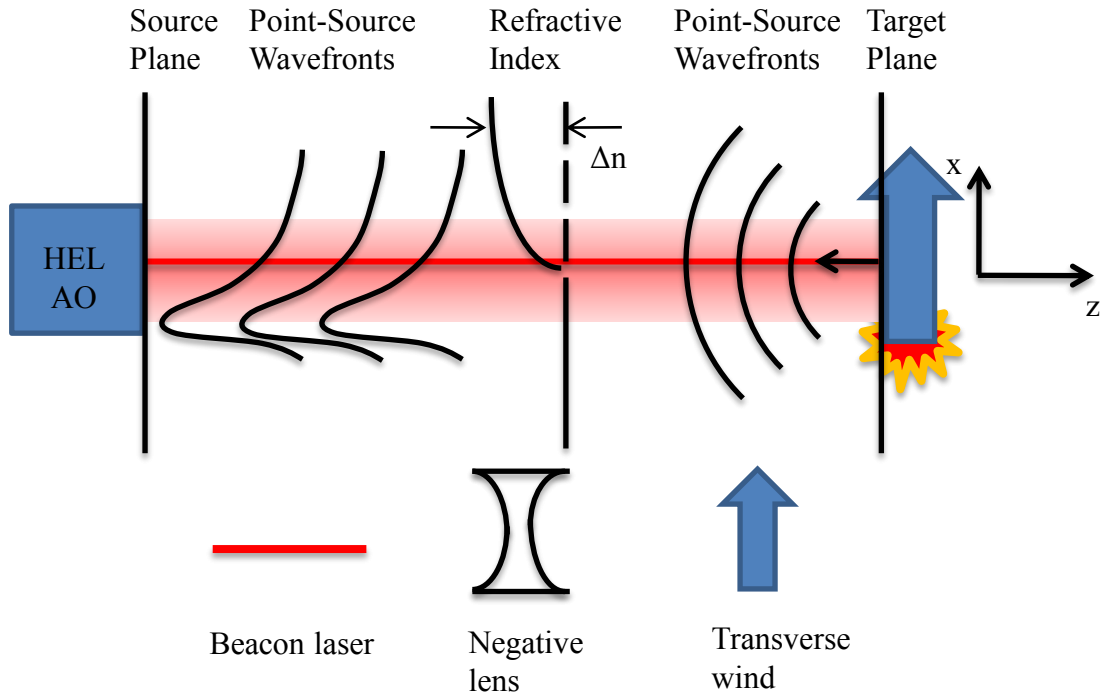
Figure 9. Description of a beacon laser illuminating a target. For all intents and purposes, the beacon laser illumination can be modeled with a point source. The point source back propagates through the atmosphere and is coupled into the AO system

The phase compensation process using an AO system is quite elegant in theory, but demanding in practice. For example, the basic components needed for an AO system include the fast steering mirror (FSM), the tracker, the deformable mirror (DM), and the wavefront sensor (WFS). The tracker and the WFS sense unwanted aberrations in the incoming point-source wavefronts and then control the FSM and the DM to apply phase compensations to the outgoing HEL wavefronts. In particular, the tracker controls the FSM with measurements made from imaging the point-source wavefronts. This is done to correct for tilt induced by propagating through the atmosphere. Noll determined that for optical turbulence, up to 87 percent of the wavefront variance σ_3^2, as given by Eq.

(140), is contained in Zernike tilt $Z_2(r,\theta)$ or $Z_3(r,\theta)$ [76]. Being able to adequately sense and correct for tilt is the first component needed for system performance.

Sensing and correcting for the higher order aberrations is the second component needed for system performance. For this purpose, the WFS is used to measure higher order aberrations present within the point-source wavefronts. In using the WFS, the point-source wavefronts are sampled and imaged. Each imaged sample is measured and related to the geometry of the DM. Through this geometry relation, the WFS measurements are then used to control the DM. This is done, so that the DM can correct for higher order aberrations. In so doing, higher-order aberrations are corrected for with phase compensation.

Subtle nuances do exist in the basic description given above. For example, with open-loop operation of the AO system, the incoming point-source wavefronts are first collimated with an optical system, as seen in Figure 10. From here, the point-source wavefronts are then sampled with beam splitters (BS) and sent to the WFS and tracker, respectively. The order is arbitrarily chosen in this case. Immediately after measurement, phase compensation is blindly applied to the HEL beam. In astronomy applications, open-loop AO is often referred to as active optics [69]; however, this terminology will not be used here. Open-loop operation is typically less effective when compared to closed-loop operation of the AO system.
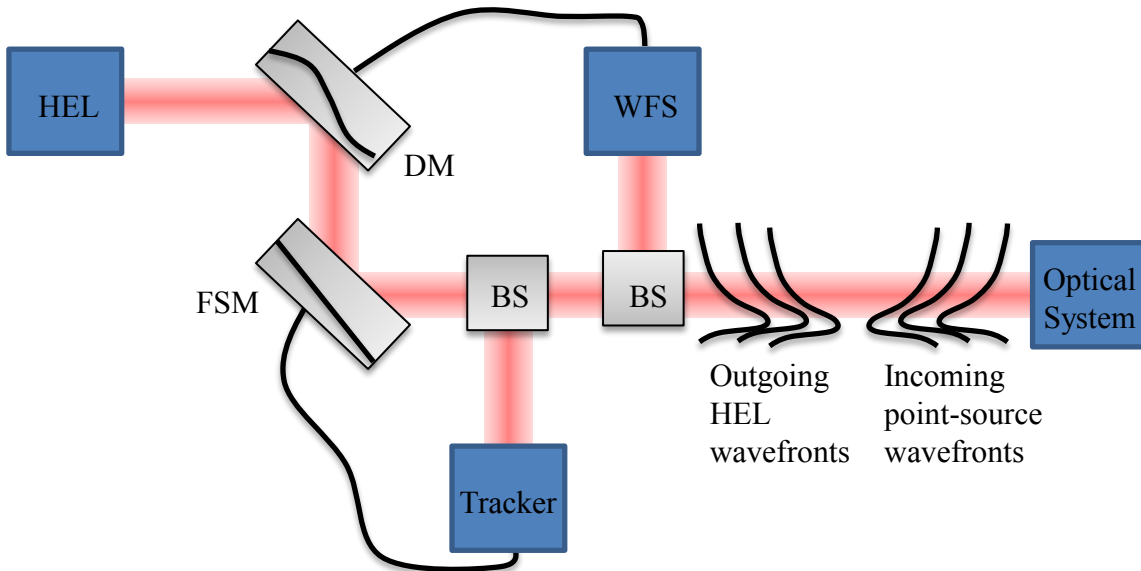
Figure 10. AO system performing open-loop phase compensation.

In closed-loop operation of the AO system, the point-source wavefronts are first reflected off of the FSM and the DM and then measured with the tracker and the WFS after being sampled with a BS. This process is appropriately described in Figure 11. In so doing, feedback is created and the measured error can be driven to zero. The term open-loop operation is sometimes associated with the case where the point-source wavefronts are sensed by the tracker and the WFS in the closed-loop configuration described in Figure 11; however, the FSM and DM are not commanded. There is a big difference between the open-loop operation of the AO system described in Figure 10, and the open-loop operation of the AO system described in Figure 11. Either case will be explicitly described in the analysis to come. Nonetheless, with open-loop operation of an AO system, there is no feedback mechanism for the error present in the AO system. This is why closed-loop operation of an AO system is typically found to be more effective in performing phase compensation.
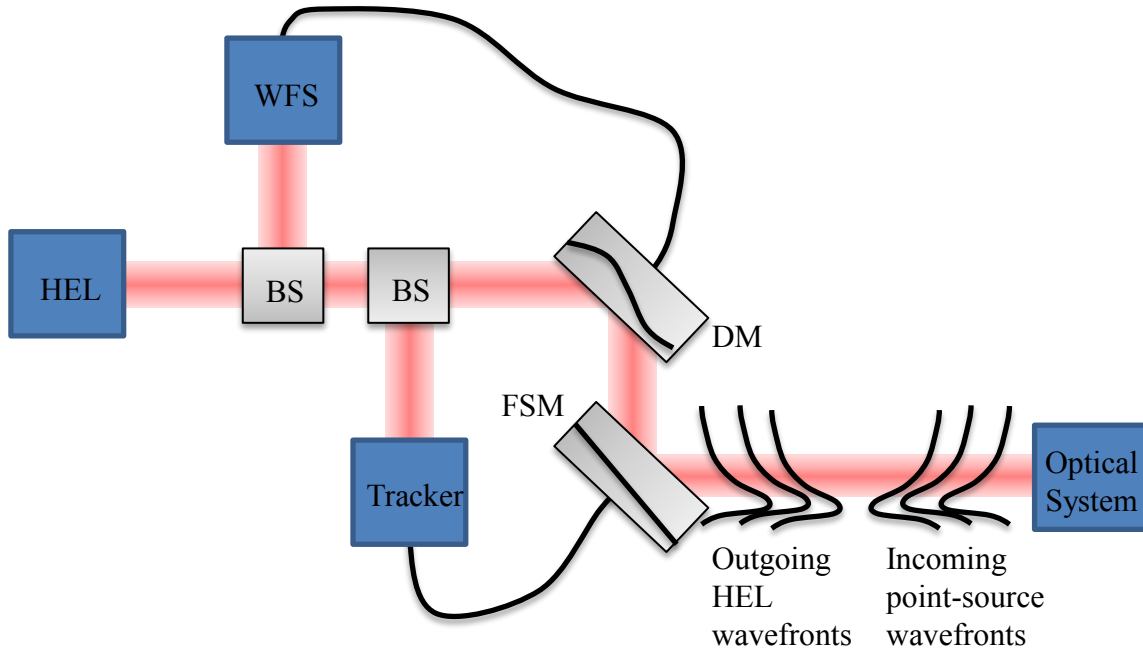
Figure 11. AO system performing closed-loop phase compensation.

The open-loop or closed-loop operation of an AO system can be broken up into specific pieces to make the analysis more tractable. For this purpose, this section introduces some of the engineering principles needed to design and test an AO system. Further in-depth design analysis is found throughout the literature [80,81,69,57,79,70]. In the discussion to follow, an introduction is given to wavefront sensing, wavefront correcting, and wavefront reconstruction and control. After, metrics for system performance is given with explanation. Branch points and branch cuts are also discussed. The section also includes a thorough analysis and review of phase compensation instability or PCI.

2.5.1 Wavefront Sensing

The art of wavefront sensing provides a means to determine the phase associated with the aberrated wavefronts of an optical disturbance. Measuring the phase of an optical disturbance directly is unfortunately not an option—the temporal frequencies associated with the sinusoidal oscillations are too fast to measure directly using modern-day optical detectors [69]. As a result, the image plane irradiance $I_i(u,v)$ can be used to infer the phase indirectly. One robust way to do this is with a Shack-Hartmann WFS as shown in Figure 12. With the Shack-Hartmann WFS, the incoming aberrated wavefronts of an optical disturbance are sampled with a group of lenslets. These lenslets are used to image the sampled portions of the wavefronts onto an optical detector where the image plane irradiances $I_i(u,v)$ are measured.
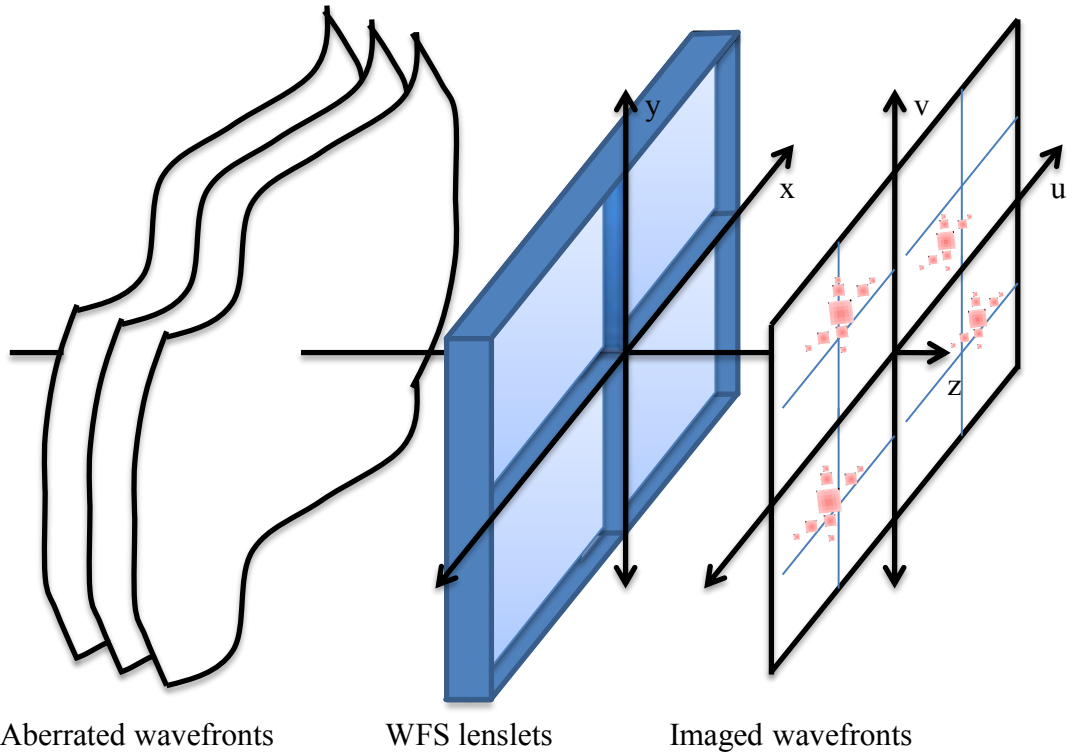
Figure 12. An example of a Shack-Hartman wavefront sensor. Here, four lenslets are used to sample the aberrated wavefronts. Once imaged on the detector, the image plane irradiance of the sampled wavefronts can be used to measure the phase of the optical disturbance.

Slope measurements are made from the measured image plane irradiances $I_i(u,v)$ of the sampled wavefronts. This is accomplished in a number of ways. One robust method is to use the center of mass equations to compute the slopes s_u and s_v in the x and y directions, respectively. The center of mass for each image plane irradiance $I_i(u,v)$ are computed using the following expressions:

$$s_u = \frac{\sum\limits_{p=1}^{P}\sum\limits_{q=1}^{Q} u_p I_i(u_p,v_q)}{\sum\limits_{p=1}^{P}\sum\limits_{q=1}^{Q} I_i(u_p,v_q)} \tag{155}$$

$$s_v = \frac{\sum\limits_{p=1}^{P}\sum\limits_{q=1}^{Q} v_q I_i(u_p,v_q)}{\sum\limits_{p=1}^{P}\sum\limits_{q=1}^{Q} I_i(u_p,v_q)}, \tag{156}$$

where p and q correspond to the image plane irradiances $I_i(u_p,v_q)$ measured for a particular pixel in the optical detector with PxQ pixels per imaged wavefront. Once the slope measurements are computed using Eq. (155) and Eq. (156), a reconstruction algorithm is then used to command the DM. This point will be addressed in greater detail with the analysis to come.

Two parameters are of major concern when designing a Shack-Hartmann WFS. The first is the number of lenslets or subapertures n_{sub} used to sample the incoming aberrated wavefronts. Typically, more subapertures are good, as it increases the spatial resolution of the AO system. This is said because when using multiple lenslets to sample the incoming aberrated wavefronts, the process essentially measures the local tilt found in the sampled portion of the wavefront. As shown above in Figure 12, an individual lenslet

is used to first sample the aberrated wavefront, and then image that sampled portion onto a detector. If there is any local tilt found in the sampled portion of the wavefront, then in the detector, the image plane irradiance $I_i(u,v)$ is shifted. This shift is measured as slope with the center of mass calculations performed using Eq. (155) and Eq. (156). Thus, increasing the number of subapertures n_{sub} in the Shack-Hartmann WFS increases the AO systems ability to resolve how much local tilt is found in the sampled portion of the wavefronts.

The second parameter of concern in the design of a Shack-Hartmann WFS is each subaperture's field of view (FOV) θ. For instance, the FOV θ determines number of waves (λ) of local tilt that can be effectively measured in each subaperture of diameter d. As shown in Figure 13, the number of waves of tilt n_{lod} is related to the FOV of the subaperture through basic geometric relations. By increasing the FOV θ or the number of waves of tilt n_{lod} of the subapertures, the diffraction-limited central spot size in the image plane decreases and vice versa. As a result, the FOV θ or the number of waves of tilt n_{lod} controls the dynamic range of the Shack-Hartmann WFS. The FOV or the number of waves of tilt n_{lod} is typically chosen so that the image plane irradiance $I_i(u,v)$ of each subaperture provides a central diffraction-limited spot that partially covers at least four pixels in the detector and does not wander into adjacent subaperture image planes.
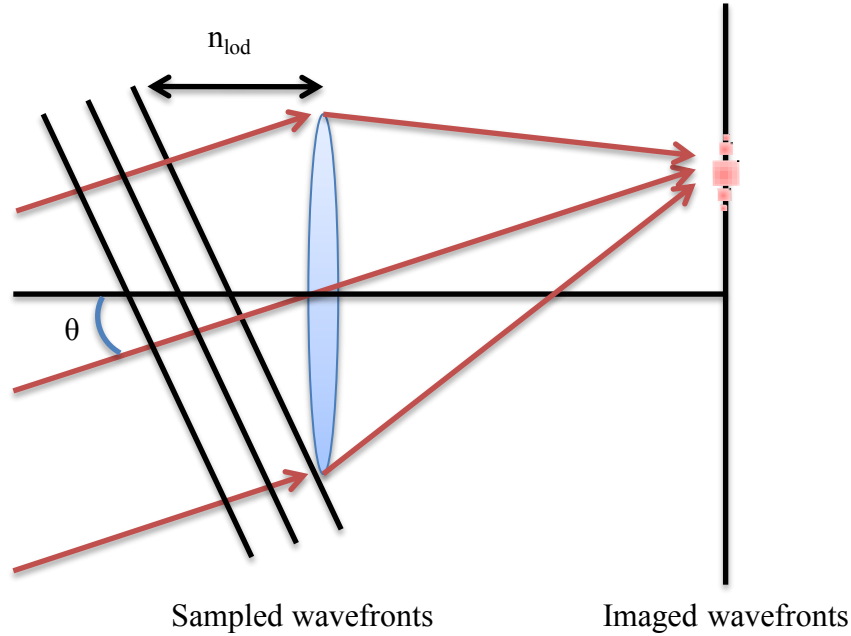
Figure 13. Description of the FOV θ of a Shack-Hartmann WFS subaperture. The number of waves of tilt n_{lod} is related to the FOV θ using simple geometric relationships.

Before moving on in the discussion of AO system design and implementation, it is important to note that a tracker follows the same basic design as that of a single subaperture of a Shack-Hartmann WFS. This concept might seem a little vague at this point in the analysis, but remember that the goal for the design of a tracker is to be able sense the *global* tilt associated with the aberrated wavefronts of an optical disturbance. Thus, a basic imaging system, such as a camera, is sufficient for the design of a tracker. In the case of a tracker, the basic imaging system is used to image the aberrated wavefronts onto an optical detector where the image plane irradiance $I_i(u,v)$ is measured. Again, slope measurements are computed from the image plane irradiances $I_i(u_p, v_q)$ measured for a particular pixel in the optical detector associated with the tracker using Eq. (155) and Eq. (156). From these slope measurements, a reconstruction

algorithm is then used to command the FSM. Similar design considerations as given above in Figure 12 and Figure 13 for a single Shack-Hartmann WFS subaperture can be used in the design of a tracker. It is all relative.

2.5.2 Wavefront Correcting

In order to effectively perform phase compensation using a traditional AO system design, a deformable mirror is needed. As shown in Figure 14, the DM of an AO system is able to match the ―shape‖ of the incoming aberrated wavefronts of an optical disturbance by commanding actuators. In so doing, quasi phase conjugation is successfully performed and the reflected wavefronts are basically flat. This is said because a DM is comprised of *BxC* grid of actuators. Because there are a discrete number of actuators in a deformable mirror design, it is impossible to match the ―shape‖ of the aberrated wavefronts exactly. Thus, the quasi phase conjugation process using a single deformable mirror is referred to as phase compensation.

There are many different considerations to take into account in the design of a DM. For example, the basic design for a DM includes a *BxC* grid of actuators, where each individual actuator is coupled in some way to an adjacent actuator. This coupling is demonstrated in Figure 14. When one actuator is pushed up or pulled down, the surface of the DM causes adjacent actuators to be move in response. This coupling mechanism is accounted for with an influence function [69,79]. When the DM actuators are segmented in design this coupling is minified; however, most AO system designs for HEL beam applications requires that the DM have a thick face sheet in order to handle the high power levels. This means that there is even more coupling associated with the DM's used in HEL beam applications. Overall, when there is a lot of coupling between

adjacent actuators, the DM's surface is less able to perform phase compensation in areas of the aberrated wavefronts where there are sharp discontinuities in the phase. Such is the case when branch points and branch cuts are in the phase of an optical disturbance. This point is re-addressed in detail with the analysis to come.

The stroke associated with each actuator, i.e. how far an actuator can be pushed or pulled, is also a major design consideration. As stated before, Noll determined that for optical turbulence, up to 87 percent of the wavefront variance σ_3^2, as given by Eq. (140), is contained in Zernike tilt $Z_2(r,\theta)$ or $Z_3(r,\theta)$ [76]. What this means in the implementation of a DM design is that all of its available stroke could potentially be used in performing phase compensation for global tilt. A FSM is typically used in most AO system designs as a result to alleviate this constraint. In the design of a FSM the surface is flat and pivots around a central point to perform phase compensation for global tilt. Commercially available DM's can provide up to $30\ \mu\text{m}$ of peak-to-valley stroke per actuator [57]. This is an important point to remember in the analysis to follow.

One final point worth mentioning about the design of a DM involves the idea of actuator spacing δ. The Nyquist sampling theorem states that spatial frequencies greater than half the sampling frequency cannot be observed. What this means in terms of design criterion for a DM is that the actuator spacing δ must be less than half the smallest required spatial frequency period in order to provide the required phase compensation [57]. In other terms, two actuator spacings on a DM satisfies the Nyquist sampling criterion for that particular AO system design. In the presence, of optical turbulence, small actuator spacing δ is typically desired, so that all of the higher-order aberrations

induced by inhomogeneities in the atmosphere can be effectively corrected for [70]. It will be discussed in the analysis to come that this is not always the desired case when in the presence of thermal blooming.

Aberrated wavefronts   Planer wavefronts

DM actuators
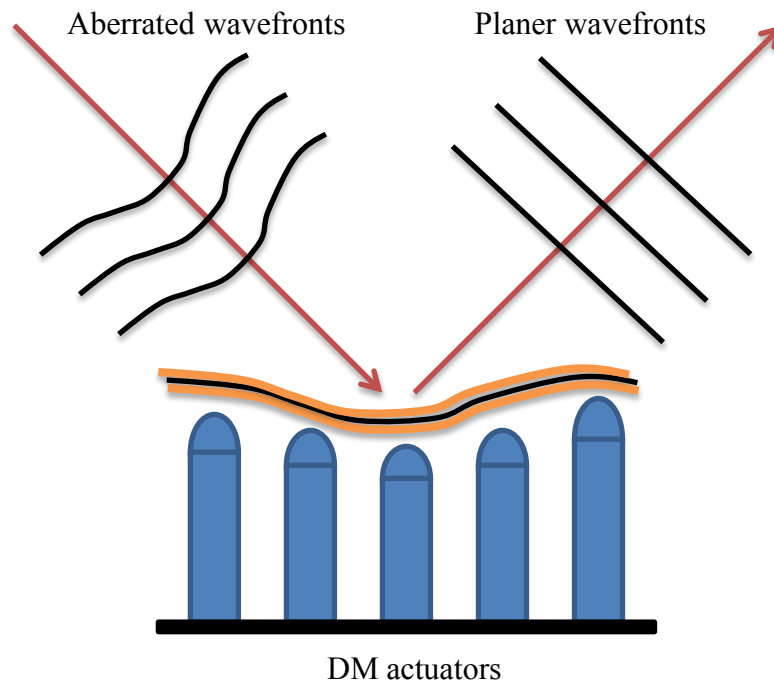
Figure 14. Example of phase compensation using a DM. The aberrated wavefronts reflect off of the surface of the DM and become planer wavefronts. Thus, phase compensation is achieved.

2.5.3 Wavefront Reconstruction and Control

Wavefront reconstruction provides a means to use the measurements from a WFS to effectively command a DM in a timely manner. To do this using the zonal approach, the geometry of the WFS must be related the geometry of the DM. The Fried reconstruction geometry is typically used to relate the Shack-Hartmann WFS geometry with a NxM number of subapertures to the DM geometry with a BxC number of actuators. This reconstruction geometry is demonstrated in Figure 15. Here, the slopes

$\left(s_u\right)_{m,n}$ and $\left(s_v\right)_{m,n}$ in the *x* and *y* directions are computed from the image plane

irradiances $I_i\left(u_m, v_n\right)$ associated with each subaperture of the Shack-Hartmann WFS

using Eq. (155) and Eq. (156). These calculated slopes are then "translated" into OPD

commands to each of the actuators located in corners of a given subaperture. This

"translation" procedure requires a reconstruction matrix G. There are numerous ways to

calculate the reconstruction matrix G for a given WFS and DM layout, such as

minimum-variance and maximum *a posteriori* methods [72].
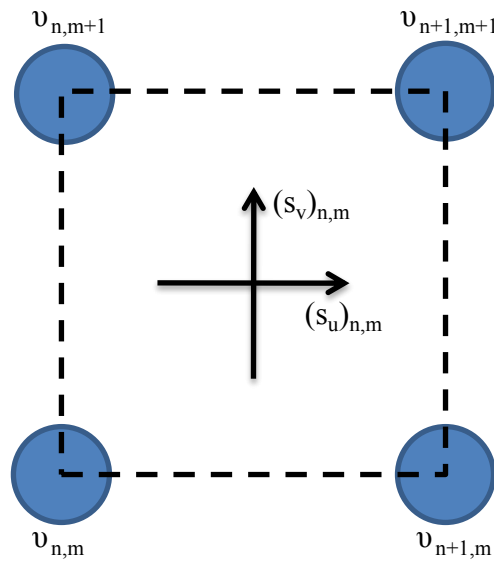
Figure 15. Description of Fried reconstruction geometry.

The measured slopes can be represented in a vector **s** and the OPD commands to

each actuator can also be represented in a vector $\boldsymbol{\varphi}$. Typically, there are more slope

measurements than there are actuators to command [70]. Thus, the system of linear

equations is overdetermined, such that

$$\mathbf{s} = G\boldsymbol{\varphi}. \tag{157}$$

To solve the overdetermined system of linear equations for the OPD commands $\boldsymbol{\varphi}$, as given in Eq. (157), least squares techniques are used. Two commonly used least-squares approaches include the Moore-Penrose pseudo inverse and single value decomposition [57].

Once the wavefront reconstruction process is completed and in working order, an AO control loop can be implemented. For instance, an AO system operating in the closed-loop regime, as shown in Figure 11, is controlled discretely using a simple "leaky" integrator control law, such that

$$\varphi_{SYS}\left(t_{j+1}\right) = a\varphi_{SYS}\left(t_{j}\right) - b\varphi_{ERR}\left(t_{j}\right). \tag{158}$$

Here, the system commands $\varphi_{SYS}\left(t_{j+1}\right)$ to the FSM and or DM at the present time are determined from a combination of the previous system commands $\varphi_{SYS}\left(t_{j}\right)$ and the error in the system $\varphi_{ERR}\left(t_{j}\right)$. The servo leakage a, determines the how much of the previous system commands $\varphi_{SYS}\left(t_{j}\right)$ are used in Eq. (158) to create the present system commands $\varphi_{SYS}\left(t_{j+1}\right)$. When the servo leakage equals one, $a=1$, Eq. (158) is referred to as a "pure" integrator control law. Typical values for the servo leakage range from 0.9 to 1.0 in practice.

The servo gain b determines how much system error $\varphi_{ERR}\left(t_{j}\right)$ is present in the system in a given time step, $\Delta t = t_{j+1} - t_{j}$. A low servo gain b cause the system to respond more slowly, to reduce the system error $\varphi_{ERR}\left(t_{j}\right)$. Increasing the servo gain b

causes the AO system to respond more quickly and have more system error $\varphi_{ERR}\left(t_j\right)$.

Typical values for the servo gain include, $b = 0.3$, which is on the conservative side and, $b = 0.5$, which is a little more edgy.

The rate at which the AO system can effectively perform the control loop presented in Eq. (158) is given by the 3dB frequency f_{3dB} [69]. The sampling rate or the sampling frequency, $f_s = 1/\Delta t$, has the largest impact on determining the 3dB frequency f_{3dB} for a given AO system design. It is desired that the 3dB frequency be at least four times the Greenwood frequency, $4 f_{3dB} > f_G$, to ensure system performance in the presence of optical turbulence [69]. However, this engineering "rule of thumb" is not written in stone. The conjectured engagement scenarios for some HEL weapons have rather large Greenwood frequencies f_G that trump the obtainable 3dB frequencies f_{3dB} with state of the art AO system designs. Nonetheless, system performance is still obtainable. A careful combination of the servo leakage a, servo gain b, and 3dB frequency f_{3dB} are all that is needed in practice to ensure system stability and system performance.

2.5.6 Measuring System Performance

In the presence of thermal blooming and or turbulence, system performance can become significantly degraded. For this purpose, peak Strehl ratio S_P and normalized power in the bucket P_B calculations can be used to measure system performance as a function of some varying parameter, such as time t or distortion number N_D. The calculated peak Strehl ratio S_P provides a normalized gauge for the max energy or max

power propagated to the target plane after phase compensation from the AO system in the source plane. The peak Strehl ratio S_P in the target plane is calculated using the following relationship:

$$S_P = \frac{I_A}{I_E},$$

(159)

where I_A is the maximum aberrated irradiance in the target plane due to thermal blooming and or turbulence and I_E is the maximum irradiance in the target plane due to extinction effects or transmission losses. In addition, normalized power in the bucket P_B gives a normalized measure for the amount of energy or power placed in a certain area in the target plane after phase compensation in the source plane. The diffraction limited bucket diameter D_B, as given by Eq. (95), is typically used in defining the area of interest in the target plane. Thus, the normalized power in the bucket P_B is calculated in terms of the diffraction limited bucket diameter D_B using the following relationship:

$$P_B = \frac{\displaystyle\int_{-\frac{D_B}{2}}^{\frac{D_B}{2}} \int_{-\frac{D_B}{2}}^{\frac{D_B}{2}} I_A(x,y,Z)\,dxdy}{\displaystyle\int_{-\frac{D_B}{2}}^{\frac{D_B}{2}} \int_{-\frac{D_B}{2}}^{\frac{D_B}{2}} I_E(x,y,Z)\,dxdy},$$

(160)

where $I_A(x,y,Z)$ is aberrated irradiance in the target plane due to thermal blooming and or turbulence and $I_E(x,y,Z)$ is the irradiance in the target plane due to extinction effects or transmission losses. Altogether, peak Strehl ratio S_P and normalized power in the bucket P_B calculations provided a means to extract information about the development of

105

system performance. This point will become more apparent with the results presented in the next chapter.

System stability is of key interest as well in the analysis of system performance. To better characterize system stability, the root mean square RMS r_{DM} of the DM commands and the , the variance σ^2_{DM} of the DM commands can be used. For example, the RMS r_{DM} of the DM commands is given by the following relationship:

$$r_{DM} = \sqrt{\frac{1}{NM} \sum_{n=1}^{N} \sum_{m=1}^{M} \left(\varphi_{n,m}\right)^2} \,, \tag{161}$$

where $\varphi_{n,m}$ is the OPD commanded to a particular actuator in an NxM grid of actuators. Equation (161) provides a measure for how the OPD commanded to the actuators varies. Additionally, the variance σ^2_{DM} of the DM commands is given by the following relationship:

$$\sigma^2_{DM} = \frac{1}{NM} \sum_{n=1}^{N} \sum_{m=1}^{M} \left[\left(\varphi_{n,m}\right) - \mu_{DM}\right]^2 \,, \tag{162}$$

where μ_{DM} is the mean of the DM commands and is determined using

$$\mu_{DM} = \frac{1}{NM} \sum_{n=1}^{N} \sum_{m=1}^{M} \left(\varphi_{n,m}\right). \tag{163}$$

Similar to the RMS r_{DM} of the DM commands, the variance σ^2_{DM} of the DM commands, as given in Eq. (162), provides a sensitive measure for the amount of variation found in the OPD commanded to the actuators. In the presence of instability, both the RMS r_{DM} of the DM commands and the variance σ^2_{DM} of the DM commands allude to exponential behavior. This is an important point, which cannot be overlooked in the analysis.

106

The correlation coefficient ρ gives a normalized measure for the similarity of two random variables. In the analysis of system performance, this is an important calculation because it provides a gauge for causality. As such, the correlation coefficient ρ for the arbitrary discrete random variables V and W is given by the following relationship:

$$\rho = \frac{\left[\frac{1}{NM}\sum_{n=1}^{N}\sum_{m=1}^{M}(V_n W_m)\right] - \left[\frac{1}{N}\sum_{n=1}^{N}(V_n)\right]\left[\frac{1}{M}\sum_{m=1}^{M}(W_m)\right]}{\sqrt{\frac{1}{N}\sum_{n=1}^{N}\left[V_n - \frac{1}{N}\sum_{n=1}^{N}(V)\right]^2}\sqrt{\frac{1}{M}\sum_{m=1}^{M}\left[W_m - \frac{1}{M}\sum_{m=1}^{M}(W_m)\right]^2}},$$

$$= \frac{C_{VW}}{\sigma_V \sigma_W}$$

(164)

where C_{VW} is the covariance between V and W, and $\sigma_{V,W}$ is the standard deviation of V and or W, respectively. Equation (164) provides a range of values from negative one to positive one. When the correlation coefficient is equated to positive one, $\rho = 1$, the random variables of interest are said to be perfectly correlated meaning that their variations are identical up to a scaling factor [67]. On the other hand, when the correlation coefficient is equated to negative one, $\rho = -1$, the random variables of interest are said to be perfectly anticorrelated meaning that the fluctuations are oppositely identical, again, up to a scaling factor [67]. From these two extremes, the degree of correlation decreases. When the correlation coefficient is equated to zero, $\rho = 0$, the random variables of interest are said to be uncorrelated. In this sense, the variations or fluctuations found between the random variables are not related, and thus, statistically independent of one another [67].

2.5.4 Phase Compensation Instability

An AO system, in theory, can be used to mitigate the nonlinear optical effects induced by thermal blooming. Bradley and Herrmann were the first to seriously investigate the idea [53]. In this ground-breaking computational study, Bradley and Herrmann were able to show improvement in system performance with phase compensation of thermal blooming. Specifically, they showed improvement in normalized irradiance as a function of distortion number for both modal and zonal phase compensation. The trend of their classic result is shown in Figure 16, and is interpreted as follows.

- An increase in distortion number is typically associated with one of two things: an increase in initial HEL beam power P_0 or a change in atmospheric parameters, such as a decrease in the transverse wind speed $v_\perp$.

- As the distortion number N_D increases, the achievable Strehl ratio S increases less and less until a critical point is reached.

- This critical point occurs when an increase in the distortion number N_D does not result in an increase in the achievable Strehl ratio S.

- When modal or zonal phase compensation is used to correct for thermal blooming, this critical point is shifted up and to the right, i.e. there is an increase in system performance.

Altogether, the results obtained by Bradley and Herrmann produced more questions than answers (the true indicator of ground-breaking research). They were the first to clearly demonstrate the idea behind the critical point; as the invention of the distortion number N_D is credited to them. This revolutionized the way researchers characterized thermal blooming. In addition, Bradley and Herrmann were the first to demonstrate the idea that phase compensation of thermal blooming resulted in a relaxation of the constraints

imposed by the critical point. When the effects of thermal blooming were found near the

aperture, as is the case for slewed HEL beams, their research showed that phase

compensation was more effective in improving system performance. Characterizing how

much improvement was actually achievable in practice for a particular engagement

scenario became the primary concern for future research efforts in phase compensation of

thermal blooming.
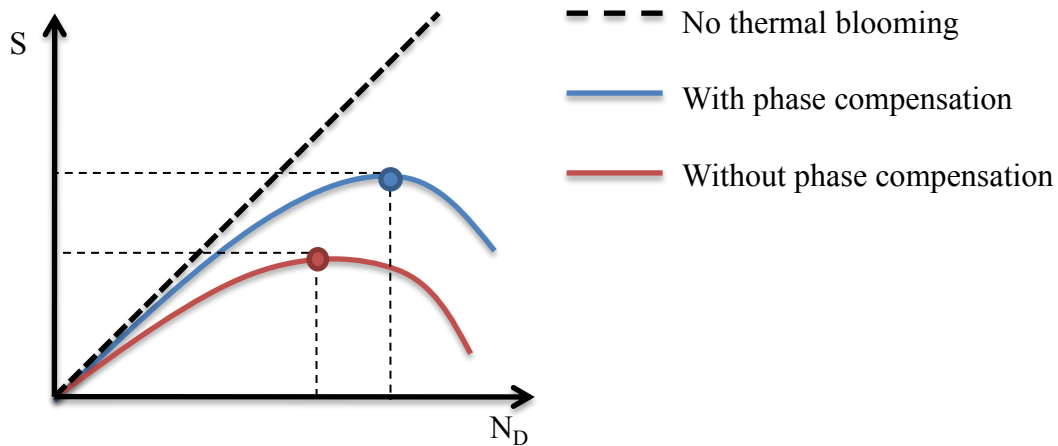
Figure 16. Description of Strehl ratio S as a function of distortion number N_D. As the distortion number N_D increases, the achievable peak Strehl ratio S_P increases less and less until a critical point is reached. After reaching the critical point, there is no increase in achievable Strehl ratio S as the distortion number N_D increases. Phase compensation of thermal blooming can be used to break the constraints imposed by the critical point.

It is quite difficult in practice to setup a complete full-scale experiment to

investigate phase compensation of thermal blooming. Such an experiment would require

an HEL system, an AO system robust enough to handle the HEL beam powers needed for

thermal blooming, a test range and facility large enough to conduct the full-scale

experiment, and enough money to purchase all of the above equipment. Thus, much of

the early experimental research in phase compensation of thermal blooming was

conducted using computational and scaled-laboratory simulations. Both types of research provide insight into the principles governing the problem without the logistics burden associated with a full-scale experiment.

Following the foundational research performed by Bradley and Herrmann, a series of scaled-laboratory experiments were conducted [82,83,84,85,86]. These scaled-laboratory experiments used both phase compensation and multidither approaches to correct for thermal blooming. Regardless of the approach, in a scaled-laboratory experiment, a lab bench, low-power laser, and absorbing medium are used to simulate thermal blooming. Some sort of phase compensation, or amplitude and phase compensation in the case of the multidither approach, is then applied to the laser to correct for thermal blooming. For the most part, the results from the scaled laboratory experiments were consistent with the results provided by Bradley and Herrmann and shown above in Figure 16 [53]. They were also successful in demonstrating improvement in system performance for phase compensation of thermal blooming.

Despite the initial success of the scaled-laboratory experiments, Herrmann threw an additional constraint into the mix—the possibility for instability. In a computational study using an iteration scheme, Herrmann demonstrated that both convergent and divergent regimes existed for phase compensation of thermal blooming [87]. Here, Herrmann used five thin lenses distributed along the propagation path to approximate the phase distortions caused by thermal blooming. He simulated phase conjugation for both a flat-top beam and a Gaussian beam, both of which were focused at the target. The irradiance of the simulated HEL beam at each thin lens was used to determine the radius of curvature for that particular lens. A simulated point source was also propagated

through the thin lenses from the target plane to the source plane. Idealized phase compensation was accomplished by directly applying the radius of curvature of the point source to the simulated HEL beam in the source plane. His results showed that for ―substantial‖ thermal blooming, the idealized phase compensation resulted in initial improvement/convergence in the simulated HEL beam radius in the target plane; however, as the simulation progressed in iterations, the HEL beam radius eventually diverged and went unstable. The results published by Herrmann were not well understood at the time. This judgment is made based on the lack of investigation presented in this ground-breaking work. Nevertheless, it was made clear from Herrmann's results that phase compensation of thermal blooming had the possibility for instability.

Further research into the instability remained unpublished for quite some time. One reason for the gap in the published literature is conjectured to result from the confidentiality involved with the topic. The Russians were developing similar theories around the same time [88], all at the height of the Cold War. An excellent overview paper was written in English by Vorob'ev with over 200 references on Russian based research in thermal blooming [89]. It is clear from the analysis made by Vorob'ev that Russian research in thermal blooming paralleled much of the efforts made by Americans. As a result, a lot of the American based research in thermal blooming was written in technical reports for U.S. government contract work. These technical reports unfortunately are not readily available to the general public.

Another potential reason for the discrepancy in the published literature on phase compensation of thermal blooming is conjectured to result from the lack of computational

power available at the time. Computer simulation of HEL beam propagation and AO phase compensation unfortunately requires a significant amount of computational accuracy in order to have good fidelity in the results. Numerical noise in an under-sampled simulation can quickly lead to erroneous results. Thus, it may have been thought that the preliminary analysis presented by Herrmann was kludged with computational artifacts. This point is briefly discussed in the introductory analysis provided by Schonfeld [90].

Nearly a decade after the discovery of the instability, Tyler et al. performed an overview study in the form of a technical report on thermal blooming in an attempt to explain the potential issues associated with simulating thermal blooming and phase compensation of thermal blooming [54]. Here, Tyler et al. came up with sampling criteria based on the distortion number N_D to validate the numerical accuracy of thermal blooming simulations. From this analysis, it was determined that the number of grid points N needed for thermal blooming simulations must satisfy the following relationship:

$$N \geq 0.75 \frac{s}{D} N_D,$$ (165)

where s is the simulation side length of interest in the source plane and or target plane and D is the associated aperture diameter. In deriving Eq. (165), it is assumed that the simulation of thermal blooming requires at least ten samples per period for the highest spatial frequency of interest. The validity of such a claim was thoroughly tested and found to be adequate at the time of publication [54,49].

From the expressions used to acquire Eq. (165), Tyler et al. also determined an analytical expression for Strehl ratio as a function of distortion number $S(N_D)$. In this analysis, a circularly collimated HEL beam was used. As such, the heat induced aberrations caused by steady-state thermal blooming were assumed to be found within the area of the HEL beam and tilt removed. Figure 17 provides a description of their result. In the large distortion number N_D limit, the Strehl ratio $S(N_D)$ was determined to be given by the following relationship [54,55,49]:

$$S(N_D) = \frac{16\sqrt{2}}{N_D}. \tag{166}$$

Since the Strehl ratio, in general, is a normalized metric, the critical distortion number N_C is estimated by setting Eq. (166) equal to one, so that [55,49]

$$N_C = 16\sqrt{2} \approx 22.6 \text{ rad}. \tag{167}$$

Equation (167) is a very useful result, at least from an engineering perspective. It provides a rough estimate for the transition point or "knee in the curve" where an increase in the distortion number N_D does not provide any more irradiance on target, i.e. the critical point. Distortion numbers greater than the critical distortion number, $N_D \geq N_C$, are referred to here as being in the "strong" thermal blooming regime. Additionally, if the critical distortion number N_C, as given in Eq. (167), is substituted into Eq. (94) for the distortion number N_D, the critical power P_C is solved for as

$$P_C = \frac{4}{k_0} \left[\int_0^z \frac{Z-z}{Z} \frac{\mu(z)}{D(z)v_x(z)} dz \right]^{-1}. \tag{168}$$

The physical significance of the critical power P_C, as given in Eq. (168), cannot be overlooked in the analysis of phase compensation of thermal blooming. Equation (168) says that an increase in the initial HEL beam power P_0 above the critical power P_C does not provide any more HEL beam irradiance on target [55,49]. An AO system, in theory, can be used to alleviate this constraint; however, the possibility for instability adds additional consideration.
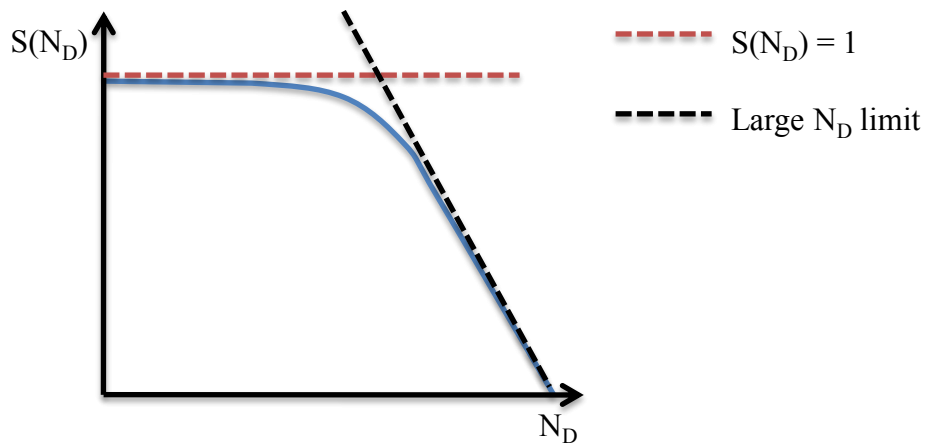
Figure 17. Description of the analytic expression determined by Tyler et al. for Strehl ratio as a function of distortion number $S(N_D)$. The point where the large distortion number N_D limit crosses a Strehl ratio of one, $S(N_D)=1$, determines the critical distortion number N_C.

As part of the overview study conducted by Tyler et al, a computational wave-optics experiment was formulated to test for instability. For instance, idealized phase compensation was simulated for a circularly collimated flat top beam and two different distortion numbers, $N_D = 36$ and $N_D = 108$. Using Eq. (165), a $256x256$ grid size and a single[3] thermal blooming phase screen were determined to be adequate for the simulated

---

[3] More thermal blooming phase screens were probably needed; however, the number of phase screens in a given wave-optics simulation of thermal blooming only imposes a constraint on the fidelity of the results.

distortion numbers. In addition, two regimes of phase compensation were simulated. The goal here was to simulate phase compensation for the case were thermal blooming developed both faster and slower than the phase compensation process. For this purpose, the HEL beam was propagated from the source plane to the thermal blooming phase screen and the information was saved. From this saved information, both the previously stored phase screen and current phase screen were applied separately to the HEL beam. The Strehl ratio was then computed for each case of thermal blooming after propagation to the target plane. From here, a beacon was propagated from the target plane to the source plane with the effects of the current phase screen due to thermal blooming. The phase of the beacon in the source plane was then applied directly to the HEL beam and the idealized phase compensation process was repeated.

Results from the wave-optics experiment conducted by Tyler et al. consistently showed the same trend—the faster regime always outperformed the slower regime in terms of system performance for phase compensation of thermal blooming. However, no further analysis was presented by Tyler et al beyond this preliminary conclusion. They claimed that more detail was needed in the simulation to fully understand the problem. Nonetheless, the research performed here served as a good stepping stone to add to the analysis performed by Herrmann. No apparent signs of instability were present in the results obtained by Tyler et al. This further supported the idea that the results presented by Herrmann may have been kludged with numerical artifacts.

Novoseller was successful in publishing a couple of papers which complemented the overview study of Tyler et al [91,92]. In these studies, Novoseller used modal reconstruction techniques for phase conjugation of thermal blooming. From this work, he

115

was also able to come up with an expression for Strehl ratio as a function of distortion number. He developed his expressions using the results from wave-optics simulations and residual error calculations from Zernike-ordered modal correction. However, the terse nature of his analysis made it difficult to infer the intent in his research. There was no mention of the possibility of instability in his publications.

Following the research conducted by Tyler et al. and Novoseller, it was still not clear whether the instability existed or not. Consequently, there was an increased effort to determine the true nature of the instability. Three main research entities led this increased effort: Lawrence Livermore National Laboratory (LLNL), MIT Lincoln Laboratory (MIT-LL), and the Optical Sciences Company (tOSC). From this ground-breaking research, the instability was officially phrased: phase compensation instability or PCI. The effects of PCI are essentially explained in terms of a macro- and micro-scale result.

Macro-scale PCI is intuitively explained with a simple lens analogy based on the results obtained by Herrmann [87][4]. For example, the heat-induced phase distortions caused by thermal blooming result in a negative-lens-like optical effect in the atmosphere. This fact is well known from the analysis of thermal blooming provided above. An AO system senses and corrects for the negative-lens-like optical effects of thermal blooming by applying positive-lens-like phase compensations to the HEL beam. In turn, the positive-lens-like phase compensations focus the HEL beam irradiance. By focusing the HEL beam irradiance, the amount of heating increases, which leads to more

---

[4] The origin of the macro-scale explanation of PCI is unknown; however, it is believed to be treated as common knowledge in the explanation of results given by Herrmann [87].

thermal blooming. Depending on the strength of the thermal blooming or the gain in the

AO system control loop, the mechanism driving the heating process eventually reaches a

tipping point and leads to a runaway condition, i.e., positive feedback, in the AO control

loop. This tipping point is referred to here as insipient PCI. With a little thought, the

macro-scale interpretation of PCI can be used to explain the results obtained by

Herrmann [87]. In his computational analysis, Herrmann used thin-lens simplifications

to simulate thermal blooming in the atmosphere. Divergent regimes existed in the results

presented by Herrmann because positive feedback was being created in the simulation of

idealized phase compensation.

Principles governing the micro-scale development of PCI were not well

understood until the late 1980's[5]. For this purpose, a linearized theory was introduced by

the work of Briggs [93], Karr [94,95,96], Barnard [97], Morris [98,99], Chambers [100],

and a few supporters of LLNL. From this linearized theory, the development of micro-

scale PCI was explained as being the time-dependent growth of small-scale spatial

perturbations in the irradiance and or phase of the HEL beam. Spatial perturbations

found within the HEL beam were believed to act as local hot spots, which in turn, drive

the thermal blooming process. Each hot spot essentially succeeds in creating a local

negative-lens-like optical effect in the atmosphere. When an AO system is used to

correct for the small-scale perturbations or hot spots found within the HEL beam, local

positive-lens-like phase compensations are applied. These local positive-lens-like phase

compensations have a similar effect as in the case of macro-scale PCI—the process

---

[5] The micro-scale effect of PCI may have been discovered earlier in terms of computational research
efforts; however, it was probably associated with numerical artifacts. This point is discussed in the
introductory analysis given by Schonfeld [90].

causes positive feedback to occur in the AO servo. However, with micro-scale PCI, the spatial perturbations grow with time.

It is worth noting that small-scale spatial perturbation growth was also found to result from interaction of thermal blooming with turbulence. This interaction is often referred to as stimulated thermal Rayleigh scattering (STRS) or more intuitively as turbulence thermal blooming interaction (TTBI). The process was first treated by Kroll and Kelley [101]; however, the introductory analysis given by Holmes et al. is particularly informative [102].

The effects of STRS or TTBI are explained as the small-scale growth in spatial perturbations in the irradiance of the HEL beam. Scintillation caused by optical turbulence produces variations or small-scale perturbations in the irradiance of the HEL beam. The variations in the HEL beam irradiance causes nonuniform heating of the atmosphere. As a result, strong phase gradients are produced which directly increase the angular spreading of the HEL beam with propagation. As time progresses, the spatial perturbations in the irradiance grow in size. This growth continues until some mitigating factor, such as variations in the wind velocity, prevents further growth.

For all intents and purposes, the effects of STRS or TTBI are particularly detrimental to collimated HEL beams under steady-state thermal blooming. According to the research presented by Chamber et al., when the distortion number remains much less than the Fresnel number, $N_D \ll N_F$, small scale scintillation caused by optical turbulence becomes intensified as a result of SRTS or TTBI [100]. The Fresnel number is given by the following relationship:

$$N_F = \frac{\pi n_0 D^2}{4\lambda_0 Z},$$ (169)

and essentially provides a gauge for when the effects of diffraction become important. When $N_F \gg 1$ the propagating optical disturbance is in the Fresnel diffraction regime, and when $N_F \ll 1$ the propagating optical disturbance is in the Fraunhofer diffraction regime. With circularly collimated HEL beams, the Fresnel numbers are relatively high for long propagation distances; therefore, the conditions for STRS of TTBI are often met. It is important to note that the spatial perturbation growth due to STRS or TTBI occurs separately from the positive feedback caused by macro- and or micro-scale PCI.

According to the linearized theory produced by LLNL, in the micro-scale interpretation of PCI, phase compensation of thermal blooming was stated as being mathematically unstable at all spatial frequencies. What is more, the growth rate of the small-scale spatial perturbations in the irradiance and or phase of the HEL beam was found to be proportional to the absorbed irradiance $\mu(z)I(\mathbf{r},t)$. An increase in the absorbed irradiance $\mu(z)I(\mathbf{r},t)$ led to an increase in the strength of the localized negative-lens-like optical effects caused by the small-scale spatial perturbations in the irradiance and or phase of the HEL beam.

As an optical disturbance propagates, modulations in phase manifest themselves as modulations in irradiance and vice versa. This is a well-known fact from the study of wave optics and the analysis of the BPM given above. Thus, when small-scale spatial perturbations present themselves in the irradiance and or phase of a thermally bloomed HEL beam, the localized negative-lens-like optical effects are thought of as thick-lens

119

effects with propagation [103]. The linearized theory produced by LLNL characterized these thick lens effects in terms of a gain factor.

In the micro scale interpretation of PCI, the spatial perturbations in irradiance and or phase were determined to grow quasi exponentially as a result of a gain factor. This gain factor for a wind clearing time t_c was found to be proportional to the distortion number N_D and a parameter known as the Fresnel perturbation number N_P. Similar to the Fresnel number, as given in Eq. (169), the Fresnel perturbation number N_P was determined as

$$N_P = \frac{\pi n_0 \Lambda^2}{4\lambda_0 Z},$$
(170)

where Λ is the characteristic scale size of the spatial perturbation of interest [95]. Typically, the characteristic scale size set to two actuator spacings, $\Lambda = 2\delta$. This criterion was experimentally determined to work well based on the research efforts of MIT-LL, which will be discussed shortly.

Two asymptotic limits were determined for the gain factor in terms of the Fresnel perturbation number N_P. A low gain factor regime corresponds to the case where the Fresnel perturbation number is much greater than one, $N_P \gg 1$, i.e. when the propagation range is small and or the spatial perturbation is large. In this case, there is less of a thick-lens effect in the atmosphere. In the low gain regime, the gain factor is proportional to the ratio of the distortion number over the Fresnel perturbation number, N_D/N_P. Conversely, in the high gain regime, the Fresnel perturbation number is much less than one, $N_P \ll 1$. In this case, the propagation range is large and or the spatial perturbation is

small. The high gain factor regime cause thick-lens effects. The gain factor in the high

gain regime is proportional to only the distortion number N_D.

In the presence of the appropriate gain conditions, the growth of the spatial

perturbations was found to grow quasi exponentially unless a dampening mechanism was

present to mitigate this spatial perturbation growth. Mitigating factors for the spatial

perturbation growth caused by micro-scale PCI were found to include fluctuations in the

wind velocity, thermal diffusion, and turbulent mixing. Of these three mitigating factors,

fluctuations in the wind velocity were stated as being the strongest dampening or blurring

mechanism. If the growth rate in the spatial perturbations was found to exceed the effects

of the mitigating factors, then the spatial perturbations would grow quasi-exponentially

until saturation, at which point the HEL beam irradiance in the target plane would break

into smaller and smaller spatial perturbations severely degrading system performance.

The research conducted by MIT-LL set out to test the results of the linearized

theories produced by LLNL. Here, Johnson led efforts in terms of scaled-laboratory

experiments [104,105,106], Schonfeld led efforts in terms of computational wave-optics

experiments [107,90,108,109,110], and Fouche et al. led full-scale experimental efforts

[103], to see if PCI could, in fact, be induced experimentally. Overall, the multiphase

research efforts of MIT Lincoln Laboratory showed that the PCI was particularly difficult

to see in practice. One conclusion claimed that interactions between thermal blooming

and mitigating factors in the atmosphere, such as wind fluctuations, prevented the onset

of PCI. The results of these experiments marked a decrease in the amount of research

performed in thermal blooming and PCI. Nonetheless, the research performed by MIT-

LL in thermal blooming and PCI was truly ground breaking.

The research performed by Fried and Szeto looked at the phase compensation of thermal blooming in the presence of turbulence. Here, the majority of their work was documented in a series of technical reports while working for tOSC [111,60,112,113,114,115,116,117]. Much of the work performed in these technical reports paralleled the work performed by LLNL in terms of developing a linearized theory to study the effects of TTBI and PCI. The analyses performed by Fried and Szeto eventually lead to one of the seminal papers on thermal blooming and PCI [118]. Here, they showed that fluctuations in the wind velocity stabilized a set of linearized equations that they developed to study the effects of PCI. Numerical results which solved their linearized equations showed that PCI was particularly difficult to induce for a ground to space engagement scenario with variations in the wind velocity. These results supported the claims made by MIT-LL based on their experimental efforts.

One recent paper by Barchers used the Rytov method to create a linearized theory and study the effects of phase compensation of thermal blooming and full-wave compensation of thermal blooming [119]. In this ground-breaking study, the linearized theory was used to check for the existence of stable solutions for HEL phase compensation and full-wave compensation in the presence of thermal blooming and random processes, i.e. optical turbulence and fluctuations in the wind velocity. Barchers was successful in finding bounded solutions for both phase compensation and full-wave compensation of thermal blooming. However, he was also able to show that the addition of time of flight effects caused unstable regimes. Further experimental analysis is needed to discern whether time of flight effects significantly affect incipient PCI with full-wave compensation.

In a recent conference proceeding of SPIE, Spencer et al. attempted to review/highlight the ground-breaking research conducted by LLNL, MIT-LL, and tOSC in thermal blooming and PCI [120]. This conference proceeding provided the basis for the research conducted in this thesis. In the analysis presented by Spencer et al. the results from a series of computational wave-optics experiments for the phase compensation of a focused Gaussian beam profile using a point-source beacon were presented. Specifically, peak Strehl ratio S_P and power in the bucket P_B measurements in the target plane as a function of time were presented. Despite a few inconsistencies in the analysis, such as the distortion number calculations being off by a factor of ten[6], the results showed the development of periodic oscillations in the system performance measurements. At the time of publication, the source of these periodic oscillations were undetermined.

With one last review of the literature, it was discovered that the Russians, Lukin and Fortes, showed similar results to those published by Spencer et al [121,7]. In this ground-breaking research, computational wave-optics experiments were conducted with idealized phase compensation of thermal blooming caused by a focused HEL beam profile. Based on their results, Lukin and Fortes were successful in discerning the cause of the periodic oscillations in system performance measurements. They conjectured that branch points present in the beacon phase were the cause the periodic oscillations.

---

[6] Spencer et al. would like to thank Jeff Barchers of Nutronics, Inc. for his help in analyzing this work [59].

2.5.5 Branch Points

Branch points are traditionally characterized as resulting from the propagation of a point source through ―strong" optical turbulence. In general, the scintillation caused by optical turbulence produces variations or small-scale perturbations in the irradiance of an optical disturbance propagating in the atmosphere. This point is known from the discussion of TTBI provided above in the analysis of PCI. Remember that optical disturbances are composed of both an amplitude A and a phase ϕ. An arbitrary optical disturbance U manifests itself mathematically in the form of a phasor, as given in Eq. (153). As such, the variations in the irradiance caused by scintillation corresponds to fluctuations in the amplitude A of an arbitrary optical disturbance U. If the log amplitude variance σ_χ^2, as given in Eq. (126), is large enough, the scintillation caused by ―strong" optical turbulence causes large scale amplitude fluctuations, and as a result, creates nulls in the irradiance [122]. When this happens, a branch point is created.

A branch point results from a mathematical anomaly that occurs when the amplitude of a phasor goes to zero. To make this manifest, the mathematical properties of phasors must be accounted for. The amplitude of an arbitrary optical disturbance U is mathematically determined using the following relationship [56]:

$$A = |U| = \sqrt{\operatorname{Re}(U)^2 + \operatorname{Im}(U)^2}, \tag{171}$$

where $\operatorname{Re}(U)$ and $\operatorname{Im}(U)$ are the real and imaginary components of the arbitrary optical disturbance U, respectively. In addition, using the properties of phasors, the phase ϕ of an arbitrary optical disturbance U is determined as [56]

$$\phi = \text{Arg}(U) = \tan^{-1}\left[\frac{\text{Im}(U)}{\text{Re}(U)}\right]. \tag{172}$$

The mathematical relationship provided in Eq. (172) is known as the argument of a phasor. When an arbitrary optical disturbance U, as given in Eq. (153), is substituted into Eq. (172), the resulting phase ϕ is often referred to as the principle value or the wrapped phase [123].

There are two mathematical peculiarities associated with the wrapped phase ϕ. Firstly, the argument of a phasor is wrapped as determined by Eq. (172). What this means is that wrapped phase ϕ is confined to the range, $(-\pi, \pi]$. Secondly, the argument of a phasor that is equal to zero is not determined and thus results in a non-single-valued function [121,124]. This corresponds to the case where the amplitude of an optical disturbance fluctuates to zero, $A = 0$, as determined by Eq. (171). It is for this reason that branch points arise in the wrapped phase ϕ.

The location of a branch point is determined when the contour integral around the principle value ϕ does not equal zero. Specifically, the gradient of the wrapped phase $\nabla\phi$ ceases to be a purely potential field, so that the following relationship holds [121]:

$$\oint_C \nabla\phi \cdot d\mathbf{r} = \pm 2\pi(N_+ - N_-), \tag{173}$$

where N_+ is the number of positively charged branch points and N_- is the number of negatively charged branch points. The sign of the closed-loop contour integration in the counter-clockwise direction determines the charge of the branch points, as given in Eq. (173). As such, in an NxN grid, Eq. (173) can be modified to detect branch points in a computational wave-optics experiment, where

$$\sum_{n=1}^{N}\sum_{m=1}^{N}\nabla\phi=\sum_{n=1}^{N}\sum_{m=1}^{N}\left[\begin{array}{c}\left(\phi_{n,m}-\phi_{n,m+1}\right)+\left(\phi_{n+1,m}-\phi_{n,m}\right)-\\\left(\phi_{n+1,m+1}-\phi_{n+1,m}\right)-\left(\phi_{n,m+1}-\phi_{n+1,m+1}\right)\end{array}\right].(174)$$

The relationship provided in Eq. (174) breaks an NxN grid into a bunch of $2x2$ grids

and sums the discrete phase derivative around each point. A positive value results in a

positively charged branch point and a negative value results in a negatively charged

branch point in accordance with Eq. (173). What is more, a branch point of a specific

charge must be connected to a branch point of the opposite charge by a 2π discontinuity

known as a branch cut [122]. This point is demonstrated in Figure 18, which was

reproduced from the thesis work of Pellizzari [125]. Branch point detection and branch

cut manipulation is a rich topic of research, as the presence branch points can

significantly degrade AO system performance.
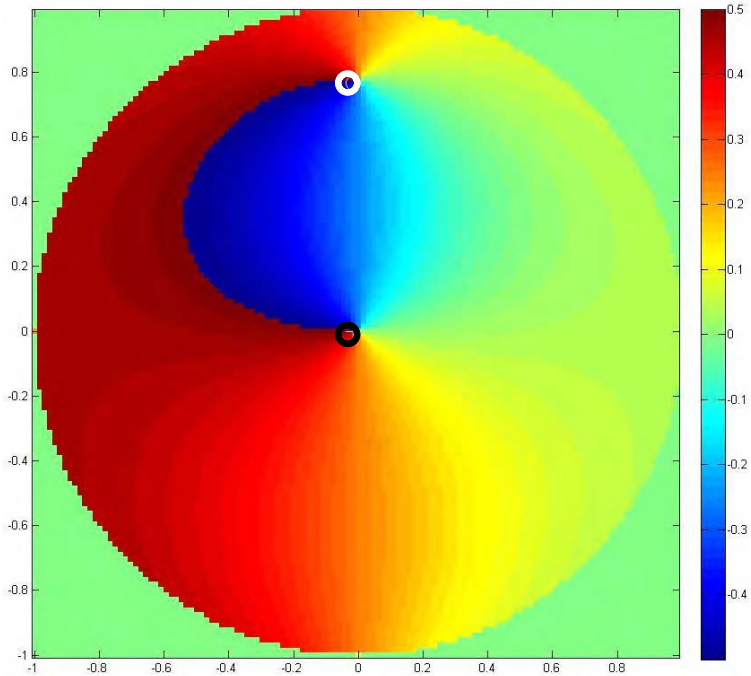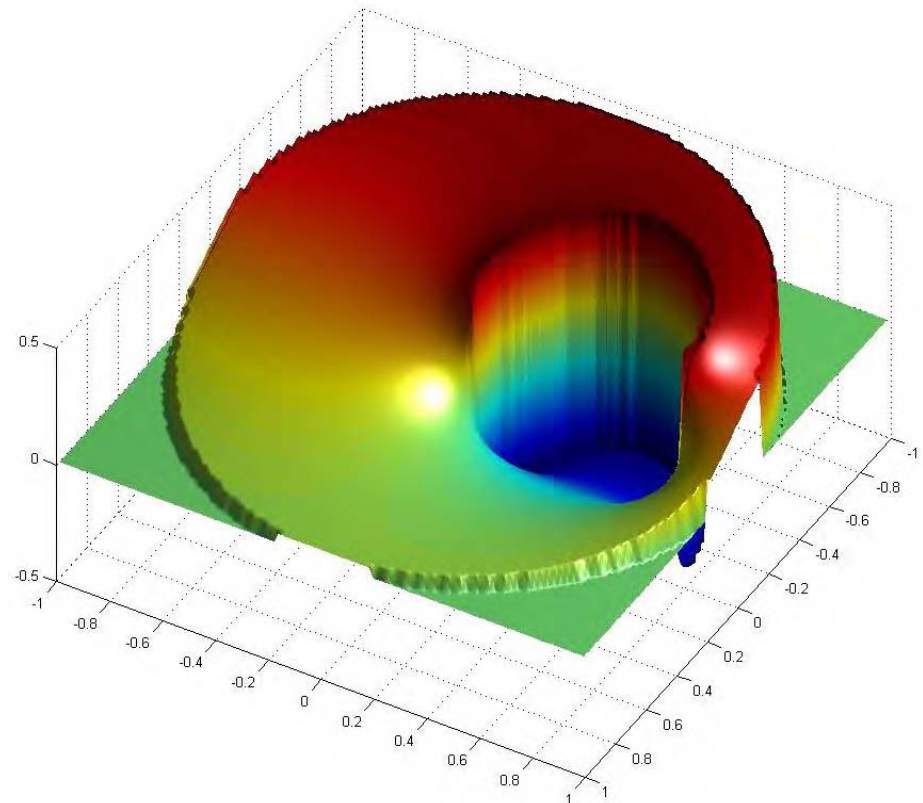
Figure 18. Example of two oppositely charged branch points connected by a 2π discontinuity known as a branch cut. In a.) the white circle surrounds the positively charged branch point and the black circle surrounds the negatively charged branch point. A 3-D view is given in b.) which clearly shows the 2π discontinuity of the branch cut connecting the branch points.

127

Branch points and branch cuts pose a major problem for traditional AO systems which perform phase compensation using a Shack-Hartmann WFS and a single DM. This is so because a Shack-Hartmann WFS is unable to detect branch points. Even if a Shack-Hartmann WFS could detect branch points, the 2π discontinuities caused by branch cuts pose a major problem for most DM's. It is particularly difficult for DM's with coupled actuators to create the exact phase conjugate associate with the 2π discontinuities caused by branch cuts. In the presence of branch points, there is a significant amount of phase that goes unsensed. This phase component is typically referred to as the hidden phase component [126,122,127]. If left uncorrected, system performance is significantly compromised. As demonstrated in Figure 19, the hidden phase component contains a significant amount of structure. It should be noted that Figure 19 is also reproduced from the thesis work of Pellizzari [125].

The least squares phase reconstruction method for the Shack-Hartmann WFS is oblivious to the presence of branch points [127]. As a result, an AO system using a Shack-Hartman WFS is unable to sense the hidden phase component associated with branch points. If the branch points go unsensed, the DM is unable to effectively perform phase compensation for the actual phase present in the optical disturbance of interest. This is an important point to remember in the analysis to follow. Furthermore, it has been shown by Voitsekhovich et al. that as the strength of optical turbulence increases with increasing log amplitude variances σ_χ^2, the number of branch points increases accordingly [124]. For weak to moderate turbulence conditions, branch points are rare. However, in conditions of strong optical turbulence, the number of branch points increases non-linearly up until a saturation point. After this saturation condition is met,

the number of branch points grows linearly. The theme worth remembering form the analysis produced by Voitsekhovich et al. is that with increased optical distortion, whether from thermal blooming and or optical turbulence, the conditions for the development of branch points are met. With a high number of branch points, system performance can become significantly degraded.
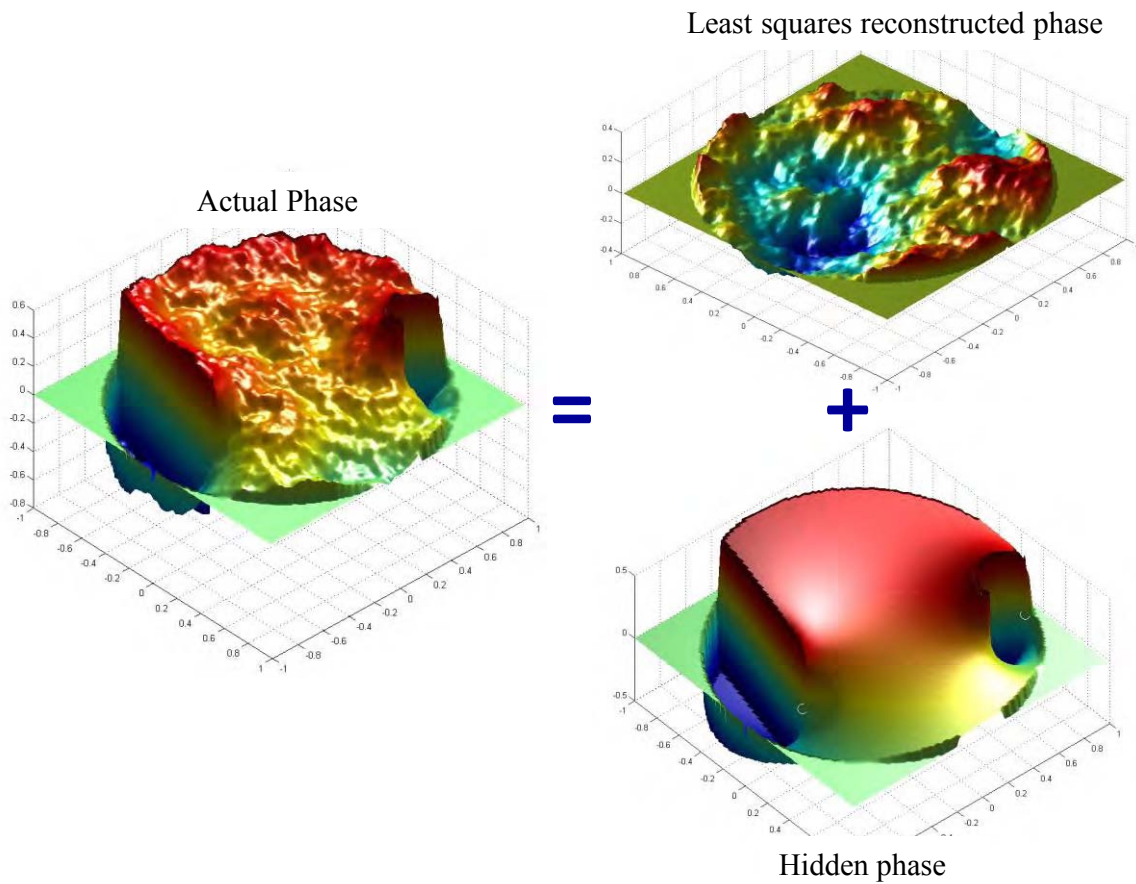
Figure 19. Example of the hidden phase component that contains branch points and branch cuts. The hidden phase component goes unsensed with a Shack-Hartmann WFS. The actual phase represents the phase that needs to be corrected for using phase compensation. The least squares reconstructed phase represents the phase that is measured and corrected for using a nominal AO system composed of a Shack-Hartmann WFS and a single DM.

3. Experimental Setup and Exploration

This chapter discusses the setup and exploration needed for a series of computational wave-optics experiments which simulate adaptive optics (AO) phase compensation of high energy laser (HEL) beam propagation in the atmosphere. The simulations were coded in MATLAB® using WaveProp [128], a wave-optics simulation system, and AOTools [129], the adaptive optics toolbox. Both are MATLAB® toolboxes provided to the Air Force Institute of Technology by the Optical Sciences Company (tOSC). WaveProp utilizes object-oriented programming in MATLAB® and contains a hierarchy of classes and functions which make the simulation of HEL beam propagation in the atmosphere and phase compensation using an AO system particularly user friendly. Similarly, AOTools contains a collection of functions and graphical user interfaces that make the setup and analysis of simulating AO systems accessible. Principles taught in a recent publication by Schmidt were also used in the setup and exploration of the computational wave-optics experiments [9].

3.1 Parameter Space Setup

The parameters used in the following wave-optics experiments were chosen to coincide with a ground- or sea-based tactical-engagement scenario including both state of the art and future designs of high-powered solid-state lasers and AO systems components. In particular, the engagement scenario parameters were selected to highlight the effects of thermal blooming. This was done in order to search for the conditions of incipient PCI.

Each component of HEL beam propagation in the atmosphere was simulated including extinction, thermal blooming, turbulent thermal blooming, and or optical turbulence. As a result, it was necessary to first characterize each component of the wave-optics experiments, so that the obtained results made sense based on the theory presented in the previous chapter. Parameters within the simulated AO system were also varied, such as the number of subapertures in the WFS, the number of actuators on the DM, and the subaperture FOV of the WFS. Based on the proposed setup and variations of the proposed setup, sampling analysis was performed to make sure that results acquired from the computational wave-optics experiments were reproducible.

3.1.1 Engagement Scenario Parameters

A typical ground- or sea-based tactical engagement scenario was simulated in the computational wave-optics experiments, as shown in Figure 20. For this purpose, the simulated CW HEL beam in the source plane was set to have an initially-collimated Gaussian beam profile with a free-space wavelength, $\lambda_0 = 1.064 \; \mu$m. The choice of this particular HEL wavelength was not arbitrary. Current and future high-powered solid state laser designs will use this particular wavelength as it is common to both Nd:YAG and Ytterbium based laser designs [70]. Another feature of this HEL laser wavelength is that the transmission losses are particularly low when compared with other commonly used HEL wavelengths, as seen in Figure 4. A Gaussian beam profile was chosen as opposed to a flat-top beam profile or a higher-order beam profile because of its analytic tractability—a Gaussian beam profile remains Gaussian with vacuum propagation and is a great analysis tool when simulating HEL propagation in the atmosphere.
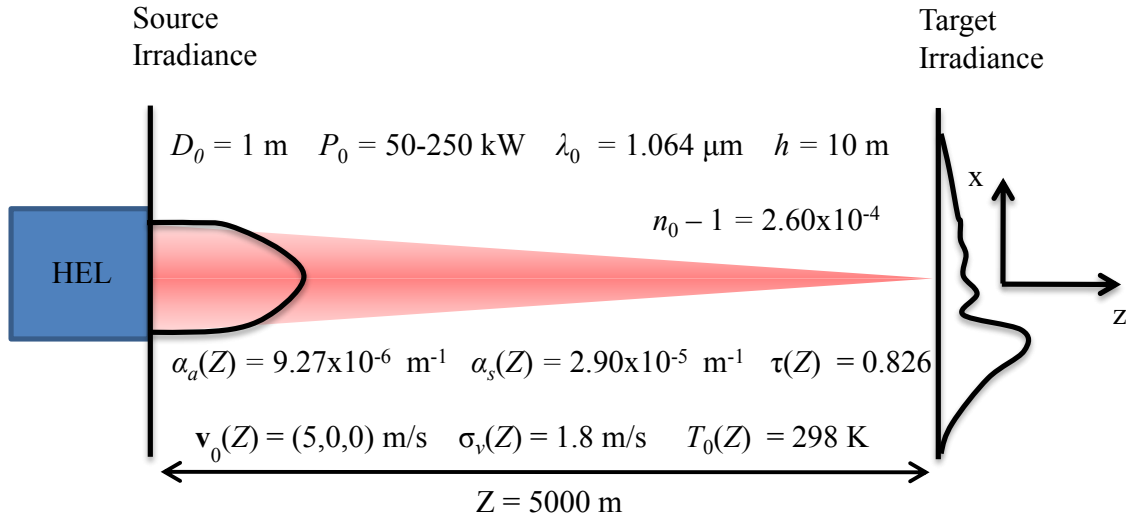
Figure 20. Engagement scenario parameters used in the computational wave-optics experiments.

A simulated pupil with no central obscuration was used to truncate the initial beam diameter, $D_0 = 1 \text{ m}$, and provided an initial beam irradiance, $I_0 = 2P_0/(\pi D_0/2)$. Following the pupil, a simulated thin lens was used to focus the HEL beam. The focal length of the simulated thin lens was set to the propagation range. For this purpose, a horizontal propagation range, $Z = 5000 \text{ m}$, was used for the simulated engagement scenario with a constant altitude, $h = 10 \text{ m}$. Based on these engagement scenario parameters, LEEDR3 was then utilized to determine a constant absorption coefficient, $\alpha_a(Z) = 9.26x10^{-6} \text{ m}^{-1}$, a constant scattering coefficient, $\alpha_s(Z) = 2.90x10^{-5} \text{ m}^{-1}$, a constant transmittance, $\tau(Z) = 0.82$, and a constant ambient temperature, $T_0(Z) = 298 \text{ K}$, for Wright-Patterson Air Force Base (AFB) during wintertime evening conditions [130].

The mean transverse wind velocity vector was assumed to be solely in the positive x direction, $\mathbf{v}_0(Z)=(5,0,0)$ m/s. This value was also determined from LEEDR3 by accessing the ExPERT database for Wright-Patterson AFB during the month of January. Specifically, wind speed percentile data was accessed. According to Fiorino, this data was collected over a period of 30 years near airplane runways located at Wright-Patterson AFB using anemometers [131]. To determine the wind velocity standard deviation $\sigma_v(z)$, the mean transverse wind speed, $v_{\perp}(Z)=5$ m/s, was first subtracted from the selected data. Next, the zero-mean data was plotted, as shown in Figure 21. It was noted that the variation in the data was approximately Gaussian to a first order approximation. Consequently, a Gaussian probability distribution function, as given in Eq. (106), was fitted to the data and a constant wind velocity standard deviation was determined, $\sigma_v(Z)=1.8$ m/s. This value was in accordance with the values cited by Fouche et al. for the SABLE experiments [103].
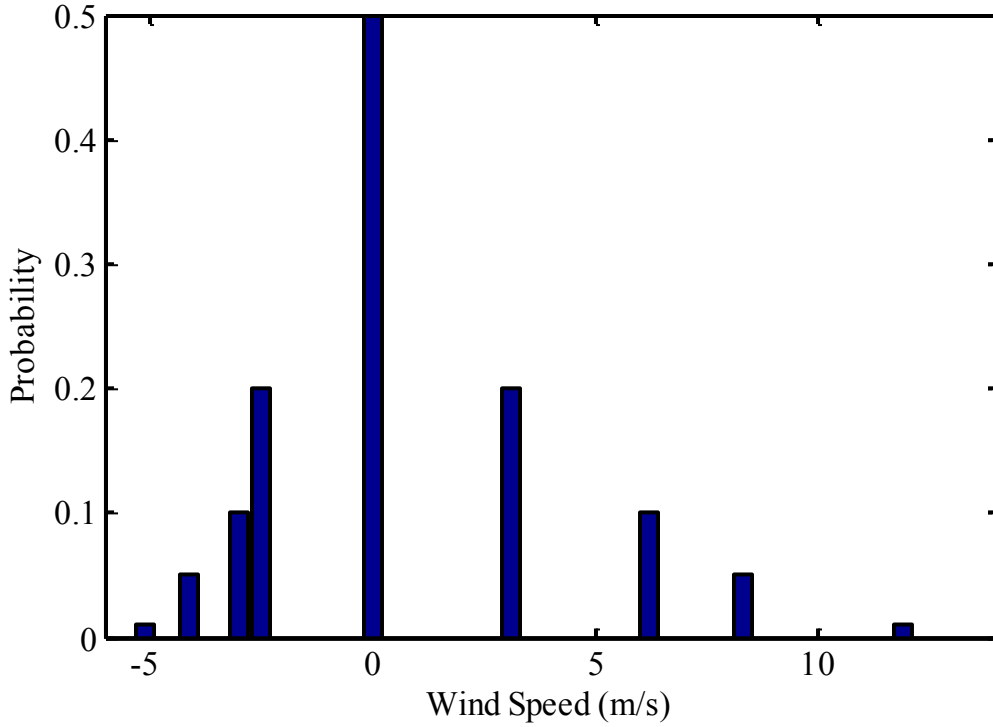
Figure 21. Zero-mean wind speed data for Wright-Patterson AFB during the month of January. The ExPERT database in LEEDR3 was used to obtain the data.

A nominal value was chosen for the index of refraction structure parameter, $C_n^2(Z) = 10^{-15}$ m$^{-2/3}$. This value was chosen, so that —moderate" optical turbulence was simulated in the wave-optics experiments. From this value, the appropriate log amplitude variances for a plane-wave source $\sigma_{\chi,pw}^2$ and a spherical-wave emitted from a point source $\sigma_{\chi,sw}^2$ were calculated using Eq. (127) and Eq. (128), respectively. In addition, Eq. (133) and Eq. (134) were used to calculate the appropriate coherence lengths for a plane-wave source $r_{0,pw}$ and a spherical-wave emitted from a point source $r_{0,sw}$. The Greenwood frequency f_G was also calculated using Eq. (152). All calculations for optical turbulence parameters were made using the engagement scenario parameters

given in Figure 20 and are included in Table 1. Note that, $n_{scn} = 10$, phase screens with

equal spacing were chosen to be adequate to simulate propagation through optical

turbulence in the atmosphere using the split-step beam propagation method (BPM). One

determining factor with regards to this decision was made based on the low percentage

errors obtained between the continuous and discrete values calculated in Table 1 [9]. The

other deciding factor was the results obtained from a validation study using the point

spread function (PSF) and optical transfer function (OTF) performed in the next section.

Table 1. Calculated parameters for optical turbulence with an index of refraction structure constant $C_n^2(Z)=10^{-15}$ m$^{-2/3}$.

Pathstats, $n_{scn} = 10$	Continuous	Discrete	Percentage error
Plane-wave coherence length, $r_{0,pw}$ (cm)	7.57	7.57	0.0
Spherical-wave coherence length, $r_{0,sw}$ (cm)	13.6	13.6	0.1
Plane-wave log amplitude variance $\sigma_{\chi,pw}^2$	0.147	0.148	0.1
Spherical-wave log amplitude variance $\sigma_{\chi,sw}^2$	0.0596	0.0600	0.7
Greenwood frequency f_G (Hz)	28.2	28.2	0.0

The initial beam power P_0 was the only engagement scenario parameter varied

within the simulations. Table 2 provides values for the initial beam powers P_0 used in

the simulations. The corresponding distortion numbers N_D were calculated using Eq.

135

(94) for the engagement scenario parameters given in Figure 20 and Table 1. These values are also provided in Table 2. To calculate the distortion numbers N_D using Eq. (94), the focused beam diameter $D(z)$ was needed. For this purpose, Eq. (98) was used in the presence of thermal blooming and Eq. (99) was used for the case when optical turbulence was also present. The difference between the ambient index of refraction and the vacuum index of refraction $n_0 - 1$ was also needed. To calculate this value, the following relationship was used:

$$n_0 - 1 = 10^{-7}\left[2589.72 + \frac{12.259}{\lambda_0^2} + \frac{0.2576}{\lambda_0^4}\right],$$
$$= 2.4x10^{-4}$$

and was provided by tOSC [49]. Furthermore, a critical power, $P_C = 118 \text{ kW}$, was calculated using Eq. (175)for the simulated engagement scenario. Referencing the values provided in Table 2, it should be noted that two values were chosen to lie below the critical point, corresponding to the "moderate" thermal blooming regime, and three values were chosen to lie above the critical point, corresponding to the "strong" thermal blooming regime.

The number of grid points N used in the simulations were determined from the calculated distortion numbers given in Table 2. Specifically, the sampling constraint, given in Eq. (165) and derived by Tyler et al. [54,49], was multiplied by ten[7], so that

$$N \geq 7.5\frac{S_s}{D_0}N_D = 30N_D.$$

---

[7] A multiple of ten was arbitrarily chosen to increase the fidelity of the obtained results. In the presence of PCI and or optical turbulence, the required number of grid points needed for the simulation of thermal blooming increases beyond the requirements predicted by Tyler et al. [54,49]. Future work could benefit from a more exact analysis.

The source plane side length, $s_s = 4\text{ m}$, used in the simulations was determined based on the turbulence simulation rule of thumb [128]. This point will be discussed further in the next section. Additionally, a target plane side length was determined by the following relationship:

$$s_t = N \frac{D_B}{20},$$

so that the calculated bucket diameter, $D_B = 1.3\text{ cm}$, for the simulated engagement scenario had at least 20 samples across. Simulation scaling for the wave-optics experiments was determined by the ratio between the target plane side length and source plane side length, $\ell = s_t/s_s$, and the obtained values are also given in Table 2. The fidelity of the simulation parameters calculated in Table 2 and used in the wave-optics experiments will be explored in the analysis to come.

Table 2. Calculated distortion numbers N_D, Number of grid points N, target-plane side length s_t, and simulation scaling ℓ for the varying initial beam powers P_0 used in the wave-optics experiments.

Initial HEL beam power P_0 (kW)	Distortion number N_D (rad), $r_{0,sw} = \infty$ cm	Distortion number N_D (rad), $r_{0,sw} = 13.6$ cm	Number of grid points $N \geq 30 N_D$	Target-plane side length $s_t = ND_B/20$ (cm)	Simulation scaling $\ell = s_t/s_s$
50	8.39	7.76	256	16.6	0.0415
100	16.8	15.5	512	33.2	0.0831
150	25.2	23.3	768	49.9	0.125
200	33.6	31.0	1024	66.5	0.166
250	42.0	38.8	1280	83.1	0.208

3.1.2 Adaptive Optics System Parameters

A nominal AO system was also simulated. Accordingly, a beacon, represented as an ideal point source, was back propagated from the target plane of the HEL beam to the source plane of the HEL beam. The simulated beacon used the same grid size NxN and side lengths as that of the simulated HEL beam given in Table 2. As mentioned above, the turbulence simulation rule of thumb was used to determine the source plane side length used in the simulations, $s_s = 4$ m. The turbulence simulation rule of thumb requires that the source plane side length be at least four times the initial beam diameter, $s_s \geq 4D_0$, as described in Figure 22 [128].
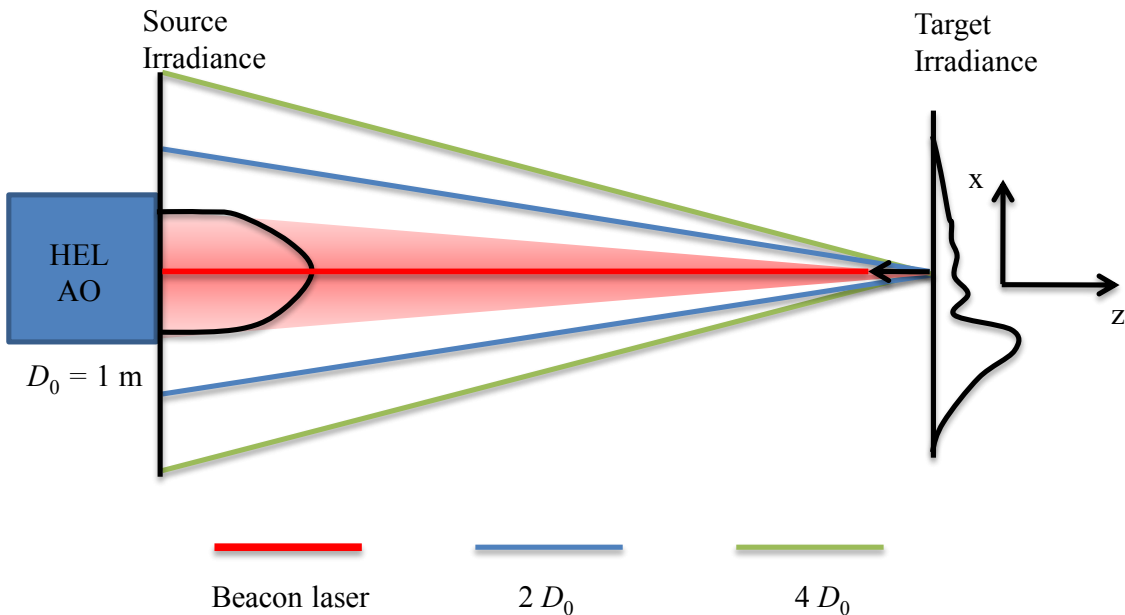
Figure 22. Description of the turbulence simulation rule of thumb. The simulated source plane side length must be four times the initial beam diameter D_0. This is done so that the simulated point-source wavefronts in the source plane are two times the initial beam diameter D_0. Thus, a guard band is set up to account for refraction effects.

A true point source, given by a Dirac delta function, contains all spatial frequencies [9]. In simulation; however, a point source must be modeled as a band-limited function. WaveProp models a band-limited point source by analytically back propagating a square grid of user-defined width from the source plane to the target plane with the proper scaling. This creates a narrow two-dimensional sinc-like pattern in the target plane which is used as the band-limited point source. After propagation from the target plane to the source plane using the BPM, the narrow two-dimensional sinc-like pattern exhibits the properties of a spherical wave in a finite region of the source plane. According to the turbulence simulation rule of thumb, this finite region needs to be at least two times the initial beam diameter D_0. Thus, a guard band is created between the edges of the source plane side length, which is at least four times the initial beam diameter, $s_s \geq 4D_0$. This guard band helps to combat against aliasing effects in the simulations. Aliasing typically results without the guard band because the refraction effects due to thermal blooming and or optical turbulence is strong enough to cause the data to wander off the simulated source plane.

The simulated AO system was comprised of a fast steering mirror (FSM) controlled through center of mass measurements made by a tracker, and a deformable mirror (DM) controlled through slope measurements made by a wavefront sensor (WFS). Altogether, the FSM, DM, tracker, and WFS used the same aperture size as the truncated HEL beam. Specifically, a camera without noise was used to simulate the hardware for the tracker. The camera had a pixel field of view (iFOV), $\theta = 1 \ \mu\text{rad}$, and a finite number of pixels, $n_{\text{pix}} = 32$. The FSM was controlled by the tracker through center of mass

measurements with a servo leakage, $a = 1$, and a servo gain, $b = 0.5$. Similarly, the WFS was modeled after a Shack-Hartmann WFS with no noise. Table 3 specifies parameters used for the WFS which controlled the DM through reconstructed slope measurements in the Fried geometry using a servo leakage, $a = 0.995$, and a servo gain, $b = 0.3$. Note that the DM actuators had infinite stroke. Table 3 also specifies the DM actuator spacings, $\delta = \Lambda/2$, used in the wave-optics experiments.

Fresnel perturbation numbers N_P were also calculated for the simulated AO systems parameters used in the computational wave-optics experiments. The corresponding values are found in Table 3. It is important to note that the simulated Fresnel perturbation numbers gave a range of values to test for the conditions of insipient PCI. According to the linearized theory introduced by Lawrence Livermore National Laboratory (LLNL), the PCI gain factor was found to be proportional to the ratio of the distortion number over the Fresnel perturbation number, N_D/N_P [103]. By varying distortion numbers N_D in the setup of the engagement scenario and the spatial resolution of the AO system, the goal was to test for regimes of both a low PCI gain factor, $N_P \gg 1$ and $N_D < N_C$, and a high PCI gain factor, $N_P \ll 1$ and $N_D > N_C$.

Table 3. Simulated AO system parameters.

Number of subapertures across D_0 n_{sub}	Number of waves of tilt across d n_{lod} (λ)	Pixel field of view, iFOV (μrad)	Number of pixels per subaperture n_{pix}	Actuator spacing, $\delta = \Lambda/2$ (cm)	Fresnel perturbation number N_P
8	6	6.38	64	12.5	9.23
8	8	8.51	64	12.5	9.23
8	10	10.6	64	12.5	9.23
16	6	12.8	128	6.25	2.31
16	8	17.0	128	6.25	2.31
16	10	21.3	128	6.25	2.31
32	6	25.5	256	3.13	0.577
32	8	34.0	256	3.13	0.577
32	10	42.6	256	3.13	0.577

AOTools was utilized in the setup of the simulated AO systems. This greatly simplified the design process required to properly simulate the AO system parameters provided in Table 3. For example, the *subapdlg* graphical user interface was used to calculate the tilt-removed reconstructor needed for the desired subaperture geometries. Figure 23 shows the subaperture geometry used for the simulated case with eight active subapertures across the aperture, $n_{sub} = 8$. Note that the DM actuators were placed in the corners of the subapertures to correspond to the Fried reconstruction geometry. A guard ring of one subaperture was also used in all of the subaperture designs. As a result, slaved actuators were created. Figure 24 shows the subaperture geometry used for the simulated case with 16 active subapertures across the aperture, $n_{sub} = 16$, while Figure 25 shows the subaperture geometry used for the simulated case with 32 active subapertures across the aperture, $n_{sub} = 32$. The simplicity found in using the *subapdlg* graphical user interface of AOTools was greatly appreciated in the analysis.
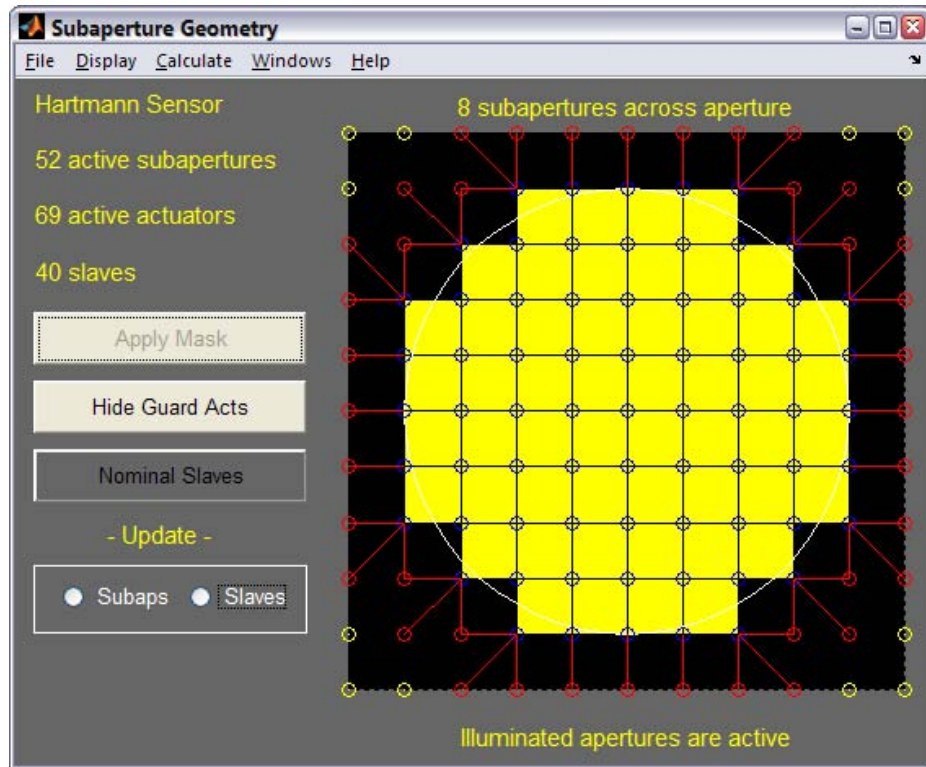
Figure 23. Subaperture geometry used to simulate a Shack-Hartmann WFS with eight active subapertures across the aperture, n_{sub}=8. Active subapertures are given by the yellow squares, while active DM actuators are given by the blue circles. The white circle outlines the diameter of the aperture, D_0=1 m, and red lines represent slave mappings to the slaved actuators given by the red circles. Yellow circles represent dead actuators. The readout in the top left corner provides the total number of active subapertures, active actuators, and slaves used in the design.
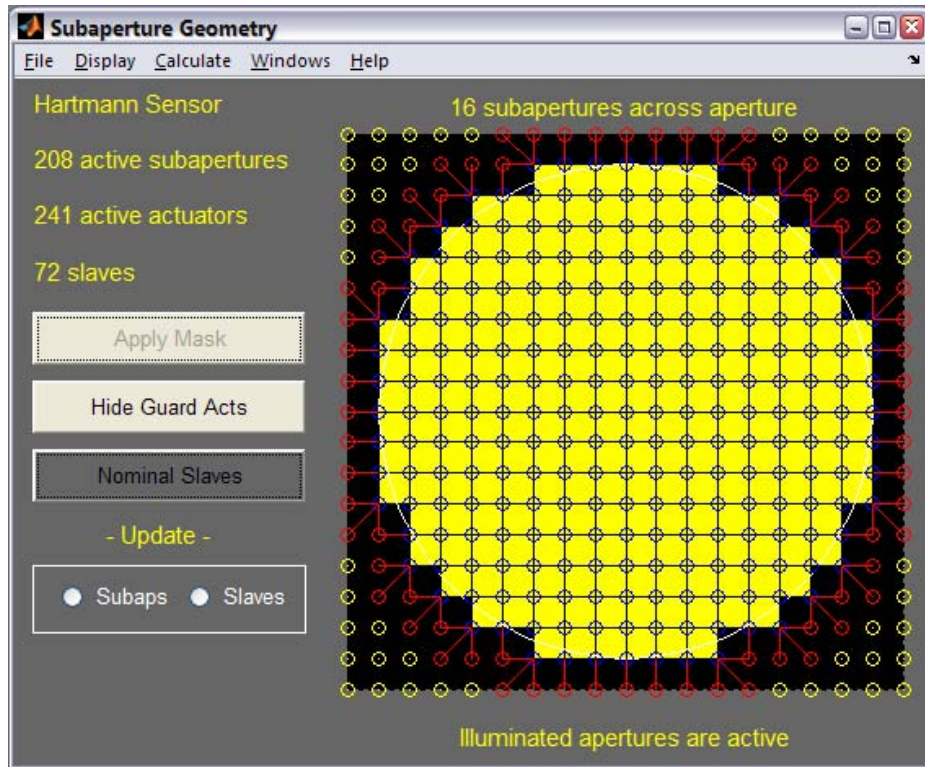
Figure 24. Subaperture geometry used to simulate an AO system with 16 active subapertures across the aperture, n_{sub}=16. Active subapertures are given by the yellow squares, while active DM actuators are given by the blue circles. The white circle outlines the diameter of the aperture, D_0=1 m, and red lines represent slave mappings to the slaved actuators given by the red circles. Yellow circles represent dead actuators. The readout in the top left corner provides the total number of active subapertures, active actuators, and slaves used in the design.
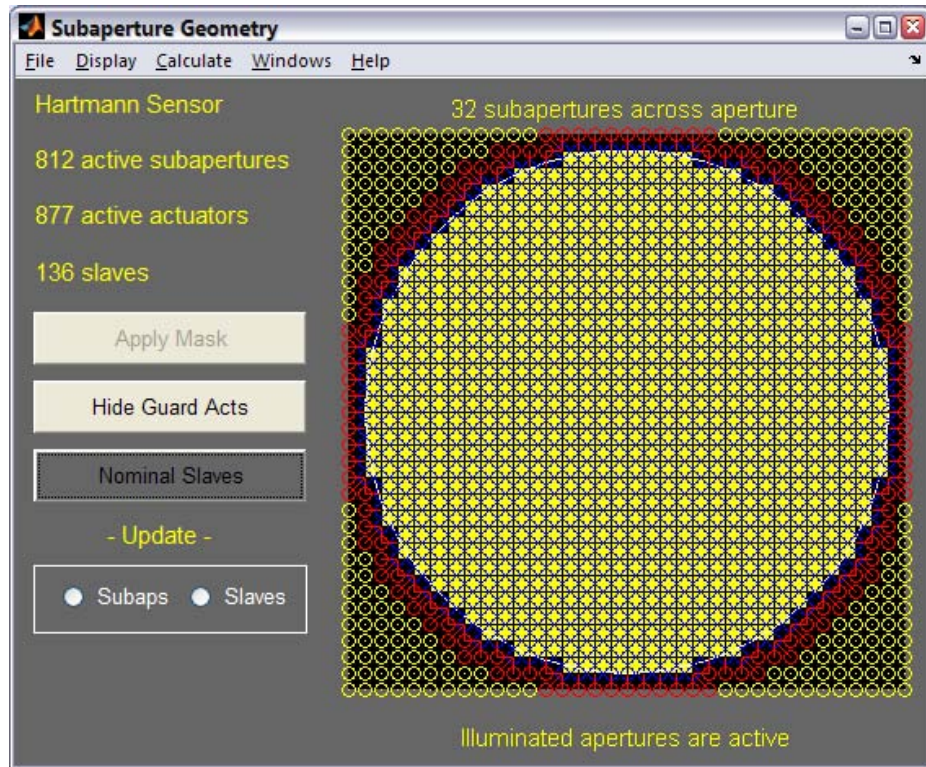
Figure 25. Subaperture geometry used to simulate an AO system with 32 active subapertures across the aperture, n_{sub}=32. Active subapertures are given by the yellow squares, while active DM actuators are given by the blue circles. The white circle outlines the diameter of the aperture, D_0=1 m, and red lines represent slave mappings to the slaved actuators given by the red circles. Yellow circles represent dead actuators. The readout in the top left corner provides the total number of active subapertures, active actuators, and slaves used in the design.

The *servodlg* graphical user interface of AOTools was also utilized in the analysis of the simulated AO systems. The closed-loop response for the AO system control parameters is shown in Figure 26. It should be noted that the sampling frequency, $f_s = 1000 \text{ Hz}$, used in all of the computational wave-optics experiments was determined from the simulation time step, $\Delta t = 1 \text{ ms}$. These values were nominally chosen. The simulated 3dB frequency, $f_{3dB} = 35.4 \text{ Hz}$, for the wave-optics experiments was determined to be slightly larger than the Greenwood frequency, $f_G = 28.2 \text{ Hz}$. Ideally, an AO system should have a 3db frequency that is a few multiples of the Greenwood frequency; however, this is not always an option. The goal for the computational wave-optics experiments was to use AO system control parameters that could easily perform phase compensation for ―moderate‖ optical turbulence. This point will be re-addressed in the next section.
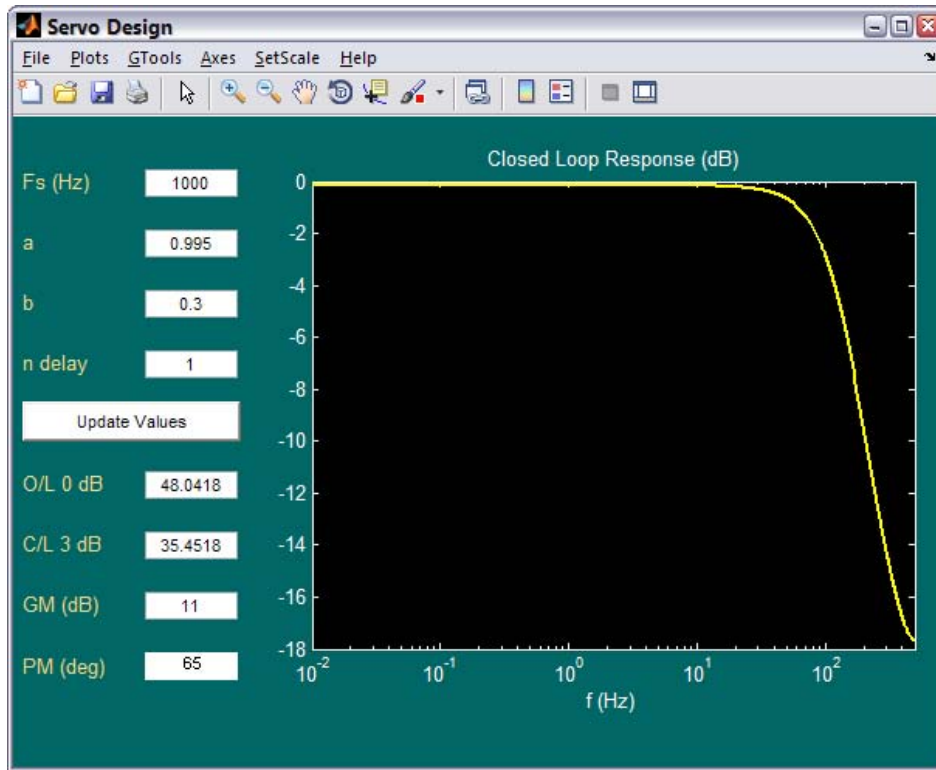
Figure 26. Closed-loop response for the simulated AO system control parameters used in the computational wave-optics experiments. The top left values are inputs and the bottom left values are outputs. O/L 0 dB is the open loop 0 db crossover frequency (Hz). C/L 3 dB is the closed loop 3 dB frequency (Hz). GM is the gain margin (dB). PM is the phase margin (deg).

3.1.3 Sampling Analysis

Sampling analysis for the simulations was also performed. This helped to combat against aliasing affects often encountered in using finite-sized grids NxN to simulate HEL beam propagation in the atmosphere using the BPM. Since the effects of thermal blooming were of primary concern in the computational wave-optics experiments, a series of sampling analysis tests were conducted with steady-state thermal blooming. This was done because steady-state thermal blooming represented the strongest form of optical distortion in the computational wave-optics experiments.

146

The first test was conducted to determine the number of thermal blooming phase screens needed for the computational wave-optics experiments. The goal of this study was to determine the minimum number of screens necessary to effectively simulate steady-state thermal blooming without a significant amount of variation in both the calculated peak Strehl ratio S_p and normalized power in the bucket P_B calculations in the target plane. This was a necessary step in the analysis because it essentially increased the reliability and reproducibility of the simulations. As shown in Figure 28, the peak Strehl ratio S_p and normalized power in the bucket P_B were calculated in the target plane as a function of the number of thermal blooming phase screens. This was done for one simulated distortion number below the critical point, $N_D = 16.8$, and one above the critical point corresponding to the highest distortion number simulated, $N_D = 42.0$. From this analysis, a "knee in the curve" was determined for 100 screens or more for both distortion numbers N_D tested. Thus, $n_{scn} = 100$, thermal blooming phase screens were determined as being adequate for all of the computational wave-optics experiments. It should be noted that WaveProp automatically set the screen spacing for the simulations, so that the each screen had approximately the same amount of distortion as calculated with the distortion number N_D [49,128].
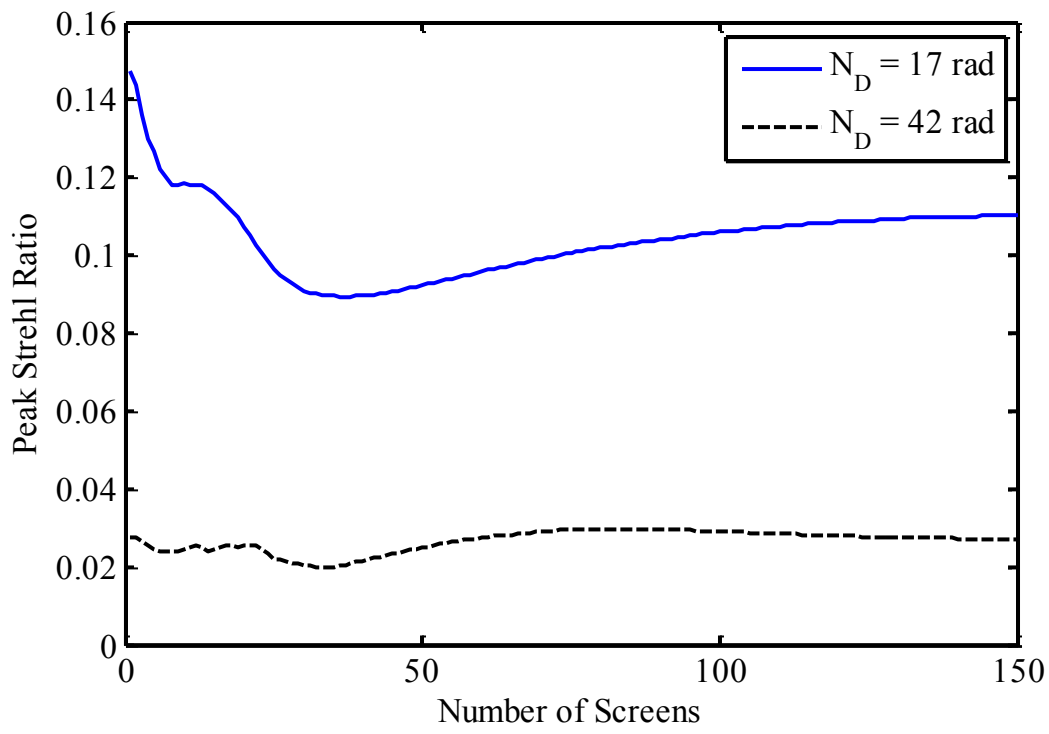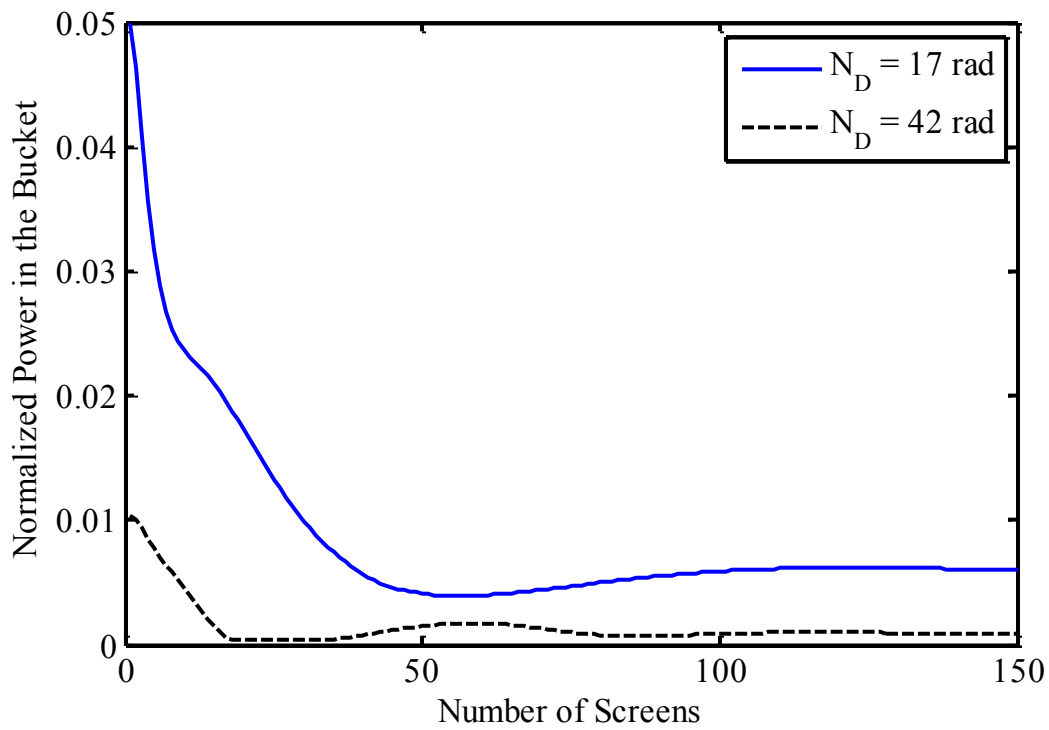
Figure 27. Thermal blooming phase screen convergence study using a.) peak Strehl ratio versus number of screens and b.) normalized power in the bucket versus number of screens.

The results from the second test are displayed in Figure 28. Here, the goal was to make sure that the number of grid points used in the computational wave-optics experiments were adequate to properly simulate HEL beam propagation in the atmosphere using the BPM. This was a necessary step in the analysis to make sure that the number of grid points given in Table 2 were satisfactory for simulating steady-state thermal blooming conditions without the effects of aliasing. Secondly, this test was conducted to make sure that the chosen number of thermal blooming phase screens, $n_{scn} = 100$, from the previous test was sufficient with the number of grid points given in Table 2. As shown in Figure 28, the peak Strehl ratio S_p and normalized power in the bucket P_B were calculated in the target plane as a function of the number of grid points N. Similarly, this was done for one simulated distortion number below the critical point, $N_D = 16.8$, and one above the critical point corresponding to the highest distortion number simulated, $N_D = 42.0$, with, $n_{scn} = 100$, thermal blooming phase screens. From this analysis, it was determined from the lack of variation past, $N = 256$, that the number of grid points listed in Table 2 were adequate to simulate steady-state thermal blooming conditions.
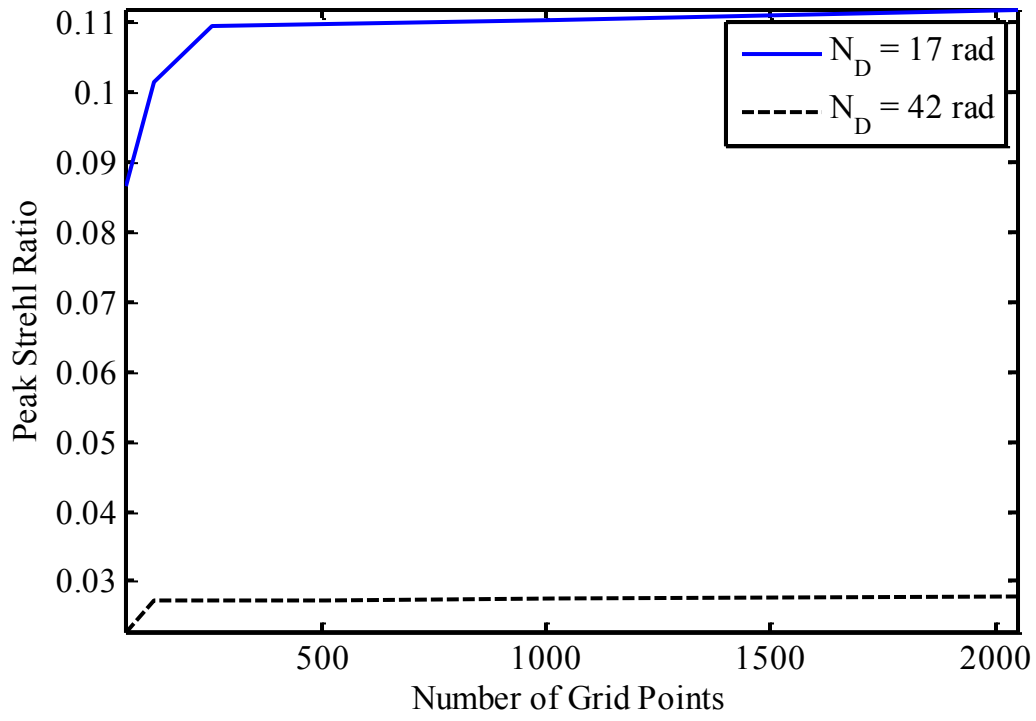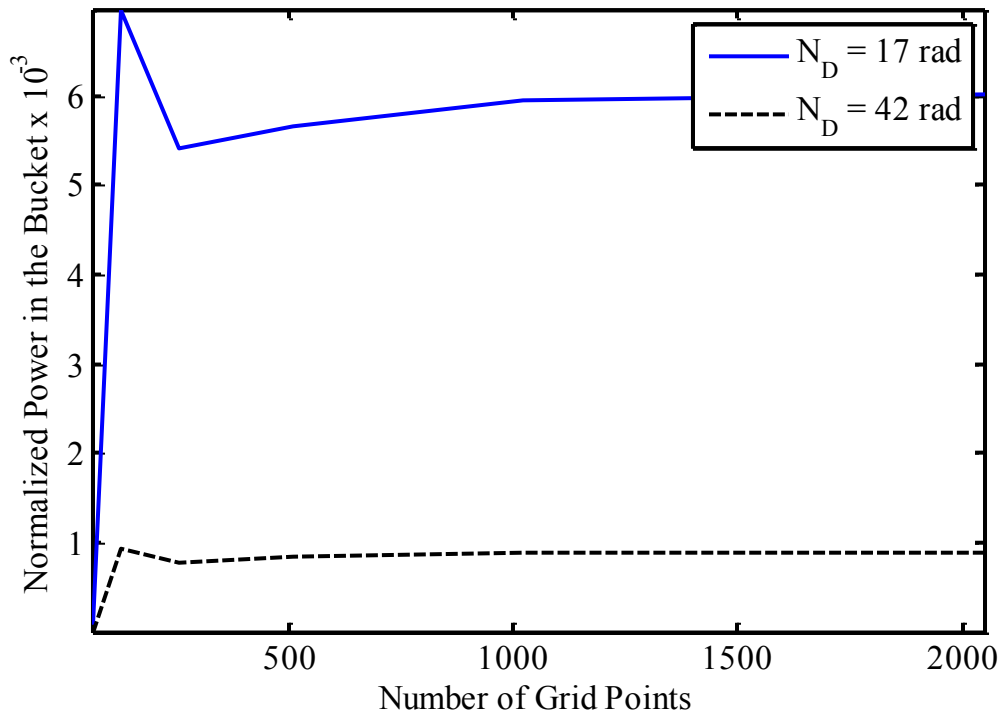
Figure 28. Number of grid points convergence study using a.) peak Strehl ratio versus number of grid points and b.) normalized power in the bucket versus number of grid points.

3.2 Parameter Space Exploration

In this section, a series of preliminary wave-optics experiments are conducted. This is done to make sure that the simulations are in working order and to present a methodology for the experimental analysis presented in the next chapter. The goal for results presented in this section are to provide bounds for the problem at hand. As such, each wave-optics experiment conducted in this section includes results for an initial HEL beam power, $P_0 = 100 \text{ kW}$, simulated just below the critical power, $P_C = 118 \text{ kW}$, as given by Eq. (168), and an initial HEL beam power, $P_0 = 250 \text{ kW}$, simulated well above. The corresponding distortion numbers, $N_D = 16.8 \text{ rad}$ and $N_D = 42.0 \text{ rad}$, are provided in Table 2 and are appropriately referred to throughout the analysis as being both below and above the critical point, i.e. the critical distortion number N_C, as given in Eq. (167). In addition, the phase compensation results presented in this section are for the "middle of the road" AO system parameters, $n_{sub} = 16$ and $n_{lod} = 8 \lambda$, simulated in the wave-optics experiments and tabulated in Table 3. Further experimental analysis using additional AO system parameters are presented in the next chapter.

3.2.1 Propagation with Extinction

As a first step in the analysis, it was nessecary to make sure that WaveProp was setup correctly to simulate the engagement scenario parameters given in the previous section with only extinction effects. This was done so that the simulated parameters in the wave-optics experiments could be checked for the appropriate initial conditions without the effects of thermal bloomining and or turbulence. For example, the HEL beam irradiance and phase in the source plane and target plane are displayed in Figure 29

for the highest initial beam power simulated, $P_0 = 250 \text{ kW}$. The top left corner of Figure 29 represents the HEL beam source plane irradiance. Note that the HEL beam profile is Gaussian and truncated with an initial beam daimeter, $D_0 = 1 \text{ m}$. Furthermore, the HEL beam phase in the souce plane is provided in the top right corner. Note here that the phase is constant/flat, as required by an intitally collimated beam. This represents the phase of the HEL beam before being sent through the lens. Also note that the chosen source plane side length, $s_s = 4 \text{ m}$, is in working order.

The HEL beam irradiance and phase in the target plane after propagation with the effects of extinction are also shown in the bottom portion of Figure 29. Here, it should be noted that the target plane irradiance fits within the bucket diameter, $D_B = 1.3 \text{ cm}$, as given by Eq. (95). The corresponding phase in the target plane has the characteristic parabolic features associated with Gaussian beam propagation. It should also be noted that the grid resolution in the target plane was significantly less than the resolution in the source plane. This is seen in the slightly blurry target plane HEL beam irradiance and phase as compared with the source plane HEL beam irradiance and phase. Nonetheless, 20 grid points across the bucket diameter was more than adequate for peak Strehl ratio S_p and normalized power in the bucket P_B calculations in the target plane. In the presence of thermal blooming and or optical turbulence, the beam spread was expected to be a lot larger than the bucket diameter, $D_B = 1.3 \text{ cm}$.
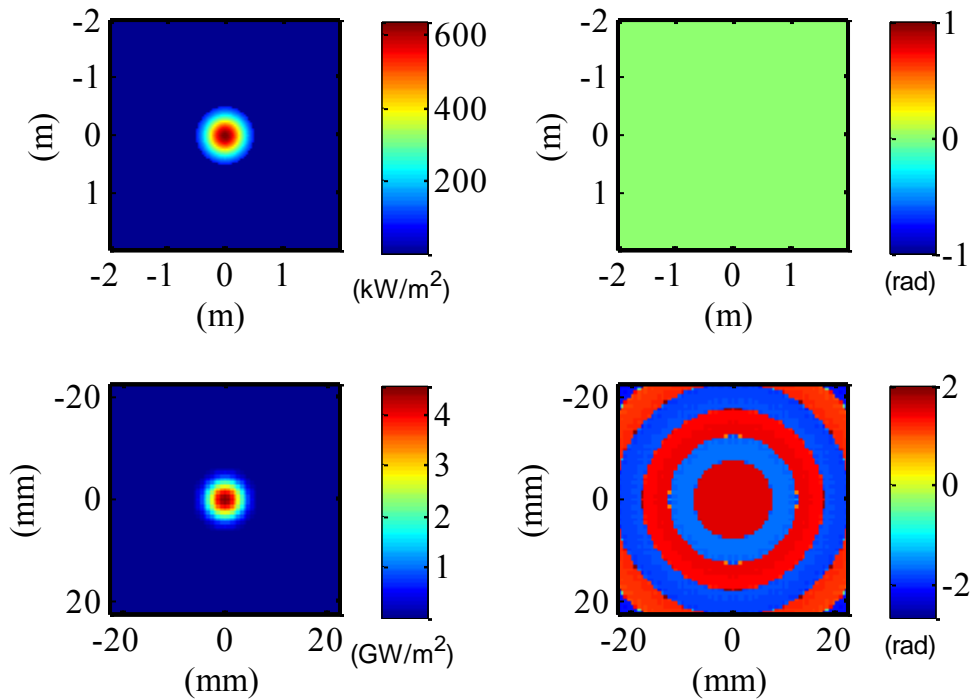
Figure 29. Propagation of the simulated HEL beam with extinction effects for an initial beam power, P_0=250 kW. The top row demonstrates the truncated irradiance and initially collimated phase in the source plane and the bottom row demonstrates the irradiance and phase in the target plane.

The setup and propagation of the point-source beacon was also verified with only the effects of extinction. As shown in Figure 30, it was noted that the point-source beacon irradiance in the target plane was represented as a narrow band-limited sinc-like pattern. This is demonstrated in the top left corner of Figure 30. After propagation to the source plane, the point-source beacon was collimated by the simulated thin lens and truncated by the pupil to have an aperture diameter, $D_0 = 1\,\mathrm{m}$. This is demonstrated in the bottom portion of Figure 30 and is characterized with a constant/flat irradiance and a constant/flat phase associated with collimation. As a final note here, the point source beacon provided adequate coverage of the shared aperture.
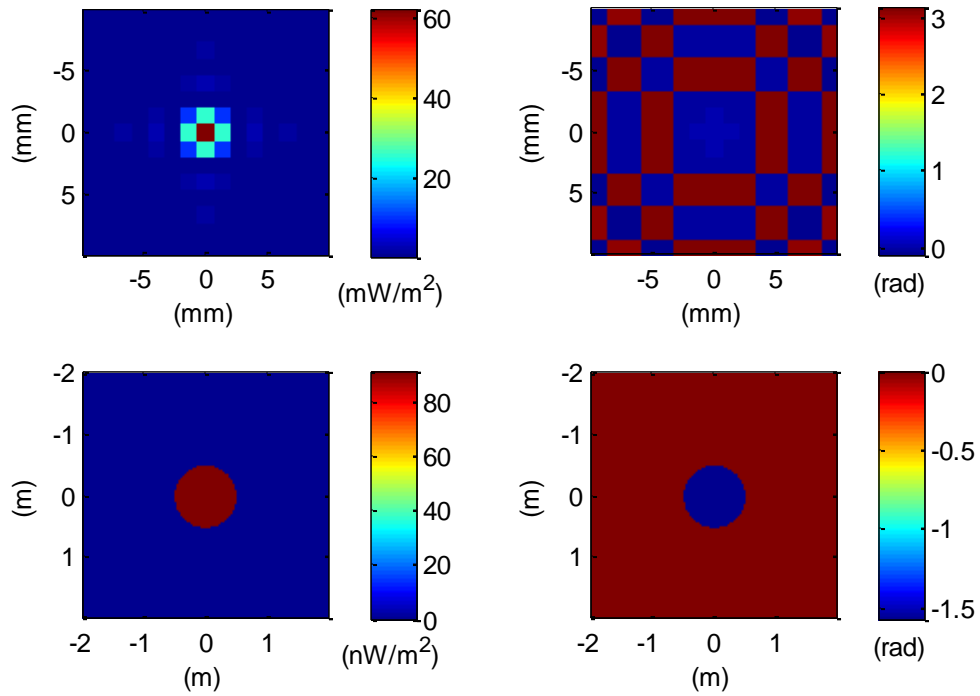
Figure 30. Propagation of the simulated point-source beacon with the effects of extinction. The top row demonstrates the irradiance and phase in the target plane and the bottom row demonstrates the irradiance and phase in the source plane after collimation.

154

3.2.2 Propagation with Thermal Blooming

The effects of time-dependent thermal blooming were explored here using the algorithm presented in Eq. (82). For instance, in Figure 31, the engagement scenario parameters presented in the previous section were used to propagate the HEL beam with the effects of time-dependent thermal blooming for a distortion number just below the critical point, $N_D = 16.8$ rad. The effects of optical turbulence were not simulated here, only the effects of time-dependent thermal blooming and extinction. It is noted from Figure 31, that in terms of normalized irradiance in the target plane, steady-state thermal blooming was reached sometime after the 50 ms time stamp. This is noted as the crescent pattern in the target plane becomes static around this time stamp and does not really change in shape. Similarly, the effects of time-dependent thermal blooming were simulated for the highest distortion number used in the wave-optics experiments, $N_D = 42.0$ rad. These results for normalized irradiance are demonstrated in Figure 32.

It is important to note the differences in the development of the crescent pattern obtained in the "strong" thermal blooming regime, $N_D = 42.0$ rad, as opposed to the crescent pattern obtained in the "moderate" thermal blooming regime, $N_D = 16.8$ rad. The effects of Fresnel ringing due to the truncated beam diameter, $D_0 = 1$ m, are amplified with an increase in the strength of the simulated thermal blooming. It is also noted that the crescent pattern in Figure 32 in the steady-state regime is nearly doubled in size when compared with Figure 31. In this case, steady-state thermal blooming is characterized in terms of normalized irradiance in the target plane as being reached after the 75 ms time stamp.

To discern the actual convergence of the crescent formation, an additional test was conducted. Here, peak Strehl ratio S_p and normalized power in the bucket P_B calculations in the target plane were plotted versus time, as shown in Figure 33. Both time-dependent and steady-state values were plotted for the distortion numbers tested in Figure 31 and Figure 32. The results of the convergence study show that the peak Strehl ratio S_p and the normalized power in the bucket P_B calculations for time-dependent thermal blooming reach their steady-state values faster for the highest distortion number tested, $N_D = 42.0$ rad, as opposed to the distortion number tested below the critical point, $N_D = 16.8$ rad. These results seem to contradict those discussed for Figure 31 and Figure 32, which show time stamps for normalized irradiance. It should be noted that normalized irradiance snapshots are sometimes deceiving; however, they serve as a great analysis tool in visualizing the results.
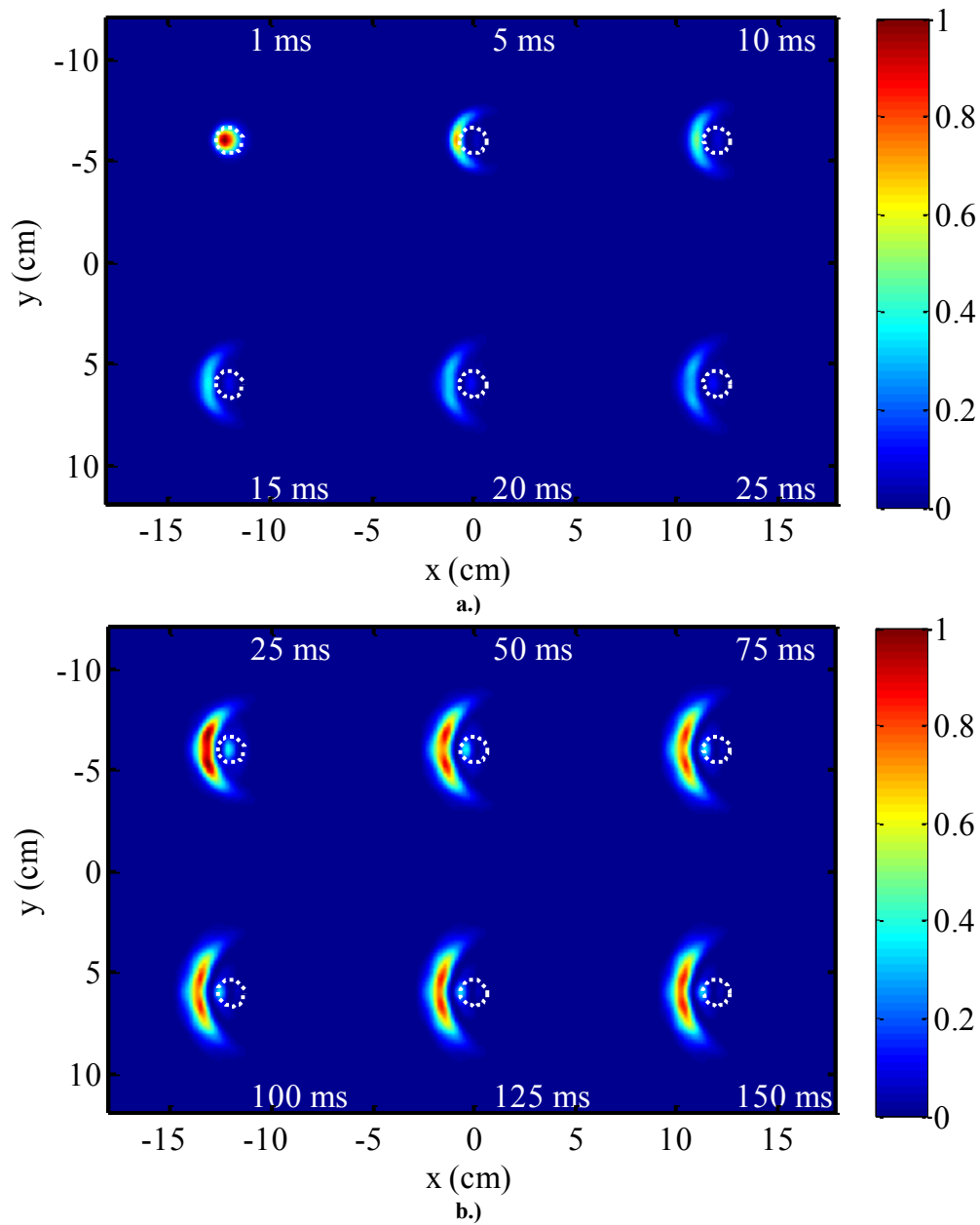
Figure 31. Normalized HEL beam irradiance for time-dependent thermal blooming and a distortion number below the critical point, N_D=16.8 rad. In a.) the simulation runs from 1 ms to 25 ms and in b.) the simulation runs from 25 ms to 150 ms. The white circles represents the diffraction limited bucket diameter D_B=1.3 cm.
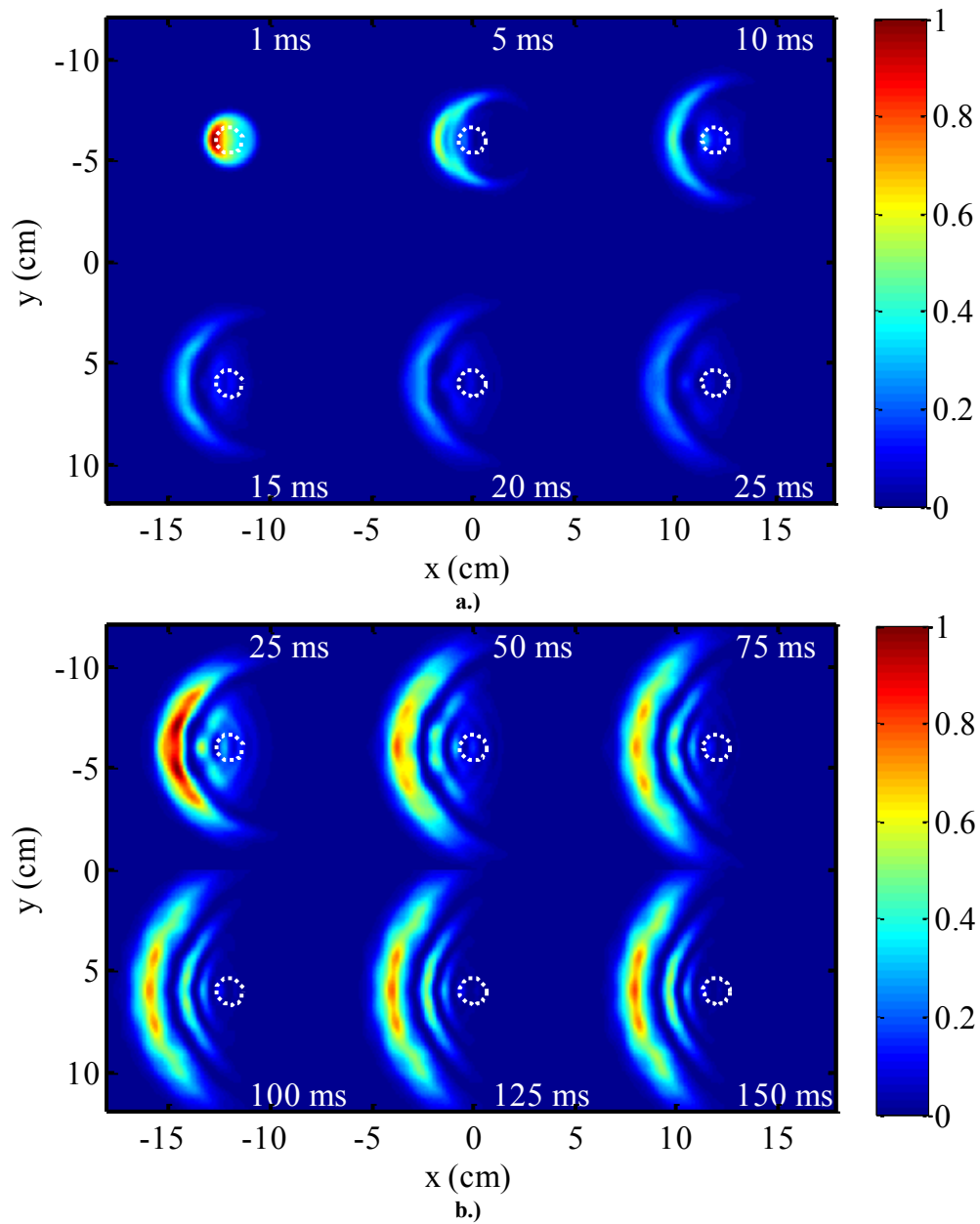
Figure 32. Normalized HEL beam irradiance for time-dependent thermal blooming and a distortion number well above the critical point, N_D=42.0 rad. In a.) the simulation runs from 1 ms to 25 ms and in b.) the simulation runs from 25 ms to 150 ms. The white circles represents the diffraction limited bucket diameter D_B=1.3 cm.
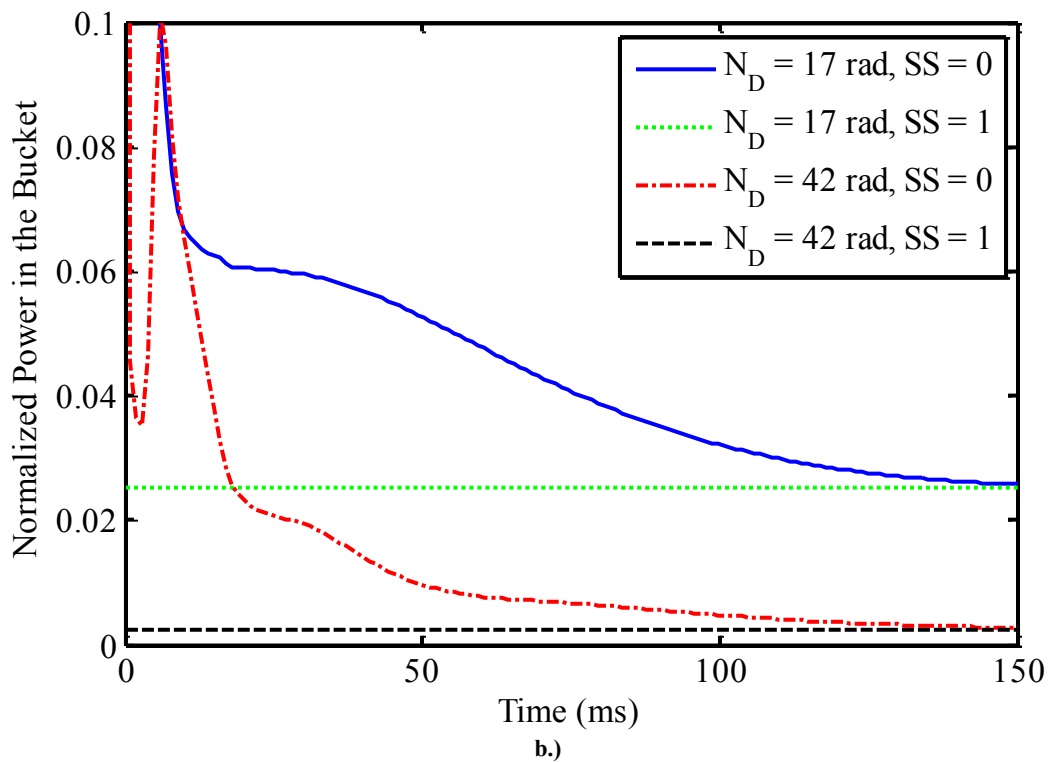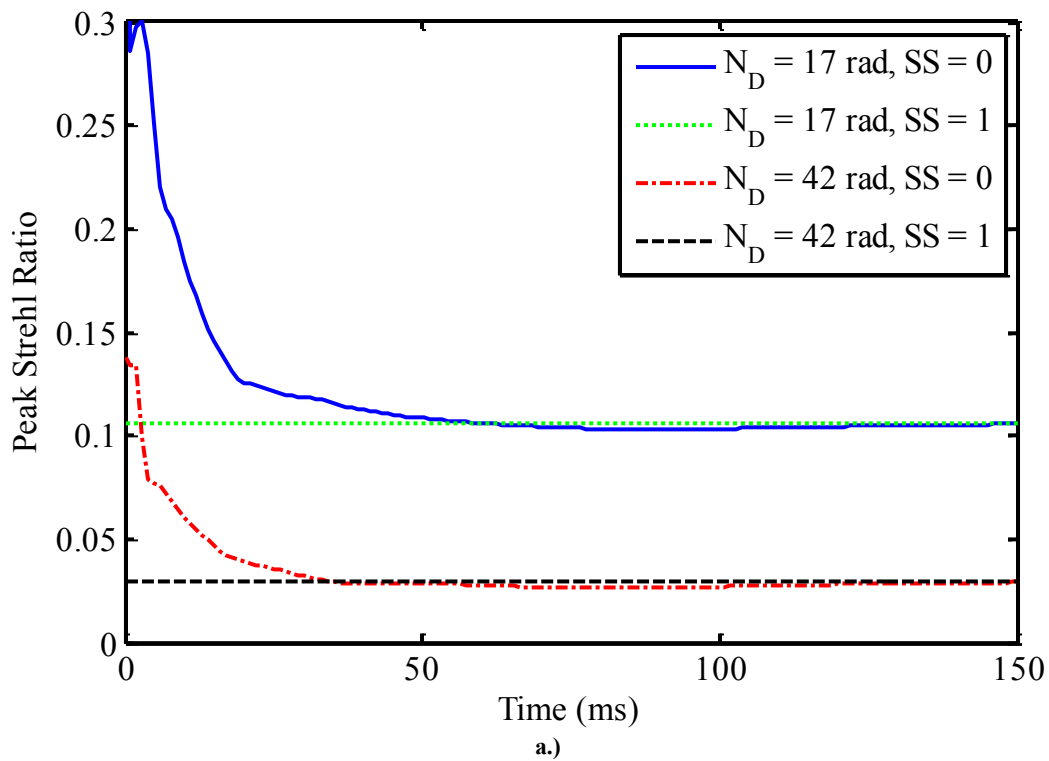
Figure 33. Thermal blooming convergence study using a.) peak Strehl ratio versus time and b.) normalized power in the bucket versus time.

3.2.3 Propagation with Turbulent Thermal Blooming

In this study, the effects of time-dependent turbulent thermal blooming were tested using the algorithm given in Eq. (111). Remember that wind speed data from the ExPERT database in LEEDR3 was used to determine the wind velocity standard deviation, $\sigma_v(Z) = 1.8$ m/s, as described above in Figure 21. It should be noted that the spatial filtering associated with the wind fluctuations characteristic function $\mathcal{P}(z,t)$, as given in Eq. (107), was realized for ten previous time steps. This was determined as being adequate based on the decreasing trend given in the Gaussian distributed spatial spread found in Figure 7. Including additional time steps only served to decrease computational efficiency with little added effect in the obtained result.

With that said, the blurring effects associated with time-dependent turbulent thermal blooming were found to nominally increase system performance. As shown in Figure 34, peak Strehl ratio S_p and normalized power in the bucket P_B calculations in the target plane versus time were compared for both time-dependent turbulent thermal blooming and time-dependent thermal blooming. The effects of the time-varying wind fluctuations were found to have minimal impact on system performance for both the "strong" thermal blooming regime, $N_D = 42.0$ rad, and the "moderate" thermal blooming regime, $N_D = 16.8$ rad. Future studies with WaveProp are needed to discern whether this discrepancy was from user error, algorithm error, or fact.
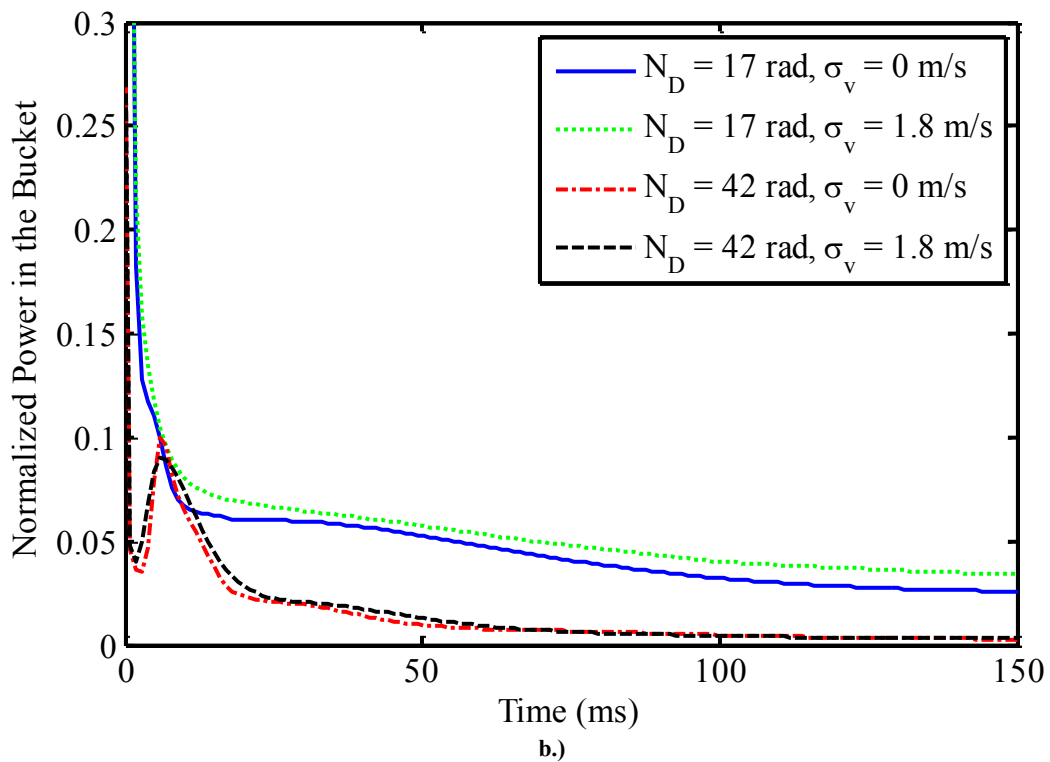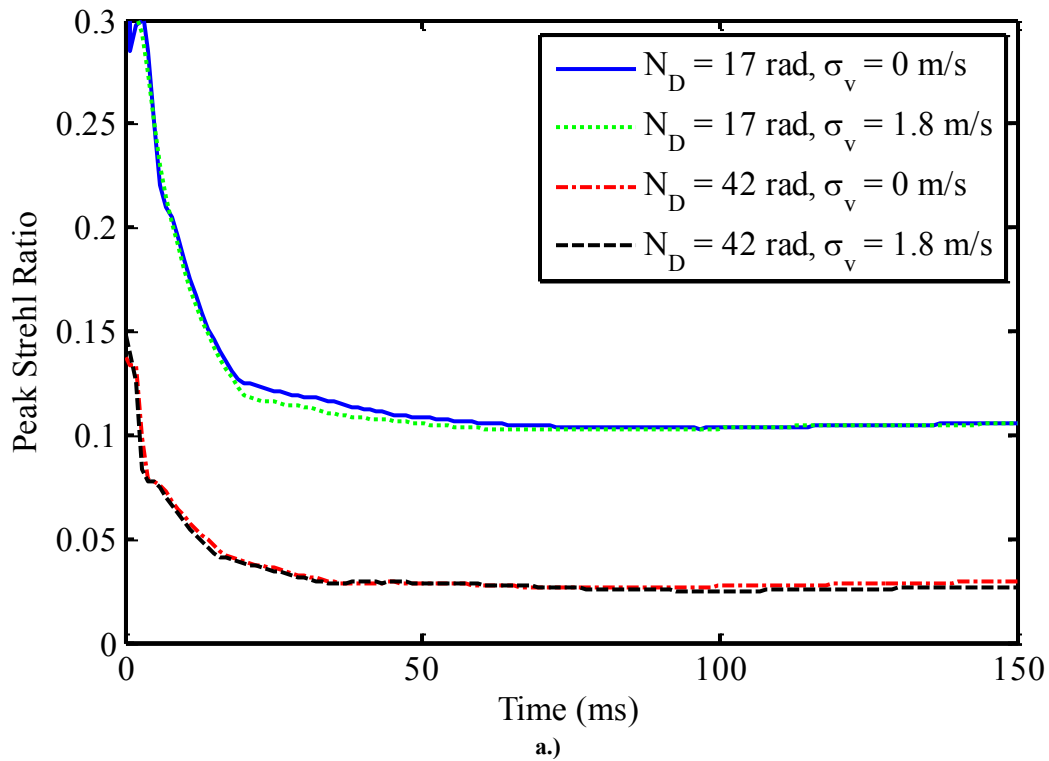
Figure 34. Turbulent thermal blooming versus thermal blooming study using a.) peak Strehl ratio versus time and b.) normalized power in the bucket versus time.

3.2.4 Propagation with Turbulence

The effects of optical turbulence were explored here. For instance, in Figure 35, the engagement scenario parameters presented in the previous section were used to propagate the HEL beam through optical turbulence with a spherical wave coherence diameter, $r_{0,sw} = 13.6 \text{ cm}$. It is stressed that the effects of time-dependent thermal blooming were not simulated in this study, only the effects of optical turbulence and extinction. The characteristic scintillation caused by optical turbulence is shown in Figure 35 in terms of normalized irradiance. It is important to note that the variations in the normalized irradiance fluctuate as time progresses.
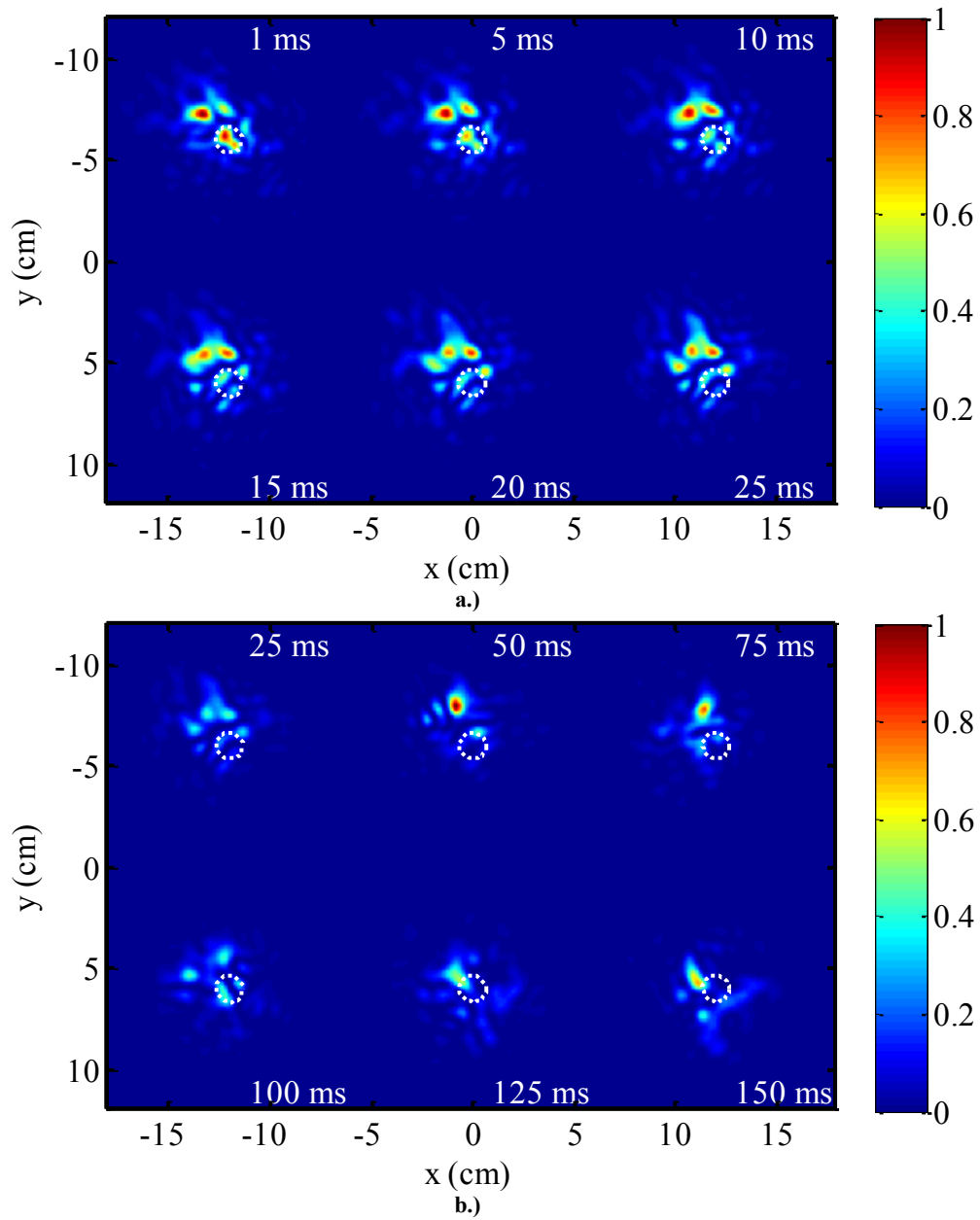
Figure 35. Normalized HEL beam irradiance for one realization of optical turbulence and a spherical-wave coherence diameter, $r_{0,sw}$=13.6 cm. In a.) the simulation runs from 1 ms to 25 ms and in b.) the simulation runs from 25 ms to 150 ms. The white circles represents the diffraction limited bucket diameter for the simulations, D_B=1.3 cm.

To make sure that the wave-optics experiments were working properly for multiple realizations of simulated optical turbulence, the PSF and OTF were used. For example, as shown in Figure 36 and Figure 37, the simulations behaved as expected for 25 independent realizations of a point-source beacon propagating through optical turbulence. The average PSF $h(u,v)$ fit within the turbulence limited bucket diameter, $D_T = 9.54$ cm, as given by Eq. (100). This was consistent with the theory presented in the previous chapter and made sense based on the spatial resolution associated with the simulated spherical wave coherence diameter, $r_{0,sw} = 13.6$ cm. In addition, the long-exposure OTF $H_{LE}(f_u, f_v)$, as given in Eq. (151), corresponded well with the experimental OTF $H_{EX}(f_u, f_v)$, which was determined from the average PSF $h(u,v)$ found in Figure 36 using Eq. (147). The diffraction limited OTF $H_{DL}(f_u, f_v)$ was also used to create an equivalent OTF, $H_{EQ}(f_u, f_v) = H_{DL}(f_u, f_v) H_{LE}(f_u, f_v)$, for comparison purposes. As shown in Figure 37, the diffraction limited OTF $H_{DL}(f_u, f_v)$ had little effect on the equivalent OTF $H_{EQ}(f_u, f_v)$ when compared with the effects of the long exposure OTF $H_{LE}(f_u, f_v)$.
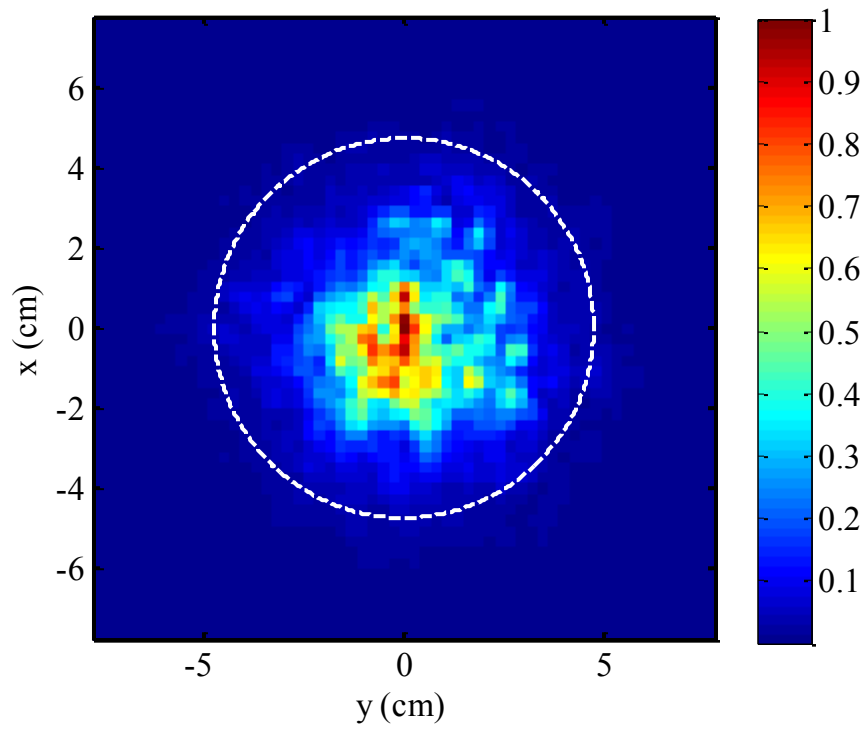
Figure 36. Optical turbulence validation study using the PSF. The normalized average PSF was calculated from 25 independent realizations of a point source propagating through optical turbulence. The dashed white line represents the optical turbulence limited bucket diameter, D_T=9.54, for a spherical-wave coherence diameter, $r_{0,sw}$=13.6 c
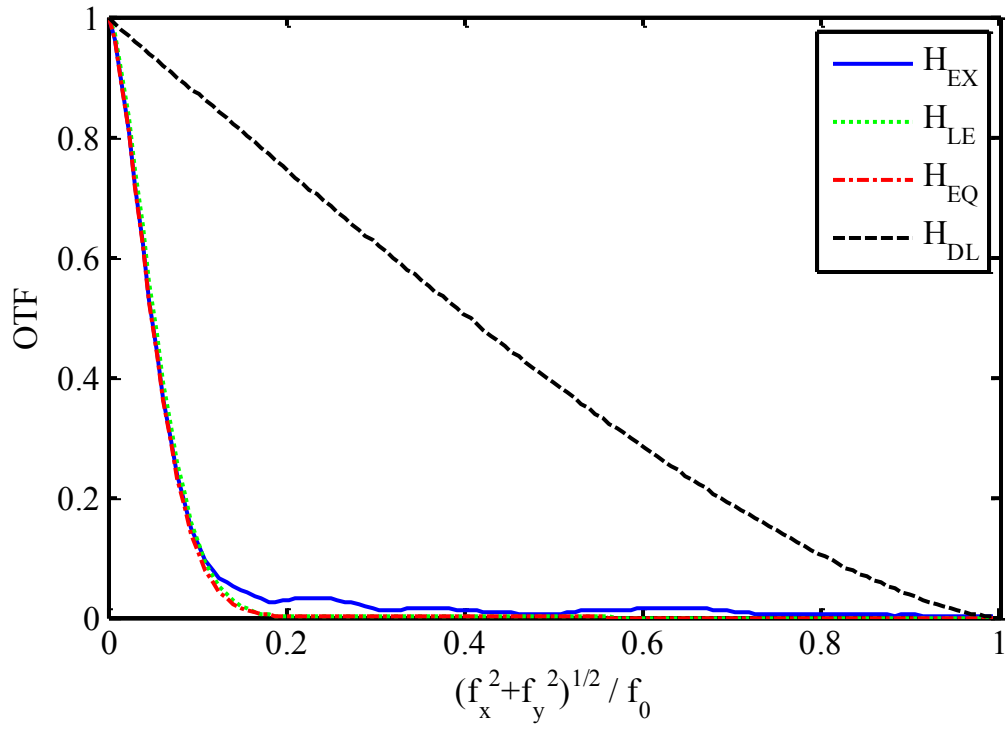
Figure 37. Optical turbulence validation study using the OTF. The experimental OTF H_{EX} is calculated from 25 independent realizations of a point source propagating through optical turbulence. The equivalent OTF is determined from the long-exposure and diffraction-limited OTF, $H_{EQ}=H_{DL}H_{LE}$

3.2.5 Propagation with Thermal Blooming and Turbulence

In the analysis presented here, the combined effects of thermal blooming and turbulence were study. This was done to provide a gauge for the effects of time-dependent thermal blooming coupled with the simulated optical turbulence. For this purpose, two different distortion numbers N_D were analyzed in this study with a simulated spherical wave coherence diameter, $r_{0,sw} = 13.6\ \mathrm{cm}$. The results from the first distortion number tested, $N_D = 15.5\ \mathrm{rad}$, are given in Figure 38 and Figure 39. These results correspond to a distortion number found below the critical distortion number N_C, as given in Eq. (167). In Figure 38, normalized irradiance for varying time stamps is studied. It is noted here that the characteristic scintillation associated with optical turbulence is eventually shifted into the transverse wind direction due to advection associated with time-dependent thermal blooming. This effect is characterized with the scintillated irradiance pattern being consistently located in the left half plane of the simulation grid in the steady-state thermal blooming limit.

Peak Strehl ratio S_P and normalized power in the bucket P_B calculations versus time are shown in Figure 39. Here, a comparison study is given for the effects of only time dependent thermal blooming, the averaged effects of 25 independent realizations of optical turbulence, and the combined effects of time-dependent thermal blooming and 25 independent realizations of optical turbulence. It was noted that the combined effects of time-dependent thermal blooming and optical turbulence were found to be more severe than those of only time-dependent thermal blooming.
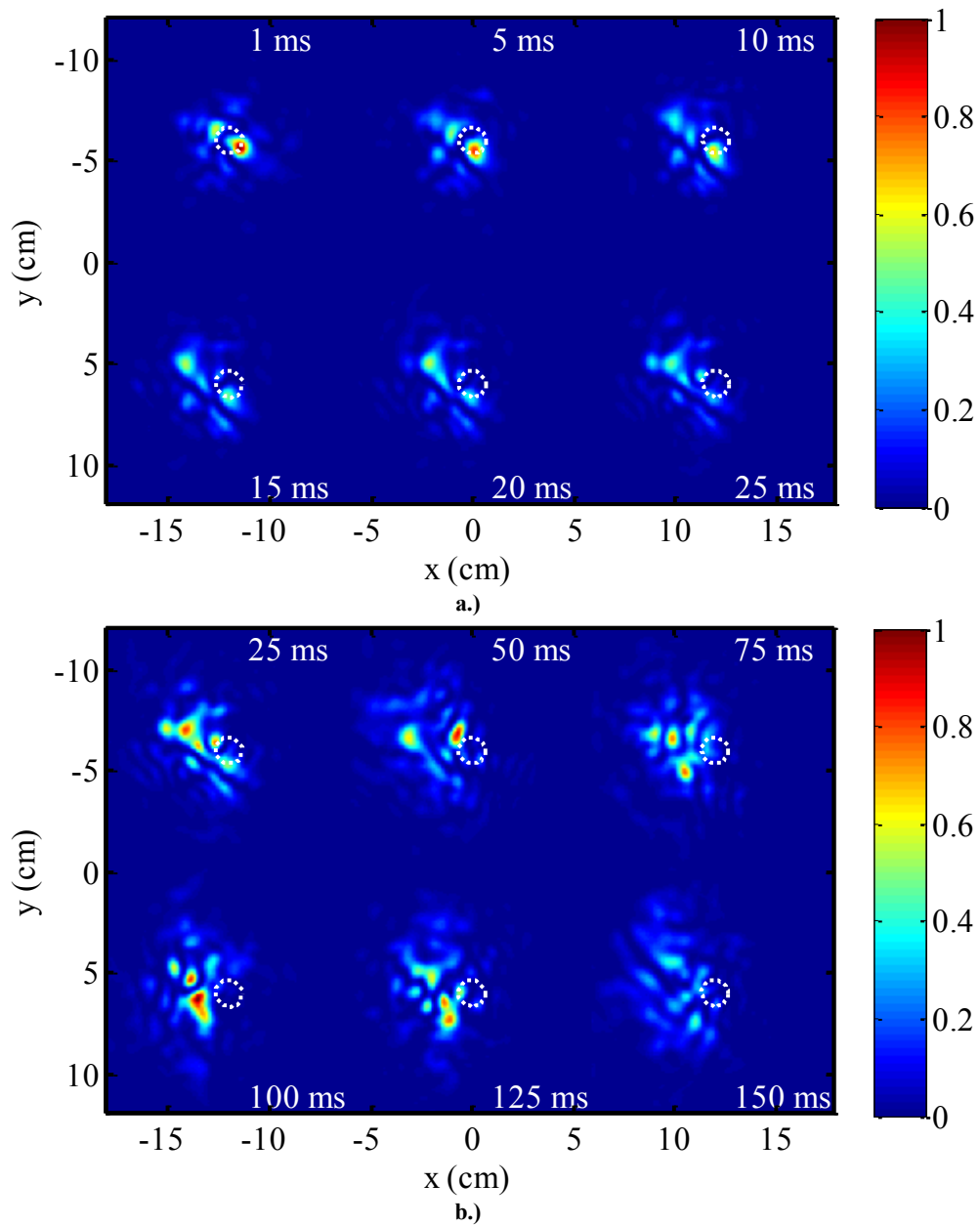
Figure 38. Normalized HEL beam irradiance with time-dependent thermal blooming and one realization of optical turbulence for a spherical-wave coherence diameter, $r_{0,sw}$=13.6 cm, and a distortion number, N_D=16.7 rad. In a.) the simulation runs from 1 ms to 25 ms and in b.) the simulation runs from 25 ms to 150 ms. The white circles represents the diffraction limited bucket diameter for the simulations, D_B=1.3 cm.
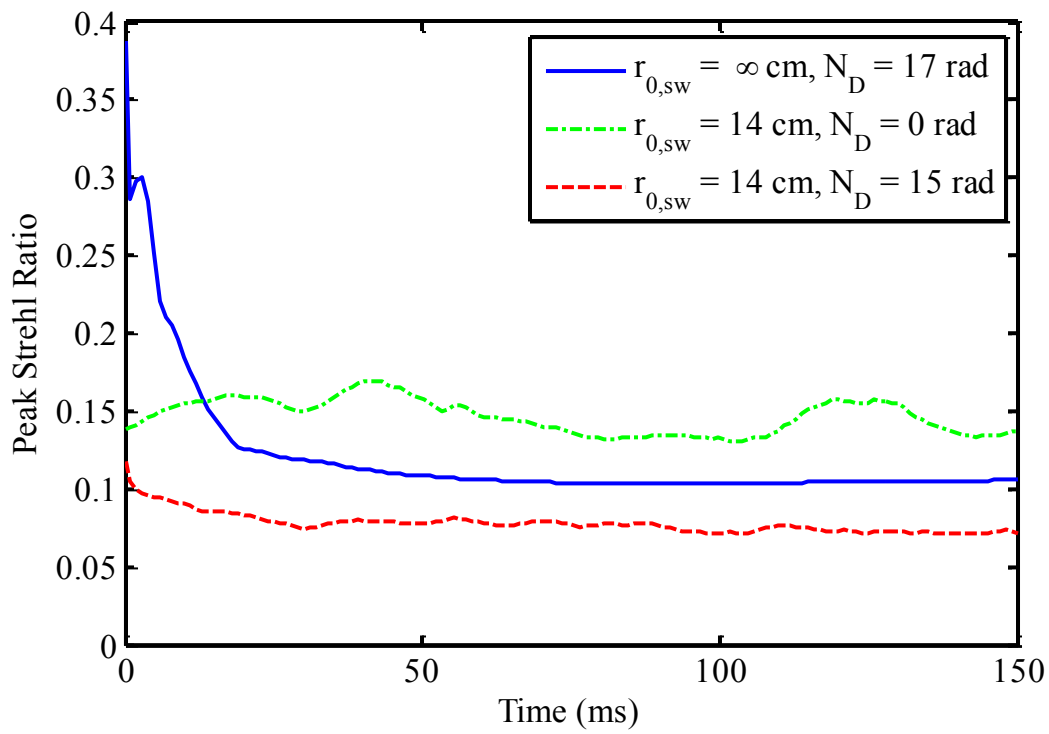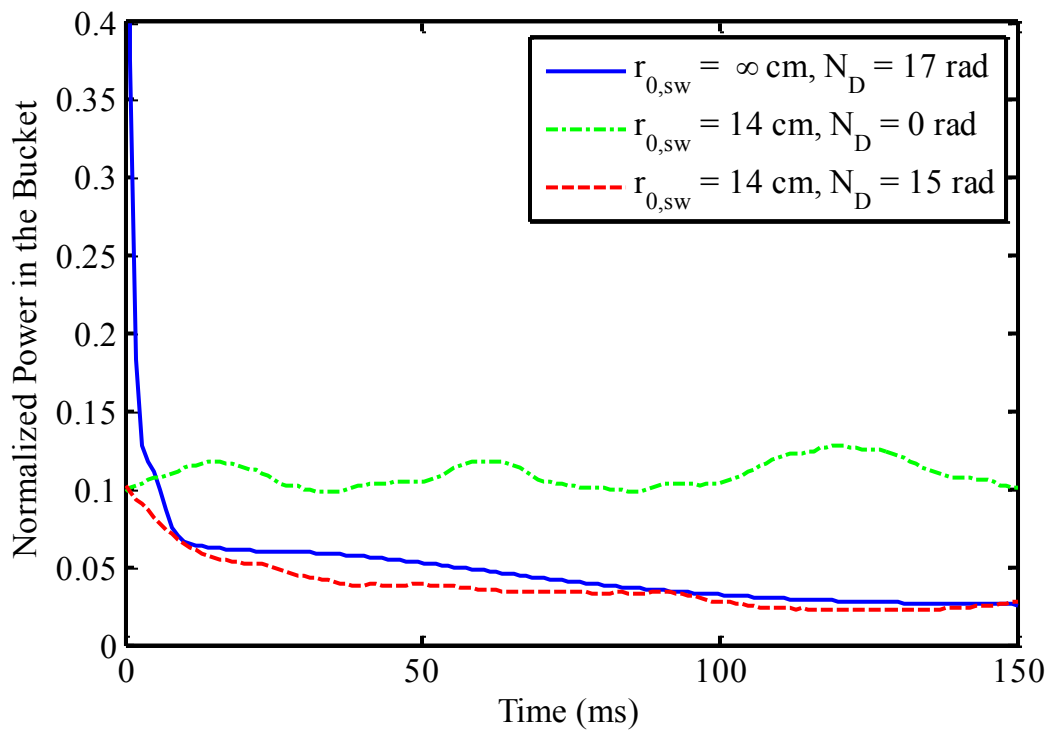
Figure 39. Comparison study for HEL beam propagation with time-dependent thermal blooming and the average of 25 independent realizations of optical turbulence using a.) peak Strehl ratio versus time and b.) normalized power in the bucket versus time.

The results from the second distortion number tested, $N_D = 42.0 \text{ rad}$, are given in Figure 40 and Figure 41. These results correspond to a distortion number found well above the critical distortion number N_C, as given in Eq. (167). In Figure 40, normalized irradiance for varying time stamps is studied. Here, the characteristic scintillation associated with optical turbulence is quickly shifted into the transverse wind direction because of advection associated with time-dependent thermal blooming. This effect is characterized with the scintillated irradiance pattern being consistently located in the left half plane of the simulation grid in the steady-state thermal blooming limit. Note that the normalized irradiance pattern given in Figure 40 is nearly twice as large as that given in Figure 38.

Peak Strehl ratio S_P and normalized power in the bucket P_B calculations versus time are also shown in Figure 41. Similar to Figure 39, a comparison study is given for the effects of only time dependent thermal blooming, the averaged effects of 25 independent realizations of optical turbulence, and the combined effects of time-dependent thermal blooming and 25 independent realizations of optical turbulence. In this case, the combined effects of time-dependent thermal blooming and optical turbulence were found to be as severe as those of only time-dependent thermal blooming. In some time stamps, even better. It is important to note that this point is accounted for with the small difference found in the calculated distortion numbers, $N_D = 42.0 \text{ rad}$ and $N_D = 38.8 \text{ rad}$, which were determined based on the initial beam diameter, $D_0 = 1 \text{ m}$, and the spherical wave coherence length, $r_{0,sw} = 13.6 \text{ cm}$, respectively.
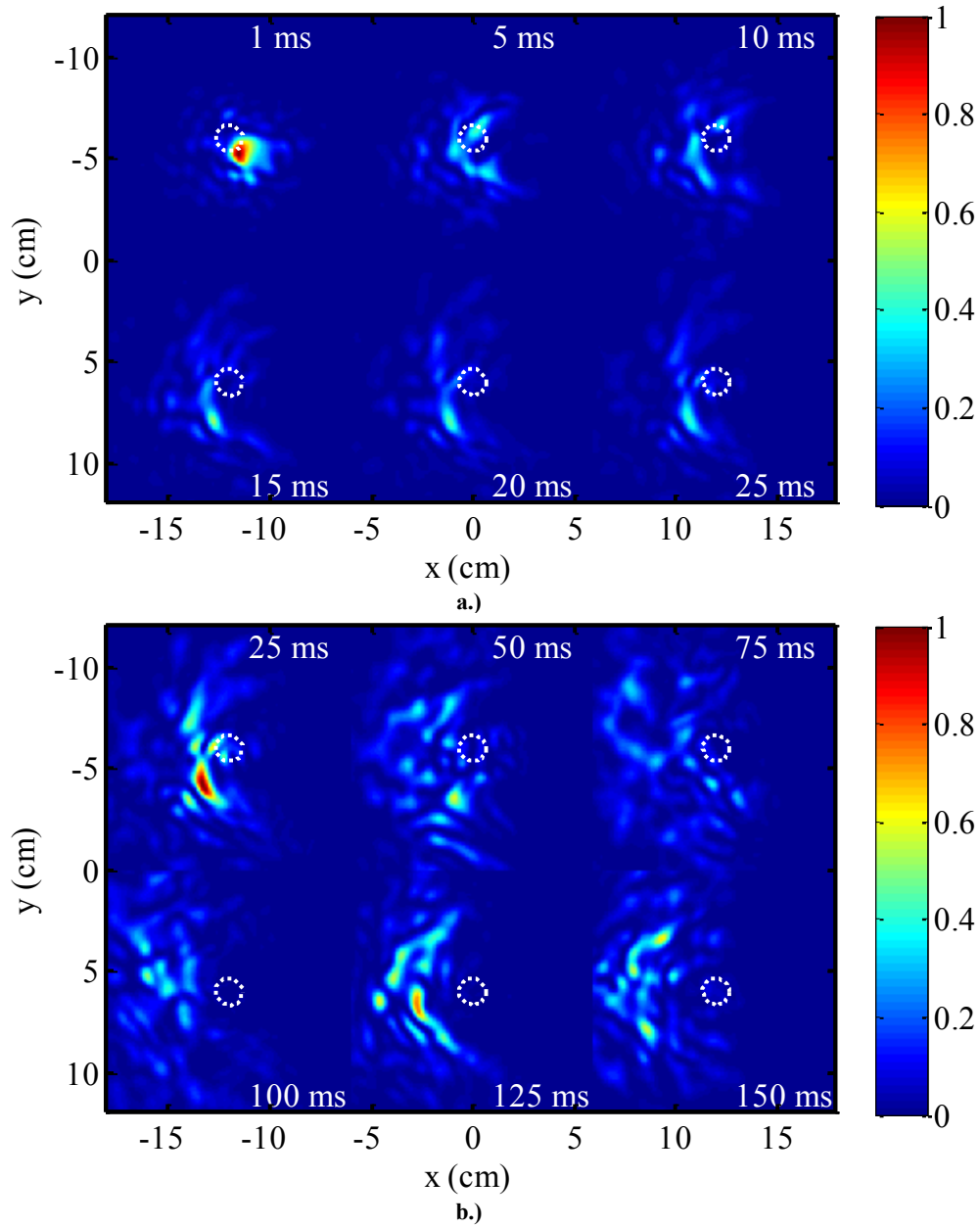
Figure 40. Normalized HEL beam irradiance with time-dependent thermal blooming and one realization of optical turbulence for a spherical-wave coherence diameter, $r_{0,sw}$=13.6 cm, and a distortion number, N_D=42.0 rad. In a.) the simulation runs from 1 ms to 25 ms and in b.) the simulation runs from 25 ms to 150 ms. The white circles represents the diffraction limited bucket diameter for the simulations, D_B=1.3 cm.
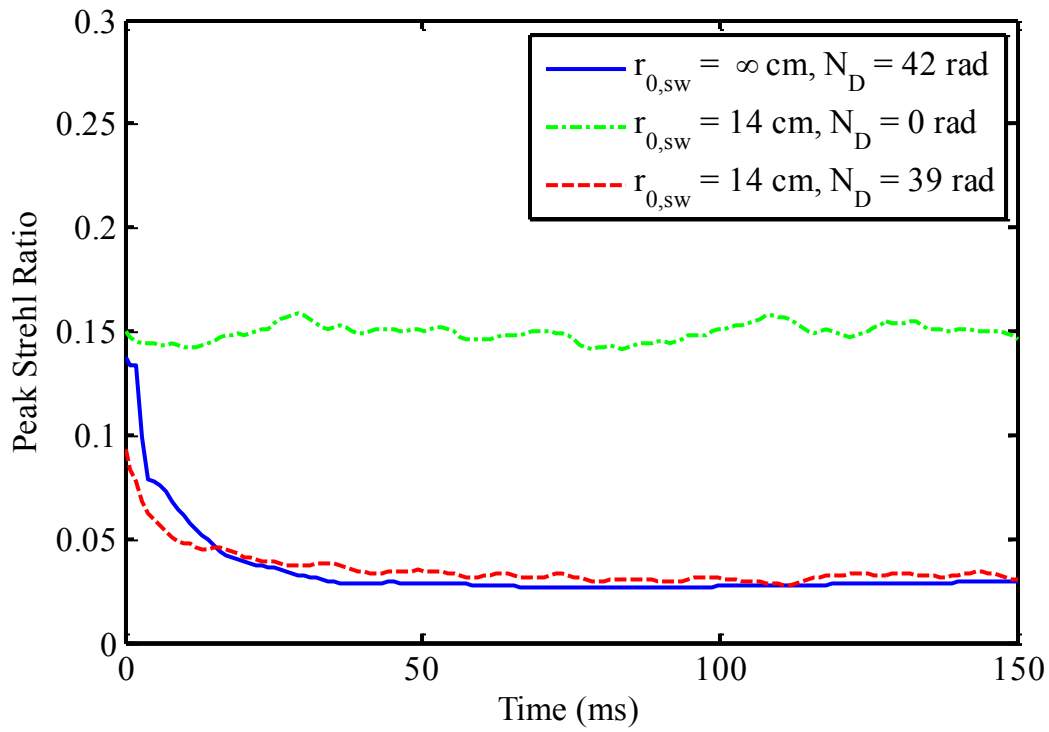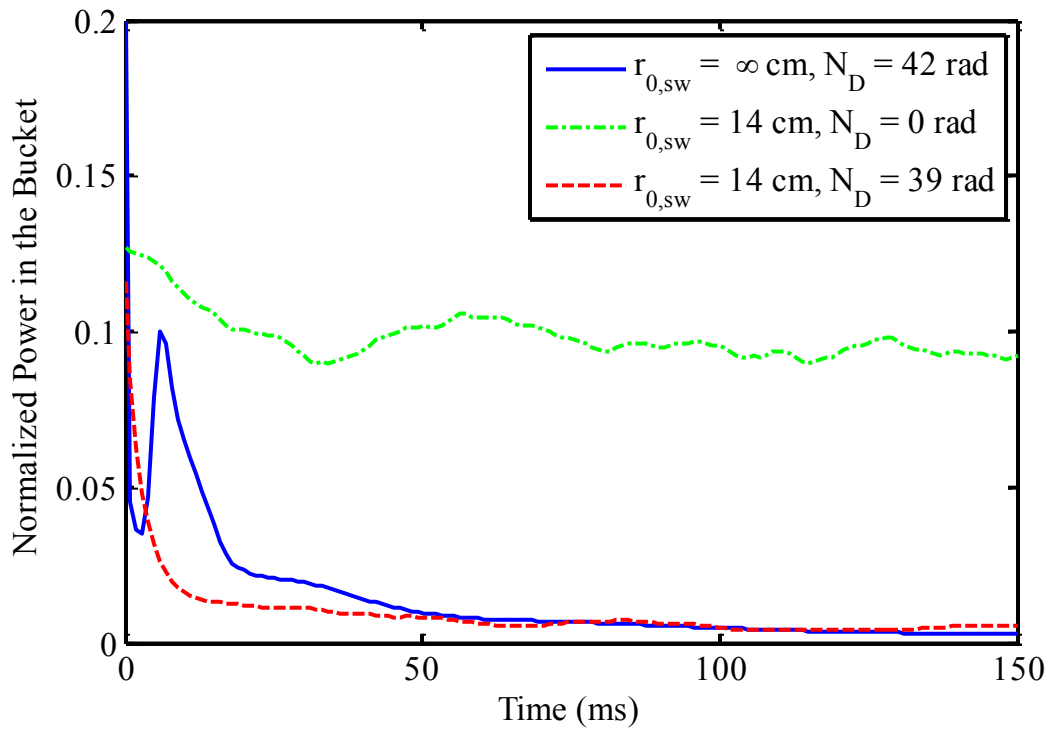
Figure 41. Comparison study for HEL beam propagation with time-dependent thermal blooming and the average of 25 independent realizations of optical turbulence using a.) peak Strehl ratio versus time and b.) normalized power in the bucket versus time.

3.2.6 Ab Initio Phase Compensation

In the ground breaking research conducted by MIT Lincoln Laboratories (MIT-LL), different regimes of phase compensation were experimented with to mitigate the effects of thermal blooming [90,106,103]. This point was referenced above in the analysis of PCI. The computational wave-optics experiment proposed here follows the experimental foundation provided by MIT-LL. Thus, the first regime of phase compensation used in this analysis is referred to as *ab initio* phase compensation. The term, a*b initio*, is Latin in origin and is translated to mean: ―from the beginning.‖ As such, with *ab initio* phase compensation, the AO system is used to compensate the HEL beam from the beginning. Put another way, the HEL beam and AO system are turned on at the same time. In the *ab initio* regime of phase compensation, the AO system is able to sense and correct for the effects of thermal blooming as they develop in the atmosphere.

As a first order of business in the analysis presented here, it was important to verify that the ―middle of the road‖ AO system parameters, $n_{sub} = 16$ and $n_{lod} = 8\,\lambda$, as given in Table 3, were capable of correcting for the refraction effects of optical turbulence. For this purpose, normalized irradiance time stamps are given in Figure 42. These results correspond to one independent realization of optical turbulence with a simulated spherical wave coherence length, $r_{0,sw} = 13.6$ cm. No thermal blooming was simulated in for the results shown in Figure 42. As discussed above in the experimental setup, the nominal goal for the wave-optics experiments was to simulate atmospheric conditions with a ―moderate‖ optical turbulence strength.

The results show the characteristic behavior associated with a properly working AO system. As shown in Figure 42, the normalized HEL beam irradiance is consistently

173

found to reside within the diffraction limited bucket diameter, $D_B = 1.3$ cm, for multiple time stamps. Small deviations from the bucket diameter are associated with the relatively high servo gain, $b = 0.5$, used for the FSM. Nonetheless, the AO system parameters used in this particular computational wave-optics experiment were more than adequate in performing phase compensation for "moderate" optical turbulence.
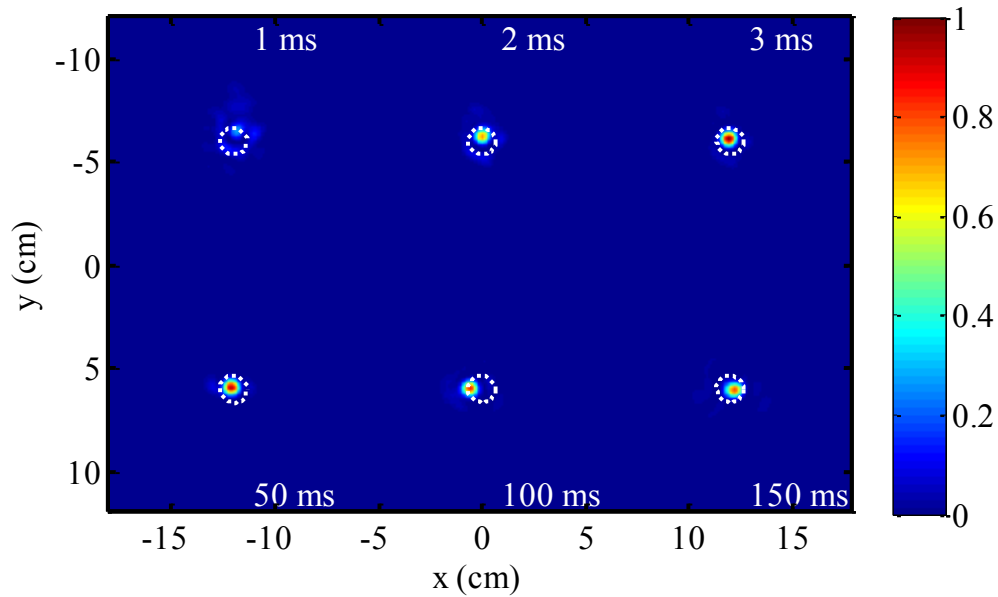
Figure 42. Normalized HEL beam irradiance with ab initio phase compensation of one realization of optical turbulence with a spherical coherence diameter, $r_{0,sw}$=13.6 cm. The simulation runs from 1 ms to 150 ms. The white circles represents the diffraction limited bucket diameter for the simulations, D_B=1.3 cm.

This last point is further supported with the results provided in Figure 43 and Figure 44. Here, peak Strehl ratio S_P and normalized power in the bucket P_B calculations in the target plane versus time are given in addition to the root mean square (RMS) r_{DM} of the DM commands and the variance σ^2_{DM} of the DM commands as a function of time. These results were averaged for 25 independent realizations of optical

174

turbulence. In Figure 43, the calculated peak Strehl ratio S_P and normalized power in the

bucket P_B in the target plane are consistently above 0.8 for the simulated time period—

system performance was definitely not an issue. Furthermore, the RMS r_{DM} of the DM

commands and the variance σ^2_{DM} of the DM commands settled down as time progressed,

as shown in Figure 44. This was a good sign in terms of characterizing system stability.

No exponential behavior was witnessed.
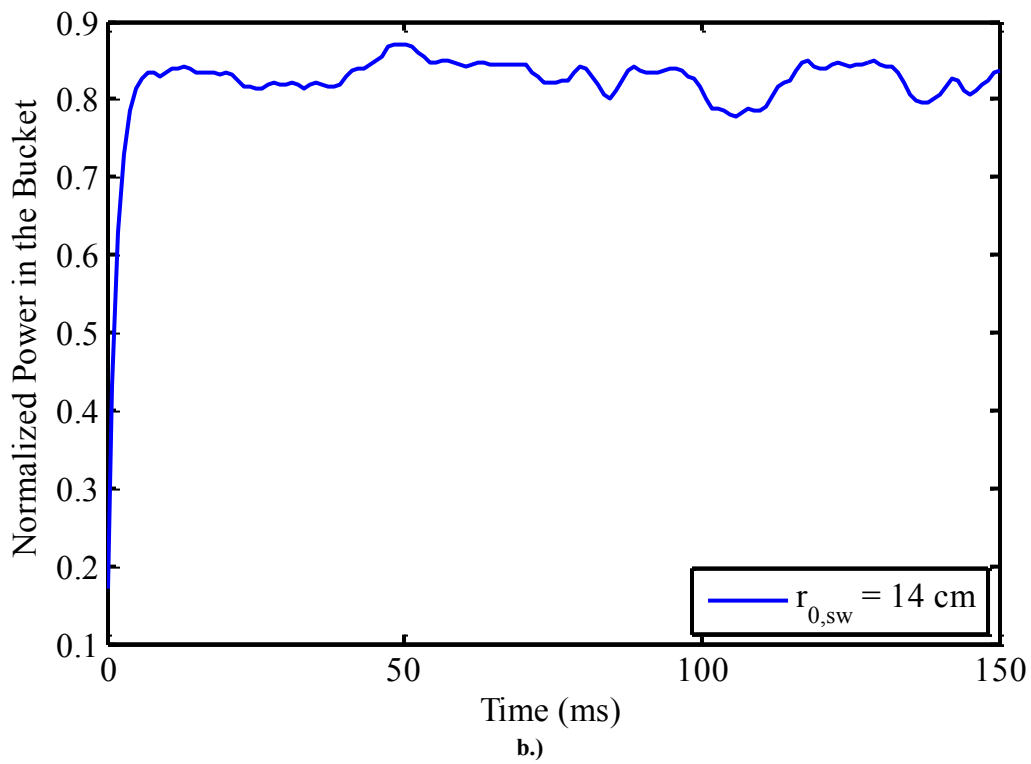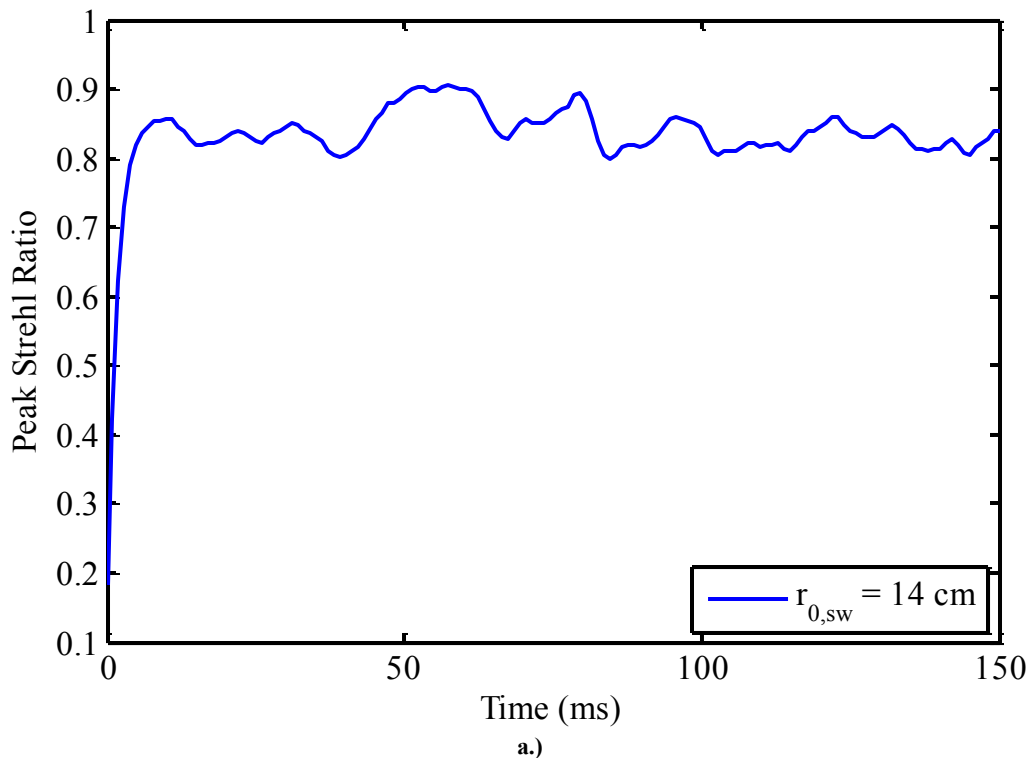
Figure 43. Ab initio phase compensation study with the average of 25 independent realizations of optical turbulence using a.) peak Strehl ratio versus time and b.) normalized power in the bucket versus time.
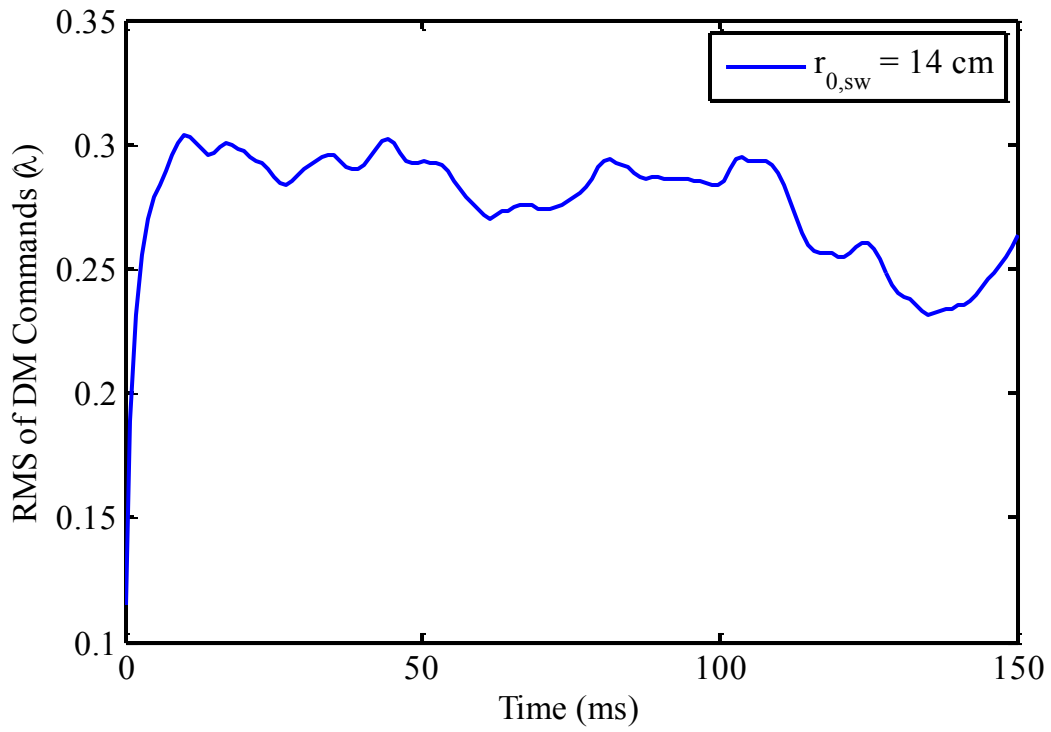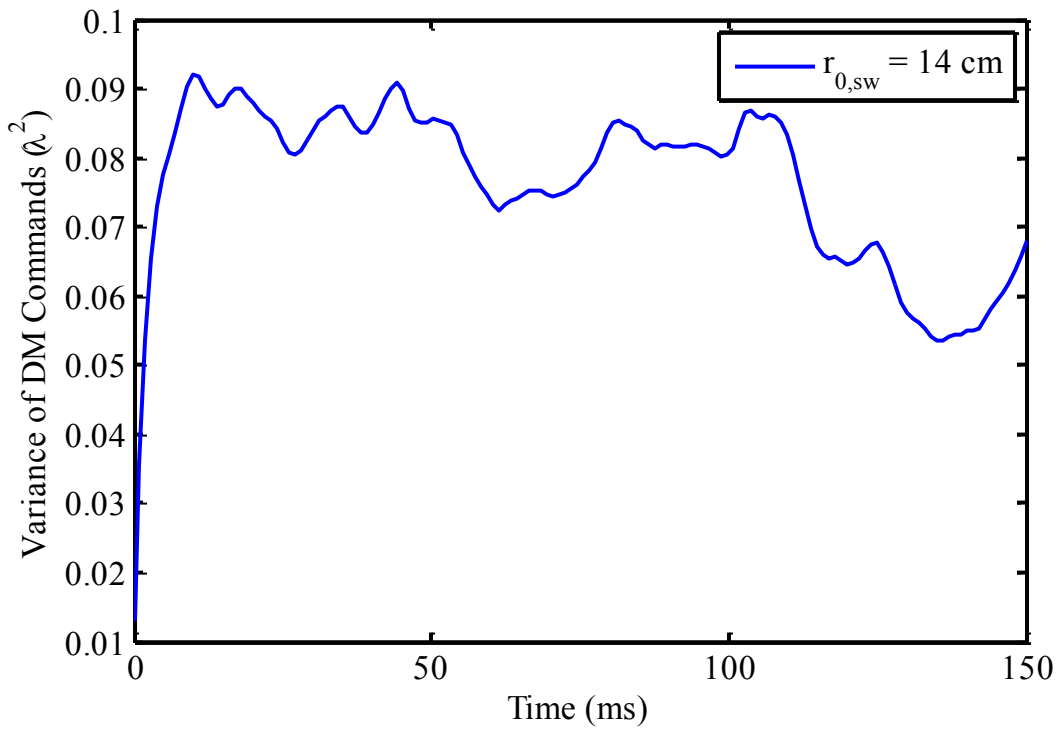
Figure 44. Ab initio phase compensation study with the average of 25 independent realizations of optical turbulence using a.) RMS of DM commands versus time and b.) variance of DM commands versus time.

The next step in the analysis was to perform *ab initio* phase compensation for

time-dependent thermal blooming. As such, normalized irradiance time stamps are given

in Figure 45 and Figure 46 for a simulated distortion number just below the critical point,

$N_D = 16.8$ rad, and a distortion number well above the critical point, $N_D = 42.0$ rad,

respectively No turbulence was simulated in these particular studies. The "middle of the

road" AO system parameters, $n_{sub} = 16$ and $n_{lod} = 8\lambda$, as given in Table 3 were also used

to create these phase compensation results. As shown in in Figure 45, the characteristic

crescent pattern associated with "moderate" thermal blooming, $N_D = 16.8$ rad, is

minified with *ab initio* phase compensation. This is said because the crescent pattern is

successfully confined to the diffraction limited bucket diameter, $D_B = 1.3$ cm. It should

be noted that some of the energy is scattered out into a wing like pattern; however,

system performance for the most part is stable and consistent. No signs of PCI were

witnessed.

The *ab initio* phase compensation results obtained for "strong" thermal blooming,

$N_D = 42.0$ rad, are shown in Figure 46. When compared to the results shown in Figure

45, the AO system struggles a lot more to obtain system performance and stability. This

comment is made based on the fact that the wing-like pattern due to scattering is more

defined in Figure 46. As time progresses, the characteristic crescent pattern is again

confined to the diffraction limited bucket diameter, $D_B = 1.3$ cm; however, upon closer

inspection, it was noticed that the peak irradiance of the confined crescent pattern seemed

to oscillate around a mean value. Further analysis was needed to discern the validity of

this claim. It should be noted; nonetheless, that there were still no apparent signs of PCI.
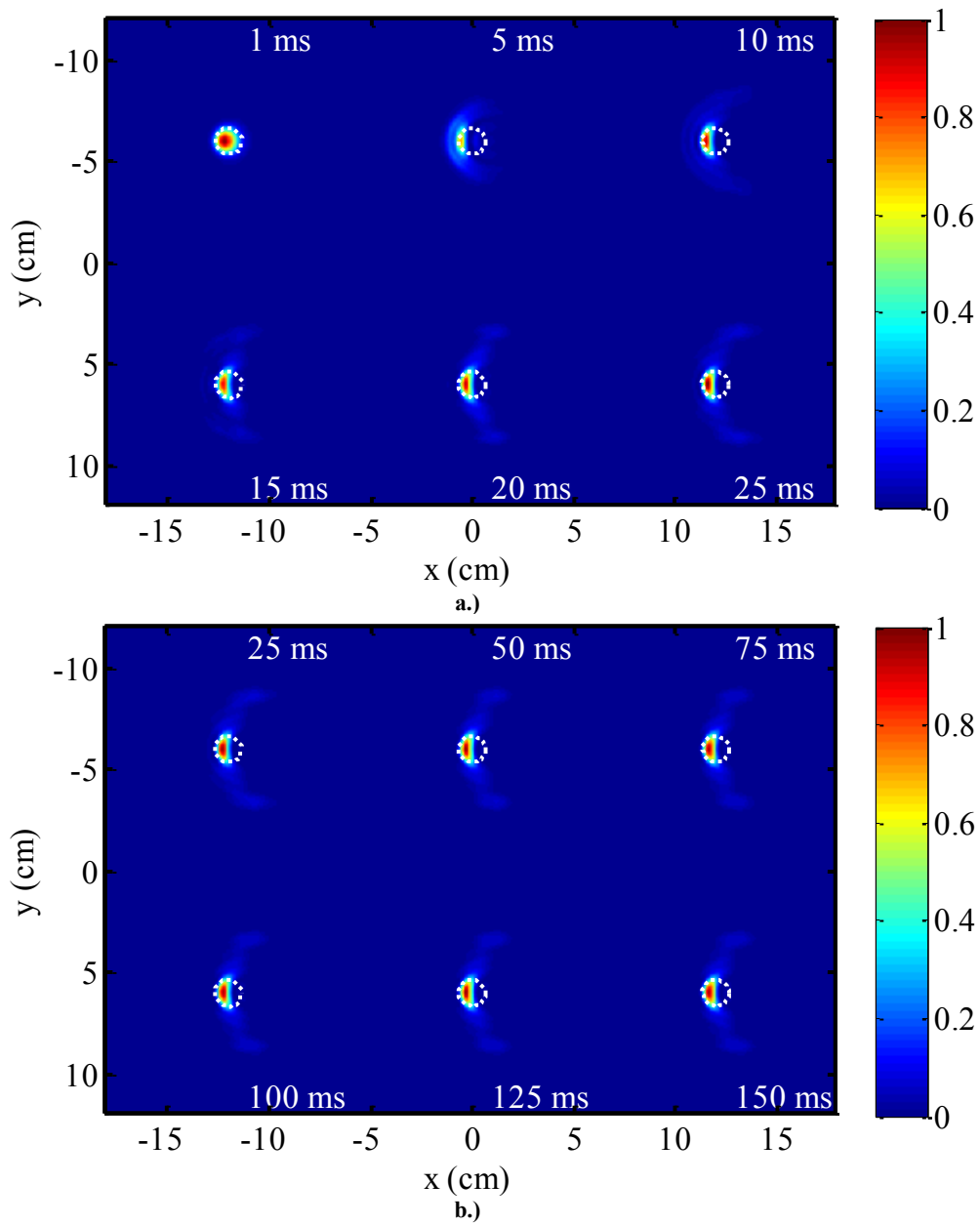
Figure 45. Normalized HEL beam irradiance with ab initio phase compensation of time-dependent thermal blooming for a distortion number, N_D=16.8 rad. In a.) the simulation runs from 1 ms to 25 ms and in b.) the simulation runs from 25 ms to 150 ms. The white circles represents the diffraction limited bucket diameter for the simulations, D_B=1.3 cm.
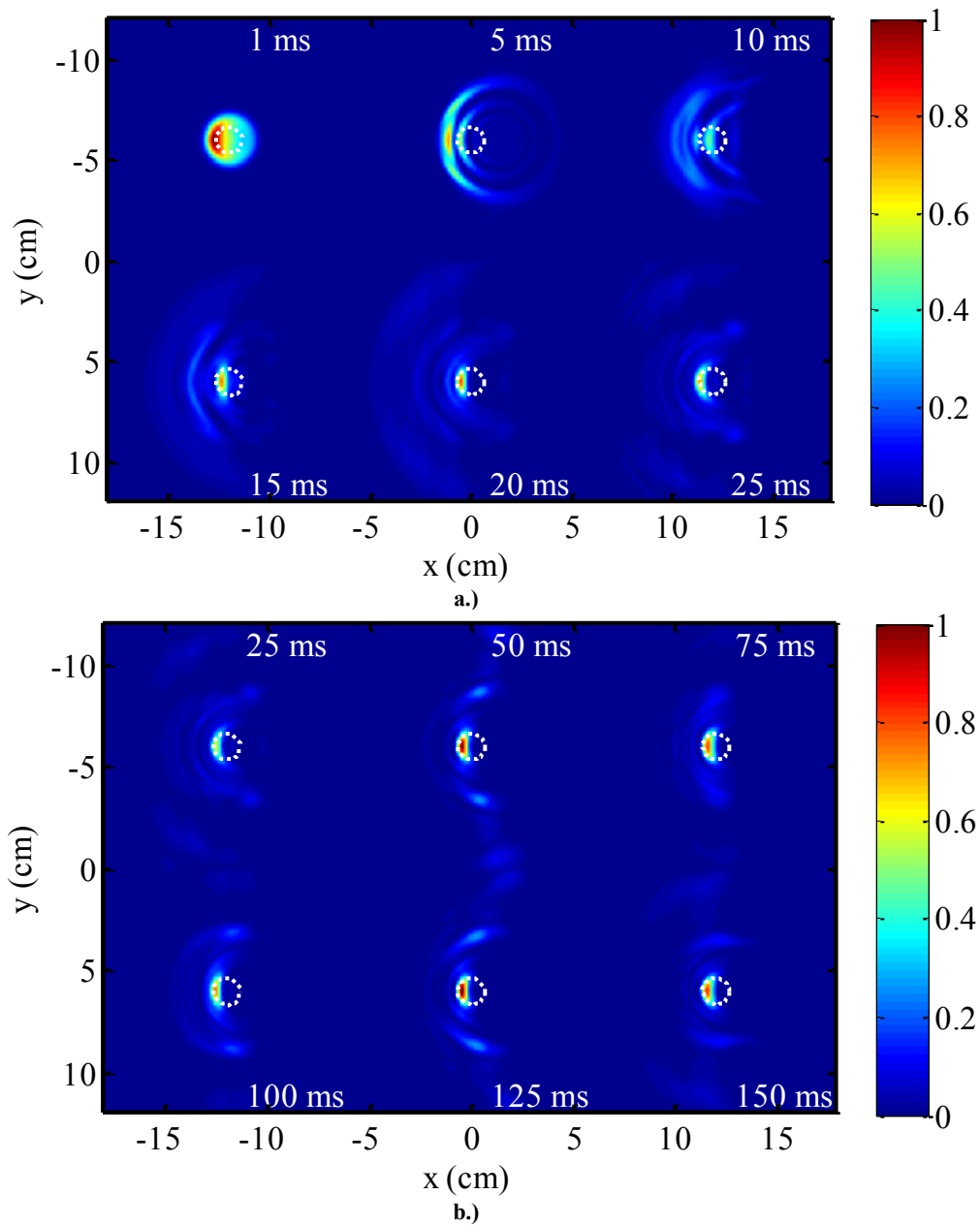
Figure 46. Normalized HEL beam irradiance with ab initio phase compensation of time-dependent thermal blooming for a distortion number, N_D=42.0 rad. In a.) the simulation runs from 1 ms to 25 ms and in b.) the simulation runs from 25 ms to 150 ms. The white circles represents the diffraction limited bucket diameter for the simulations, D_B=1.3 cm.

A comparison study for system performance was conducted next. As shown in Figure 47 and Figure 48, system performance and system stability were analyzed. Specifically, in Figure 47, peak Strehl ratio S_P and normalized power in the bucket P_B calculations in the target plane as a function of time were compared for the same data and simulated distortion numbers, $N_D = 16.8 \text{ rad}$ and $N_D = 42.0 \text{ rad}$, as used to create the normalized irradiance time stamps in Figure 45 and Figure 46. The results show definite improvements in system performance. This claim is made based on comparisons with Figure 33 and or Figure 34, where no phase compensation was applied to the same time dependent thermal blooming conditions.

In the "moderate" thermal blooming regime corresponding to a simulated distortion number, $N_D = 16.8 \text{ rad}$, just below the critical point, the system performance measurements showed signs of excellent system stability. This is said based on the fact that both the peak Strehl ratio S_P and normalized power in the bucket P_B calculations in the target plane as a function of time reached a steady-state equilibrium. However, in the "strong" thermal blooming regime corresponding to a simulated distortion number, $N_D = 42.0 \text{ rad}$, well above the critical point, the system performance measurements showed signs of inconsistent system performance. This is said based on the observation of what looks like periodic oscillations in the system performance measurements. These periodic oscillations seemed to be deterministic in nature, as they oscillated around a mean steady-state value. The fact that a steady-state mean value was eventually achieved demonstrated that incipient PCI was not met in this particular computational wave-optics experiment.

The same periodic oscillations were also witnessed in the root mean square (RMS) r_{DM} of the DM commands and the variance σ^2_{DM} of the DM commands as a function of time. As shown in Figure 48, system stability was achieved in both cases. This is said because the RMS r_{DM} of the DM commands and the variance σ^2_{DM} of the DM commands eventually settled down as time progressed. For both simulated distortion numbers, $N_D = 16.8$ rad and $N_D = 42.0$ rad, exponential behavior was witnessed early on in the computational wave-optics experiment. This was almost expected in the analysis given the nature of the problem. Positive feedback results from phase compensation of thermal blooming. The fact that the system measurements eventually settled down demonstrated the fact the positive feedback was unsuccessful in creating the runaway behavior associated with the conditions for insipient PCI.
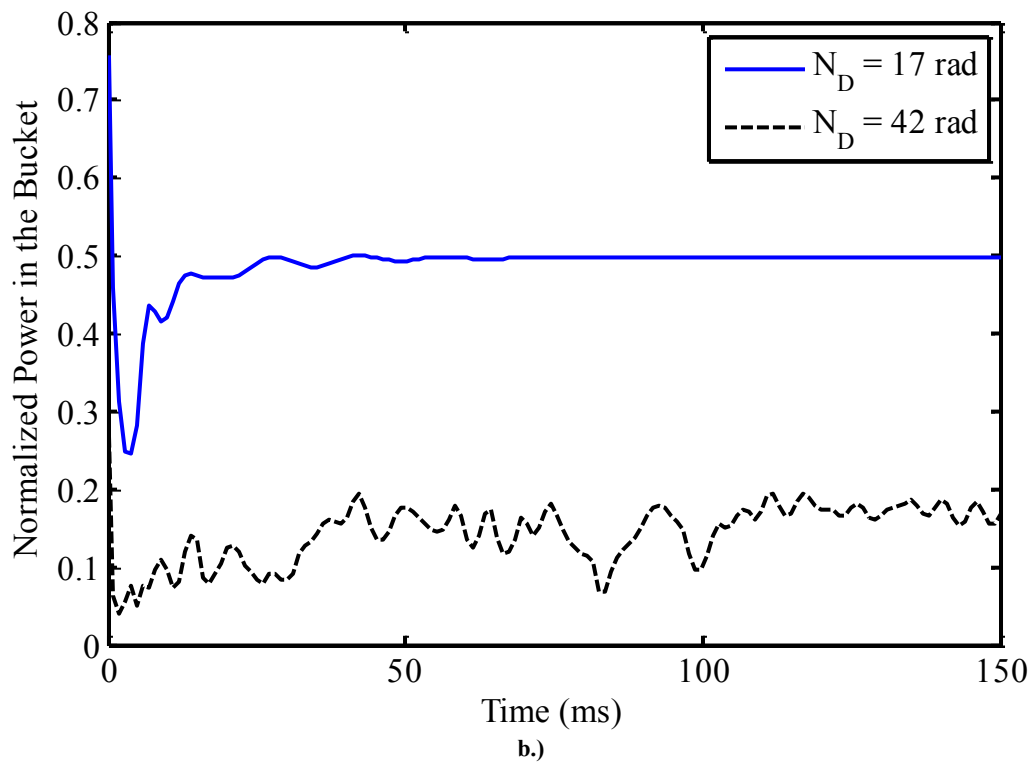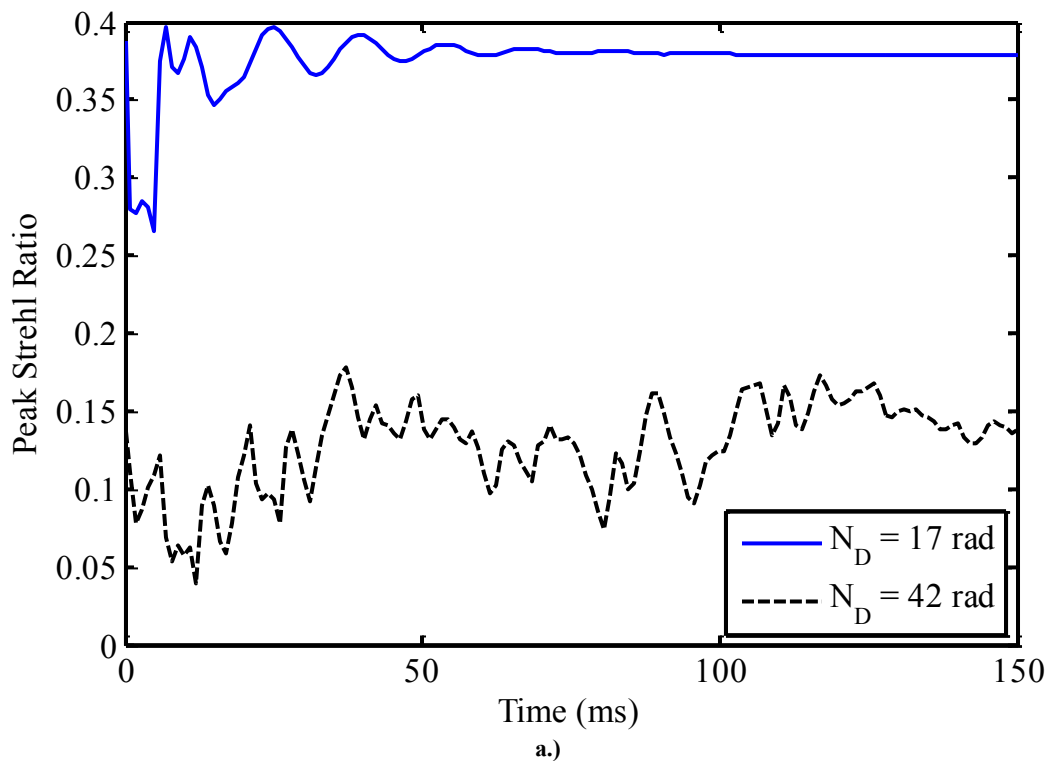
Figure 47. Comparison study for ab initio phase compensation of time-dependent thermal blooming using a.) peak Strehl ratio versus time and b.) normalized power in the bucket versus time.
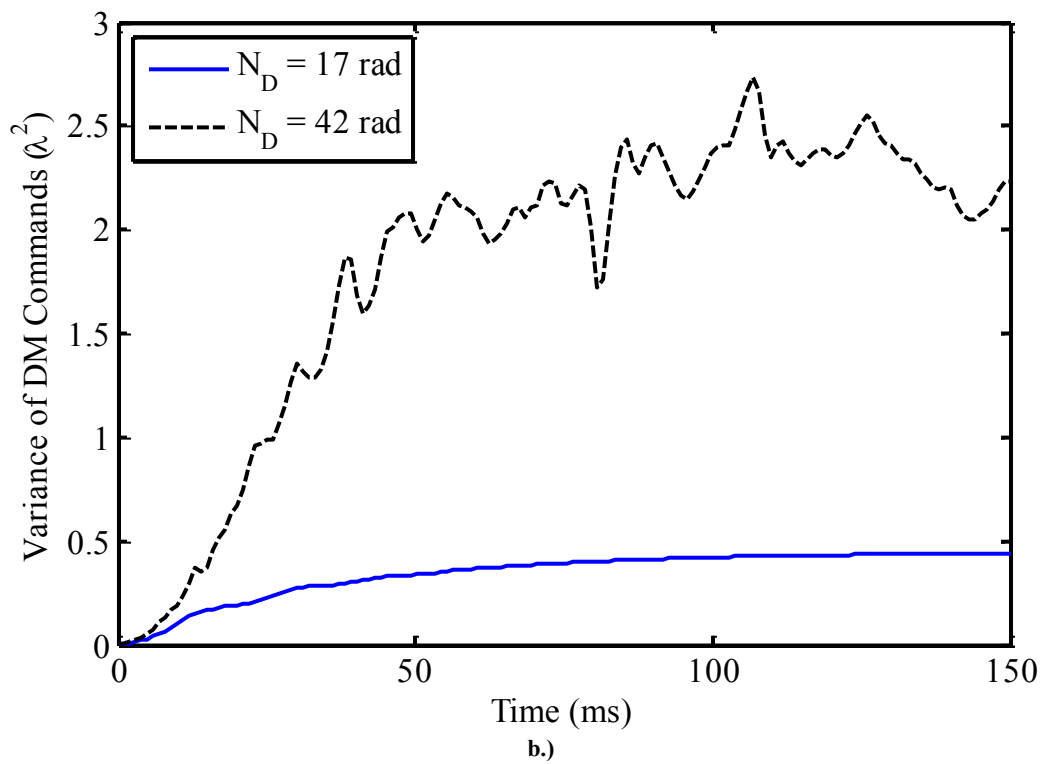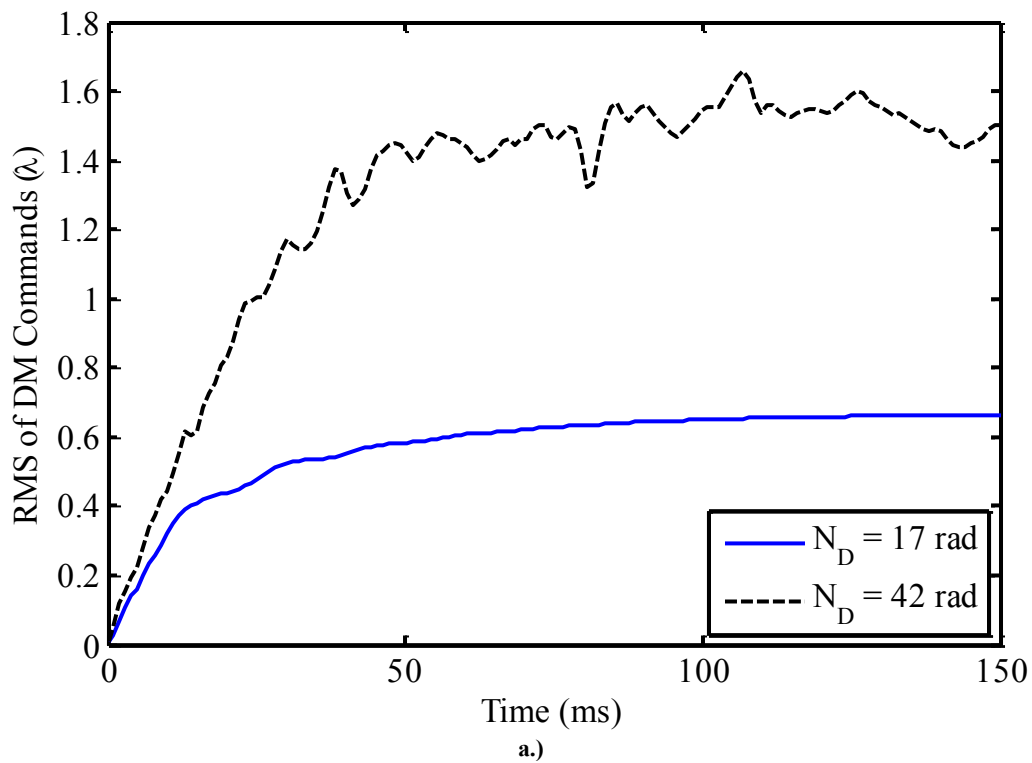
Figure 48. Comparison study for ab initio phase compensation of time-dependent thermal blooming using a.) RMS of DM commands versus time and b.) variance of DM commands versus time.

3.2.7 Deferred Phase Compensation

The second regime of phase compensation studied in the analysis is referred to as *deferred* phase compensation. With *deferred* phase compensation, the AO system is operated in a closed-loop configuration, but the AO control loop is not closed right away. This corresponds to the case where the AO system is operated in open loop; however, in the closed-loop configuration as described in Figure 11. Simply put, in the *deferred* phase compensation regime, the AO control loop remains open for a user-defined amount of time.

The computational wave-optics experiment proposed here, simulates the case where the AO system is allowed to run in open loop until steady-state thermal blooming conditions are achieved. While in open loop operation, both the DM and the FSM are commanded to flat. Thus, the WFS and tracker are able to sense the effects of time-dependent thermal blooming; however, no phase compensation is applied until steady-state thermal blooming conditions are achieved. In WaveProp, the proposed *deferred* regime of phase compensation is particularly easy to simulate. This is said because steady-state thermal blooming conditions are readily achieved by seeding the computational wave-optics experiment with steady-state thermal blooming conditions from the algorithm proposed in Eq. (87). From here, the computational wave-optics experiment proceeds with the phase compensation of time-dependent steady-state thermal blooming as determined by the algorithm proposed in Eq. (82). This process was effectively tested in creating the time-dependent steady-state thermal blooming results found in Figure 33, $SS = 1$.

185

It should be noted that the *deferred* regime of phase compensation was originally proposed by MIT-LL [90,106,103]. The experimental results published by MIT-LL claimed that the level of thermal blooming in the atmosphere had a significant impact on the conditions for insipient PCI. Specifically, the results published by MIT-LL showed that the *deferred* phase compensation always outperformed the *ab initio* phase compensation. To explain the results, it was conjectured by MIT-LL that if the AO system was given the opportunity to sense and correct for the small-scale perturbations in the irradiance and or phase as they developed from time-dependent thermal blooming (such is the case with *ab initio* phase compensation), then the conditions for incipient PCI were met a lot sooner in the analysis. This conjecture was grounded with the micro-scale interpretation of PCI developed by the linearized theory produced by LLNL and discussed above.

With this in mind, the results for the *deferred* phase compensation of time-dependent steady-state thermal blooming are given in Figure 49-Figure 52. For all intents and purposes, the results showed the same exact trends as those for *ab initio* phase compensation, despite the results published by MIT-LL. The high points worth mentioning here are as follows.

- Normalized irradiance time stamps are given in Figure 49 and Figure 50 for a simulated distortion number just below the critical point, $N_D = 16.8 \text{ rad}$, and a distortion number well above the critical point, $N_D = 42.0 \text{ rad}$, respectively.

- As shown in Figure 49 and Figure 50, the characteristic crescent pattern associated with steady-state thermal blooming are provided in the first time stamp.

- With *deferred* phase compensation, the characteristic crescent pattern was again confined to the diffraction limited bucket diameter, $D_B = 1.3$ cm, as time progressed.

- In Figure 51, peak Strehl ratio S_P and normalized power in the bucket P_B calculations in the target plane as a function of time were compared for the same data and simulated distortion numbers, $N_D = 16.8$ rad and $N_D = 42.0$ rad, and the results again show definite improvements in system performance.

- For the distortion number above the critical point, $N_D = 42.0$ rad, periodic oscillations in the system performance measurements were observed.

- The same periodic oscillations were also witnessed in the root mean square (RMS) r_{DM} of the DM commands and variance σ_{DM}^2 of the DM commands as a function of time, as shown in Figure 52.
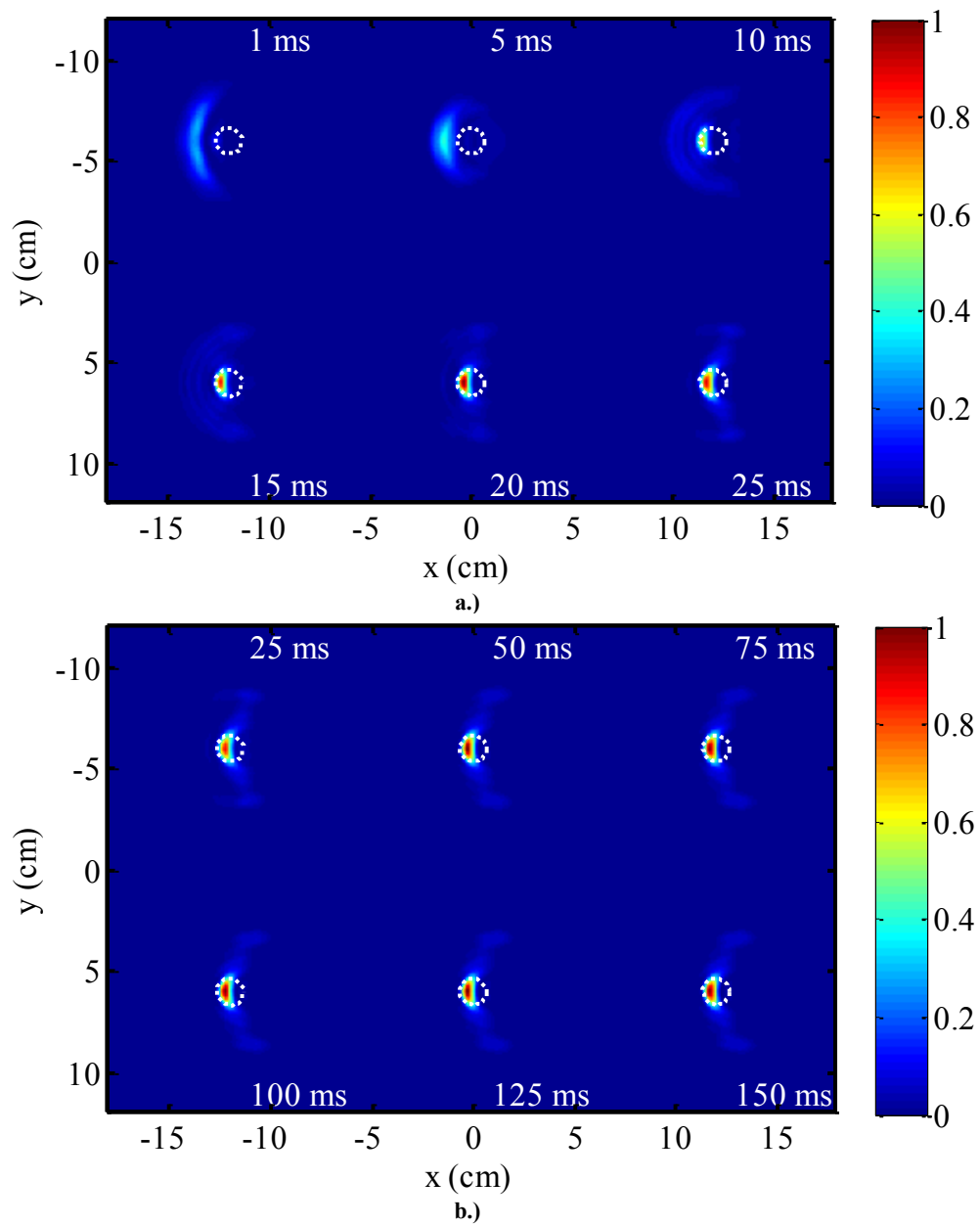
Figure 49. Normalized HEL beam irradiance with deferred phase compensation of time-dependent thermal blooming for a distortion number, N_D=16.8 rad. In a.) the simulation runs from 1 ms to 25 ms and in b.) the simulation runs from 25 ms to 150 ms. The white circles represents the diffraction limited bucket diameter for the simulations, D_B=1.3 cm
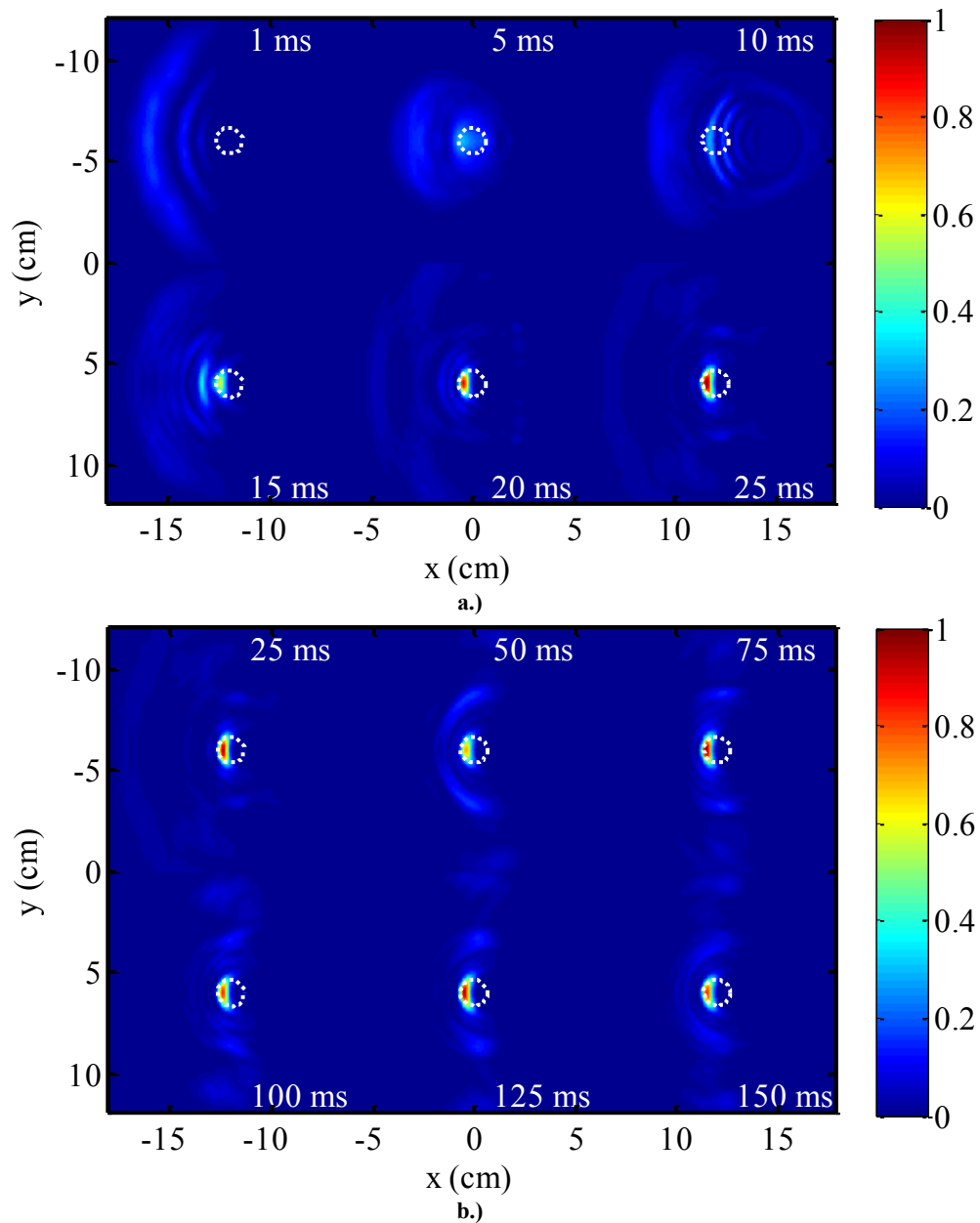
Figure 50. Normalized HEL beam irradiance with deferred phase compensation of time-dependent thermal blooming for a distortion number, N_D=42.0 rad. In a.) the simulation runs from 1 ms to 25 ms and in b.) the simulation runs from 25 ms to 150 ms. The white circles represents the diffraction limited bucket diameter for the simulations, D_B=1.3 cm
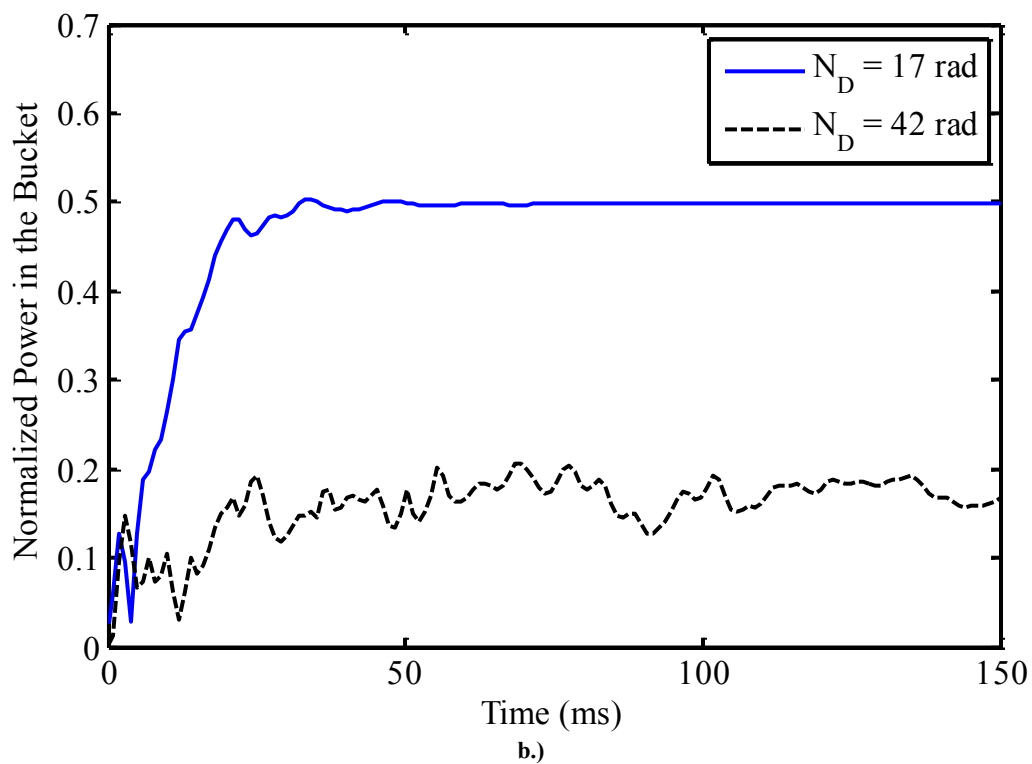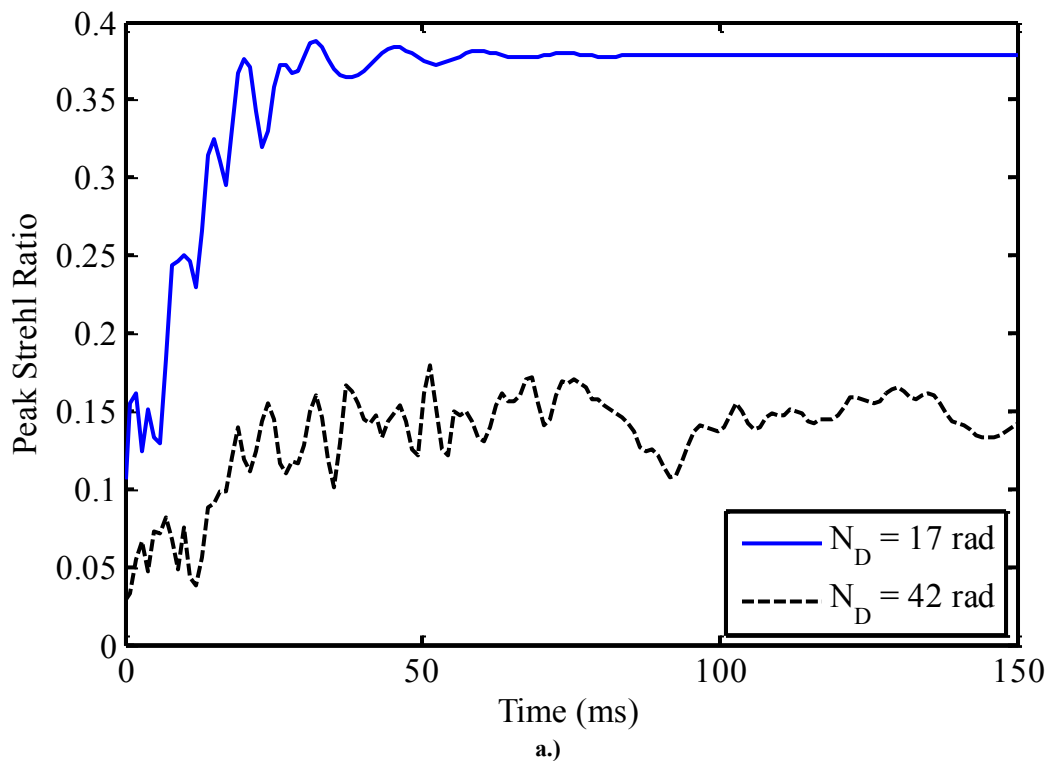
Figure 51. Comparison study for deferred phase compensation with time-dependent thermal blooming using a.) peak Strehl ratio versus time and b.) normalized power in the bucket versus time.
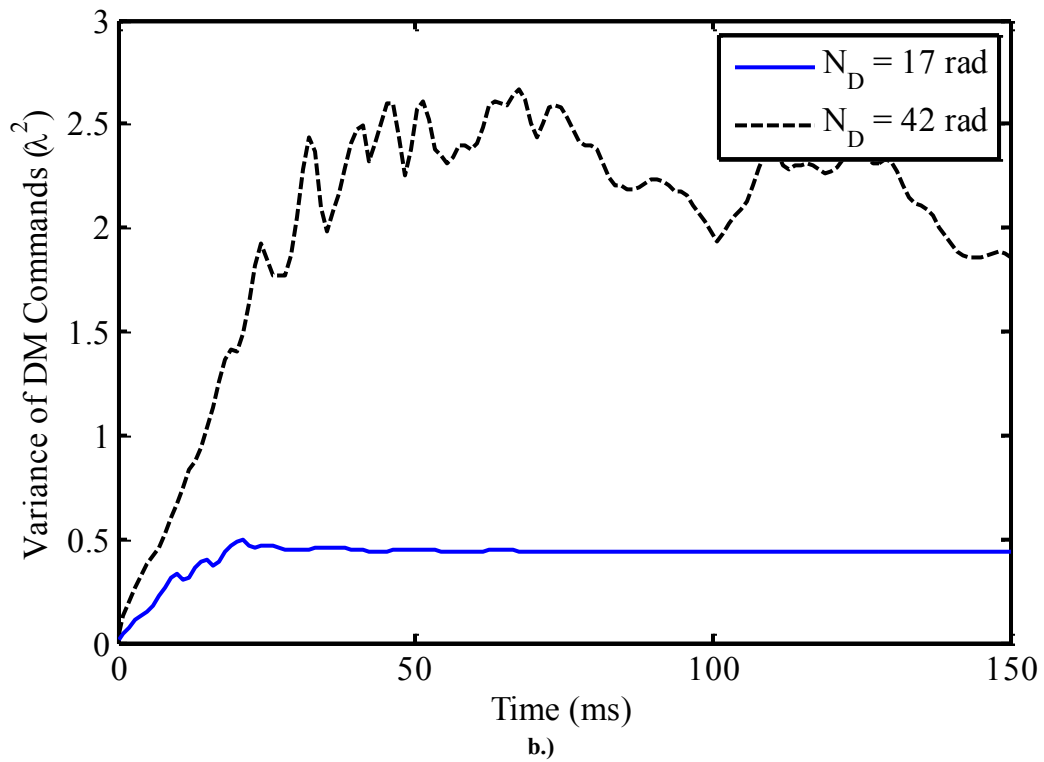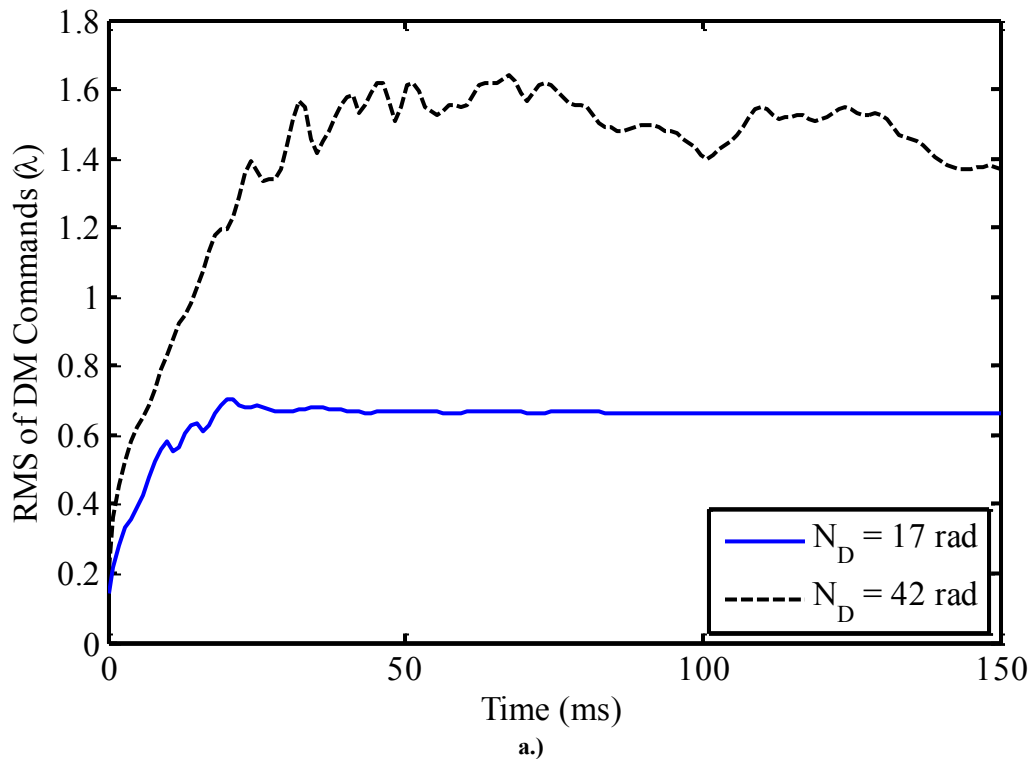
Figure 52. Comparison study for deferred phase compensation of time-dependent thermal blooming using a.) RMS of DM commands versus time and b.) variance of DM commands versus time.

3.2.8 Open-Loop Ab Initio Phase Compensation of Thermal Blooming

To continue the analysis, results are presented which support the micro-scale interpretation of PCI. They also support the fact that computational wave-optics experiments are a good vehicle in which to study the conditions for insipient PCI. With this said, the computational wave-optics experiment conducted here explored the possibility for insipient PCI with an adaptive optics system operating in the open loop regime. The experimental setup is essentially demonstrated above in Figure 10.

The open-loop phase compensation simulated here, directly measured the incoming point-source beacon with the WFS and tracker. It is important to note that the DM and FSM were essentially bypassed with the point source beacon. Next, the measurements from the WFS and tracker were then blindly used to control the DM and FSM with the same AO control parameters described above in Figure 26. With this experimental design, no feedback was simulated for the phase compensation of the outgoing HEL beam. Thus, the simulated AO system essentially had a tremendous amount of servo gain.

The results for open-loop *ab initio* phase compensation of time-dependent thermal blooming are given in Figure 53 and Figure 54. Here, normalized irradiance time-stamps are given. The lowest distortion number, $N_D = 8.39$ rad, as given in Table 2 was simulated here to obtain the results. For all intents and purposes, the results demonstrate all of the symptoms associated with the micro-scale interpretation of PCI. This is said because with a high servo gain, the conditions for runaway in the adaptive optics control loop are met. As shown in Figure 53 in terms of normalized irradiance time stamps, the positive feedback caused by the open-loop phase compensation of thermal blooming

192

essentially causes the HEL beam to break apart into smaller and smaller spatial

perturbations. Eventually, the spatial perturbations wander off the edge of the grid and

cause aliasing; however, there is a significant decrease in peak irradiance beforehand.
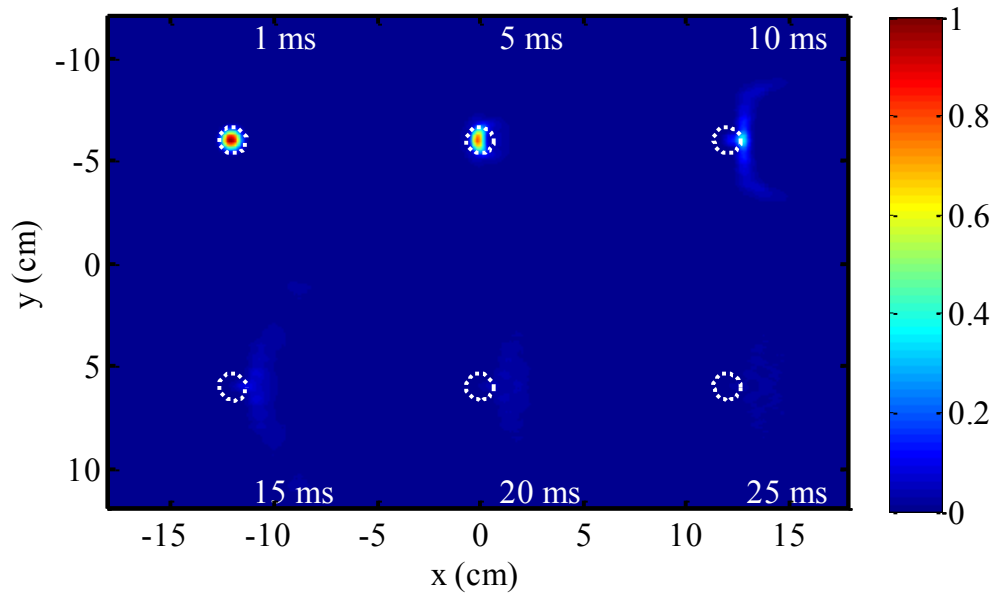
Figure 53. Normalized HEL beam irradiance with open-loop ab initio phase compensation of time-dependent thermal blooming for a distortion number, N_D=8.39 rad. The simulation runs from 1 ms to 25 ms. The white circles represents the diffraction limited bucket diameter for the simulations, D_B=1.3 cm

The idea associated with small-scale perturbation growth is better demonstrated in

Figure 54. Here, normalized irradiance is given for the 25 ms time stamp. Based on the

micro-scale interpretation of PCI, the result makes sense. This is said because the

positive feedback in the AO control loop essentially causes the HEL beam to break up

into a bunch of small scale spatial perturbations. These spatial perturbations grow in time

and with propagation.
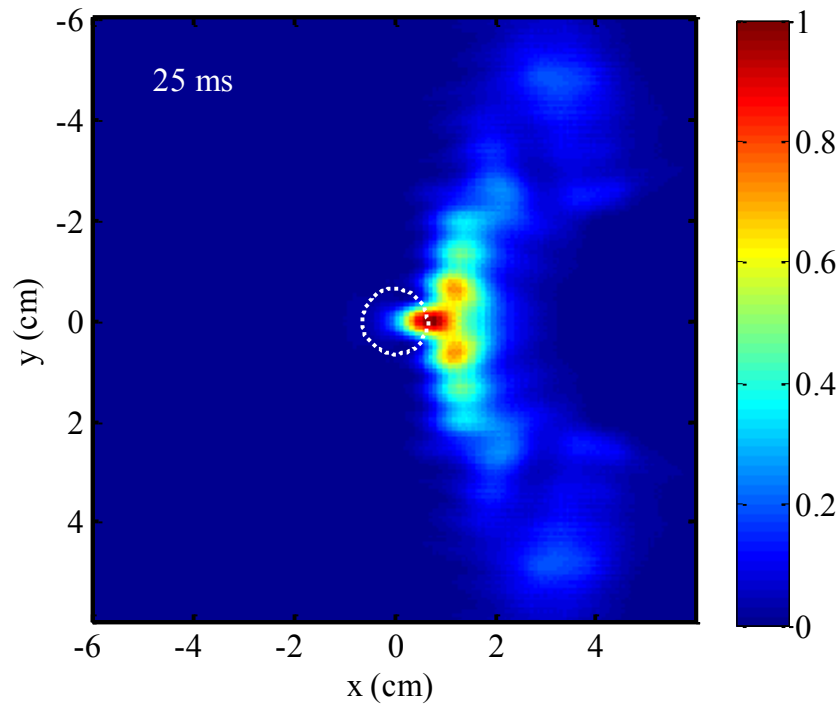
Figure 54. Simulation time stamp, t=25 ms, for normalized HEL beam irradiance with open-loop ab initio phase compensation of time-dependent thermal blooming and a distortion number, N_D=8.39 rad. The white circle represents the diffraction limited bucket diameter for the simulation, D_B=1.3 cm.

System performance measurements also demonstrate signs of severe PCI. For example, as shown in Figure 55, both the peak Strehl ratio S_P and the normalized power in the bucket P_B calculations in the target plane versus time quickly degrade as time progresses. This is very indicative of the conditions for incipient PCI. System stability is also severely compromised. This is witnessed in Figure 56 with the RMS r_{DM} of the DM commands and the variance σ^2_{DM} of the DM commands as a function of time. Both stability measurement give raise to exponential behavior, a true indicator of instability.
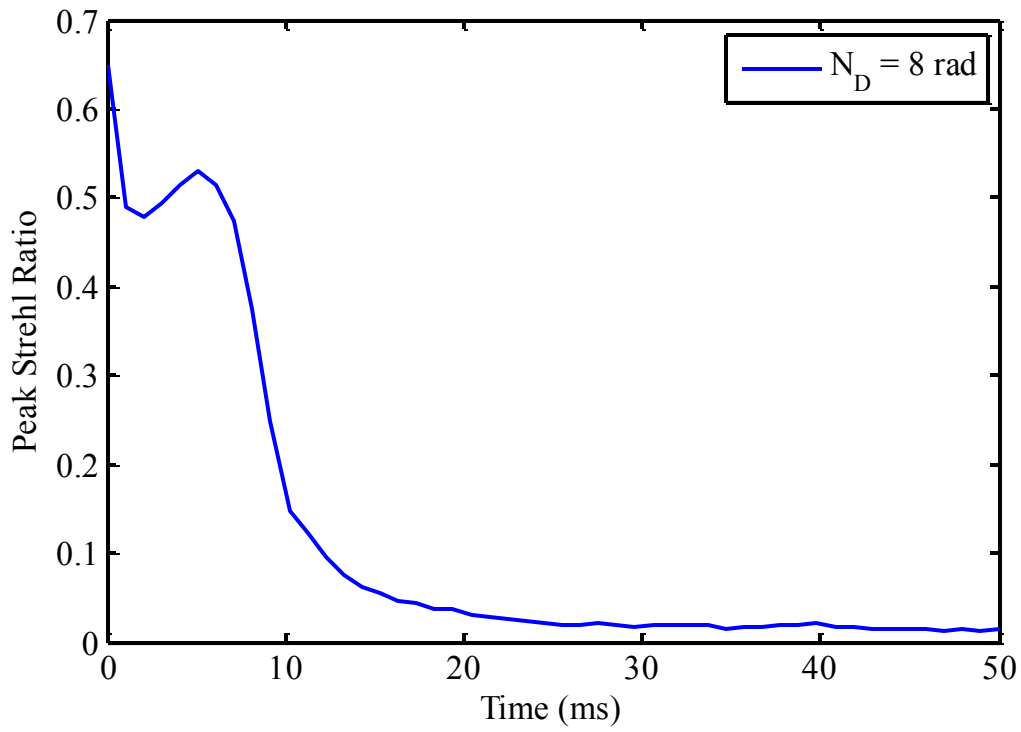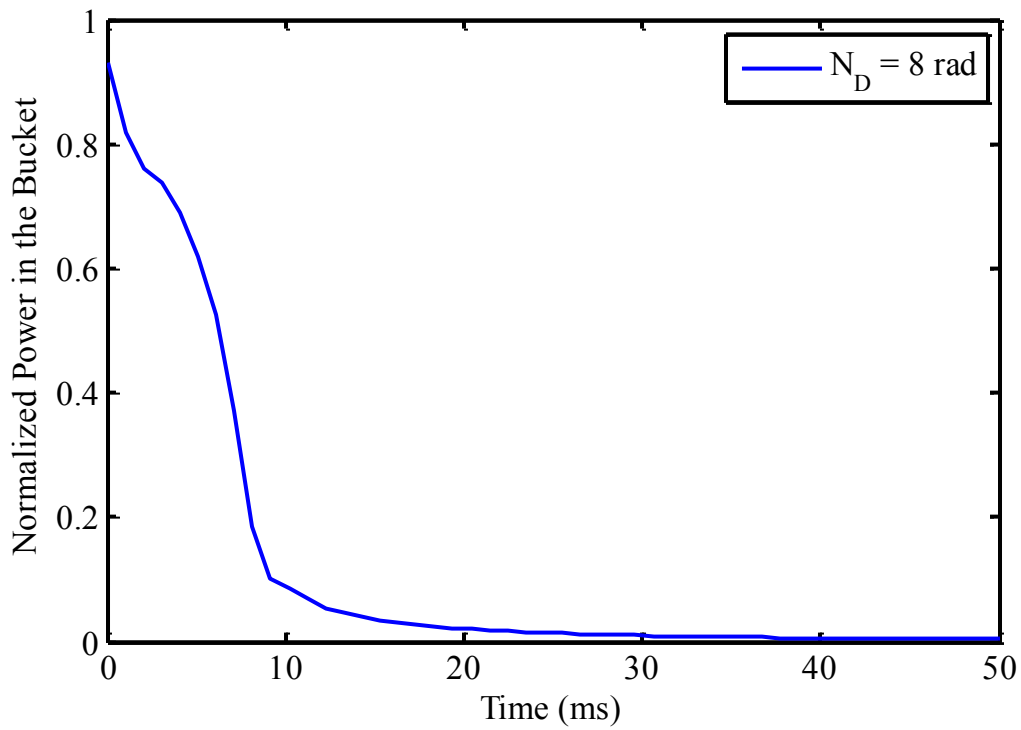
Figure 55. Instability study for open-loop ab initio phase compensation with time-dependent thermal blooming using a.) peak Strehl ratio versus time and b.) normalized power in the bucket versus time.
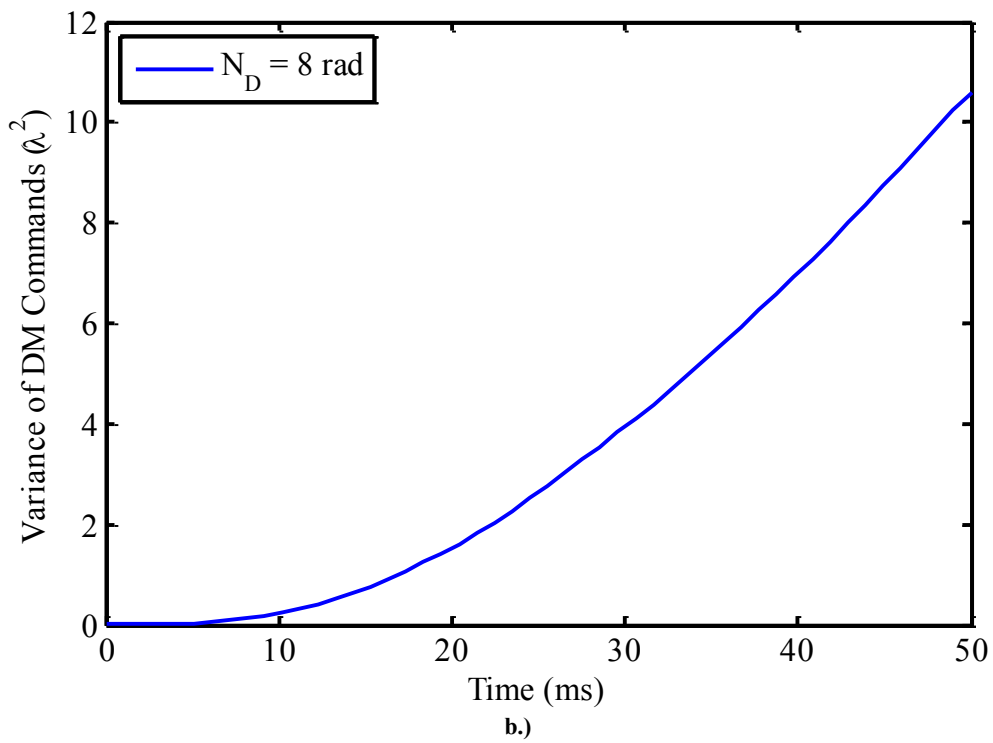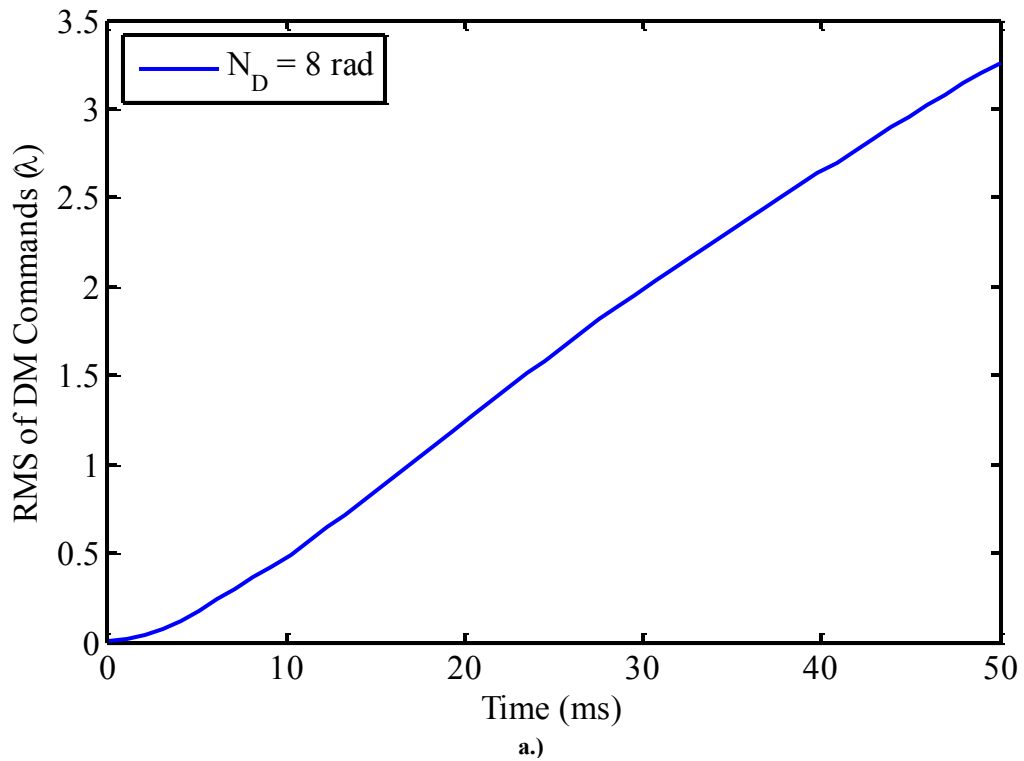
Figure 56. Instability study for open-loop ab initio phase compensation of time-dependent thermal blooming using a.) RMS of DM commands versus time and b.) variance of DM commands versus time.

3.2.9 Ab Initio Phase Compensation of Thermal Blooming and Turbulence

The results presented in this subsection are a culmination of the results presented throughout this entire chapter. With that said, normalized irradiance time stamps are given in Figure 57 for the *ab initio* phase compensation of time-dependent turbulent thermal blooming and one independent realization of optical turbulence. The distortion number, $N_D = 15.5$ rad, simulated here corresponds to one found just below the critical point. Note that the AO system struggles to perform phase compensation for both time-dependent turbulent thermal blooming and one realization of optical turbulence.

This statement is supported with the results presented in Figure 58. Here, peak Strehl ratio S_P and the normalized power in the bucket P_B calculations in the target plane versus time are provided for the average of 25 individual realizations of optical turbulence combined with time-dependent turbulent thermal blooming and or time-dependent thermal blooming. Note that the system measurements steadily ─fizzle" out as time progresses. The results are also compared to the results obtained for *ab initio* phase compensation of only time-dependent turbulent thermal blooming and or time-dependent thermal blooming. The results presented in Figure 59 correspond to system stability. Here, the RMS r_{DM} of the DM commands and the variance σ^2_{DM} of the DM commands as a function of time were plotted for the same simulation conditions as previously stated. No further insight is added, as there are no apparent signs of instability in the turbulence/thermal blooming results.
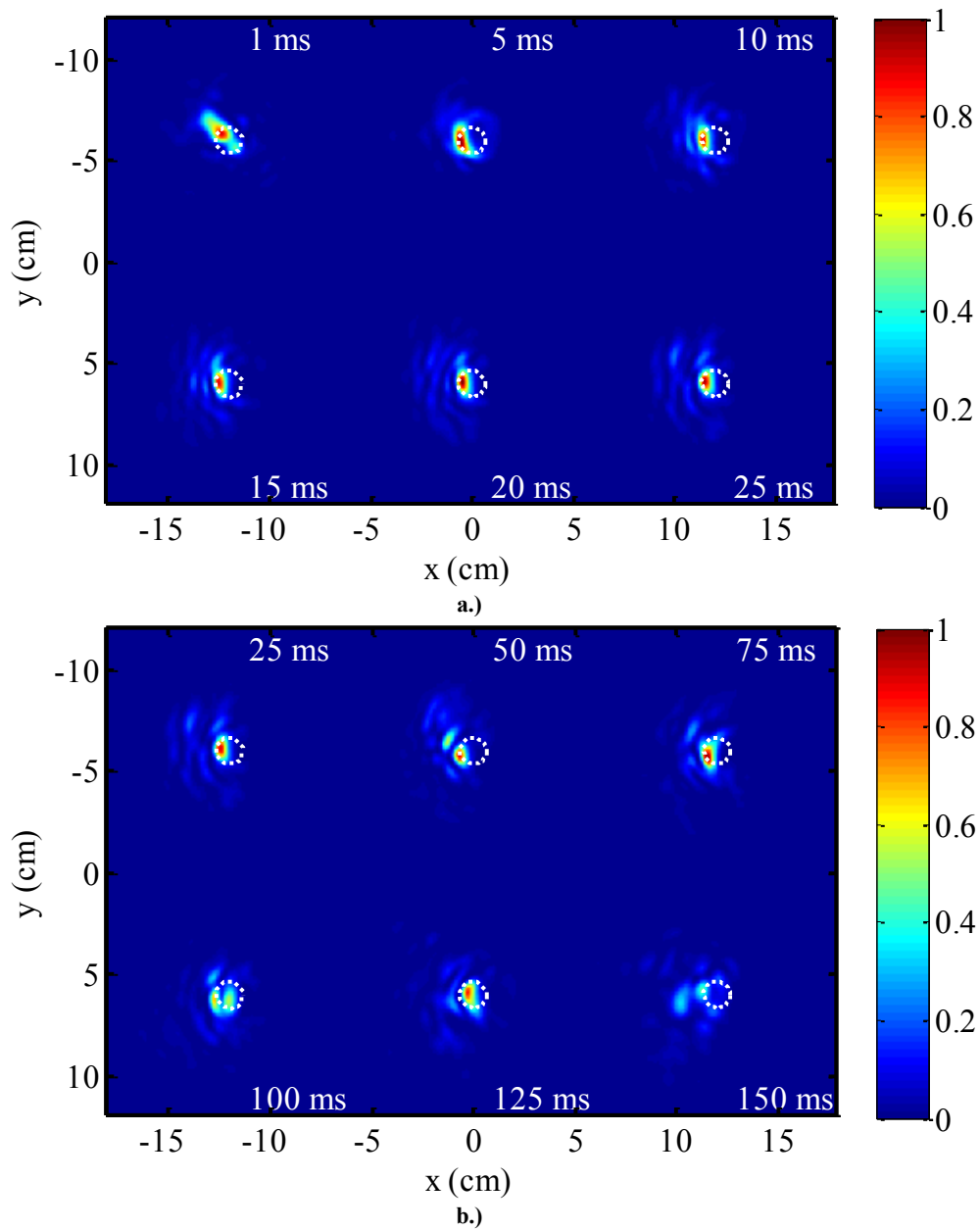
Figure 57. Normalized HEL beam irradiance with ab initio phase compensation of time-dependent turbulent thermal blooming and one realization of optical turbulence for a distortion number, N_D=15.5 rad, a wind velocity standard deviation, σ_v=1.8 m/s, and a spherical coherence diameter, $r_{0,sw}$=13.6 cm. In a.) the simulation runs from 1 ms to 25 ms and in b.) the simulation runs from 25 ms to 150 ms. The white circles represents the diffraction limited bucket diameter for the simulations, D_B=1.3 cm.
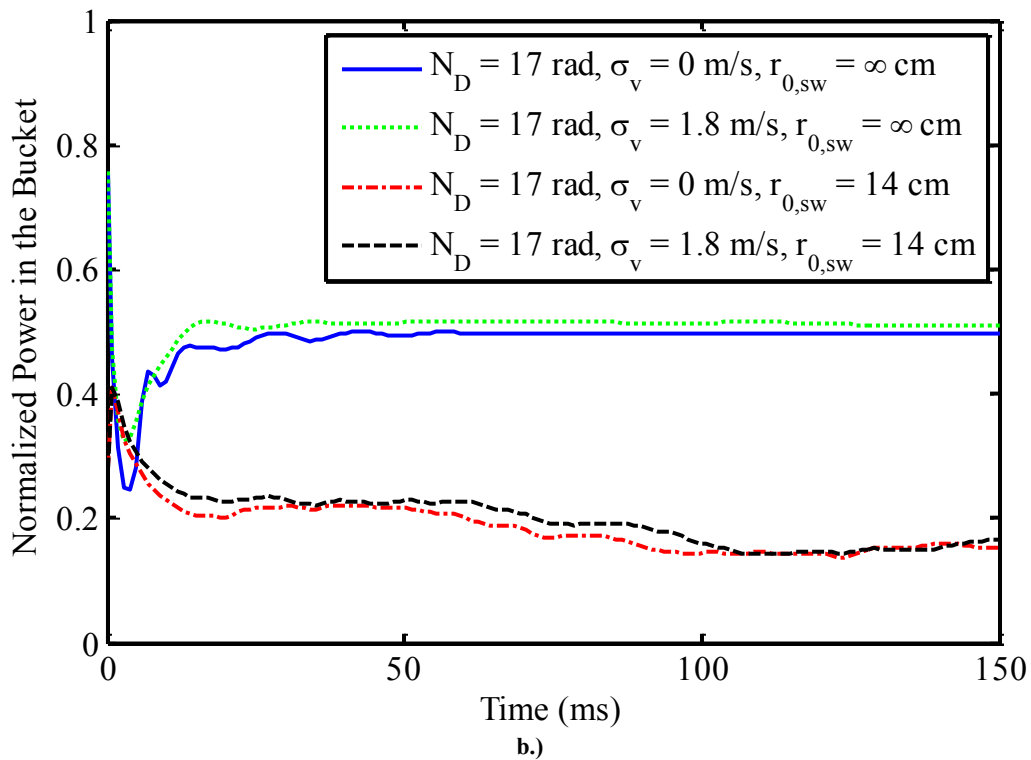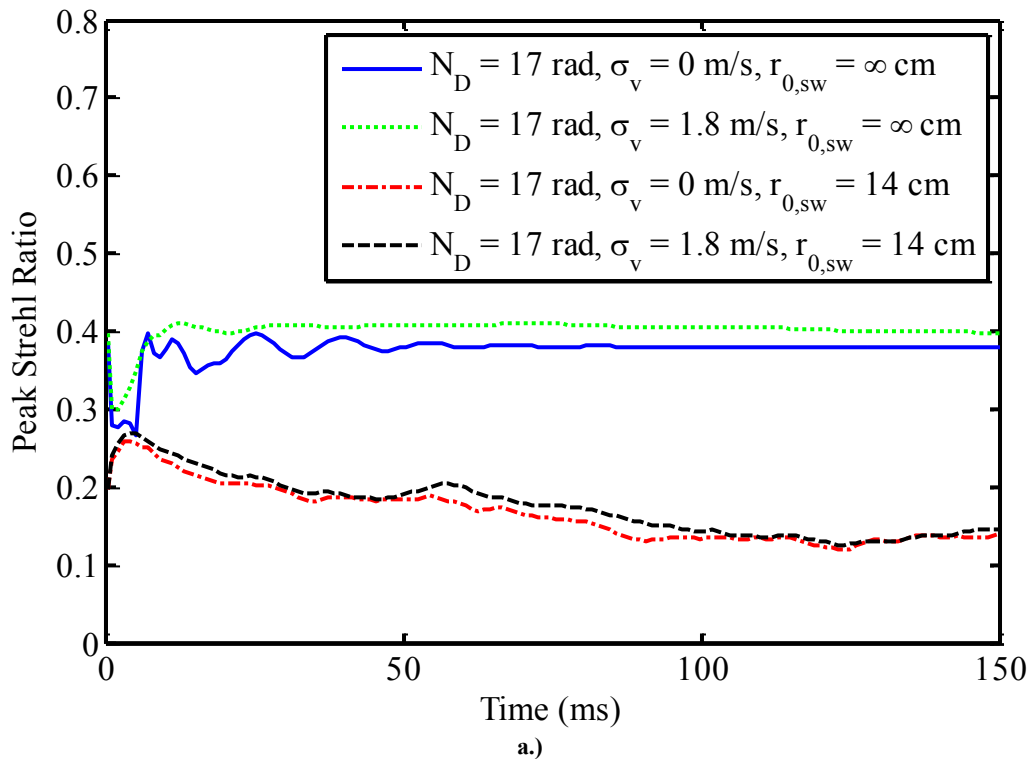
Figure 58. Comparison study for ab initio phase compensation with time-dependent turbulent thermal blooming and the average of 25 realizations of optical turbulence using a.) peak Strehl ratio versus time and b.) normalized power in the bucket versus time.
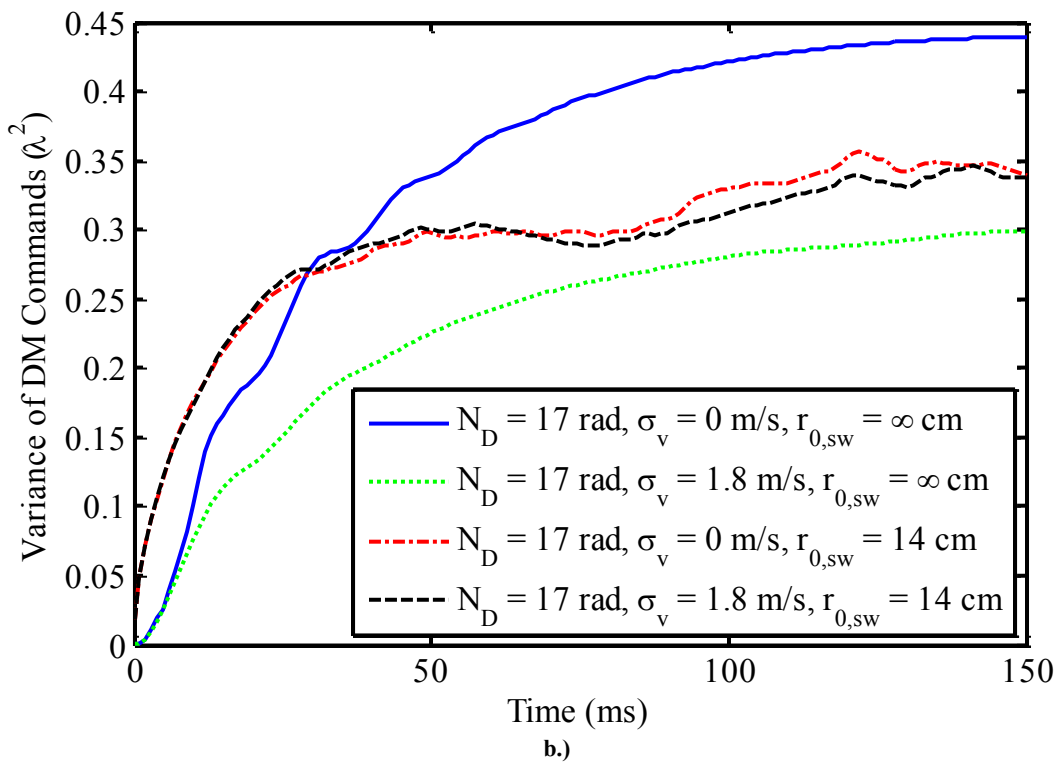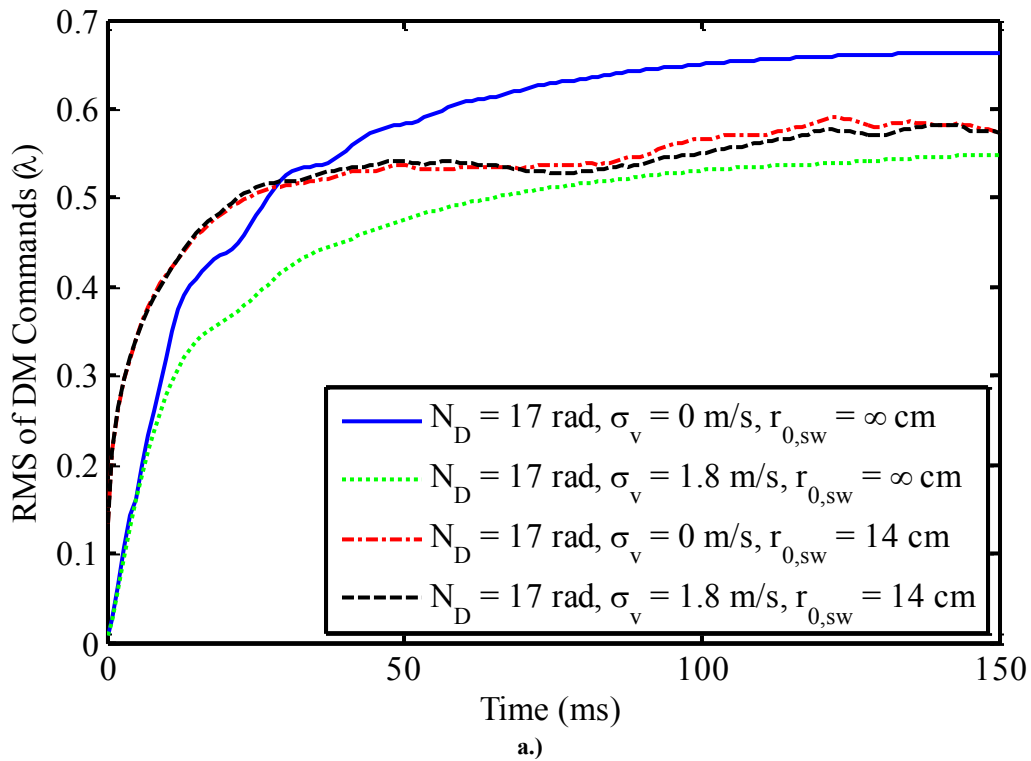
Figure 59. Comparison study for ab initio phase compensation with time-dependent turbulent thermal blooming and the average of 25 realizations of optical turbulence using a.) RMS of DM commands versus time and b.) variance of DM commands versus time.

Normalized irradiance time stamps are also given in Figure 60 for the *ab initio* phase compensation of time-dependent turbulent thermal blooming and one independent realization of optical turbulence. The distortion number, $N_D = 38.8$ rad, simulated here corresponds to one found well above the critical point. Note that the AO system is unable to perform phase compensation for both time-dependent turbulent thermal blooming and one realization of optical turbulence. System performance in this case is completely compromised.

This statement is supported with the results presented in Figure 61. Here, peak Strehl ratio S_P and the normalized power in the bucket P_B calculations in the target plane versus time are provided for the average of 25 individual realizations of optical turbulence combined with time-dependent turbulent thermal blooming and or time-dependent thermal blooming. Note that the system measurements are basically non-existent as time progresses. This is better realized when compared to the results obtained for *ab initio* phase compensation of only time-dependent turbulent thermal blooming and or time-dependent thermal blooming. The results presented in Figure 59 correspond to system stability. Here, the RMS r_{DM} of the DM commands and the variance σ^2_{DM} of the DM commands as a function of time were plotted for the same simulation conditions as previously stated. No further insight is added, as there are no apparent signs of instability in the turbulence/thermal blooming results. One thing worth noting in the analysis before moving on is the fact the periodic oscillations are mitigated when optical turbulence is added to the mix.
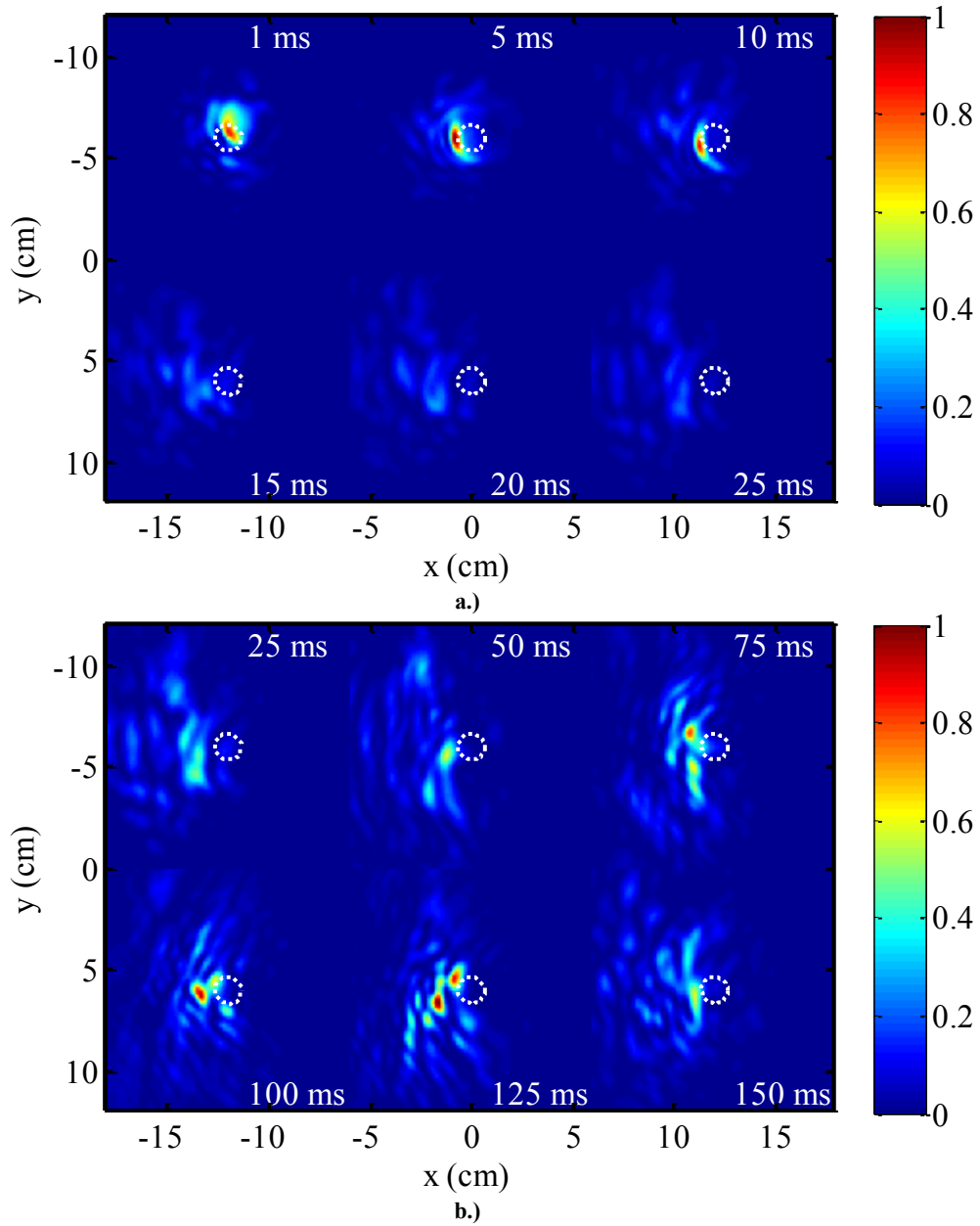
Figure 60. Normalized HEL beam irradiance with ab initio phase compensation of time-dependent turbulent thermal blooming and one realization of optical turbulence for a distortion number, N_D=38.8 rad, a wind velocity standard deviation, σ_v=1.8 m/s, and a spherical coherence diameter, $r_{0,sw}$=13.6 cm. In a.) the simulation runs from 1 ms to 25 ms and in b.) the simulation runs from 25 ms to 150 ms. The white circles represents the diffraction limited bucket diameter for the simulations, D_B=1.3 cm.
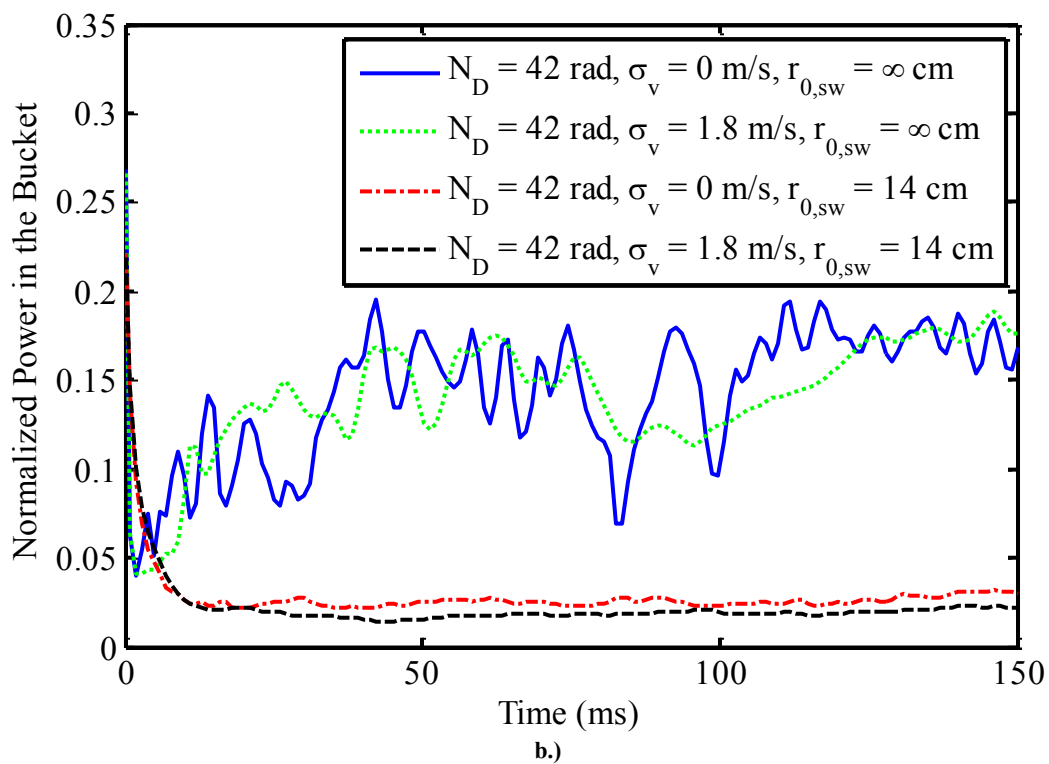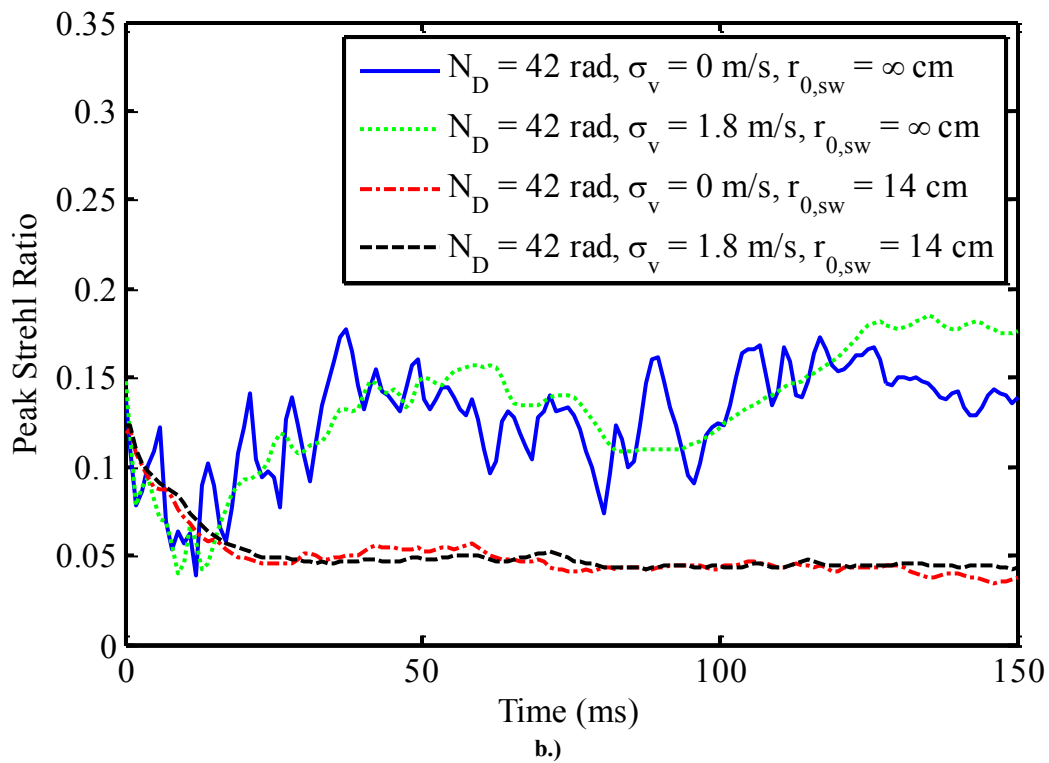
Figure 61. Comparison study for ab initio phase compensation with time-dependent turbulent thermal blooming and the average of 25 realizations of optical turbulence using a.) peak Strehl ratio versus time and b.) normalized power in the bucket versus time.
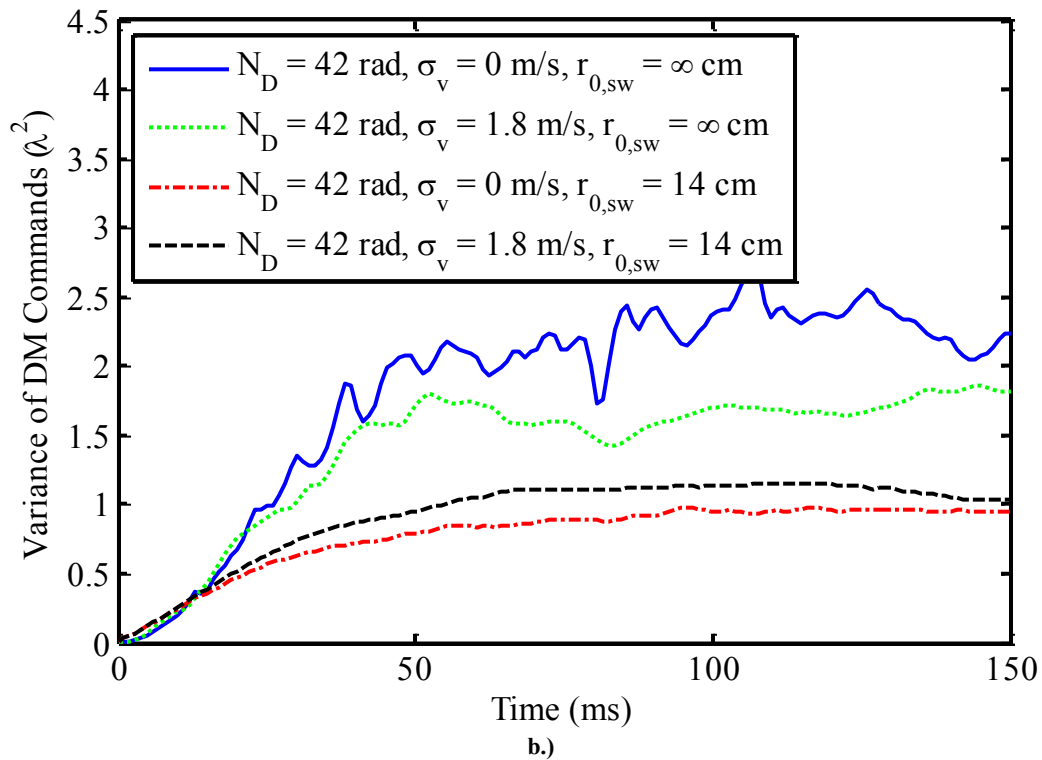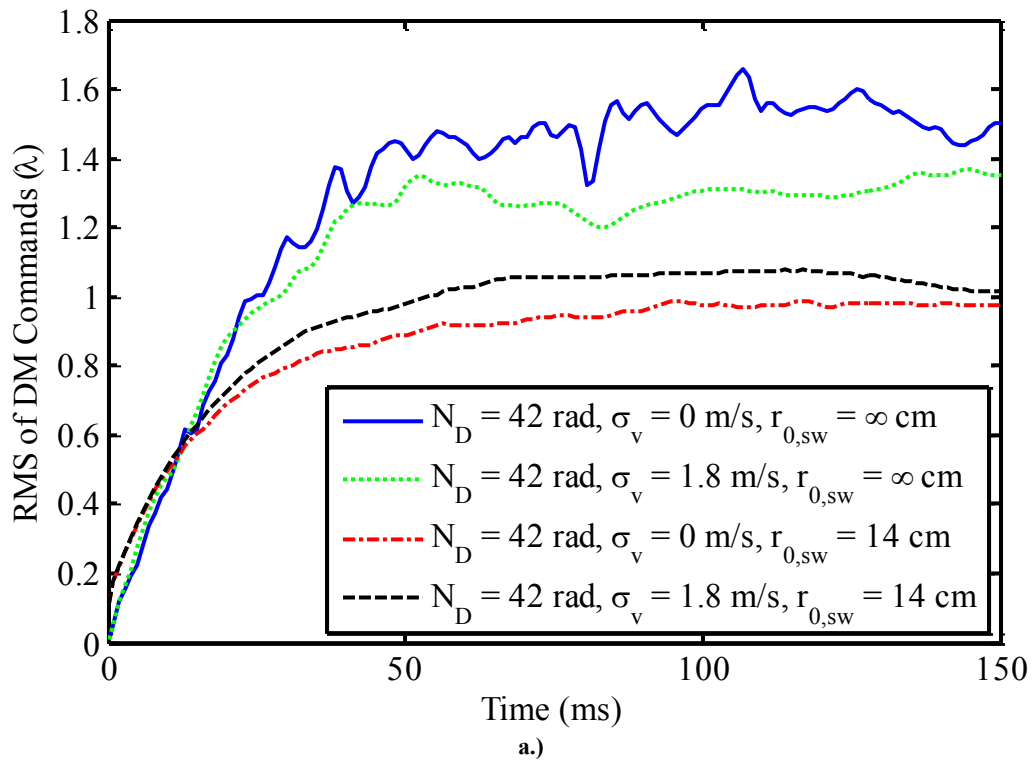
Figure 62. Comparison study for ab initio phase compensation with time-dependent turbulent thermal blooming and the average of 25 realizations of optical turbulence using a.) RMS of DM commands versus time and b.) variance of DM commands versus time.

4. Experimental Analysis and Discussion

In this chapter, further analysis is presented in support of the parameter space exploration given in the previous chapter. The goal for this analysis is to discern the cause of the periodic oscillations witnessed in the system performance measurements. It is shown that branch points result from the phase compensation of ―strong‖ thermal blooming and are the cause the periodic oscillations. In turn, these branch points limit insipient phase compensation instability (PCI). This conjecture is strongly supported with a correlation study, which shows that the system performance measurements are correlated with the number of branch points. What is more, the correlation is strongly influenced by the strength of the thermal blooming. As the strength of thermal blooming is increased, the correlation study shows that the measured system performance becomes increasingly uncorrelated with an increased number of branch points.

When the spatial resolution of the wavefront sensor (WFS) and the strength of the thermal blooming are increased, it is shown that system performance becomes compromised with the conditions of insipient PCI. Here, the correlation analysis shows that the measured system performance becomes anticorrelated with the number of branch points. The branch points present in this regime ensue their traditional role in directly decreasing system performance.

The measured system performance becomes increasingly anticorrelated when optical turbulence is added to the mix. These results make sense based on the system performance measurements presented in the previous chapter. In addition, these results offer definite trends. With increased optical distortion, whether from thermal blooming,

insipient PCI, and or optical turbulence, the branch point mitigation of PCI is increasingly less effective. The observed trends are consistent with previous work in turbulence [124]; however, are new in terms of characterizing the effects of thermal blooming and PCI.

4.1 Impact of Branch Points on Incipient PCI

In the exploration of the parameter space provided in the previous chapter, it was noticed that periodic oscillations arise in the system performance measurements as the strength of the simulated thermal blooming is increased. These periodic oscillations were first described by Lukin and Fortes as a result of branch points [121,7]. In this ground-breaking research, the periodic oscillations were referred to as auto oscillations. It was determined by Lukin and Fortes that the branch points arise with idealized phase compensation of a focused HEL beam in the presence of thermal blooming. Since this discovery, no further research has been published to better characterize the effects of branch points in the presence of ―strong" thermal blooming. The analysis provided here, uses the correlation coefficient ρ as defined in Eq. (164) to relate the similarities found between the measured peak Strehl ratio S_P and the number of branch points as a function of time.

4.1.1 Branch Points in the Presence of Strong Thermal Blooming

From the parameter space exploration provided in the previous chapter, it was noted that the point-source beacon irradiance in the source plane varied as a result of the phase compensation of time-dependent thermal blooming. This point is demonstrated in Figure 63 with varying time stamps for the normalized beacon irradiance in the source plane and a simulated distortion number well above the critical point, $N_D = 42.0$ rad . The "middle of the road" AO system parameters, $n_{sub} = 16$ and $n_{lod} = 8 \lambda$, as given in Table 3, were also used to obtain these results. It is important to note that the point-source beacon irradiance variations were consistently found in the results obtained with *ab initio* and *deferred* phase compensation regimes of time-dependent thermal blooming.

Large-scale variations in the point-source beacon irradiance provide the conditions needed for branch points to arise in the point-source principle value or wrapped phase. This topic was addressed above with the introductory analysis given on branch points. As such, the point-source wrapped phase in the source plane is shown in Figure 64 for the same distortion number, $N_D = 42.0$ rad , and the same time stamps as those shown in Figure 63 for the normalized point-source beacon irradiance in the source plane. The "middle of the road" AO system parameters, $n_{sub} = 16$ and $n_{lod} = 8 \lambda$, as given in Table 3, were also used to obtain these results. From the results presented in Figure 64, it was made clear that the point-source wrapped phase in the source plane showed the symptoms associated with the presence of numerous branch points. Thus, a branch point study was conducted.

The algorithm given in Eq. (174) was used to detect branch points present in the source plane for each simulated time step. From this analysis, it was officially discovered that there were a significant number of branch points present in the wave-optics experiments as a result of "strong" thermal blooming. As shown in Figure 65, as many as 3806 branch points were present in the source plane at a given time stamp. The mean number of branch points for the various distortion numbers N_D and AO system parameters tested are tabulated in the Appendix. It should be noted that branch points only arise in the wave-optics experiments with simulated distortion numbers above the critical distortion number, $N_D > N_C$, i.e. "strong" thermal blooming.

Unfortunately, the results provided in Figure 64 and Figure 65 also show symptoms of aliasing. It is conjectured that the aliasing artificially increased the number of branch points obtained in some of the results. The high number of branch points could have also caused some of the aliasing. Future computational wave-optics experiments will require a higher number of grid points to combat these aliasing effects. Nonetheless, this small setback was noted and a correlation analysis was conducted.
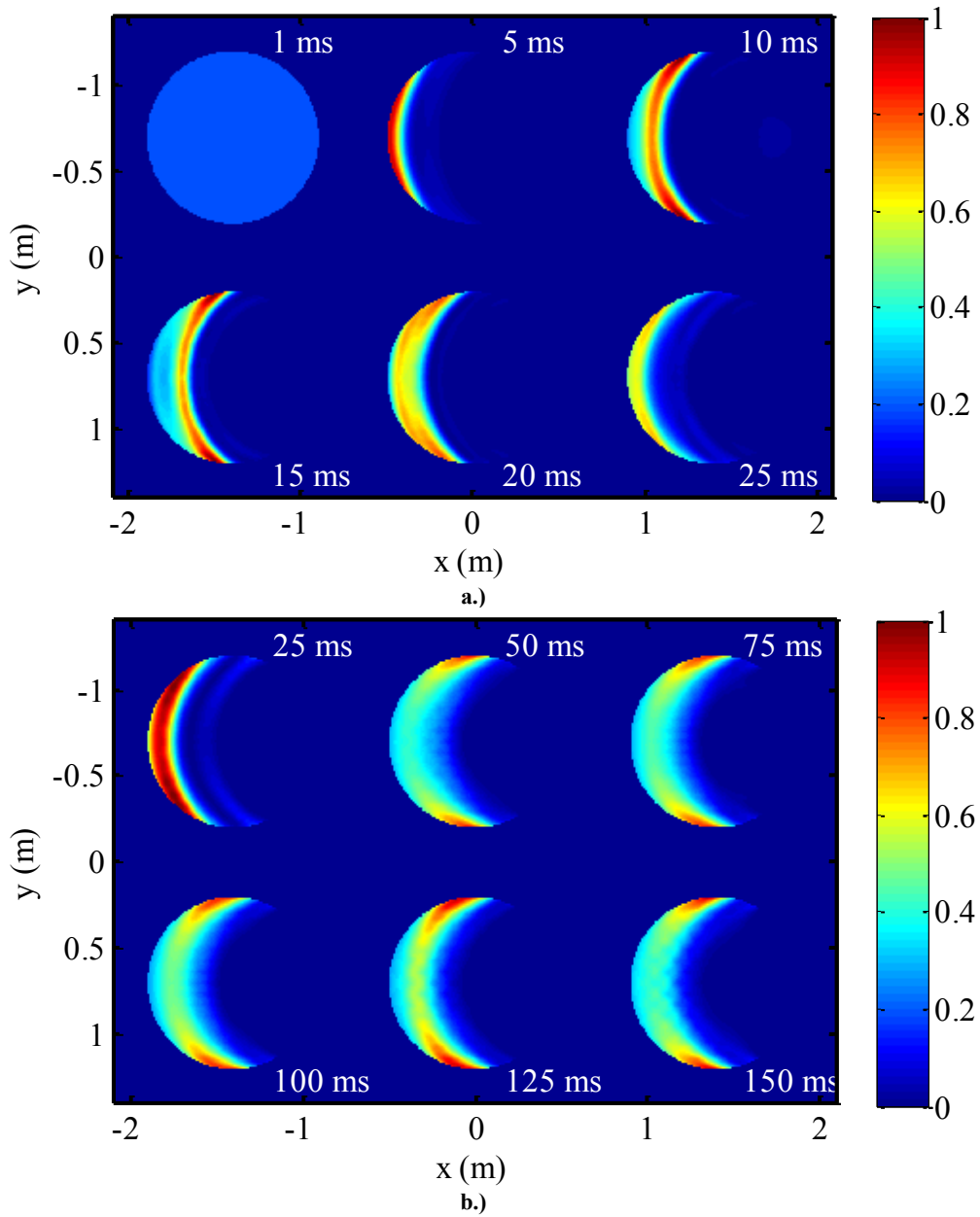
Figure 63. Normalized point-source beacon irradiance in the source plane with ab initio phase compensation of time-dependent thermal blooming for a distortion number, N_D=42.0 rad. In a.) the simulation runs from 1 ms to 25 ms and in b.) the simulation runs from 25 ms to 150 ms.
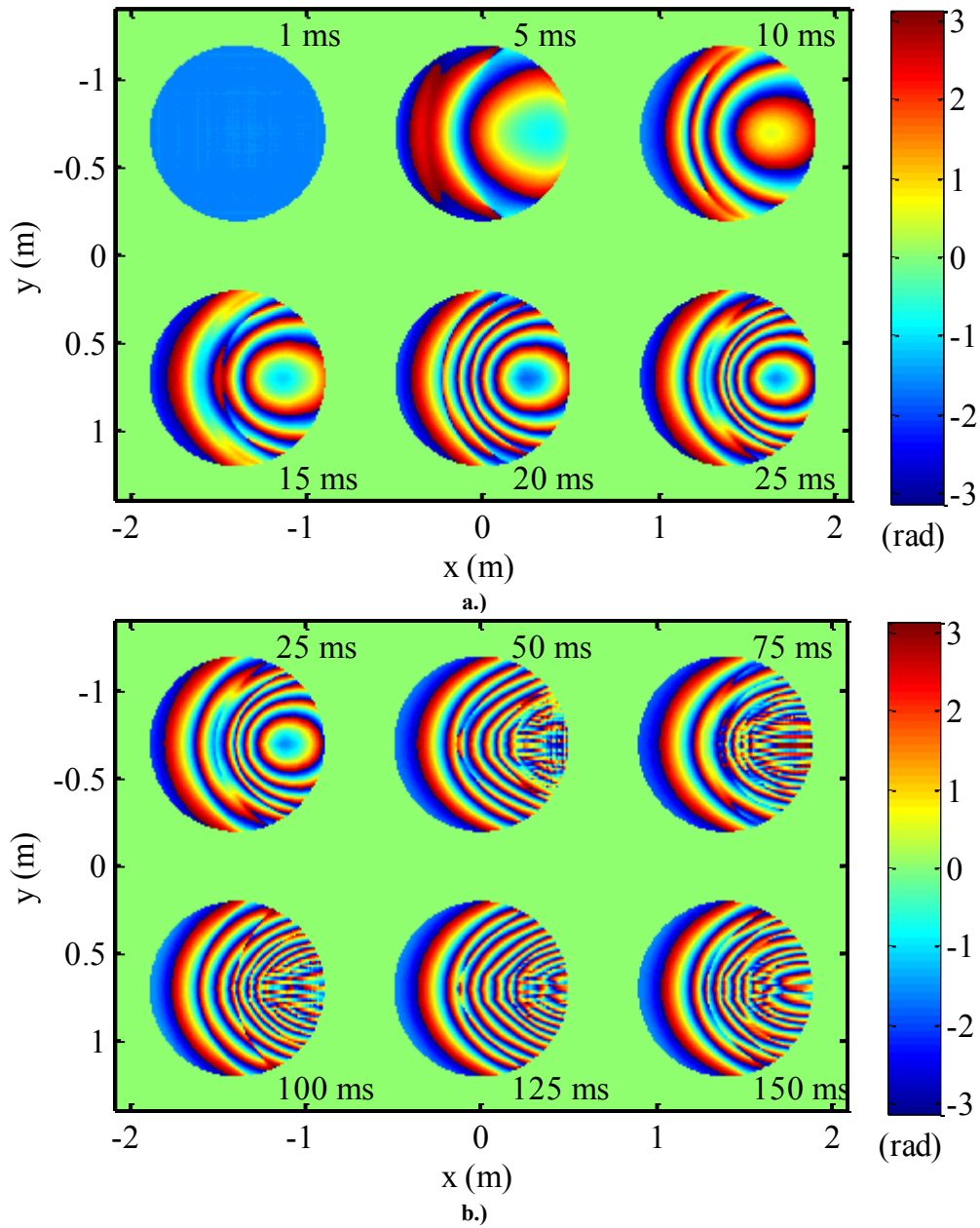
Figure 64. Measured point-source beacon wrapped phase in the source plane with ab initio phase compensation of time-dependent thermal blooming for a distortion number, N_D=42.0 rad. In a.) the simulation runs from 1 ms to 25 ms and in b.) the simulation runs from 25 ms to 150 ms..
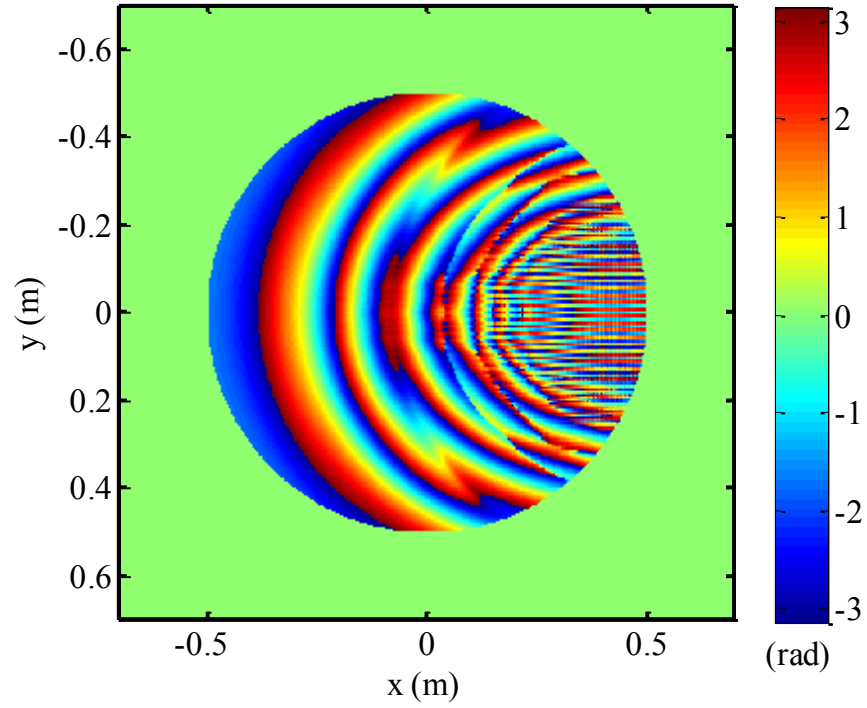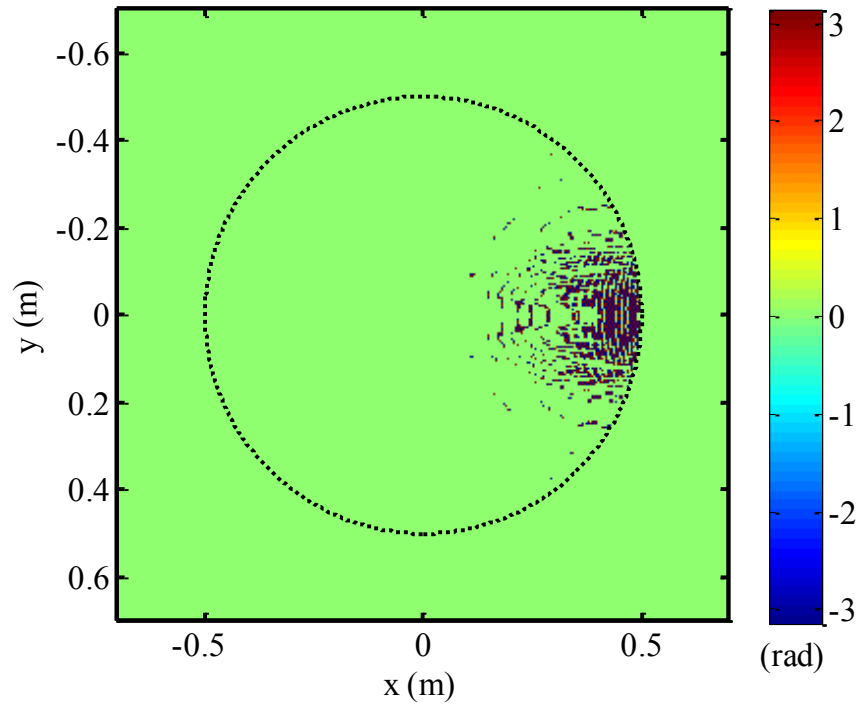
Figure 65. The highest number of branch points present in the source plane with ab initio phase compensation of time-dependent thermal blooming for a distortion number, N_D=42.0 rad. In a.) the point-source beacon wrapped phase for the t=87 ms time stamp is given and in b.) the associated placement of the branch points is given.

4.1.2 System Performance in Presence of Branch Points

The next step in the analysis was to relate the presence of branch points in the source plane to system performance in the target plane. For this purpose, a correlation study was conducted using the correlation coefficient ρ, as given in Eq. (164). The results are tabulated in the Appendix for the various distortion numbers N_D and AO system parameters tested. It was determined that the number of branch points in the source plane as a function of time were correlated with the peak Strehl ratio S_P calculations in the target plane as a function of time. This relationship is shown in Figure 66, where a correlation coefficient, $\rho = 0.118$, was obtained for a simulated distortion number well above the critical point, $N_D = 42.0 \text{ rad}$, and the "middle of the road" AO system parameters, $n_{sub} = 16$ and $n_{lod} = 8\lambda$, as provided in Table 3.

What this means in the analysis is that as system performance increases due to phase compensation of time-dependent thermal blooming, the number of branch points increases. With an increase in the number of branch points, the simulated AO system is unable to sense and correct for the effects of time-dependent thermal blooming. As a result, system performance decreases. This decrease in system performance also marks a decrease in the number of branch points and the process is essentially repeated—hence the presence of periodic oscillations in the system performance measurements.

The presence of branch points effectively mitigates PCI. This is said because the branch points prevent system performance and in so doing prevent the positive feedback associated with the macro- and micro-scale interpretations of PCI. The branch point mitigation of PCI does not provide stellar system performance, as noted in Figure 66.

However, system performance was not completely compromised as is the case when in the presence of PCI.
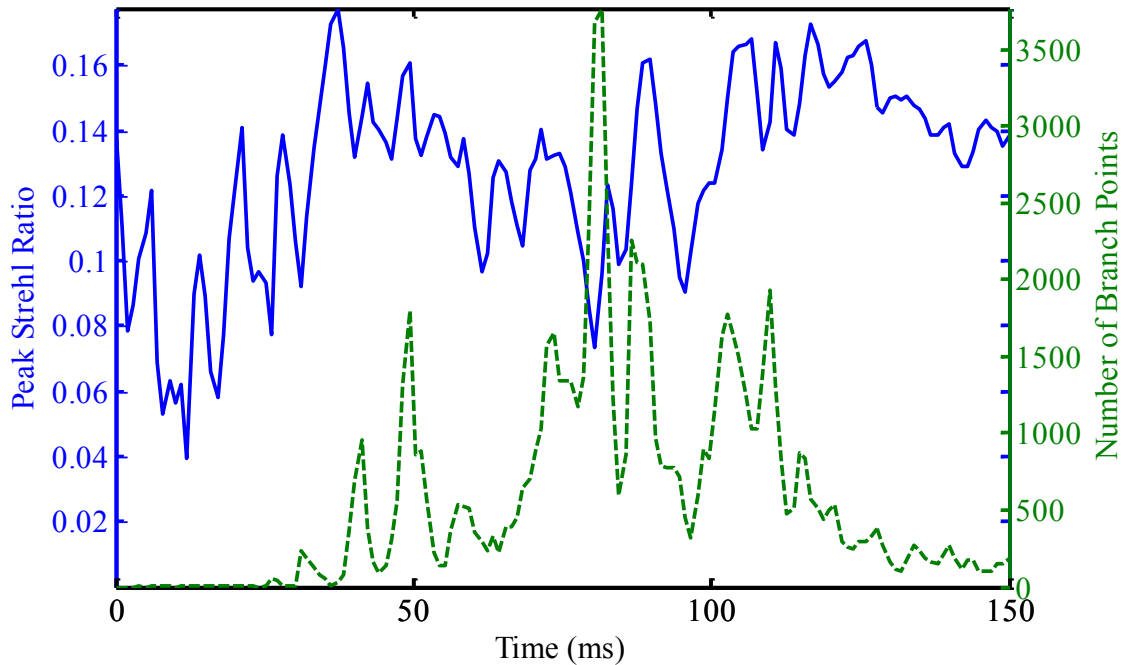
Figure 66. Comparison of peak Strehl ratio calculations in the target plane as a function of time with the number of branch points in the source plane as a function of time for a distortion number, N_D=42.0 rad, 16 subapertures across the aperture, n_{lod}=32, and ten waves of tilt per subaperture, n_{lod}=10 λ. The results show that the two measurements are correlated for time-dependent thermal blooming.

4.2 Impact of Spatial Resolution on Incipient PCI

To continue the analysis, the conditions for insipient PCI are explored. The results from the previous chapter only showed phase compensation results for the "middle of the road" case for the AO system parameters simulated, $n_{sub} = 16$ and $n_{lod} = 8\,\lambda$. However, as organized in Table 3, many more AO system parameters were used in the wave-optics experiments. These combinations corresponded to regimes for both a low PCI gain factor, $N_P \gg 1$ and $N_D < N_C$, and a high PCI gain factor, $N_P \ll 1$

213

and $N_D > N_C$. It is shown here, that as the Fresnel perturbation number N_P is decreased

and the distortion number N_d is increased well above the critical distortion number N_C,

the conditions for insipient PCI are met, and system performance becomes compromised.

However, the Fresnel perturbation number N_P does not characterize the conditions for

insipient PCI entirely. Subaperture field of view (FOV) on the simulated Shack-

Hartmann WFS must be taken into account as well when in the presence of branch points.

The analysis shows that when the conditions for insipient PCI are met, the number of

branch points becomes anticorrelated with the system performance measurements.

4.2.1 Spatial Resolution in the Presence of Thermal Blooming

By increasing the AO system spatial resolution, the conditions for incipient PCI

were met. For example, as shown in Figure 67, the normalized irradiance time stamps

show symptoms associated with incipient PCI—as time progresses, energy slowly leaks

out of the diffraction limited bucket diameter and never comes back. To produce the

results shown in Figure 67 a distortion number, $N_D = 33.6 \text{ rad}$, was used. This

corresponded to a distortion number well above the critical point; thus, half of the

criterion for a high PCI gain factor was met. The other half of the criterion included a

low Fresnel perturbation number, $N_P = 0.577$, as given in Table 3.

The number of waves of tilt n_{lod} used in the Shack-Hartmann WFS design also

played a big role in the decrease in system performance. This point is not addressed in

the results given in Figure 67. Remember that the number of waves of tilt n_{lod} is directly

related to subaperture FOV, as discussed in Figure 13. Unfortunately, this engineering

parameter is not taken into account in the calculation of the Fresnel perturbation number

N_P, as given in Eq. (170). As a result, a new constraint was thrown into the mix. This point is demonstrated in Figure 68 and Figure 69. Here, the number of subapertures n_{sub} and the number of waves of tilt n_{lod} are varied in the simulated Shack-Hartmann WFS design. These results were obtained for the same distortion number, $N_D = 33.6$ rad, used to create the normalized irradiance time stamps found in Figure 67. Peak Strehl ratio S_P and normalized power in the bucket P_B calculations in the target plane versus time are shown in Figure 68. When the right criterion is met, where $N_D = 33.6$ rad, $n_{sub} = 32$, and $n_{lod} = 8$, system performance is compromised with the symptoms of insipient PCI. These conclusions are also made in the analysis of Figure 69. Here, system stability is compromised with exponential behavior in the RMS r_{DM} of the DM commands and the variance σ^2_{DM} of the DM commands. It is important to note that the periodic oscillations were also present in the compromised results presented in Figure 68 and Figure 69; thus, a correlation analysis was conducted to discern their cause.
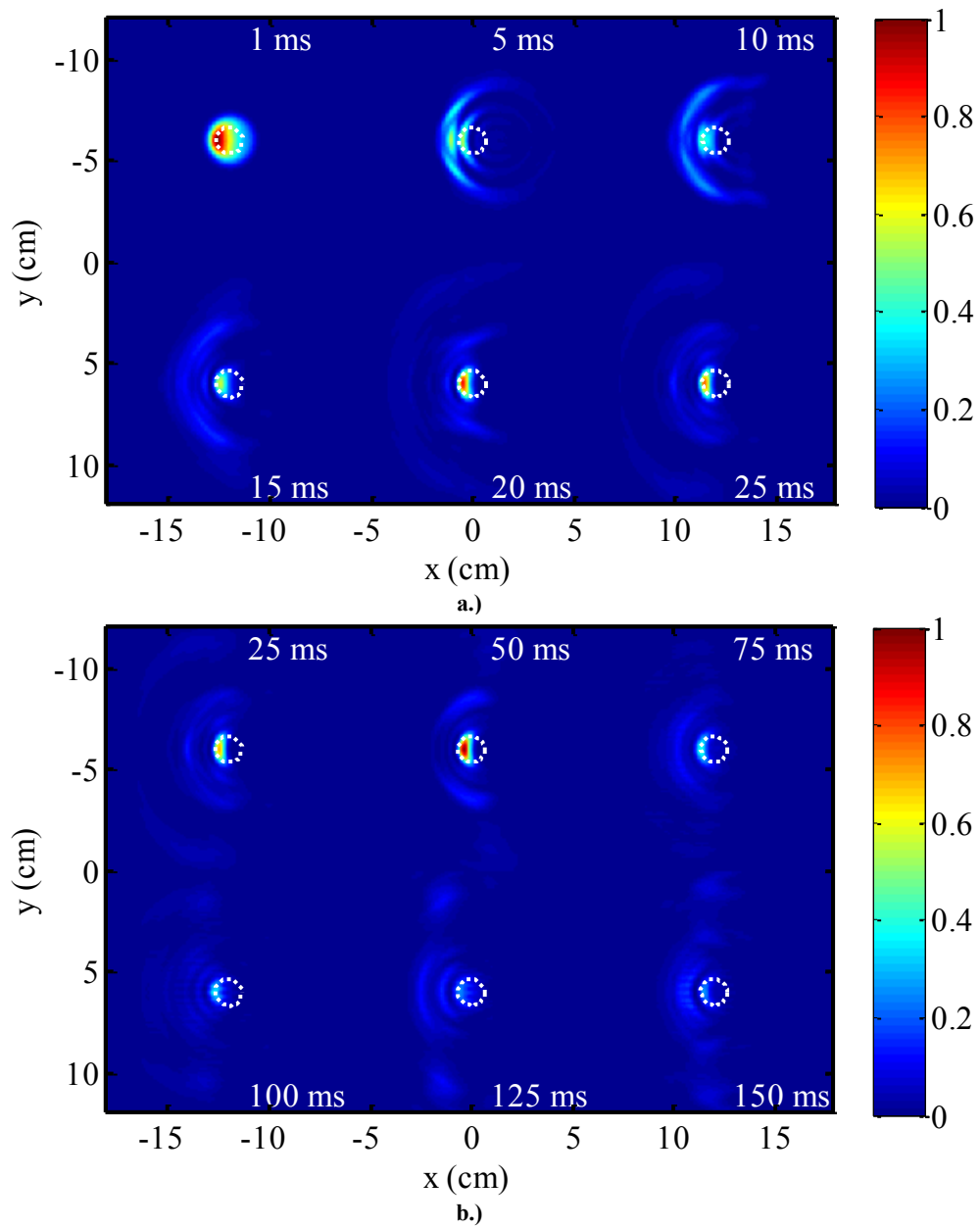
Figure 67. Normalized HEL beam irradiance with ab initio phase compensation of time-dependent thermal blooming for a distortion number, N_D=33.6 rad, 32 subapertures across the aperture, n_{lod}=32, and eight waves of tilt per subaperture, n_{lod}=8 λ. In a.) the simulation runs from 1 ms to 25 ms and in b.) the simulation runs from 25 ms to 150 ms. The white circles represents the diffraction limited bucket diameter for the simulations, D_B=1.3 cm.
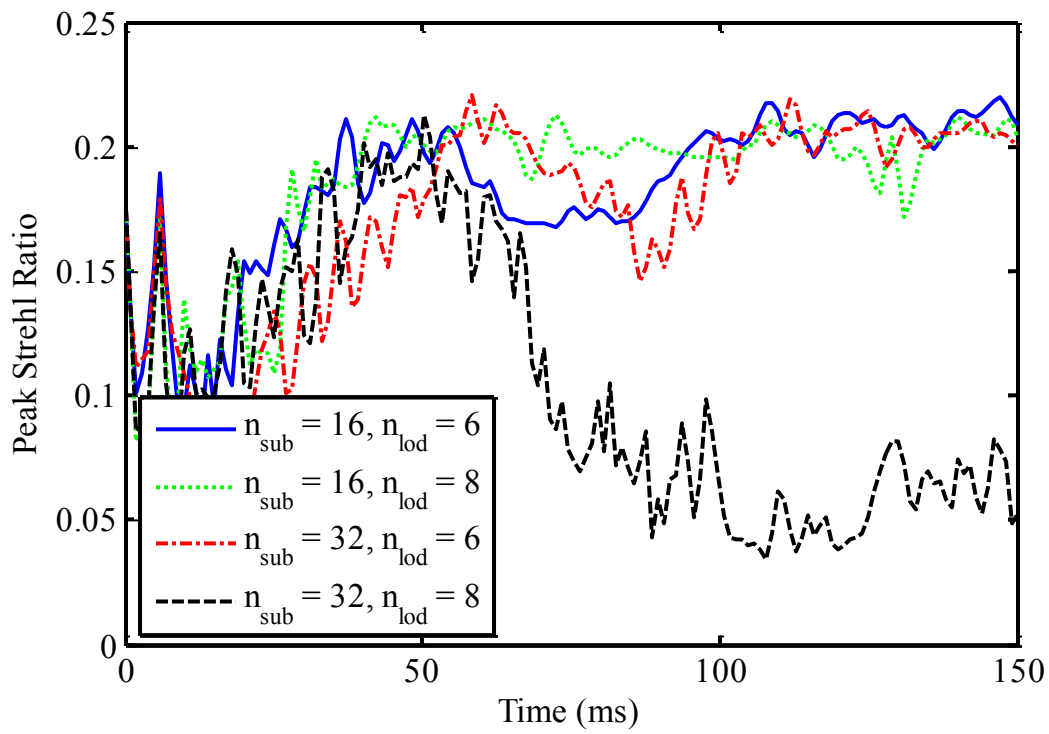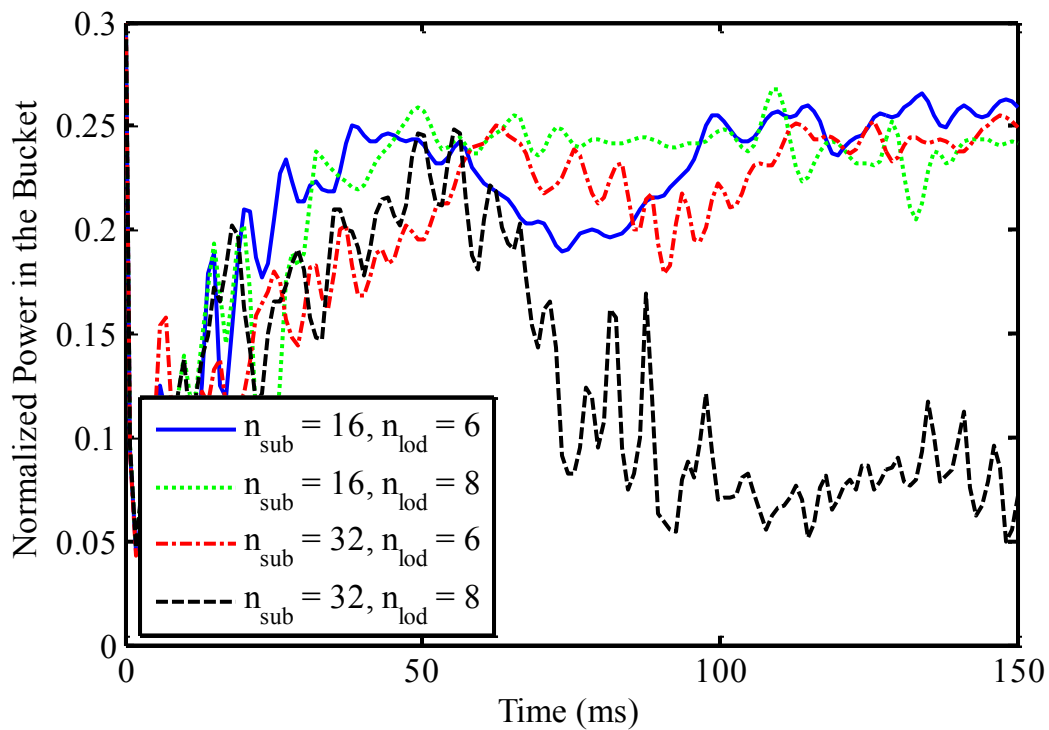
Figure 68. Spatial resolution study to determine insipient PCI for ab initio phase compensation with time-dependent thermal blooming and a distortion number, N_D=33.6 rad, using a.) peak Strehl ratio versus time and b.) normalized power in the bucket versus time.
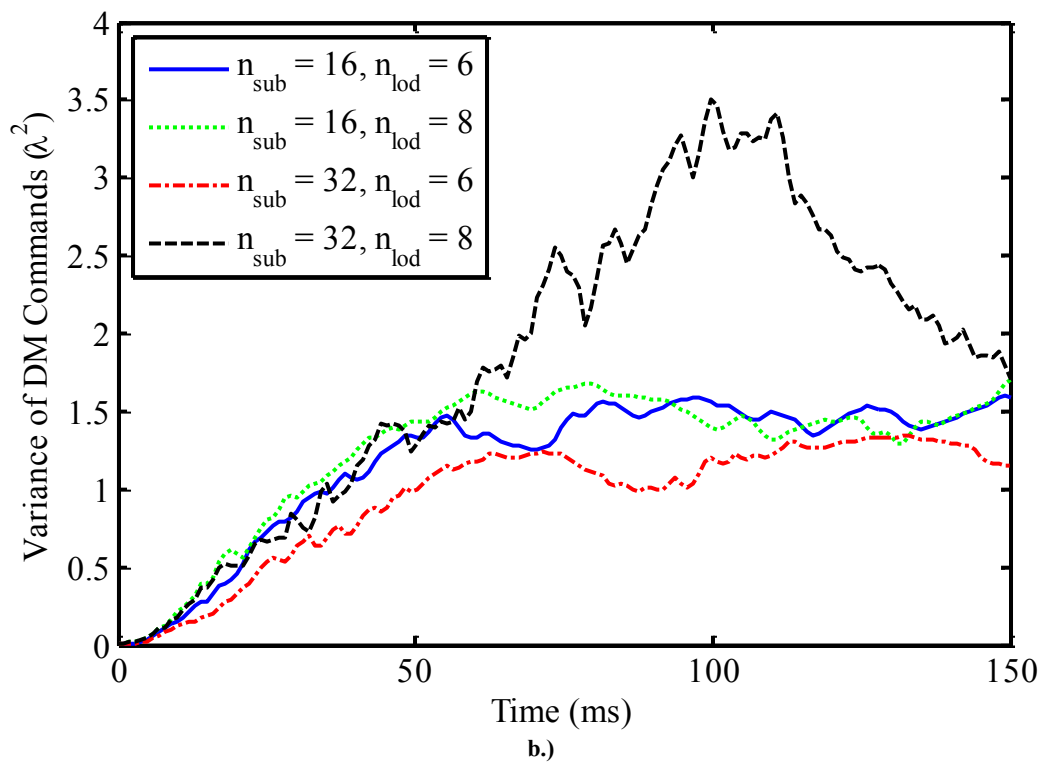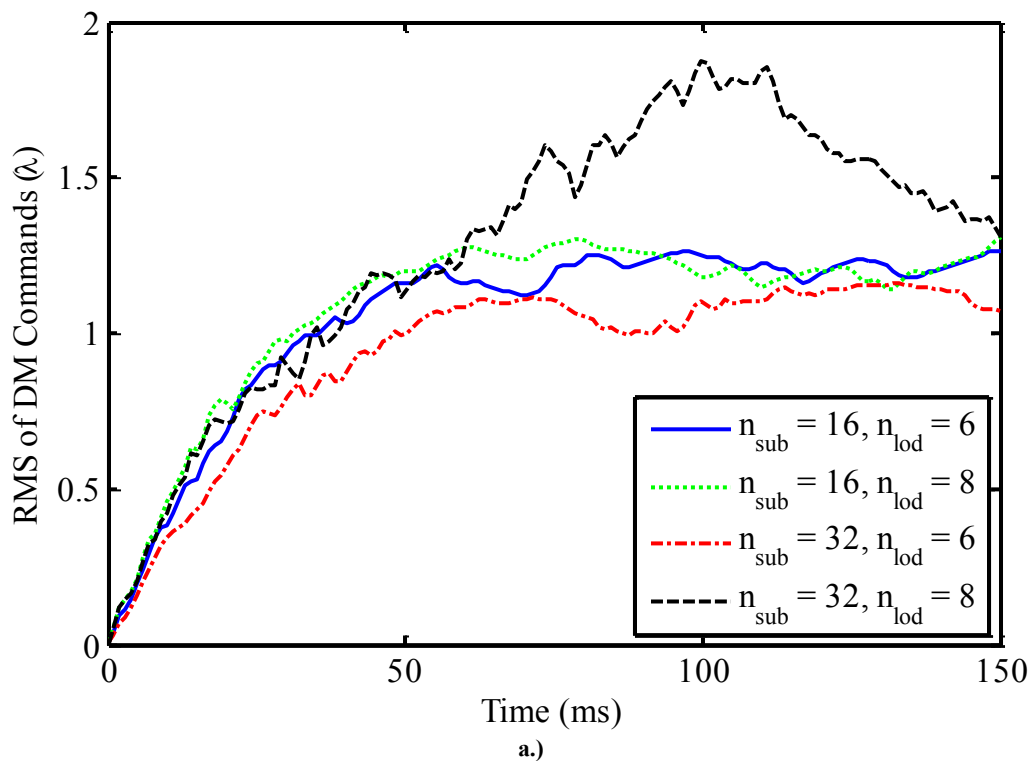
Figure 69. Spatial resolution study to determine insipient PCI for ab initio phase compensation with time-dependent thermal blooming and a distortion number, N_D=33.6 rad, using a.) RMS of DM commands versus time and b.) variance of DM commands versus time.

4.2.2 System Performance with Increased Spatial Resolution

The next step in the analysis was to relate the presence of branch points in the source plane to system performance in the target plane; however, in this case the spatial resolution of the simulated AO system parameters were increased. For this purpose, a correlation study was conducted using the correlation coefficient ρ, as given in Eq. (164). The results are tabulated in the Appendix for the various distortion numbers N_D and AO system parameters tested. It was determined that the number of branch points in the source plane as a function of time were anticorrelated with the peak Strehl ratio S_P calculations in the target plane as a function of time. This relationship is shown in Figure 70, where a correlation coefficient, $\rho = -0.279$, was obtained for a simulated distortion number well above the critical point, $N_D = 42.0$ rad, and the highest spatial resolution AO system parameters tested, $n_{sub} = 32$ and $n_{lod} = 10\,\lambda$, as provided in Table 3.

What this means in the analysis is that as system performance decreases due to phase compensation of time-dependent thermal blooming the number of branch points increases. With an increase in the number of branch points, the simulated AO system is unable to sense and correct for the effects of time-dependent thermal blooming. As a result, system performance decreases even more. This decrease in system performance marks a regime where the AO system is completely unable to sense and correct for the effects of time-dependent thermal blooming.

The presence of branch points effectively drives the AO system to failure when in the presence of increased spatial resolution AO system parameters. This is said because the branch points essentially induce insipient PCI. In so doing the positive feedback

associated with the macro- and micro-scale interpretations of PCI are too great to overcome. It should be noted that system performance is compromised when in the presence of PCI.
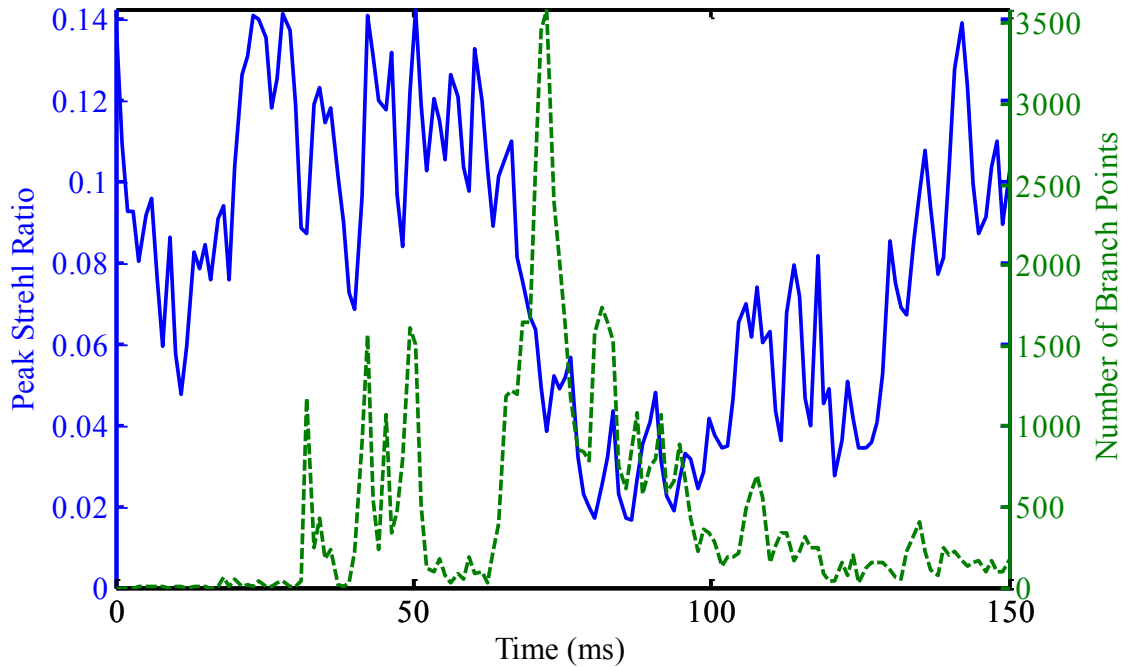
Figure 70. Comparison of peak Strehl ratio calculations in the target plane as a function of time with the number of branch points in the source plane as a function of time for a distortion number, N_D=42.0 rad, 32 subapertures across the aperture, n_{lod}=32, and ten waves of tilt per subaperture, n_{lod}=10 λ. The results show that the two measurements are anticorrelated for time-dependent thermal blooming.

4.3 Impact of Optical Turbulence on incipient PCI

It was shown in the previous chapter that the periodic oscillations associated with the phase compensation of ―strong‖ thermal blooming essentially go away when optical turbulence is added to the mix. However, this does not mean that branch points are not

present in the results. The analysis provided here shows that system performance and the number of branch points are highly anticorrelated.

4.3.1 Branch Points in the Presence of Thermal Blooming and Turbulence

From the parameter space exploration provided in the previous chapter, it was noted that the point-source beacon irradiance in the source plane also varied as a result of the phase compensation of time-dependent turbulent thermal blooming and one realization of optical turbulence. This point is demonstrated in Figure 71 with varying time stamps for the normalized beacon irradiance in the source plane and a simulated distortion number well above the critical point, $N_D = 38.8 \text{ rad}$. The ―middle of the road" AO system parameters, $n_{sub} = 16$ and $n_{lod} = 8 \lambda$, as given in Table 3, were also used to obtain these results.

Large-scale variations in the point-source beacon irradiance provided the conditions needed for branch points to arise in the point-source principle value or wrapped phase. This topic was addressed above with the introductory analysis given on branch points and branch cuts. As such, the point-source wrapped phase in the source plane is shown in Figure 72 for the same distortion number, $N_D = 38.8 \text{ rad}$, and the same time stamps as those shown in Figure 71 for the normalized point-source beacon irradiance in the source plane. From the results presented in Figure 72, it was made clear that the point-source wrapped phase in the source plane showed the symptoms associated with the presence of numerous branch points.

The algorithm given in Eq. (174) was used to detect branch points present in the source plane for each simulated time step. From this analysis, it was officially discovered

that there were a significant number of branch points present in the wave-optics experiments as a result of "strong" thermal blooming; however, not as many as in the case with only time-dependent thermal blooming[8]. For example, a mean number of branch points, $\mu_{BP} = 325$, was determined for the results given in Figure 72. It should be noted that branch points were also present in the wave-optics experiments with simulated distortion numbers below the critical distortion number, $N_D < N_C$, i.e. "moderate" thermal blooming. This was not the case with only time-dependent thermal blooming simulated in the wave-optics experiments. It should also be noted that no branch points were detected for the case where only "moderate" optical turbulence was simulated in the wave-optics experiments.

As shown in Figure 73, as many as 806 branch points were present in the source plane at a given time stamp. No apparent aliasing was present in these results. The simulated optical turbulence tended to "wash out" the high spatial frequencies associated with the aliasing seen in Figure 65. A correlation study was conducted to discern the impact of the branch points on system performance.

---

[8] Aliasing in the results may or may not have artificially increased the number of branch points obtained with only time-dependent thermal blooming. Future research is needed to discern this conjecture definitively.
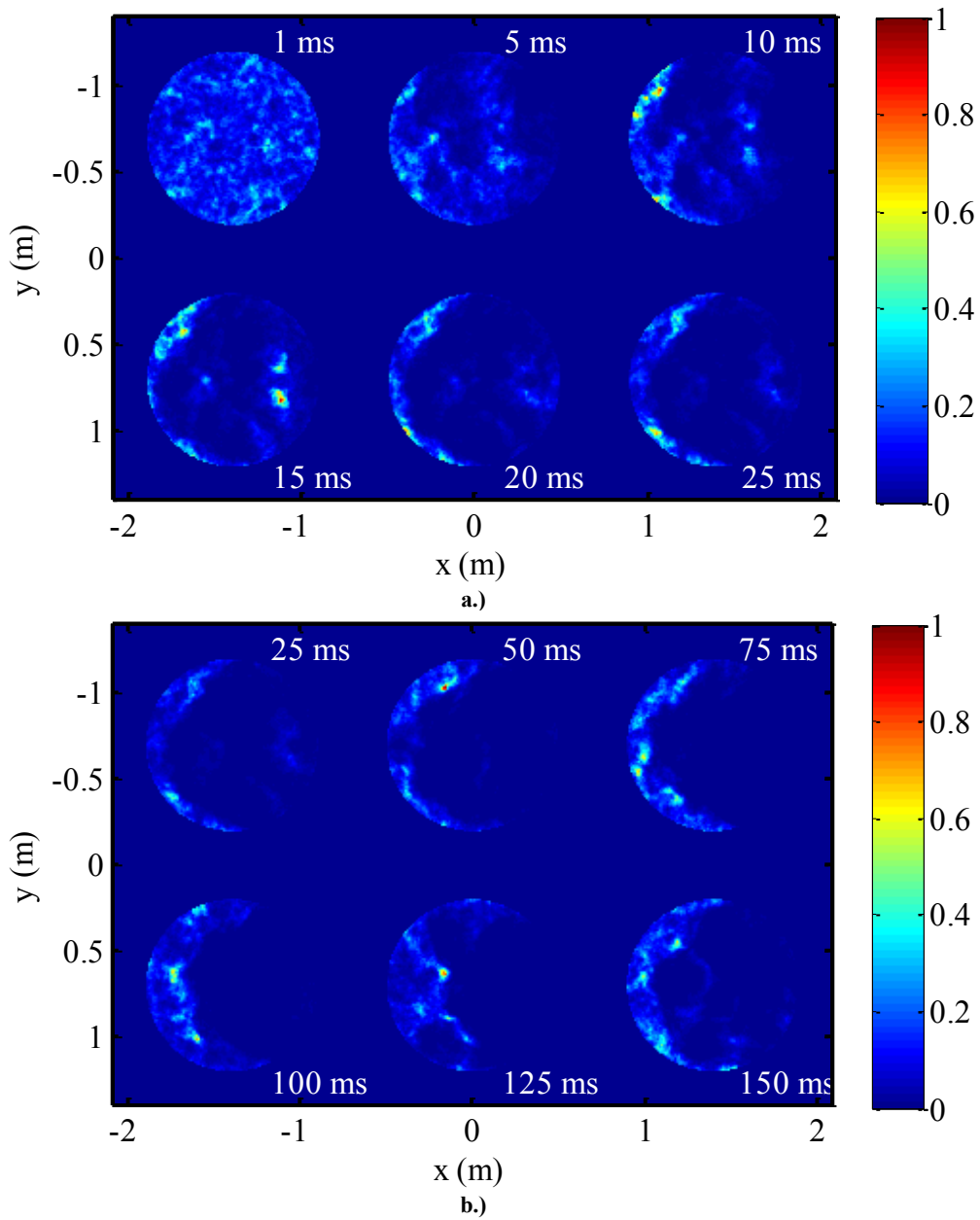
Figure 71. Normalized point-source beacon irradiance in the source plane with ab initio phase compensation of time-dependent turbulent thermal blooming and one independent realization of optical turbulence for a distortion number, N_D=38.8 rad, and a spherical-wave coherence diameter, $r_{0,sw}$=13.6 cm. In a.) the simulation runs from 1 ms to 25 ms and in b.) the simulation runs from 25 ms to 150 ms.
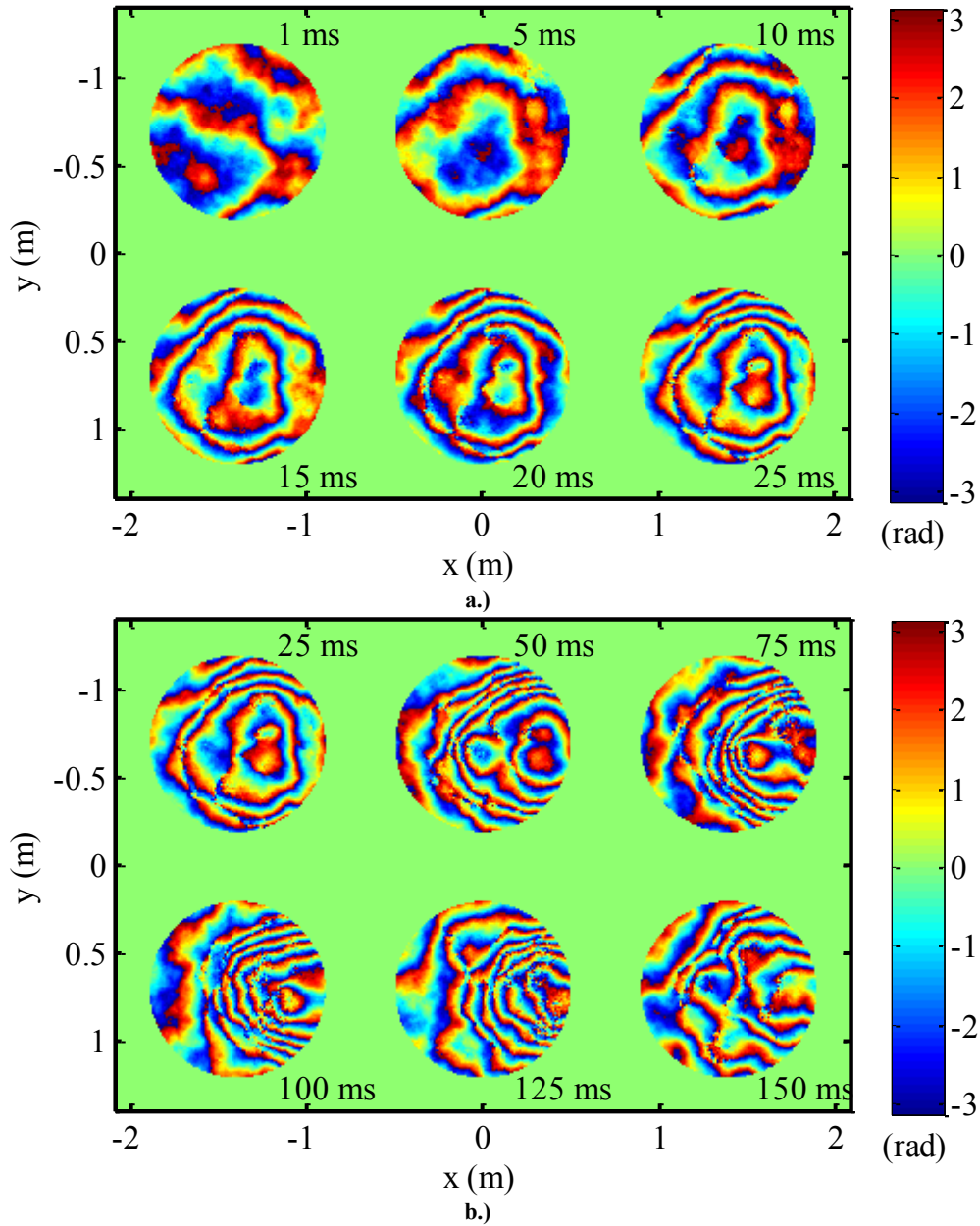
Figure 72. Measured point-source beacon wrapped phase in the source plane with ab initio phase compensation of time-dependent turbulent thermal blooming and one independent realization of optical turbulence for a distortion number, N_D=38.8 rad, and a spherical-wave coherence diameter, $r_{0,sw}$=13.6 cm. In a.) the simulation runs from 1 ms to 25 ms and in b.) the simulation runs from 25 ms to 150 ms.
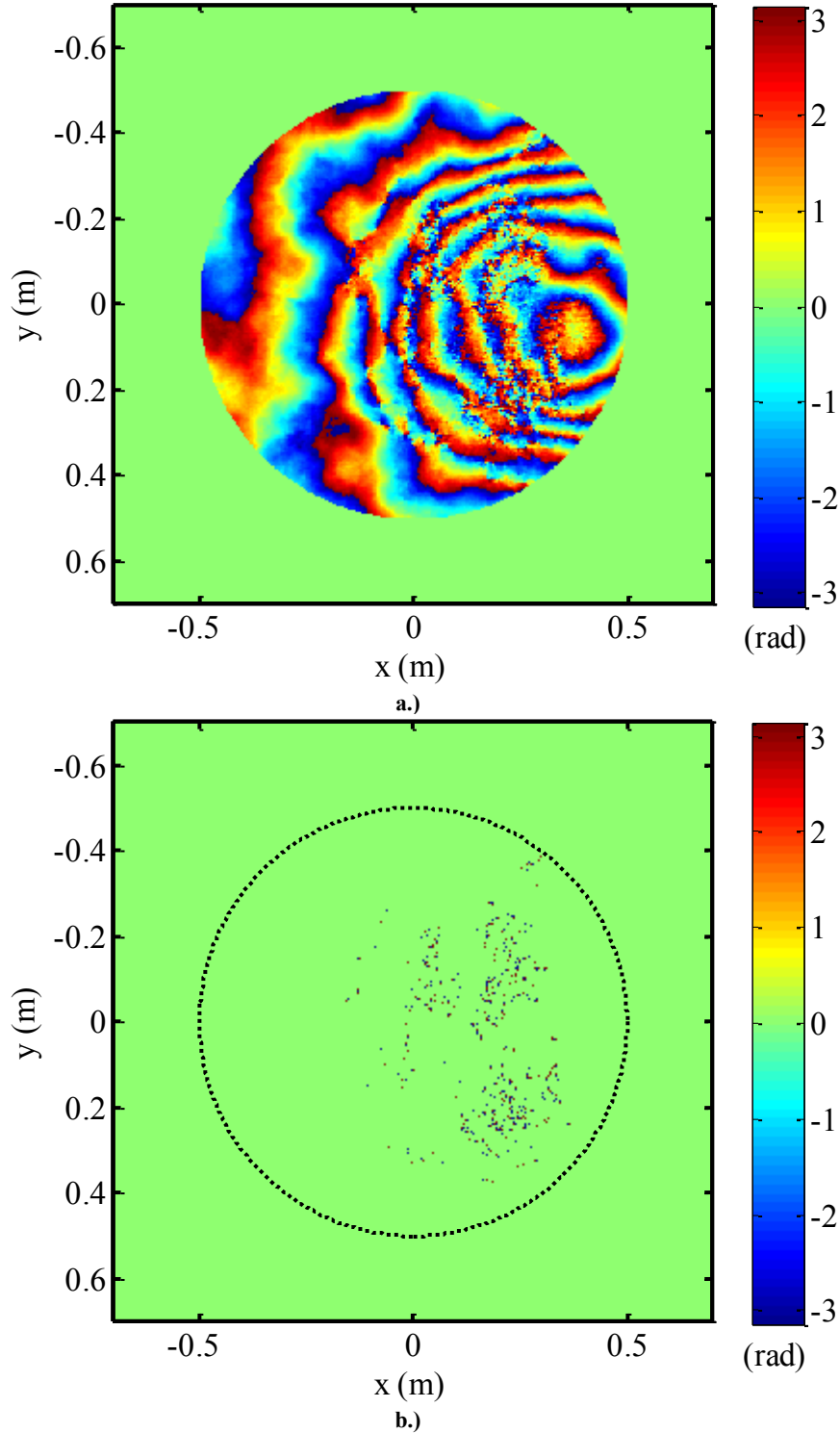
Figure 73. The highest number of branch points present in the source plane with ab initio phase compensation of time-dependent turbulent thermal blooming and one independent realization of optical turbulence for a distortion number, N_D=38.8 rad, and a spherical-wave coherence diameter, $r_{0,sw}$=13.6 cm. In a.) the point-source beacon wrapped phase for the t=87 ms time stamp is given and in b.) the associated placement of the branch points is given.

4.3.2 System Performance with branch points and Turbulence

The next step in the analysis was to relate the presence of branch points in the source plane to system performance in the target plane. Here, the refraction effects of time-dependent turbulent thermal blooming and 25 independent realizations of optical turbulence were included in the analysis. A correlation study was conducted using the correlation coefficient ρ, as given in Eq. (164).

Under "strong" thermal blooming conditions, it was determined that the number of branch points in the source plane as a function of time were highly anticorrelated with the peak Strehl ratio S_P calculations in the target plane as a function of time. This relationship is shown in Figure 74, where a correlation coefficient, $\rho = -0.507$, was obtained for a simulated distortion number well above the critical point, $N_D = 38.8$ rad, and the "middle of the road" AO system parameters, $n_{sub} = 16$ and $n_{lod} = 8\,\lambda$, as provided in Table 3. Under "moderate" thermal blooming conditions, it was determined that the number of branch points in the source plane as a function of time were uncorrelated with the peak Strehl ratio S_P calculations in the target plane as a function of time. In this regime, a correlation coefficient, $\rho = -0.026$, was obtained for a simulated distortion number just below the critical point, $N_D = 15.5$ rad, and the "middle of the road" AO system parameters, $n_{sub} = 16$ and $n_{lod} = 8\,\lambda$, as provided in Table 3.

What this means in the analysis is that as system performance decreases due to phase compensation of time-dependent thermal blooming the number of branch points increases tenfold. With an large increase in the number of branch points, the simulated AO system is unable to sense and correct for the effects of time-dependent turbulent

thermal blooming. As a result, system performance decreases even more. This decrease

in system performance marks a regime where the AO system is completely unable to

sense and correct for the effects of time-dependent turbulent thermal blooming. The

presence of branch points effectively drives the AO system to failure for ―strong‖ thermal

blooming and ―moderate‖ optical turbulence conditions.
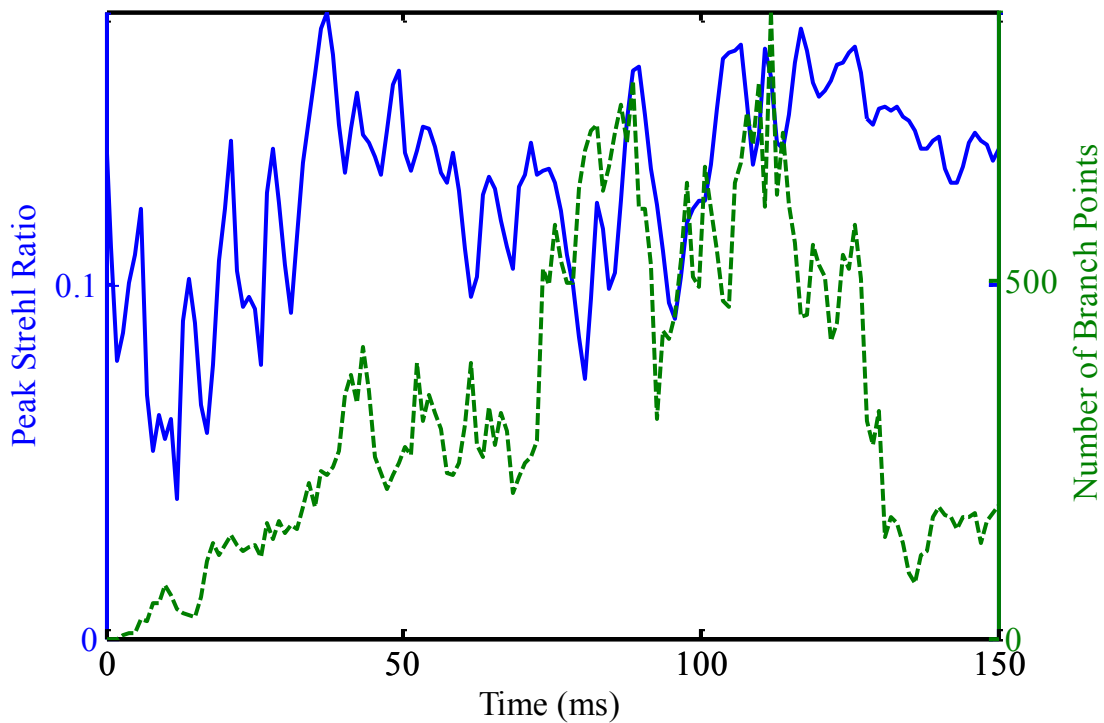
Figure 74. Comparison of peak Strehl ratio calculations in the target plane as a function of time with the number of branch points in the source plane as a function of time for a distortion number, N_D=38.8 rad, and a spherical-wave coherence diameter, $r_{0,sw}$=13.6 cm. The results show that the two measurements are anticorrelated for time-dependent turbulent thermal blooming and 25 independent realizations of optical turbulence.

5. Conclusion

Past research efforts have studied thermal blooming in depth; however, there is still much to be discovered in terms of characterizing its detrimental effects. With that said, the phase compensation instability (PCI) that arises in using an adaptive optics (AO) system to ―correct" for thermal blooming is still an important area of research in the directed energy (DE) community. The research conducted in this thesis attempted to determine bounds for the onset of PCI. In so doing, an additional limitation was discovered involving branch points. The limitation of branch points was not well characterized in the literature for thermal blooming prior to this research effort. As such, the analysis provided in this thesis serves as a significant contribution to the DE community.

The analysis shows that branch points severely degrade an AO system in its ability to ―correct" for thermal blooming. As a result, PCI is mitigated in specific regimes. The mitigation of PCI is short lived in practice, as the analysis presented in this thesis shows that regimes exist outside the ideal case where PCI cannot be overcome. This is said because spatial resolution considerations and optical turbulence levy additional constraints.

The conditions for insipient PCI are met with increased spatial resolution AO system parameters. This is said with confidence based on the experimental results presented from previous research efforts [90,106,103] and the analysis given in this thesis effort. However, the analysis conducted in this thesis shows that additional AO system parameters must be accounted for in determining bounds for insipient PCI.

High spatial resolution AO system parameters are typically desired when considering the detrimental effects of optical turbulence. Nonetheless, this is not effective when in the presence of thermal blooming. The analysis given in this thesis supports this claim. In fact, it takes this idea one step further with the results from a correlation analysis. The results from the correlation analysis are given in Figure 75 and are explained as follows.

- When an AO system is used to ‒correct" for ‒strong" thermal blooming conditions, branch points develop.

- An increase in system performance leads to an increase in the number of branch points and vice versa, thus PCI is mitigated.

- With increased spatial resolution, system performance is compromised with an increase in the number of branch points and the conditions for insipient PCI are met.

- Optical turbulence and branch points pose a major problem for an adaptive optics system trying to ‒correct" for ‒strong" thermal blooming conditions.
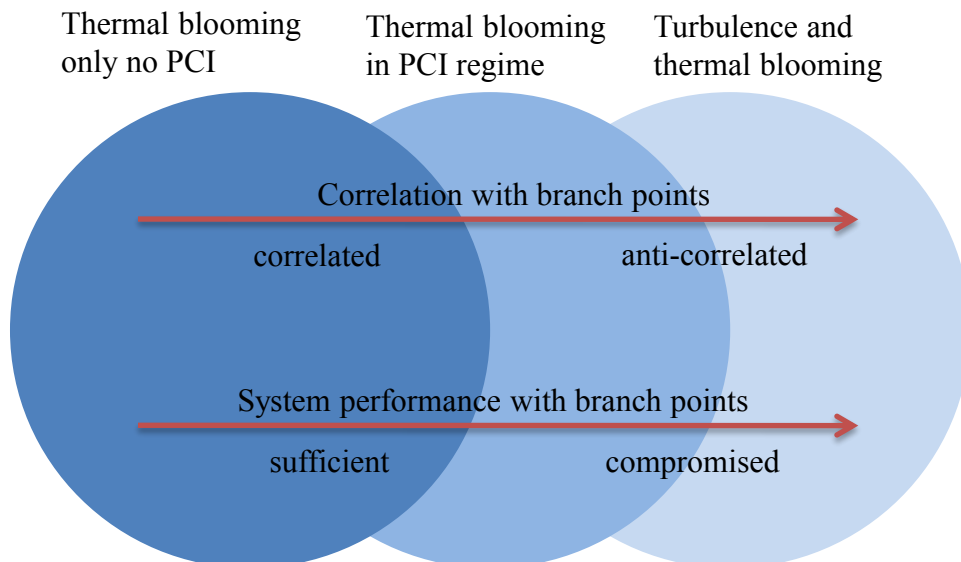
Figure 75. Conclusion diagram.

The thorough analysis presented in this thesis took into account over 40 years worth of published research in thermal blooming and PCI. For instance, the engineering parameters reviewed and used in this thesis served their purpose in giving rough bounds for insipient PCI. However, the analysis shows that branch points add additional constraints to the problem. These constraints are effectively described above in Figure 75. A refinement of the metrics used to characterize thermal blooming and PCI is in order for future research efforts. Additionally, there is still a lot to be discovered in terms of characterizing the effects of branch points on insipient PCI. For example, different types of AO systems respond differently to the presence of branch points. The type of wavefront sensor and or deformable mirror used in the AO system design can have a significant impact on system performance. Future research efforts could look at using different AO system designs to determine the optimal case.

Figure 75 contains many ideas never before seen in the analysis of thermal blooming and PCI. The branch point mitigation of PCI cannot be overlooked as a significant contribution. This discovery could be used in future research efforts as a way to improve system performance. However, the analysis also shows that spatial resolution considerations and optical turbulence cannot be disregarded. These engineering constraints must be overcome to see that the technology DE weapons offer makes its way onto the battlefield in the near future.

Appendix

Table 4. Results corresponding to the correlation analysis for *ab initio* phase compensation of time-dependent thermal blooming.

Number of waves of tilt n_{lod} (λ)	Number of subapertures n_{sub}	Fresnel perturbation number N_P	Distortion number N_D (rad)	Mean # of branch points μ_{BP}	Correlation coefficient ρ
6	8	9.23	25.2	91.8	0.600
6	8	9.23	33.6	279	0.402
6	8	9.23	42.0	608	0.628
6	16	2.31	25.2	19.1	0.255
6	16	2.31	33.6	247	0.166
6	16	2.31	42.0	169	0.277
6	32	0.577	25.2	19.3	0.419
6	32	0.577	33.6	84.8	0.434
6	32	0.577	42.0	130	0.163
8	8	9.23	25.2	102	0.515
8	8	9.23	33.6	315	0.492
8	8	9.23	42.0	348	0.179
8	16	2.31	25.2	56.8	0.350
8	16	2.31	33.6	252	0.516
8	16	2.31	42.0	573	0.118
8	32	0.577	25.2	93.1	-0.254
8	32	0.577	33.6	438	-0.224
8	32	0.577	42.0	649	0.0678
10	8	9.23	25.2	31.2	0.565
10	8	9.23	33.6	45.7	0.179
10	8	9.23	42.0	65.8	-0.395
10	16	2.31	25.2	70.5	0.359
10	16	2.31	33.6	222	0.511
10	16	2.31	42.0	812	0.0142
10	32	0.577	25.2	81.5	-0.119
10	32	0.577	33.6	240	-0.279
10	32	0.577	42.0	452	-0.279

Table 5. Results corresponding to the correlation analysis for *deferred* phase compensation of time-dependent steady-state thermal blooming.

Number of waves of tilt n_{lod} (λ)	Number of subapertures n_{sub}	Fresnel perturbation number N_P	Distortion number N_D (rad)	Mean # of branch points μ_{BP}	Correlation coefficient ρ
6	8	9.23	25.2	152	0.623
6	8	9.23	33.6	478	0.403
6	8	9.23	42.0	538	0.358
6	16	2.31	25.2	50.7	0.495
6	16	2.31	33.6	527	0.461
6	16	2.31	42.0	437	0.282
6	32	0.577	25.2	43.6	0.333
6	32	0.577	33.6	137	0.128
6	32	0.577	42.0	183	0.203
8	8	9.23	25.2	184	0.500
8	8	9.23	33.6	595	0.480
8	8	9.23	42.0	573	0.276
8	16	2.31	25.2	84.1	0.378
8	16	2.31	33.6	475	0.422
8	16	2.31	42.0	820	0.341
8	32	0.577	25.2	205	0.346
8	32	0.577	33.6	419	0.482
8	32	0.577	42.0	1028	-0.0611

Bibliography

[1] David Scott and David Robie, "Directed Energy A Look into the Future," *Air and Space Power Journal*, vol. 23, no. 4, pp. 6-12, Winter 2009.

[2] Jeff Hect, "Short History of laser development," *Optical Engineering*, vol. 49, no. 9, pp. 1-23, September 2010.

[3] Kathy Sheehan, "Lasers As Weapons," *SPIE Professional* , pp. 6-9, April 2010.

[4] J A Jr. Fleck, J R Morris, and M D Feit, "Time-Dependent Propagation of High Energy Laser Beams through the Atmosphere," *Applied Physics by Springer Verlag*, no. 10, pp. 129-160, 1976.

[5] J A Jr. Fleck, J R Morris, and M D Feit, "Time-Dependent Propagation of High-Energy Laser Beams through the Atmosphere: II," *Applied Physics by Springer Verlag*, pp. 99-115, 1977.

[6] J L Ulrich and Walsh P B, "Thermal Blooming in the Atmosphere," in *Laser Beam Propagation in the Atmosphere*, J.W. Strohbehn, Ed. Heidelberg, New York, USA: Springer-Verlag, 1978, ch. 7, pp. 223-314.

[7] Vlamimir P. Lukin and Boris V. Fortes, *Adaptive Beaming and Imaging in the Turbulent Atmosphere*. Bellingham, Washington, USA: SPIE, 2002.

[8] Ting-Chung Kim and Taegeun Poon, *Engineering Optics with Matlab*. Singapore: World Scientific, 2006.

[9] Jason D Schmidt, *Numerical simulation of optical wave propagation using MATLAB*. Bellingham: SPIE Press, 2010.

[10] Dietrich Marcuse, *Light Transmission Optics*, 2nd ed. New York, New York, USA: Van Nostrand Reinhold, 1982.

[11] Bahaa Saleh and Malvin C Teich, *Fundementals of Photonics Second Edition*, 2nd ed. Hoboken, New Jersey, USA: John Wiley and Sons, 2007.

[12] Frank L S.J. Pedrotti and Leno S Pedrotti, *Introduction to Optics*, 2nd ed. Englewood Cliffs, New Jersey, USA: Prentice Hall, 1993.

[13] Larry C Andrews and Ronald R Phillips, *Laser Beam Propagation through*

Random Media, 2nd ed. Bellingham, USA: SPIE Press, 2005.

[14] Joeseph W Goodman, *Introduction to Fourier Optics*, 3rd ed. Englewood, Colorado, USA: Roberts and Company, 2005.

[15] Phillup E Nielsen, *Effects of Directed Energy Weapons*. Albuquerque, USA: Directed Energy Professional Society, 2009.

[16] David J Griffiths, *Introduction to Quantum Mechanics*, 2nd ed. Upper Saddle River, NJ: Pearson Prentice Hall, 2005.

[17] V. N. Uzhegov et al., "Statistical Estimation of the Atmospheric Aerosol Absorption Coefficient Based on the Data of Optical Measurements," in *Fifteenth ARM Science Team Meeting*, Daytona Beach, 2005, pp. 1-9.

[18] Phillip Sprangle, Joseph Penano, and Hafizi Bahman, "Optimum Wavelength and Power for Efficient Laser Propagation in Various Atmospheric Environments ," *Journal of Directed Energy*, vol. 2, no. Summer, pp. 71-95, 2006.

[19] Frederick G. Gebhardt, "Self-Induced Thermal Distortion Effects on Target Image Quality," *Appl. Opt.*, vol. 11, no. 6, pp. 1419-1423, June 1972.

[20] Frederick G. Gebhardt, "High power laser propagation," *Applied Optics*, vol. 15, no. 6, pp. 1479-1493, 1976.

[21] Frederick G. Gebhardt, "Overview of Atmospheric Effects on Propagation of High energy Laser Radiation," in *SPIE Proceedings Vol. 195 Atmospheric Effects on Radiative Transfer*, 1979, pp. 162-170.

[22] Frederick G. Gebhardt, "Twenty-Five Years of Thermal Blooming: An Overview," *SPIE Vol. 1221, Propigation of High Energy Laser Beams Through the Earths Atmosphere*, pp. 1-25, 1990.

[23] Frederick G. Gebhardt, "Airbourne laser blooming and turbulence simulations," in *Proceedings SPIE 2120 Lasr Beam Propagation and Control*, 1994, pp. 87-94.

[24] Frederick G. Gebhardt, "Atmospheric Effects Modeling for High Energy Laser Systems," in *Invited Paper SPIE Vol. 2502*, 1995, pp. 101-109.

[25] David C. Smith, "Thermal Defocusing of CO2 Laser Radiation in Gases," *IEEE Journal of Quantum Electronics*, vol. 5, pp. 600-607, December 1969.

[26] David C. Smith, "High-Power Laser Propigation: Thermal Blooming," in *Proceedings of the IEEE*, 1977, pp. 1679-1714.

[27] David C. Smith and Sallie S. Townsend, "Thermal blooming critical power and adaptive optics correction for the ground based laser," in *Proc. SPIE Vol. 1408 0-8194-0498-5*, 1991, pp. 112-118.

[28] Freerick G. Gebhardt and David C. Smith, "Effects of wind on thermal defocusing of CO2 Laser Radiation," *Applied Physics Letters*, vol. 14, no. 2, pp. 52-54, January 1969.

[29] David C. Smith and Frederick G. Gebhardt, "Saturation of the Self-Induced Thermal Distortion of Laser Radiation in a Wind," *Appl. Phys. Letts.*, vol. 16, no. 7, pp. 275-278, April 1970.

[30] Frederick G. Gebhardt and David C. Smith, "Self-Induced Thermal Distortion in the Near Field for a Laser Beam in a Moving Medium," *IEEE Journal of Quantum Electronics*, vol. 7, no. 2, pp. 63-73, Feburary 1971.

[31] Frederick G. Gebhardt and David C. Smith, "Effects of Diffraction on the Self-induced Thermal Distortion of a Laser Beam in a Crosswind," *Appl. Opt.*, vol. 11, no. 2, pp. 244-248, Feburary 1972.

[32] Frederick G. Gebhardt, David C. Smith, R. G. Buser, and R. S. Rohde, "Turbulence Effects on Thermal Blooming," *Appl. Opt.*, vol. 12, no. 8, pp. 1794-1805, August 1973.

[33] Barry C. Hogge, "Propagaiton of High Energy Laser Beams in the Atmosphere," in *Physics of Quantum Electronics, Vol. 1 High energy Lasers and Thier Applications*, S. Jacobs, M. Sargent III, and M. O. Scully, Eds. Reading, USA: Addison Wesley, 1974, pp. 177-246.

[34] Weichel Hugo, *Laser Beam Propagation in the Atmosphere*. Bellingham, USA: SPIE Press, 1989.

[35] P. J. Berger, P.B. Ulrich, Ulrich J.T., and Frederick G. Gebhardt, "Transient Blooming of a Slewed Laser Beam Containing a Region of Stagnant Absorber," *Appl. Opt.*, vol. 11, no. 2, pp. 345-354, Feburary 1977.

[36] Joeseph Penano, Phillip Sprangle, and Bahman Hafizi, "Propagation of High-Energy Laser Beams Through Atmospheric Stagnation Zones," *Journal of Directed Energy*, vol. 2, no. Fall, pp. 107-117, 2006.

235

[37] Scott N. Long, J. O. Miller, Robert T. Brigantic, and Matthew E. Goda, "Using Defocus to Improve Peak Irradiance for Air-toGround High-Energy Laser Weapons," *Journal of Directed Energy*, vol. 2, no. 3, Spring 2007.

[38] Scott N. Long, "Characterizing Effects and Benifits of Beam Defocus on High Energy LAser Performance under Thermal Blooming and Turbulence Conditions for Air-to-Ground Engagements," Air Force Institute of Technology, Wright-Patterson Air Force Base, Dissertation AFIT/DS/ENS/08-05, 2008.

[39] H. Breaux, W. Evers, Sepucha R., and Whitney C., "Algebraic model for cw thermal-blooming effects," *Appl. Opt.*, vol. 18, no. 15, pp. 2638-2644, August 1979.

[40] Amy M. Ngwele and Matthew R. Whiteley, "Scaling Law Modeling of Thermal Blooming in wave Optics," MZA Associates Corporation, Dayton, Technical Report NGIT ABL A&AS, 2006.

[41] K. Petrowski et al., "Turbulent Thermal Blooming," in *SPIE Proceeding Vol. 6951 Atmospheric Propagation V*, 2008.

[42] Robert L. Armstrong, "Aerosol heating and vaporization by pulsed light beams," *Appl. Opt.*, vol. 23, no. 1, pp. 148-155, 1984.

[43] A.A. Ageichik et al., "Thermal blooming of repetitively-pulsed CO2-laser radiation propagating in the atmosphere," *J. Opt. Technology*, vol. 66, no. 11, pp. 939-944, November 1999.

[44] Mark J. Schmitt, "Mitigation of thermal blooming and diffraction effects with high-power beams," *JOSA B*, vol. 20, no. 4, pp. 719-724, 2003.

[45] J, C Owens, "Optical refractive index of air: Dependence on pressure, temperture and compositions," *Applied Optics*, pp. 51-59, 1967.

[46] Phillip H. Roberts, "Time Development of Thermal Blooming," the Optical Sciences Company, Anaheim, Tech Report TR-1574, 2002.

[47] Larry C Andrews and Ronald L Phillips, *Mathematical Techniques for Engineers and Scientists*. Bellinham: SPIE Press, 2003.

[48] P. A. Konyaev and VladmirP. Lukin, "Thermal distortions of focused laser beams in the atmopshere," *Appl. Opt.*, vol. 24, no. 3, pp. 415-421, February 1985.

[49] David C. Zimmerman, "Wave Optics Simulation of Thermal Blooming," the Optical Sciences Company, 2008, Tech Report TR-1771, 2008.

[50] L.S. Hills, J.E. Long, and Frederick G. Gebhardt, "Variable Wind Direction Effects on Thermal Blooming Correction," in *SPIE Proceedings Vol. 1408 Propagation of High-Energy Laser Beams Through the Earth's Atmosphere II* , 1991, pp. 41-57.

[51] T. R. Berkopec, "Thermal Blooming in WaveTrain," MZA Associates Corporation, Albuquerque, Technical Report AFRL-DE-PS-TR-2004-1099, 2003.

[52] David, L. Fried, "The Effect of Slab Thickness on the Accuracy in Thermal Blooming Calculations," the Optical Sciences Company, Anaheim, Technical Report TR-906, 1988.

[53] Lee C. Bradley and Jan Herrmann, "Phase Compensation for Thermal Blooming," *Applied Optics*, vol. 13, no. 2, pp. 331-334, February 1974.

[54] Glen A. Tyler, John F. Belsher, and Phillip H. Roberts, "A Discussion of Some Issues Associated with the Evaluation and Compensation of Thermal Blooming," the Optical Sciences Company, Anaheim, Tech Report TR-779, 1986.

[55] Phillip H. Roberts, Glen A. Tyler, and William Moretti, "ATL Thermal Blooming Study," the Optical Sciences Company, Anaheim, Tech Report TR-1569, 2002.

[56] Jack D. Gaskill, *Linear Systems, Fourier Transforms, and Optics*. New York, USA: John Wiley and Sons, 1978.

[57] Robert K. Tyson and Benjamin W. Frazier, *Field Guide to Adaptive Optics*. Bellingham: SPIE Press, 2004.

[58] Kolmogorov, "The local structure of turbulence in an incompressible viscous fluid for very large Reynolds numbers," *C.R. (Doki) Acad. Sci. U.S.S.R*, pp. 301-305, 1941.

[59] Jeffrey D. Barchers, Private Communication, 2010, Nutronics Inc.

[60] David L. Fried, "Blurring Effects in Thermal Blooming," the Optical Sciences Company, Anaheim, Technical Report TR-902R2, 1988 Revised 1989 and 1991.

[61] A. M. Obukhov, "Structure of the temperture field in turbulent flow," *Ser. Georgr. I Geofiz*, pp. 58-69, 1949.

[62] S. Corrsin, "On the spectrum of isotropic temperture fluctuations in isotropic turbulence," *J. Appl. Phys.*, pp. 469-473, 1951.

[63] James C. Bowers, "Numerical Investigation of Statistical Turbulence Effects on Beam Propigation Through 2-D Shear Mixing Layer," Air Force Institute of Technology, Wright-Patterson Air Force Base, Thesis 2010.

[64] S. F. Clifford, "The Classical Theory of Wave Propagation in the Atmosphere," in *Laser Beam Propagation in the Atmosphere*, J. W. Strohbehn, Ed. New York, USA: Springer Verlag, 1978, ch. 2, pp. 9-41.

[65] A. Ishimaru, *Wave Propagation and Scaterring in a Random Media*. New York: IEEE Press, 1999.

[66] R. J. Sasiela, *Electromagnetic Wave Propagation in Turbulence: Evaluation and Application of Mellin Transforms Second Edition*. Bellingham: SPIE Press, 2007.

[67] Joeseph W. Goodman, *Statistical Optics*. New York : John Wiley & Sons, 1985.

[68] Larry C. Andrews, *Field Guide to Atmospheric Optics*. Bellingham: SPIE Press, 2004.

[69] Robert K. Tyson, *Introduction to Adaptive Optics*. Bellingham, USA: SPIE Press, 2000.

[70] Glen P. Perram, Salvatore J. Cusumano, Robert L. Hengehold, and Steven T. Fiorino, *An Introduction to Laser Weapon Systems*. Albuquerque, USA: Directed Energy Professional Society, 2010.

[71] David L. Fried, "Statistics of a geometric representation of wavefront distortion," *J. Opt. Soc. Am.*, vol. 55, no. 11, pp. 1427-1431, 1965.

[72] Michael C. Roggemann and Byron M. Welsh, *Imaging Through Turbulence*. Boca Raton, USA: CRC Press, 1996.

[73] David A. Nahrstedt, "Influence of a thermally bloomed atmosphere on target image quality," *Applied Optics*, vol. 21, no. 4, pp. 596-609, February 1982.

[74] David A. Nahrstedt, "Image compensation in the presence of thermal blooming," *Applied Optics*, vol. 22, no. 2, pp. 244-252, January 1983.

[75] Max Born and Emil Wolf, *Principles of Optics*, 7th ed. Cambridge, UK:

Cambridge University Press, 1999.

[76]   Robert J. Noll, "Zernike polynomials and atmospheric turbulence," *J. Opt. Soc. Am.*, vol. 66, no. 3, pp. 207-211, 1976.

[77]   Virendra N. Mahajan, *Optical Imaging and Aberration Part II Wave Diffraction Optics*. Bellingham, USA: SPIE Press, 1998.

[78]   D. L. Greenwood, "Bandwidth specifications for adaptive optics systems," *J. Opt. Soc. Am.*, vol. 67, pp. 390-392, 1977.

[79]   Robert K. Tyson, *Principles of Adaptive Optics*, 3rd ed. Boca Raton, USA: CRC Press, 2010.

[80]   John W. Hardy, *Adaptive Optics for Astronomical Telescopes*. Oxford, New York: Oxford University Press, 1998.

[81]   Francois Roddier, Ed., *Adaptive Optics in Astronomy*. Cambridge, United Kingdom: Cambridge University Press, 1999.

[82]   William B. Bridges and James E. Pearson, "Thermal blooming compensation using coherent optical adaptive techniques (COAT)," *Applied Physics Letters*, vol. 26, no. 9, pp. 539-543, May 1975.

[83]   C. A. Primmerman and D. G. Fouche, "Thermal-blooming compensation: experimental observations using a deformable-mirror system," *Applied Optics*, vol. 15, no. 4, pp. 990-995, April 1976.

[84]   James E. Pearson, "Thermal blooming compensation with adaptive optics," *Optics Letters*, vol. 2, no. 1, pp. 7-9, January 1978.

[85]   C.A. Primmerman, B. F. Johnson, and Wigdor I., "Thermal-blooming compensation using CLASP system," *Applied Optics*, vol. 17, no. 18, pp. 2909-2919, September 1978.

[86]   Prasad R. Akkapeddi, E.T. Siebert, J. Baker, G. T. Volpe, and H. J. Robertson, "Target loop adaptive optics: thermal blooming correction," *Applied Optics*, vol. 20, no. 4, pp. 564-572, February 1981.

[87]   Jan Herrmann, "Properties of phase conjugate adaptive optical systems," *Journal Optical Society of America*, vol. 67, no. 3, pp. 290-295, March 1977.

[88] V. V. Vorobev and V. V. Shemetov, "Stability of a Light Beam and Its Decomposition with Thermal Self-Stress in a Moving Media," *Izv. Vyssh Uchebn. Zaved. Radiofiz.*, vol. 21, p. 1610, 1978.

[89] V. V. Vorob'ev, "Thermal Blooming of Laser Beams in the Atmosphere," *Prog. Quant. Electr.*, vol. 15, pp. 1-152, 1991.

[90] Jonathan, F. Schonfeld, "The Theory of Compensated Laser Propagation through Strong Thermal Blooming," *The Lincoln Laboratory Journal*, vol. 5, no. 1, pp. 131-150, 1992.

[91] Daniel E. Novoseller, "Adaptive optics model for thermal blooming," *Applied Optics*, vol. 26, no. 19, pp. 4149-4150, October 1987.

[92] Daniel E. Novoseller, "Zernike-ordered adaptive-optics correction of thermal blooming," *J. Opt. Soc. Am. A*, vol. 5, no. 11, pp. 1937-1942, November 1988.

[93] R. J. Briggs, "Models of high spatial frequency thermal blooming instabilities," Lawrence Livermore National Labortory, Livermore, Technical Report UCID-21118, 1987.

[94] Karr T.J., "Thermal Blooming Compensation Instabilities," Lawrence Livermore National Laboratory, Livermore, Technical Report UCID-21172, 1987.

[95] T. J. Karr, "Thermal bloomin compensation instabilities," *J. Opt. Soc. Am.*, vol. 6, no. 7, pp. 1038-1048, July 1989.

[96] T. J. Karr, J. R. Morris, D. H. Chambers, J. A. Viecelli, and P. G. Cramer, "Perturbation growth by thermal blooming in turbulence," *J. Opt. Soc. Am.*, vol. 7, no. 6, pp. 1103-1124, June 1990.

[97] John J. Barnard, "Fine scale thermal blooming instability: a linear stability analysis," *Applied Optics*, vol. 28, no. 3, p. 1989, February 1989.

[98] J. R. Morris, "Scalar Green's-function derivation of the thermal lbooming compensation instability equations," *J. Opt. Soc. Am.*, vol. 6, no. 12, pp. 1859-1862, 1989.

[99] J. R. Morris, J. A. Viecelli, and T. J. Karr, "Effects of a random wind field on thermal blooming instabilites," in *SPIE Vol. 1221 Propagation of High-Energy Laser Beams through the Earth's Atmosphere*, 1990, pp. 229-240.

[100] D. H. Chamber, T. J. Karr, J. R. Morris, P. Cramer, and J. A. Viecelli, "Linear theory of uncompensated thermal blooming in turbulence," *Phys. Rev. A*, vol. 41, no. 12, pp. 6982-6991, June 1990.

[101] N. M. Kroll and P. L. Kelley, "Temporal and Spatial Gain in Stimulated Light Scattering," *Phys. Rev. A*, vol. 4, no. 2, pp. 763-776, October 1971.

[102] R. Holmes, R. Myers, and C. Duzy, "A linearized theory of transient laser heating in fluids.," *Phys. Rev. A*, vol. 44, no. 10, pp. 6862-6876, 1991.

[103] Daniel, G. Fouche, Charles Higgs, and C. Frederick Pearson, "Scaled Atmospheric Blooming Experiments," *The Lincoln Laboratory Journal*, vol. 5, no. 2, pp. 273-293, 1992.

[104] Bernadette Johnson and Charles A. Primmerman, "Experimental observation of thermal-blooming phase-compensation instability," *Optics Letters*, vol. 14, no. 12, pp. 639-641, June 1989.

[105] Bernadette Johnson and Jonathan F. Schonfeld, "Demonstration of spontaneous thermal-blooming phase-compensation instability," *Optics Letters*, vol. 16, no. 16, pp. 1258-1260, August 1991.

[106] Bernadette Johnson, "Thermal-Blooming Laboratory Experiments," *The Lincoln Laboratory Journal*, vol. 5, no. 1, pp. 151-170, 1992.

[107] Jonathan F. Schonfeld, "Analysis and modeling of thermal-blooming compensation," in *Invited Paper, SPIE Vol. 1221, Propagation of High-Energy Laser Beams through the Earth's Atmosphere*, 1990, pp. 118-131.

[108] Jonathan F. Schonfeld and Bernadette Johnson, "Pattern formation from thermal-blooming phase-compensation instability," *J. Opt. Soc. Am. B*, vol. 9, no. 10, pp. 1800-1802, October 1992.

[109] Jonathan F. Schonfeld, "Instability in saturated full-field compensation for thermal blooming," *J. Opt. Soc. Am. B*, vol. 9, no. 10, pp. 1794-1799, October 1992.

[110] Jonathan F. Schonfeld, "Linearized theory of thermal-blooming phase-compensation instability with realistic adaptive-optics geometry," *J. Opt. Soc. Am. B*, vol. 9, no. 10, pp. 1803-1812, October 1992.

[111] David L. Fried, "Analysis of Turbulence Velocity Spread Data," the Optical Sciences Company, Anaheim, Technical Report TR-923, 1988.

241

[112] Roque K. Szeto and David L. Fried, "Turbulence Thermal Blooming Interactions (TTBI): Static," the Optical Sciences Company, Anaheim, Technical Report TR-921R2, 1988.

[113] Roque K. Szeto and David L. Fried, "Analysis of the Time-Dependence of TTBI," the Optical Sciences Company, Anaheim, Technical Report TR-967, 1989.

[114] Roque K. Szeto and David L. Fried, "Random Wind Sampling Considerations for Time-Dependent TTBI Calculations," the Optical Sciences Company, Anaheim, Technical Report TR-1004, 1989.

[115] David L. Fried, "Numerical Simulation of the Effects of Mini-Shear," the Optical Sciences Company, Anaheim, Technical Report TR-1024, 1989.

[116] Roque K. Szeto and David L. Fried, "Mini-Shear Effects and PCI," the Optical Sciences Company, Anaheim, 1076 TR-1076, 1990.

[117] Roque K. Szeto and David L. Fried, "Steady State TTBI Singular Point and PCI Thresholds," the Optical Sciences Company, Anaheim, Technical Report TR-1083, 1990.

[118] David L. Fried and Roque K. Szeto, "Wind-shear induced stabilization of PCI," *J. Opt. Soc. Am.*, vol. 15, no. 5, pp. 1212-1226, May 1998.

[119] Jeffrey D. Barchers, "Linear analysis of thermal blooming compensation instabilities in laser propagation," *J. Opt. Soc. Am. A.*, vol. 26, no. 7, pp. 1638-1653, July 2009.

[120] Mark F. Spencer, Salvatore J. Cusumano, Jason D. Schmidt, and Steven T. Fiorino, "Impact of spatial resolution on thermal bloming phase compensation instability," in *Proc. of SPIE Vol 7816 781609-1*, San Diego, 2010.

[121] Vladimir P. Lukin and Boris V. Fortes, "The influence of wavefront dislocations on phase conjugation instability with thermal blooming compensation," *Optical Engineering*, vol. 2989, no. 277-786X19, pp. 256-269, 1997.

[122] David L. Fried, "Branch Cuts in the Phase Function," *J. Opt. Soc. Am. A.*, vol. 31, no. 15, pp. 2865-2881, 1992.

[123] Dennis C. Ghiglia and Mark D. Pritt, *Two-Dimensional Phase Unwrapping Theory, Algorithms, and Software*. New York, USA: John Wiley & Sons, 1998.

[124] V. V. Voitsekhovich, D. Kouznetsov, and D. K. Morozov, "Desity of turbulence induced phase dislocations," *Appl. Opt.*, vol. 37, no. 21, pp. 4525-4535, 1998.

[125] Casey J. Pellizzari, "Phase Unwrapping in the Presence of Strong Turbulence," Air Force Institute of Technology, Wright-Patterson AFB, Thesis AFIT/GE/ENG/10-23, 2010.

[126] David L. Fried, "Adaptive optics wave function reconstruction and phase unwrapping when branch points are present," *Opt. Commun.*, vol. 200, pp. 43-72, 1992.

[127] David L. Fried, "Branch Point Problem in Adaptive Optics," *J. Opt. Soc Am. A*, vol. 15, no. 10, pp. 2759-2768, 1998.

[128] Terry J. Brennan, Phillip H. Roberts, and David C. and Mann, "WaveProp A Wave Optics Simulation System For Use with MATLAB," the Optical Sciences Company, Anaheim, User's Guide Version 1.3, 2010.

[129] Terry J. Brennan and Phillip H. Roberts Roberts, "AOTools The Adaptive Optics Toolbox For Use with MATLAB," the Optical Sciences Company, Anaheim, Users Guide Version 1.4, 2010.

[130] Steven, T. Fiorino et al., "A First Principles Atmospheric Propagation & Characterization Tool-the Laser Environment Effects Definition and Reference (LEEDR)," in *SPIE Lasers and Applications in Science and Engineering (LASE) 6878-10*, 2008.

[131] Steven T. Fiorino, Research Associate Professor of Atmospheric Physics, Air Force Institute of Technology, 2011, Private Communication.

REPORT DOCUMENTATION PAGE

1. REPORT DATE *(DD-MM-YYYY)* 24-03-2010	2. REPORT TYPE Master's Thesis	3. DATES COVERED *(From – To)* Mar 2009-Mar 2011

4. TITLE AND SUBTITLE Branch Point Mitigation of Thermal Blooming Phase Compensation Instability	5a. CONTRACT NUMBER
	5b. GRANT NUMBER
	5c. PROGRAM ELEMENT NUMBER
6. AUTHOR(S) Mark F. Spencer	5d. PROJECT NUMBER N/A
	5e. TASK NUMBER
	5f. WORK UNIT NUMBER

7. PERFORMING ORGANIZATION NAMES(S) AND ADDRESS(S) Air Force Institute of Technology Graduate School of Engineering and Management (AFIT/EN) 2950 Hobson Way WPAFB OH 45433-7765	8. PERFORMING ORGANIZATION REPORT NUMBER AFIT/OSE/ENP/11-M02

9. SPONSORING/MONITORING AGENCY NAME(S) AND ADDRESS(ES) Dr. Harro Ackermann HEL - JTO Air Force Rep. 801 University Blvd. SE, Suite 209 Albuquerque, NM 87106	10. SPONSOR/MONITOR'S ACRONYM(S) HEL JTO
	11. SPONSOR/MONITOR'S REPORT NUMBER(S)

12. DISTRIBUTION/AVAILABILITY STATEMENT
APPROVED FOR PUBLIC RELEASE; DISTRIBUTION UNLIMITED

13. SUPPLEMENTARY NOTES

14. ABSTRACT
Thermal blooming can have a major impact on high-energy laser (HEL) beam propagation in the atmosphere. In theory, an adaptive-optics (AO) system can mitigate the nonlinear optical effects induced by thermal blooming; however, when a single deformable mirror is used for phase-only compensation, analysis predicts the possibility of instability. This instability is appropriately termed phase compensation instability (PCI) and arises with the time-dependent development of spatial perturbations found within the HEL beam. These spatial perturbations act as local hot spots that produce negative-lens-like optical effects in the atmosphere. An AO system corrects for the hot spots by applying positive-lens-like phase compensations. In turn, this increases the strength of the thermal blooming and leads to a runaway condition, i.e. positive feedback in the AO control loop. This study uses a series of computational wave-optics experiments to explore the conditions for insipient PCI. Horizontal propagation is modeled with the effects of extinction, thermal blooming, and turbulence for a focused Gaussian beam. In addition, a nominal AO system is used for phase compensation from a point source beacon. Results show that the development of branch points under strong thermal blooming reduces the possibility of PCI. Parameters within the AO system, such as the number of actuators on the deformable mirror and the resolution of the wavefront sensor, are varied to determine the impact of branch points in the development of PCI.

15. SUBJECT TERMS
Directed Energy, High Energy Laser Weapons, Computational Wave-Optics, Adaptive Optics

16. SECURITY CLASSIFICATION OF:			17. LIMITATION OF ABSTRACT	18. NUMBER OF PAGES	19a. NAME OF RESPONSIBLE PERSON Salvatore J. Cusumano (AFIT/ENP)
a. REPORT U	b. ABSTRACT U	c. THIS PAGE U	UU	266	19b. TELEPHONE NUMBER *(Include area code)* (937) 255-3636 Ext: 7294